From conventional to delay/Doppler altimetry

Abderrahim Halimi

Université de Toulouse

THÈSE

En vue de l'obtention du

DOCTORAT DE L'UNIVERSITÉ DE TOULOUSE

Délivré par :
Institut National Polytechnique de Toulouse (INP Toulouse)

Discipline ou spécialité :

Signal, Image, Acoustique et Optimisation

Présentée et soutenue par :
Abderrahim HALIMI

le : jeudi 17 octobre 2013

Titre :

From conventional to delay/Doppler altimetry

Ecole doctorale :
Mathématiques Informatique Télécommunications (MITT)

Unité de recherche :
Institut de Recherche en Informatique de Toulouse - IRIT (UMR 5505)

Directeur(s) de Thèse :
Corinne MAILHES, Professeur à l'INP de Toulouse, Directrice de thèse
Jean-Yves TOURNERET, Professeur à l'INP de Toulouse, Co-Directeur de thèse

Rapporteurs :
Bertrand CHAPRON, Ingénieur de recherche, IFREMER
André FERRARI, Professeur à l'Université de Nice
Philippe FORSTER, Professeur à l'Université de Paris-Ouest Nanterre

Membre(s) du jury :
Olivier BESSON, Enseignant-Chercheur, ISAE, Toulouse, Président du Jury
Grégoire MERCIER, Professeur à ENST Bretagne, Examinateur
Bertrand CHAPRON, Ingénieur de recherche, IFREMER
André FERRARI, Professeur à l'Université de Nice
Philippe FORSTER, Professeur à l'Université de Paris-Ouest Nanterre

Remerciements

Je tiens d'abord à remercier chaleureusement ma directrice de thèse Corinne Mailhes et mon co-directeur Jean-Yves Tourneret qui m'ont encadré durant ces trois années de thèse. Je les remercie pour leur disponibilité en toutes circonstances, leur suivi continu, leur bonne humeur ainsi que leurs conseils avisés qui ont permis de bien guider ce travail et d'améliorer sa qualité. Je les remercie aussi pour la confiance qu'ils m'ont accordé tout au long de cette thèse en me laissant une grande liberté pour mener à bien ce travail de recherche.

Durant ces trois années, j'ai eu la chance de collaborer avec des industriels de haut niveau qui m'ont apporté leurs conseils et expériences à travers de nombreuses réunions. Je pense notamment à Pierre Thibaut et Thomas Moreau de CLS et Francois Boy et Nicolas Picot du CNES. Je leur exprime mes sincères remerciements pour ces trois années de recherche. Je remercie aussi tous ceux de CLS et du CNES qui ont participé, de près ou de loin, à l'aboutissement de cette thèse de doctorat.

Olivier Besson, professeur à l'université de Toulouse, m'a fait l'honneur de présider le jury, qu'il soit remercié pour son intérêt pour mon travail. J'adresse mes sincères remerciements à Bertrand Chapron, ingénieur de recherche à IFREMER, André Ferrari, professeur à l'université de Nice, et Philippe Forster, professeur à l'université de Paris-Ouest, qui ont accepté de rapporter cette thèse, ainsi qu'à Grégoire Mercier, professeur à ENST bretagne, pour l'avoir examinée.

Ma gratitude s'adresse aussi à tout le personnel de l'IRIT et plus spécialement à celui de l'équipe SC: Benoit, Charly, Hasan, Herwig, Marie, Marie-Laure, Martial, Nathalie, Nicolas, ..., sans qui cette thèse ne serait pas ce qu'elle est. Je remercie également Sylvie Eichen, Sylvie Armengaud et Frédéric Peyré qui ont été disponibles à chaque fois que j'ai eu besoin d'une aide.

Je passe ensuite une dédicace spéciale à mes camarades de bureau Cécile, Qi, Yoann ainsi qu'à tous les jeunes que j'ai eu le plaisir de côtoyer durant ces années: Abdelaziz, Adnan, Bouchra, Chao, Emilie, Fabian, Farouk, Florian, Hichem, Jean-Adrien, Jorge, Mohammed, Nesrine, Ning-Ning, Nil, Olivier, Raoul, Romain, Sébastien, Sokchenda, Tarik, Tony, Victor, ... Les moments magnifiques que nous avons passé ensemble au bureau, dans le couloir, à la cantine, en conférence, au foyer et sur le terrain de foot, je les garde précieusement au fond de mon coeur.

Je tiens finalement à remercier ma famille dont mes trois frères ainsi que mes parents sans qui rien de cela n'aurait été possible. Qu'ils trouvent dans ces lignes toute mon admiration, mon affection et ma gratitude.

Abderrahim

Résumé

Depuis plus de vingt ans, les altimètres classiques comme Topex, Poseidon-2 ou Poséidon-3, ont fourni des formes d'onde qui sont utilisées pour estimer de nombreux paramètres tels que la distance entre le satellite et la scène observée, la hauteur des vagues et la vitesse du vent. L'amélioration de la qualité des paramètres altimétriques a nécessité le développement de plusieurs modèles d'échos et d'algorithmes d'estimation paramétrique. Par ailleurs, un grand effort est récemment dédié au traitement des échos côtiers afin d'analyser les mesures altimétriques le plus près possible des côtes. Cette thèse s'intéresse à la résolution de ces deux problèmes, à savoir, le traitement des formes d'onde côtières et l'amélioration de la qualité des paramètres océaniques estimés. La première partie de l'étude traite le problème des formes d'onde côtières en proposant un nouveau modèle altimétrique tenant compte de la présence éventuelle d'un pic sur l'écho altimétrique. Dans la seconde partie de notre travail, nous nous sommes intéressés à l'étude de l'altimétrie SAR/Doppler. Cette nouvelle technologie vise à réduire le bruit de mesure et à augmenter la résolution le long de la trace par rapport à l'altimétrie conventionnelle. Deux modèles altimétriques ont été développés afin d'estimer les paramètres associés aux échos SAR/Doppler. Ces modèles montrent une nette amélioration de la qualité des paramètres estimés par rapport à l'altimétrie conventionnelle.

Abstract

For more than twenty years, conventional altimeters like Topex, Poseidon-2 or Poseidon-3, have been delivering waveforms that are used to estimate many parameters such as the range between the satellite and the observed scene, the wave height and the wind speed. Several waveform models and estimation processing have been developed for the oceanic data in order to improve the quality of the estimated altimetric parameters. Moreover, a great effort has been devoted to process coastal echoes in order to move the altimetric measurements closer to the coast. In this thesis, we are interested in resolving these two problems, i.e., processing coastal waveforms and improving the quality of the estimated oceanic parameters. The first part of the study considers the problem of coastal waveforms and proposes a new altimetric model taking into account the possible presence of peaks affecting altimetric echoes. In a second part of our work, we have been interested in the delay/Doppler altimetry. This new technology aims at reducing the measurement noise and increasing the along-track resolution when compared to conventional altimetry. Two altimetric models have been developed in order to estimate the resulting delay/Doppler echoes. These models allow a clear improvement in parameter estimation when compared to conventional altimetry.

Abreviations and notations

Abreviations

ANRE	Averaged normalized reconstruction error
ARE	Averaged reconstruction error
BAGP	Brown with asymmetric Gaussian peak
BGP	Brown with Gaussian peak
BRF	Burst repetition frequency
Bias	Parameter bias
CA	Conventional altimetry
CA“n”	“n” parameters conventional altimetry
CA-LRM	Conventional altimetry from LRM mode
CA-SARM	Conventional altimetry from SAR mode
CLS	Collecte localisation satellite
CNES	Centre national d’études spatiales
CPP	Cryosat processing prototype
CRB	Cramér-Rao bound
DD	Delay/Doppler
DDA	Delay/Doppler altimetry
DDA“n”	“n” parameters delay/Doppler altimetry
DDM	Delay/Doppler map

FFT	Fast Fourier Transform
FIM	Fisher information matrix
FSIR	Flat surface impulse response
G-DDA	Generalized delay/Doppler altimetry
GPS	Global positioning system
LM	Levenberg-Marquardt method
LRM	Low resolution mode
LS	Least squares
ML	Maximum likelihood
MLE	Maximum likelihood estimator
MSS	Mean sea surface
NM	Nelder-Mead method
NR	Newton-Raphson method
NRE	Normalized reconstruction error
NQE	Normalized quadratic error
OCOG	Offset center of gravity
PDF	Probability density function
PRF	Pulse repetition frequency
PTR	Point target response of the radar
RCRB	Square root of the Cramér-Rao bound
RE	Reconstruction error
RMSE	Root mean square error
SAR	Synthetic aperture radar
SARInM	Synthetic aperture radar interferometric mode
SIRAL	Synthetic aperture interferometric radar altimeter
SSB	Sea state bias
SSH	Sea surface height

SSHA	Sea surface height anomaly
STD	Standard-deviation
WLS	Weighted least squares

Modeling notations

t :	Two-way incremental ranging times
t' :	Time referenced to the instant of transmission
f :	Doppler frequency
K :	Number of time (delay) samples
$s(t)$:	Continuous altimetric signal
$\boldsymbol{s}$:	Discrete altimetric vector
$p(t)$:	Continuous Gaussian peak
$\boldsymbol{p}$:	Discrete Gaussian peak vector
$\tilde{s}(t)$:	Continuous Brown plus Gaussian peak
$\tilde{\boldsymbol{s}}$:	Discrete Brown plus Gaussian peak
$y(t)$:	Continuous noisy altimetric signal
$\boldsymbol{y}$:	Discrete noisy altimetric vector (or observed signal)
$\boldsymbol{n}$:	Noise vector corrupting the altimetric vector
$\boldsymbol{q}$:	Noise corrupting the DDM
$P(t, f)$:	Power of a delay/Doppler map
G :	Gain of the radar antenna
N :	Number of Doppler beams
N_{eff} :	Effective number of looks
N_{useful} :	Number of useful Doppler beams
ρ :	Radius from polar coordinate
ϕ :	Angle from polar coordinate
r :	Range between the satellite and the observed surface

P_u : Amplitude of the waveform

τ : Epoch of the waveform

τ_s : Epoch of the waveform expressed in seconds

SWH : Significant wave height of the waveform

λ_s : Skewness of the waveform

ξ : Mispointing angle with respect to the z axis

$\tilde{\phi}$: Mispointing angle with respect to the x axis

ξ_{ac} : Across-track mispointing angle

ξ_{al} : Along-track mispointing angle

A : Amplitude of the peak

T : Location of the peak

σ : Standard deviation of the Gaussian peak

η : Asymmetry coefficient of the peak

N_t : Thermal noise

m_p : Number of parameter of interest

σ_s : Standard deviation of the PDF ($\sigma_s = \frac{\text{SWH}}{2c}$)

σ_p : Standard deviation of the Gaussian approximation of the PTR_T

σ_c : Standard deviation of the Gaussian approximation of $\text{PTR}_T * \text{PDF}$ ($\sigma_c^2 = \sigma_s^2 + \sigma_p^2$)

f_n : Doppler frequency of the nth Doppler beam

y_n : Along-track coordinate of the nth Doppler beam

y_{dop} Width of the Doppler beam

m : Number of terms required to approximate the infinite sum in the DDA FSIR

T_s : Sampling period or time resolution

F : Frequency resolution

B : Reception bandwidth of the altimeter

τ_b : Burst length

N_t : Time oversampling factor

N_f : Frequency oversampling factor

c Speed of light

λ : Wavelength

σ^0 : Backscatter coefficient of the surface

γ : Antenna bandwidth parameter ($\gamma = \frac{1}{2\ln 2}\sin^2\theta_{3\text{dB}}$)

$\theta_{3\text{dB}}$: 3 dB antenna beam width

L_p : Two-way propagation loss

v_s : Satellite velocity

G_0 : Antenna power gain at boresight

α_r : Curvature factor

R : Earth radius

h : Altitude of the satellite

L : Number of incoherent summation of consecutive echoes for DDA

L_c : Number of incoherent summation of consecutive echoes for CA

N_{MC} : Number of Monte Carlo realizations

Mathematical functions

erf(.) : Gaussian error function

$\delta(.)$: Delta function

$U(.)$: Heaviside function

$\Gamma(.)$: Gamma function

$\mathcal{G}(.)$: Gamma distribution

$I_k(.)$: kth order modified Bessel function of the first kind

$\mathcal{I}_{\mathbb{R}^+}$: Indicator function on $\mathbb{R}^+$

$E(.)$: Expectation operator

Re(.) : Real part operator

Estimation methods and Cramér-Rao bounds

$f(\boldsymbol{y}|\boldsymbol{\theta})$: Likelihood function of the observed samples

f_{B} : Likelihood function associated with the Brown model

$\mathcal{C}$: Cost function

$\mathcal{C}_{\text{B}}$: Cost function associated with the Brown model

$\boldsymbol{\theta}$: Parameter vector of interest

$\boldsymbol{\theta}_{\text{B}}$: Parameter vector of Brown's model

$\boldsymbol{\theta}_{\text{p}}$: Parameter vector containing peak parameter

$\boldsymbol{F}$: The Fisher information matrix

$\boldsymbol{F}_{\text{B}}$: The Fisher information matrix associated with Brown's model

$\boldsymbol{F}_{c}$: The Fisher information matrix associated with CA

$\boldsymbol{F}_{d}$: The Fisher information matrix associated with DDA

$\boldsymbol{H}_{\text{B}}$: Hessian of $\mathcal{C}_{\text{B}}$

$\widetilde{\boldsymbol{B}}$: Matrix containing the derivatives of $\tilde{s}_k$ according to $\theta_{\text{B,i}}$

$\boldsymbol{B}_{\text{B}}$: Matrix containing the derivatives of s_k according to $\theta_{\text{B,i}}$

$\widetilde{\boldsymbol{d}}$: Vector of size $(K \times 1)$ related to $\tilde{s}_k$ and y_k

$\boldsymbol{d}_{\text{B}}$: Vector of size $(K \times 1)$ related to s_k and y_k

$\widetilde{\boldsymbol{P}}$: Matrix containing the derivatives of the peak $\boldsymbol{p}$ according to $\theta_{\text{p,i}}$

$\boldsymbol{g}$: Vector of residues

$\boldsymbol{J}$: Matrix containing the derivatives of $\boldsymbol{g}$ according to θ_i

$\boldsymbol{D}_{c}$: Matrix containing the derivatives of the conventional echo $\boldsymbol{s}$ according to θ_i

$\boldsymbol{D}_{d}$: Matrix containing the derivatives of the multi-look echo $\boldsymbol{s}$ according to θ_i

$\boldsymbol{\Sigma}$: Covariance matrix of the observed conventional echo

$\boldsymbol{\Lambda}$: Covariance matrix of the observed multi-look echo

Contents

List of Figures

List of Tables

Introduction (in French)

Cette thèse s'est déroulée au sein de l'équipe *Signal et Communications* de l'*Institut de Recherche en Informatique de Toulouse (IRIT)*. Elle a été financée par le ministère de l'enseignement supérieur français et a été menée en étroite collaboration avec l'entreprise "*Collecte Localisation Satellite*" (CLS) et le "*Centre National d'Études Spatiales*" (CNES). Cette thèse fait suite au travail effectué par J. Severini dans la même équipe, et a été consacrée à la modélisation et l'estimation des paramètres des signaux altimétriques. L'ensemble de la thèse a été rédigée en anglais afin de permettre une plus large diffusion. Toutefois, nous avons pris soin de rajouter dans chaque chapitre une introduction et une conclusion en français, en plus de la version anglaise.

Depuis plus de vingt ans, les altimètres classiques comme Topex, Poseidon-2 ou Poséidon-3, ont fourni des formes d'onde qui sont utilisées pour estimer de nombreux paramètres physiques tels que la distance entre le satellite et la scène observée, la hauteur des vagues et la vitesse du vent. Ces formes d'onde résultent principalement de l'observation des surfaces océaniques pour lesquelles plusieurs modèles de formes d'onde et des algorithmes d'estimation ont été développés afin d'améliorer la qualité des paramètres altimétriques estimés. Cependant, les formes d'onde altimétriques peuvent être corrompues par l'énergie réfléchie par la terre, par la pluie ou par des surfaces présentant des coefficients de rétrodiffusion différents de la surface océanique, ce qui rend les algorithmes classiques inefficaces. De ce fait, un grand effort est maintenant consacré au traitement des échos côtiers afin de valider les mesures altimétriques près de la côte. La première partie de cette thèse traite cette question en proposant un nouveau modèle altimétrique approprié pour les zones côtières. Ce modèle

tient compte de la présence éventuelle d'un pic affectant les échos altimétriques côtiers. Deux algorithmes d'estimation sont alors proposés afin de valider ce modèle. Ces algorithmes montrent une amélioration de la qualité des paramètres estimés.

La précision des paramètres altimétriques estimés constitue un point très important en altimétrie en raison de l'utilisation de ces paramètres dans de nombreuses applications telles que la géophysique, la bathymétrie, etc. Cette précision est réduite en raison de la corruption des mesures altimétriques par un bruit de chatoiement et à cause de l'énergie réfléchie par la terre dans les zones côtières. L'altimétrie SAR/Doppler, proposée par [Raney, 1998], se présente alors comme une solution pour améliorer la qualité de la mesure et réduire l'effet de la côte. En effet, cette nouvelle technologie s'inscrit dans la logique de l'amélioration de la mesure et a deux objectifs principaux. Le premier est de réduire le bruit de mesure en augmentant le nombre d'observations ce qui permet d'améliorer la qualité des paramètres géophysiques estimés. Le second est d'augmenter la résolution dans la direction de déplacement du satellite ce qui permet aux mesures de rester valides jusqu'à une distance d'environ 300 mètres de la côte (alors qu'elle est d'environ 10 km pour l'altimétrie conventionnelle). Cependant, l'altimétrie SAR/Doppler nécessite l'élaboration de nouveaux modèles altimétriques puisqu'elle fournit des échos de forme différente de celle des échos conventionnels. Ainsi, la deuxième partie de la thèse s'intéresse à ce point en proposant deux modèles altimétriques pour l'altimétrie SAR/Doppler. Les paramètres de ces modèles seront estimés par l'élaboration d'algorithmes d'estimation appropriés fondés sur le maximum de vraisemblance ou des approches de moindres carrés. Les résultats obtenus sont très prometteurs et montrent l'intérêt d'utiliser l'altimétrie SAR/Doppler comme un nouvel outil d'observation de l'océan.

Structure du manuscrit

La thèse est organisée comme suit

- **Chapitre 1:** Ce chapitre décrit tout d'abord les principes et objectifs de l'altimétrie spatiale.

Deuxièmement, il présente la forme d'onde altimétrique et fournit un état de l'art des différents modèles de forme d'onde et les stratégies d'estimation disponibles dans la littérature. Les limitations de l'altimétrie conventionnelle sont ensuite décrites. Ces dernières sont principalement dues, premièrement, à la contamination des échos par des retours de la terre dans les zones côtières en raison de la grande taille de la tache au sol et, deuxièmement, à la précision des paramètres estimés qui est réduite en raison de la corruption des formes d'onde par le bruit de chatoiement. Certaines solutions techniques à ces problèmes sont finalement présentées.

- **Chapitre 2:** Ce chapitre s'intéresse à l'étude des formes d'onde côtières. Ces échos sont parfois corrompus par des pics provoqués par des zones de fort coefficient de rétrodiffusion à l'intérieur de la surface illuminée ou par la modification de l'état de la mer près du rivage. Nous proposons alors un nouveau modèle altimétrique comme la somme du modèle de Brown et d'un pic gaussien asymétrique. Ce pic est paramétré par une position, une amplitude, une largeur et d'un coefficient d'asymétrie. Un estimateur du maximum de vraisemblance est étudié pour estimer les paramètres du modèle de Brown avec pic. Les bornes de Cramér-Rao des paramètres sont ensuite calculées afin de fournir une référence en termes d'erreur d'estimation. Les performances du modèle proposé ainsi que de la stratégie d'estimation correspondante sont alors évaluées par de nombreuses simulations effectuées sur des données synthétiques et réelles. Les résultats obtenus dans ce travail montrent l'efficacité du modèle proposé notamment lors du traitement des échos conventionnels ainsi que des échos côtiers corrompus par des pics gaussiens symétriques ou asymétriques.

- **Chapitre 3:** Nous proposons dans ce chapitre un nouveau modèle semi-analytique à trois paramètres pour l'altimétrie SAR/Doppler. La première partie de ce chapitre décrit le modèle proposé qui s'exprime comme une double convolution entre trois termes analytiques: la réponse impulsionnelle d'une mer plate, la densité de probabilité de la hauteur des points de dispersion et la réponse impulsionnelle du radar. Une formule analytique est calculée pour la réponse impulsionnelle d'une mer plate lorsque l'on considère un diagramme d'antenne circulaire sans dépointage, une vitesse verticale nulle pour le satellite et un coefficient de rétrodiffusion constant

dans la surface observée. Le traitement nécessaire pour obtenir l'écho multi-vues est aussi présenté. La deuxième partie de l'étude s'intéresse à l'estimation des paramètres altimétriques à partir de l'écho multi-vues en utilisant une procédure des moindres carrés. Les bornes de Cramér-Rao des paramètres sont ensuite établies afin d'évaluer les performances de l'estimateur par moindres carrés et d'autres stratégies d'estimation tel que l'estimateur du maximum de vraisemblance. Le modèle et l'algorithme proposés sont ensuite validés par des simulations effectuées sur des formes d'onde altimétriques synthétiques. L'analyse d'échos réels obtenus par Cryosat-2 montre une nette amélioration de la qualité des paramètres estimés par rapport à l'altimétrie conventionnelle.

- **Chapitre 4:** Ce chapitre généralise le modèle proposé dans le précédent chapitre afin de tenir compte des angles du dépointage de l'antenne. Une formule analytique généralisée de la réponse impulsionnelle d'une mer plate est obtenue en considérant deux approximations. Une analyse de ces approximations est réalisée en bornant les erreurs introduites par ces dernières. Dans une deuxième étape, et de manière identique au chapitre 3, plusieurs algorithmes d'estimation basés sur un principe de moindres carrés sont proposés. Par ailleurs, le modèle et les algorithmes proposés sont validés sur des signaux à la fois synthétiques et réels en comparant leurs performances à celles obtenues avec le modèle présenté dans le chapitre 3 et les résultats de l'altimétrie conventionnelle. Les résultats obtenus sont très prometteurs et montrent la pertinence de ce modèle généralisé.

Contributions principales

Les principales contributions de cette thèse sont

- **Contribution** 1 Un nouveau modèle altimétrique est proposé pour les signaux côtiers [Halimi et al., 2011a,b, 2013d]. L'estimation des paramètres est réalisée en utilisant un estimateur du maximum de vraisemblance. L'expression des bornes de Cramér-Rao des paramètres du modèle est donnée. Ces innovations sont évaluées par de nombreuses simulations effectuées sur des

données synthétiques et réelles.

- **Contribution** 2 Un modèle semi-analytique à trois paramètres est proposé pour l'altimétrie SAR/Doppler [Halimi et al., 2012, 2013b,e]. La stratégie d'estimation s'appuie sur un critère des moindres carrés. Les bornes inférieures de Cramér-Rao sont ensuite établies afin d'évaluer les performances de la procédure d'estimation par moindres carrés [Halimi et al., 2013a]. Le modèle proposé est validé sur des données synthétiques ainsi que sur des données réelles fournies par le satellite Cryosat-2.

- **Contribution** 3 Le modèle précédent est généralisé pour tenir compte du dépointage de l'antenne [Halimi et al., 2013c]. Le nouveau modèle est analysé et ses approximations justifiées. Plusieurs algorithmes d'estimation basés sur un critère de moindres carrés sont proposés. La validation du modèle proposé est réalisée en traitant des échos synthétiques et réels.

Introduction

This thesis has been conducted in the "Signal and Communications" team of the "Institut de Recherche en Informatique de Toulouse". It has been funded by the french ministry of national education and has been conducted in close collaboration with the Collecte Localisation Satellite (CLS) company and the "Centre national d'études spatiales" (CNES). This thesis follows the Phd work of J. Sévérini, that was conducted in the same team, and was devoted to the modeling and parameter estimation of altimetric signals.

For more than twenty years, conventional altimeters like Topex, Poseidon-2 or Poseidon-3, have been delivering waveforms that are used to estimate many parameters such as the range between the satellite and the observed scene, the wave height and the wind speed. These waveforms mainly result from the observation of oceanic surfaces for which several waveform models and estimation algorithms have been developed in order to improve the quality of the estimated altimetric parameters. However, the altimetric waveforms can be corrupted by land returns, by rain or by the summation of backscattered signals coming from separate reflective ocean surfaces which make the conventional algorithms ineffective. Therefore, a great effort is now devoted to process coastal echoes in order to move the altimetric measurements closer to the coast. The first part of this thesis deals with this issue by proposing a new altimetric model suitable for coastal areas. This model takes into account the possible presence of peaks affecting the coastal altimetric echoes. Two estimation algorithms are then proposed in order to take advantage of the proposed model. These algorithms provide an improvement in the quality of the estimated parameters.

A major point in altimetry is the measurement accuracy because of the use of the estimated parameters in many applications such as geophysics, bathymetry, etc. This accuracy is reduced because of the corruption of the altimetric measurements by speckle noise and by land return as in coastal areas. A solution for improving the measurement quality and the coastal issue is provided by the delay/Doppler altimetry (DDA) proposed in [Raney, 1998]. Indeed, this new technology fits into the logic of measurement improvement and has two main objectives. The first one is to reduce the measurement noise by increasing the number of observations (looks) which provide better geophysical parameter estimates. The second one is to increase the along-track resolution which allows the measurements to remain valid until a distance of about 300 meters from the coast (while it was about 10 km for conventional altimetry (CA)). However, DDA requires the elaboration of new altimetric models since the echoes present a different shape than the conventional one. The second part of the thesis deals with this point and proposes two altimetric models for DDA. The parameters of these models can be estimated by elaborating appropriate estimation algorithms based on maximum likelihood or least squares approaches. The obtained results are very promising and show the interest of using DDA as a new tool for the observations of the ocean.

Structure of the manuscript

This thesis is organized as follows

- **Chapter 1:** This chapter first describes the principles and objectives of spatial altimetry. Second, it presents the altimetric waveform and provides a state of the art of the different waveform models and estimation strategies available in the literature. The limitations of conventional altimetry are then described. These limitations are mainly due to the contamination of the echoes by land return in coastal areas because of the large footprint of the observed surface and the accuracy of the estimated parameters that is reduced because of the waveform corruption by speckle noise. Some technical solutions to these problems are then presented.

- **Chapter 2:** This chapter is interested in the study of coastal altimetric waveforms. Echoes resulting from the backscattering on coastal areas are sometimes corrupted by peaks caused by high reflective areas inside the illuminated land surfaces or by the modification of the sea state close to the shoreline. We define a new altimetric model as the sum of the well known Brown model and an asymmetric Gaussian peak. The asymmetric Gaussian peak is parameterized by a location, an amplitude, a width and an asymmetry coefficient. A maximum likelihood estimator is studied to estimate the Brown plus peak model parameters. The Cramér-Rao lower bounds of the model parameters are then derived providing minimum variances of any unbiased estimator, i.e., a reference in terms of estimation error. The performance of the proposed model and the resulting estimation strategy are evaluated via many simulations conducted on synthetic and real data. Results obtained in this work show that the proposed model can be used to retrack efficiently conventional Brown echoes as well as coastal echoes corrupted by symmetric or asymmetric Gaussian peaks.

- **Chapter 3:** In this chapter, we propose a semi-analytical model depending on three altimetric parameters for delay/Doppler altimetry. The first part of this chapter describes the proposed model that is expressed as a convolution of three analytical terms: the flat surface impulse response, the probability density function of the heights of the specular scatterers and the time/frequency point target response of the radar. An analytical formula is derived for the flat surface impulse response when considering circular antenna pattern, no mispointing, no vertical speed effect and a uniform scattering. The necessary processing to obtain the multi-look echo is then presented. The second part of the study consists of estimating the multi-look altimetric parameters by a least squares procedure. The Cramér-Rao lower bounds of the model parameters are then derived and compared to the proposed least squares estimation procedure and other estimation strategies such as the maximum likelihood estimator. The proposed model and algorithm are then evaluated via simulations conducted on synthetic altimetric waveforms. The analysis of Cryosat-2 waveforms clearly shows an improvement in parameter estimation when compared to conventional altimetry.

- **Chapter 4:** The semi-analytical model introduced in Chapter 3 is generalized to account for mispointing angles of the antenna. A generalized analytical formula of the flat surface impulse response is obtained by considering two approximations. An analysis of these approximations is conducted by deriving analytical bounds for the resulting errors induced by the approximations. In a second step, and similarly to Chapter 3, several least squares estimation algorithms are proposed. Moreover, the proposed model and algorithms are validated on both synthetic and real waveforms by comparing their performance with those obtained with the model presented in Chapter 3 and the results of conventional altimetry. The obtained results are very promising and show the accuracy of this generalized model.

Main contributions

The main contributions of this thesis are

- **Contribution** 1 A new altimetric model is proposed for coastal waveforms [Halimi et al., 2011a,b, 2013d]. The parameter estimation is achieved using a maximum likelihood estimator. The Cramér-Rao lower bounds of the model parameters are also derived. These innovations are evaluated via many simulations conducted on synthetic and real data.

- **Contribution** 2 A three parameter semi-analytical model is proposed for delay/Doppler altimetry [Halimi et al., 2012, 2013b,e]. The related estimation strategy is based on a least squares criterion. The Cramér-Rao lower bounds of the model parameters are then derived in order to evaluate the performance of the proposed least squares estimation procedure [Halimi et al., 2013a]. The proposed model is validated using synthetic and real Cryosat-2 data.

- **Contribution** 3 The previous DDA model is generalized to a five parameter model that accounts for antenna mispointing [Halimi et al., 2013c]. The new model is analyzed and its approximations are justified. Several estimation strategies based on the least squares estimation procedure are proposed to estimate its parameters. Processing simulated and real Cryosat-2 data allow this new model to be validated.

Personal publications

Journals related to the Phd

1. A. Halimi, C. Mailhes, J.-Y. Tourneret, T. Moreau, and F. Boy, "A generalized semi-analytical model for delay/Doppler altimetry and its estimation algorithm," *IEEE Trans. Geosci. and Remote Sensing*, submitted.

2. A. Halimi, C. Mailhes, J.-Y. Tourneret, P. Thibaut, and F. Boy, "A semi-analytical model for delay/Doppler altimetry and its estimation algorithm," *IEEE Trans. Geosci. and Remote Sensing*, to appear.

3. A. Halimi, C. Mailhes, J.-Y. Tourneret, P. Thibaut, and F. Boy, "Parameter estimation for peaky altimetric waveforms," *IEEE Trans. Geosci. and Remote Sensing*, vol. 51, no. 3, pp. 1568-1577, March 2013.

International conferences

1. A. Halimi, C. Mailhes, J.-Y. Tourneret, "Cramér-Rao bounds and estimation algorithms for delay/Doppler and conventional altimetry," *Proc. European Signal Processing Conf. (EUSIPCO)*, Marrakech, Marocco, Sept. 2013.

2. A. Halimi, C. Mailhes, J.-Y. Tourneret, F. Boy, N. Picot and P. Thibaut, "An analytical model for Doppler altimetry and its estimation algorithm," in *Ocean Surface Topography Science Team Meeting (OSTST)*, Venice, Italy, Sept. 2012.

3. P. Thibaut, T. Moreau, L. Amarouche, A. Halimi, C. Mailhes, J.-Y. Tourneret, F. Boy and N. Picot, "SAR Data over ocean, Processing strategy and continuity with LRM data," in *Ocean Surface Topography Science Team Meeting (OSTST)*, San Diego, USA, Oct. 2011.

4. A. Halimi, C. Mailhes, J.-Y. Tourneret, and P. Thibaut, "A new model for peaky altimetric waveforms," in *Proc. IEEE Int. Conf. Geosci. and Remote Sensing (IGARSS)*, Vancouver, Canada, July 24-29, 2011, pp. 2825-2828.

National conference papers

1. A. Halimi, C. Mailhes, J.-Y. Tourneret, F. Boy and T. Moreau, "Modèle semi-analytique pour l'altimétrie SAR/Doppler sur océan," in *Actes du XXIVième Colloque GRETSI*, to appear.

2. A. Halimi, C. Mailhes, J.-Y. Tourneret and P. Thibaut, "Modélisation des signaux altimétriques en présence de pics," in *Actes du XXIIIième Colloque GRETSI*, Bordeaux, France, Sept. 2011, in French.

Publications related to the master degree

1. A. Halimi, Y. Altmann, N. Dobigeon and J.-Y. Tourneret, "Nonlinear unmixing of hyperspectral images using a generalized bilinear model," *IEEE Trans. Geoscience and Remote Sensing*, vol. 49, no. 11, pp. 4153-4162, Nov. 2011.

2. Y. Altmann, A. Halimi, N. Dobigeon and J.-Y. Tourneret, "Supervised nonlinear spectral unmixing using a post-nonlinear mixing model for hyperspectral imagery," *IEEE Trans. Image Processing*, vol. 21, no. 6, pp. 3017-3025, June 2012.

3. A. Halimi, Y. Altmann, N. Dobigeon and J.-Y. Tourneret, "Unmixing hyperspectral images using the generalized bilinear model," in *Proc. IEEE Int. Conf. Geosci. and Remote Sensing (IGARSS)*, Vancouver, Canada, July 24-29, 2011, pp. 2825-2828.

4. A. Halimi, Y. Altmann, N. Dobigeon and J.-Y. Tourneret, "Nonlinear unmixing of hyperspectral images using a generalized bilinear model," in *IEEE Workshop on Statistical Signal Processing (SSP)*, Nice, France, June 2011, pp. 413-416.

5. Y. Altmann, A. Halimi, N. Dobigeon and J.-Y. Tourneret, "A polynomial post nonlinear model for hyperspectral image unmixing," in *Proc. IEEE Int. Conf. Geosci. and Remote Sensing (IGARSS)*, Vancouver, Canada, July 24-29, 2011, pp. 2825-2828.

6. Y. Altmann, A. Halimi, N. Dobigeon and J.-Y. Tourneret, "Supervised nonlinear spectral unmixing using a polynomial post nonlinear model for hyperspectral imagery," in *IEEE Int. Conf. Acoust., Speech, and Signal Processing (ICASSP)*, Prague, Czech Republic, May 2011, pp. 1009-1012.

Chapter 1

Altimetry

Contents

1.1 Introduction (in French)

La Terre abrite des millions d'espèces vivantes, y compris les être humains. De nombreux phénomènes physiques, qui ont un impact direct sur nos vies, se produisent sur cette planète qui est en constante évolution. Ces phénomènes sont, par exemple, le réchauffement climatique qui a un effet sur l'augmentation de la hauteur de la surface de la mer et la fonte des glaces, les tremblements de terre qui peuvent causer des tsunamis et le déplacement de la chaleur qui mène à El Niño. Presque tous ces phénomènes ont un impact sur l'océan, car il couvre 71% de notre planète. Donc, afin de les étudier, on doit observer leurs effets sur la surface océanique ce qui est réalisé par l'altimétrie radar. En effet, l'objectif principal de l'altimétrie radar est la mesure de la topographie de la surface des océans.

Un altimètre est un radar à visée nadir qui émet des impulsions régulières et enregistre le temps de trajet, l'amplitude et la forme de chaque signal de retour après réflexion sur la surface de la Terre. Cet instrument mesure la distance entre le satellite et la surface de la mer ce qui nous permet, moyennant des corrections atmosphériques et instrumentales, d'obtenir la hauteur de la surface de mer (appelée sea surface height SSH) ainsi que sa fluctuation autour d'un valeur moyenne appelée l'anomalie de la hauteur de la surface de mer (sea surface height anomaly SSHA). Ces mesures sont d'une grande importance et interviennent dans diverses applications telles que la bathymétrie et la géophysique. Cet importance a conduit à l'amélioration de la qualité des paramètres estimés en optimisant les instruments de mesure altimétriques. On note alors différentes missions altimétriques qui n'ont pas cessé de s'améliorer telles que ERS-1, ERS-2, TOPEX/POSEIDON, Jason-1, Jason-2, ENVISAT, AltiKa et Cryosat-2.

L'obtention des paramètres altimétriques (voir figure 1.4) est basée sur l'analyse de l'écho altimétrique. Ce signal est généralement modélisé par une double convolution entre trois termes qui sont la réponse impulsionnelle d'une mer plate (FSIR), la densité de probabilité (PDF) de la hauteur des points de dispersion et la réponse impulsionnelle du radar (PTR). Le premier modèle analytique de cette double convolution a été proposé par [Brown, 1977] en considérant une approximation exponentielle de la FSIR et gaussienne pour la PDF de la hauteur des points de dispersion et la PTR. Plusieurs études ont tenté par la suite d'améliorer ce modèle en s'intéressant à chacun des termes de la double convolution. [Amarouche et al., 2004, Rodriguez, 1988] ont proposé des améliorations de l'approximation exponentielle de la FSIR. [Hayne, 1980, Huang and Long, 1980] ont introduit un coefficient d'asymétrie dans la PDF gaussienne afin de tenir compte de l'asymétrie des vagues. [Callahan and Rodriguez, 2004, Rodriguez and Martin, 1994, Zanifé et al., 2006] ont considéré une approximation par une somme de gaussiennes de la PTR. Ces améliorations ont permis de mieux modéliser le signal altimétrique afin d'améliorer la qualité des paramètres altimétriques estimés. Cette estimation peut s'effectuer suivant plusieurs procédures. On note alors la procédure du maximum de vraisemblance [Challenor et al., 1990, Rodriguez, 1988], le critère des moindres carrés [Deng and Featherstone, 2006, Dumont, 1985, Rodriguez, 1988] et celui des moindres carrés pondérés [Maus et al., 1998].

L'ensemble des modèles décrits précédemment concerne le cas des échos océaniques. Ceci dit, l'une des limitations de l'altimétrie conventionnelle est la large tache au sol qui augmente la probabilité de corruption par des surfaces autre qu'océanique. On note alors des formes d'échos différentes près des côtes ce qui rend les modèles ainsi que les algorithmes d'estimation classiques inefficaces. Une autre limitation de l'altimétrie conventionnelle est le haut niveau de bruit de chatoiement affectant les mesures. Ce bruit aura un effet direct sur la qualité des paramètres altimétriques estimés et il devient alors nécessaire de réduire son effet.

Il existe deux classes de solutions pour améliorer les limitations de l'altimétrie conventionnelle. La première classe améliore le traitement des échos disponibles en se basant sur les outils de traitement du signal tels que le filtrage [Ollivier, 2006, Sandwell and Smith, 2005], la modélisation [Amarouche et al., 2004, Brown, 1977, Rodriguez, 1988] et les méthodes d'estimation [Dumont, 1985, Maus et al., 1998, Rodriguez, 1988]. La deuxième classe considère les améliorations de la technologie de mesure altimétrique. On évoque dans ce cas le nouvel instrument AltiKa qui permet de réduire les dimensions de la tâche au sol ainsi que le niveau de bruit affectant les mesures. On note aussi la nouvelle technologie SAR/Doppler qui vise la réduction du bruit de mesure et l'augmentation de la résolution spatiale dans la direction de marche du satellite en comparaison avec l'altimétrie conventionnelle.

On s'intéressera dans cette thèse à l'amélioration de la mesure côtière en proposant un nouveau modèle pour les échos côtiers. On proposera par ailleurs des outils de modélisation et d'estimation paramétriques des échos SAR/Doppler afin de tirer profit des performances de cette nouvelle technologie.

1.2 Spatial altimetry

Earth is a home to millions of species of life, including humans. Many physical phenomena, that have a direct impact on our lives, occur in this planet making it in constant evolution. These phenomena include, for example, the global warming that has an effect on the rise of the sea surface height and melting ice, earthquakes that can cause tsunami and heat transport that leads to El Niño. Almost all of these phenomena have an impact on the ocean since it covers 71% of our planet. Therefore, in order to study them, one has to observe their effects on the oceanic surface which is achieved by radar altimetry. Indeed, the primary objective of radar altimetry is the measure of the ocean surface topography. This measure provides a lot of information about many phenomena such as the ones described in Table 1.1 which shows many physical phenomena according to their spatial scale (i.e., the scale on which they may show some change) and their vertical variability (i.e., the change on the observed sea level). It can be seen for example that the geoid may present an elevation of the order of 30 m over thousands of kilometers. This table also shows that many phenomena, such as climate changes and small scale gravity features as ridge axes, have a very low vertical amplitude and hence require a very accurate measure of the sea surface height. Therefore, the altimetric instruments are in constant evolution in order to improve the measure quality and to explain new physical phenomena. The next section introduces the principles of altimetry and the different quantities of interest. After that, a brief description of the past and future altimetric missions is provided.

Table 1.1: Vertical variability of ocean phenomena versus the spatial scale [Sandwell, 2011].

Feature	Vertical variability (m)	Spatial scale (km)
Geoid	30	10000
Dynamic topography	1	10000
Climate changes	0.01	10000
Tides	$0.2 - 2$	100-10000
El Niño	0.1	6000
Front and eddies	0.3	100-1000
Seamounts	1	50
Ridge axes	0.02	10

1.2.1 Principle

A satellite altimeter is a nadir viewing radar that emits regular pulses and records the travel time, the magnitude and the shape of each return signal after reflection on the Earth's surface. This instrument measures the range between the satellite and the sea surface h_a. The range measurement $h_a = t_0 \frac{c}{2}$, where c is the speed of light, is based on a perfect knowledge of the round-trip travel time (t_0) of the emitted electromagnetic pulse from the satellite to the observed surface. The emitted pulse should be very narrow in order to achieve a good range resolution. However, this requires a high emission power, which can be prohibitive on board a satellite, in order to have a good signal to noise ratio for the received signal. The emission is then achieved using the pulse compression technique (also known as full deramp technique) that has substantially reduced peak power requirements. This is achieved using a frequency modulated chirp at the emission and a matched filter at the receiver[1]. This provides a good range resolution h_r (which is related to the reception bandwidth of the altimeter B as follows $h_r = c/(2B)$) which improves the accuracy of the desired h_a. Note that h_a is generally used to derive the variable part of the dynamic sea surface topography which is known as sea surface height anomaly (SSHA). In order to derive the expression of SSHA, complementary height definitions are given in what follows. The altimeter height is generally known according to the reference ellipsoid which is a mathematical determinable model of the Earth. This distance denoted by H_s in Fig. 1.1 serves to maintain the satellite on its orbit (the accuracy is about 1 cm in the most recent satellites [Vignudelli et al., 2011]). This is achieved using some terrestrial or on-board DORIS instrument (based on the Doppler effect) or by using the triangulation method as in the GPS (global positioning system). At this point, one can evaluate the sea surface height (SSH) by subtracting the measured h_a from H_s. However, some corrections must be applied to the measured h_a in order to improve its accuracy. These corrections are divided into two main parts [Chelton et al., 2001, Vignudelli et al., 2011]. The first ones are mainly due to the pulse travel through the atmospheric layers and are known as atmospheric corrections (denoted by h_{atm}). These corrections are due to the presence of dry gasses, water vapor and free electrons in the atmosphere. Those phenomena reduce the propagation speed of the emitted pulse resulting in a longer measured range and then a lower SSH. The second corrections

[1] The reader is invited to consult [Chelton, 1989, Ollivier, 2006] for more details about this technique.

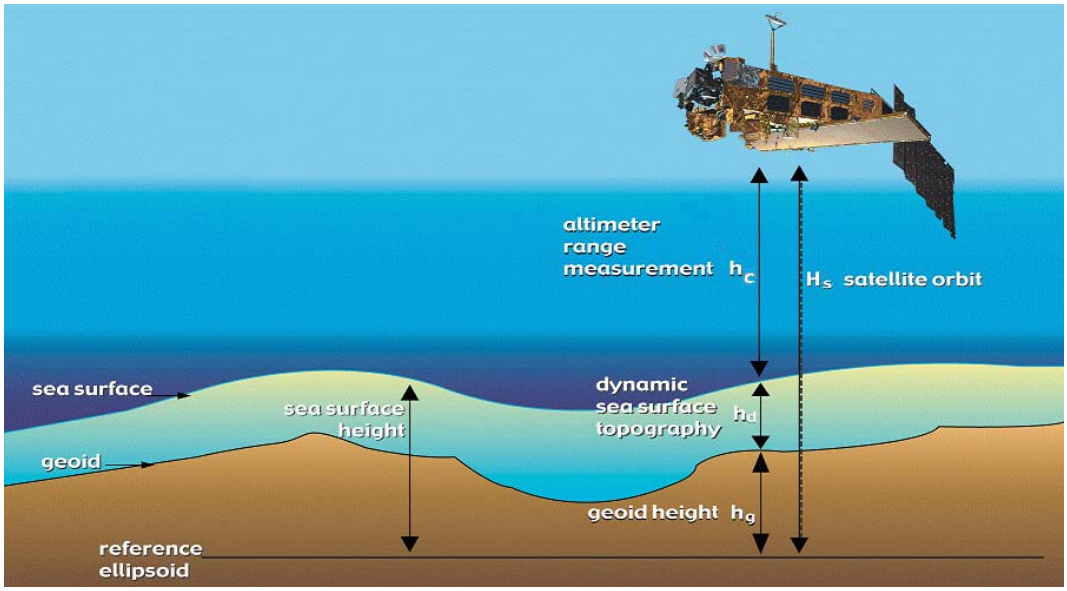

Figure 1.1: The principle of radar altimetry [Benveniste, 2011].

are related to the observed sea surface which is not perfectly Gaussian. Indeed, the wave troughs are more prevalent and reflect more signal than the wave crest resulting in a bias in the detected sea level. This bias is commonly known as sea state bias (SSB) and the corresponding correction is denoted by h_{SSB}. Thus, the corrected range h_{c} is given by $h_{\mathrm{c}} = h_a - h_{\mathrm{atm}} - h_{\mathrm{SSB}}$ and the corrected SSH is deduced as follows

$$\mathrm{SSH} = H_s - h_{\mathrm{c}} = H_s - h_a + h_{\mathrm{atm}} + h_{\mathrm{SSB}}. \tag{1.1}$$

The primary focus of satellite altimetry is the study of the dynamic part of the SSH. Therefore, one has to determine the main contributors of the SSH in order to deduce its dynamic part. Several physical factors contribute to the SSH. The first is the distribution of gravity over the Earth which is represented by the geoid (height h_g from the reference ellipsoid). The geoid is the equipotential surface of the effective gravitational field of the Earth which incorporates Earth rotation forces and the gravitation of the solid Earth, the ocean itself, and the atmosphere [Robinson, 2010]. It represents the largest part of the SSH and can be seen as a new reference instead of the elliptical reference. The SSH expressed in this new reference will have a meter scale. The second factor is represented by tidal

effects h_t that are mainly obtained by the ocean tides but also include solid Earth tides, loading tides and pole tides. The third factor results from the dynamic atmosphere that exerts a downward force on the sea surface (denoted by h_{atm2}). Indeed, an increase on the atmospheric pressure distribution over the ocean lowers the sea level. For example, an increased pressure of 1 mbar lowers sea level by 1 cm. The last factor is the dynamic sea surface topography h_d which represents the displacement of the sea surface associated with the motion of the sea. The SSH is finally given by

$$\text{SSH} = h_t + h_{\text{atm2}} + h_d + h_g. \tag{1.2}$$

Eqs. (1.1) and (1.2) lead to the following expression for the dynamic sea surface topography

$$h_d = H_s - h_a + h_{\text{atm}} + h_{\text{SSB}} - h_t - h_{\text{atm2}} - h_g. \tag{1.3}$$

This equation shows the effect of range corrections that should be applied to the range (in order to reduce the range and increase the SSH) and geophysical corrections that are applied to SSH. Note finally that h_d presents a mean value known as the mean dynamic topography $\overline{h_d}$ and that it fluctuates around this value by what is known as the sea surface height anomaly (SSHA). The latter is given by

$$\text{SSHA} = H_s - h_a + h_{\text{atm}} + h_{\text{SSB}} - h_t - h_{\text{atm2}} - h_{\text{MSS}}. \tag{1.4}$$

where $h_{\text{MSS}} = h_g + \overline{h_d}$ is the mean sea surface height that can be considered as a new reference instead of the geoid. The obtained variable SSHA is used to study the sea surface height variations and is of great importance since it provides a lot of information about many physical phenomena such as the wind speed. Table 1.2 shows typical values of the mean and standard deviation of all the time variable corrections applied to SSH and the range (atmospheric corrections and SSB). It can be seen that dry troposphere introduces the greatest error while the tides have the largest standard-deviations.

1.2.2 Missions

Spatial altimetry first appeared in the 70th aiming at the observation of the Earth. Since then, altimetry has known an incredible improvement that has allowed to better understand many aspects of the ocean such as ocean surface topography, marine currents, heat transport, etc. The earliest

Table 1.2: Typical values of the mean and standard deviation of all the time variable corrections applied to SSH [Vignudelli et al., 2011].

Corrections	Mean(cm)	Time variable deep ocean (std dev) (cm)	Time variable Coastal (std dev) (cm)
Dry troposphere	231	$0-2$	$0-2$
Wet troposphere	16	$5-6$	$5-8$
Ionosphere	8	$2-5$	$2-5$
Sea state bias	5	$1-4$	$2-5$
Tides	$\sim 0-2$	$0-80$	$0-500$
Dynamic atmosphere	$\sim 0-2$	$5-15$	$5-15$

altimeters were embarked in multi-disciplinary satellites such as: GEOS-3 (1975), SEASAT (1978), GEOSAT (1985), ERS-1 (1991). However, the first satellite dedicated to the observation of the ocean surface topography is the Franco-American TOPEX/POSEIDON satellite that was launched in 1992. This satellite embarked two altimeters, an American altimeter Topex (TOPographic EXperiment) and a French altimeter POSEIDON and has provided 13 years of useful data while a three year mission was initially planned. Moreover, its high performance has allowed, for the first time, the global measure of some temporal variability of the ocean such as the seasonal cycle. This satellite was followed by Jason-1 (2001) and Jason-2 (2008) in order to take advantage of the measure continuity. Indeed, the availability of many year data has allowed to study the seasonal and annual behavior of the ocean hence the importance of the measure continuity. Similarly, the European mission ERS-1 was followed by the ERS-2 (1995) where both of them were devoted to the study of the atmosphere and the ocean. These missions were followed by ENVISAT (Environmental Satellite) launched in 2002 and devoted to environmental studies and in particular to climate change.

More recently, the CNES (Centre National d'Études Spatiales) and the ISRO (Indian Space Research Organization) agencies have launched a new mission Saral (satellite with ARgos and ALtika) that aims at the observation of ice, rain, coastal zones, land masses, etc. These goals are achieved by the altimeter ALtiKa that has the particularity to work on a Ka-band frequency (the effect of this

new configuration will be discussed later). Moreover, the new technology known as delay/Doppler altimetry is also considered in many missions as the recent Cryosat-2 (2010) satellite that embarks the SIRAL (Synthetic aperture radar interferometric mode) altimeter and the future missions Sentinel-3 and Swot (Surface Water and Ocean Topography). More details about this new technology are provided in the rest of this thesis. Some of these satellites are illustrated in Fig. 1.2.

Figure 1.2: Altimetric missions (from http://www.aviso.oceanobs.com/en/missions.html).

Table 1.3 shows examples of altimetric missions and some of their characteristics. These missions highlight the objective of improving the range accuracy. Indeed, the range precision is an important issue since many physical applications depend on it as shown in Table 1.1. Except the AltiKa altimeter that operates at Ka-band (35 GHz), all the other altimeters operate at Ku-band (between 12 and 18 GHz). This choice is motivated by the fact that high frequencies are significantly attenuated by the atmosphere. Moreover, and in order to determine the ionospheric delay affecting the emitted pulse, some altimeters such as Topex, Jason-1 and Jason-2 operate at two frequencies. The correction is then possible since the free electrons in the ionosphere affect the traveling signals proportionally to their frequencies (this ionospheric correction is included in h_{atm} as described previously).

Table 1.3: Example of altimetric missions, technologies and performance [Rosmorduc et al., 2009].

Satellite	Launch	Altimeter	Frequency	Range error (open ocean)
SEASAT	1978	ALT	Ku-band	5 cm
ERS-1	1991	RA	Ku-band	3 cm
Topex/Poseidon	1992	Topex Poseidon-1	Ku and C-band Ku-band	2 cm
ERS-2	1995	RA	Ku-band	3 cm
Jason-1	2001	Poseidon-2	Ku and C-band	2 cm
Envisat	2002	RA-2	Ku and S-band	2-3 cm
Jason-2	2008	Poseidon-3	Ku and C-band	/
Cryosat	2010	SIRAL	Ku-band	/
Saral	2013	AltiKa	Ka-band	/
Sentinel-3	2014	SRAL	Ku and C-band	/

1.3 Conventional altimetry

This section is interested in the description of the conventional pulse limited altimetry. The altimetric waveform is first described by presenting its shape and its dependence according to the physical parameters of interest. Second, the conventional altimetric models are described. The third part deals with parameter estimation and describes briefly the different strategies available in the literature. The last part shows the limitations of this technology which justifies the need for new technologies and processing improvement.

1.3.1 Waveform description

As explained previously, the altimeter measures the range h_a between the satellite and the observed surface. This is achieved by the study of the reflected altimetric echo. The shape of this signal depends on the observed surface which is generally the oceanic one. This surface is spatially homogeneous and allows the extraction of many geophysical parameters such as the sea wave height and the wind speed. The formation of the oceanic waveform is described in Fig. 1.3 for a calm and rough sea surface. First, the signal shows a low constant level before the emitted pulse reaches the surface.

This received signal (also called "echo") results from radiations which are natural (cosmic radiations, atmospheric radiations, etc.), and/or coming from the satellite instruments and known as the thermal noise. The second step shows an increasing signal as the pulse reaches the observed surface. The latter is represented by circles of increasing radius whose surface is proportional to the received altimetric power [Chelton, 1989]. The obtained signal continues to rise, as the pulse goes deeper in the observed surface, showing a slope that is directly related to the surface roughness, i.e., the wave height (see steps 2 and 3 in Fig. 1.3.a and Fig. 1.3.b). This increasing part of the signal is known as the leading edge of the echo. In the last step, the observed surface becomes an annulus (of constant surface) and the signal decreases as the pulse moves away from nadir because of the antenna gain. This decreasing part of the signal is known as the trailing edge of the echo. The resulting altimetric echo depends on

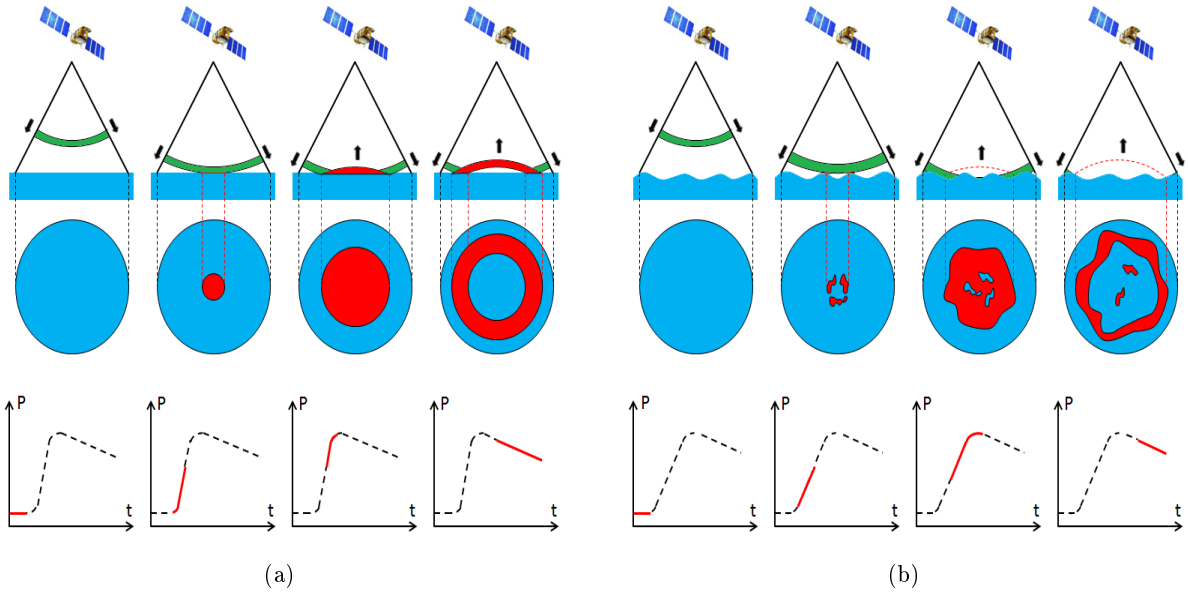

Figure 1.3: Formation of an altimetric waveform for (a) a calm sea surface (b) a rough sea surface.

five altimetric parameters as described in Fig. 1.4. The parameter N_t is the thermal noise that has been described previously, P_u is the amplitude of the altimetric echo that is related to the speed of wind, SWH is the significant wave height, τ is the epoch related to the range between the satellite and the observed surface, ξ is the mispointing of the radar antenna and λ_s is the skewness related to the curvature of the leading edge.

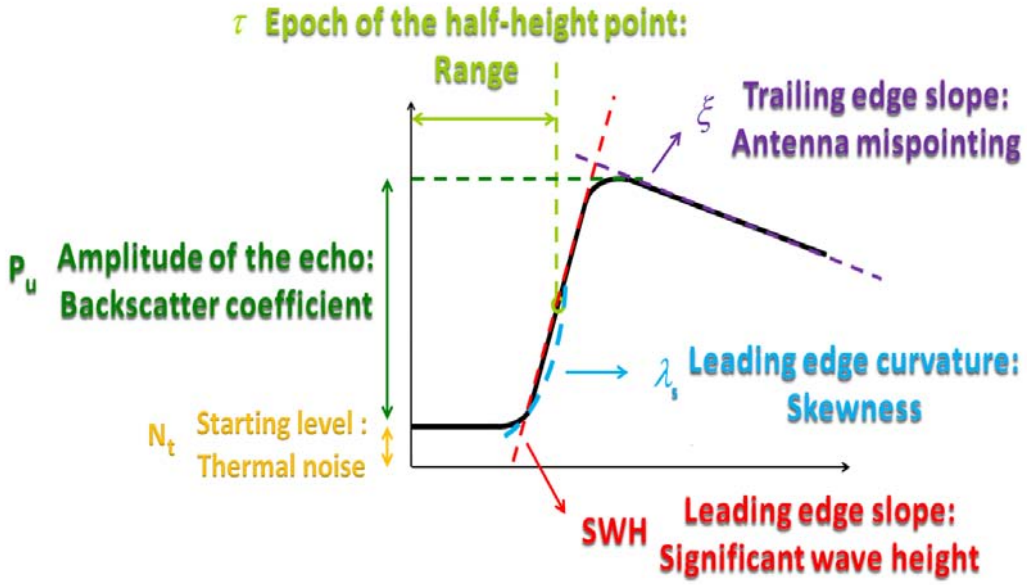

Figure 1.4: Geophysical parameters of a theoretical waveform.

Note that the satellite altitude is provided by the epoch parameter. This parameter represents a time shift and then it can be expressed in seconds. In this case, it is denoted by τ_s. The epoch τ is also commonly expressed in terms of gates which are discrete units related to the time resolution T_s as follows $\tau_s = \tau T_s$. Note finally, that τ can also be considered as a distance where a gate is related to the spatial resolution h_r, with $h_r = cT_s/2 = 46$ cm. This latter unit (i.e., meter) is the one of interest since it allows to directly evaluate the effect on the satellite altitude.

1.3.2 Waveform models

The mean power $s(t)$ of a conventional altimetric echo depends on the observed surface and the configuration of the measuring instrument. The echo model has known many evolutions. First, it has been shown in [Moore and Williams, 1957] that the backscattered power can be obtained by convoluting the emitted pulse with a function dependent on the surface backscattered coefficient. In [Barrick, 1972], it has been shown that the power can be written as a double integral that was finally expressed as a double convolution in [Barrick and Lipa, 1985]. This double convolution is achieved

between three terms (whose shapes are shown in Fig. 1.5): the flat surface impulse response (FSIR), the probability density function (PDF) of the heights of the specular scatterers and the point target response of the radar (PTR) as follows [Brown, 1977]

$$s(t) = \mathrm{FSIR}(t) * \mathrm{PDF}(t) * \mathrm{PTR}_T(t) \tag{1.5}$$

where t is the two-way incremental ranging times, i.e., $t = t' - \frac{2h}{c}$, with t' the travel time of the echo from the instant of transmission, h the altitude of the satellite[2] and c the speed of light. The following subsections describe the three terms of (1.5).

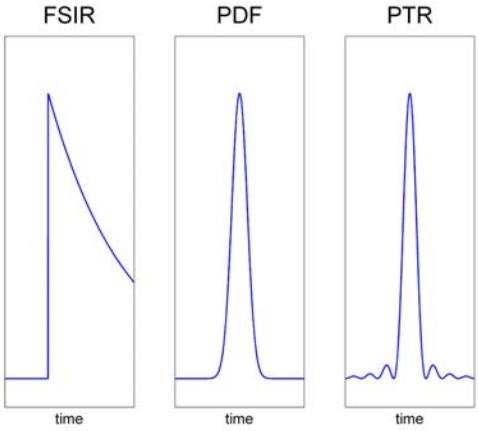

Figure 1.5: Shapes of FSIR, PDF and PTR_T.

Flat surface impulse response

The FSIR is an important term in the double convolution (1.5) since it introduces the effect of the antenna gain and the backscattering properties of the observed surface. Therefore, it has known many approximation formulas that are described in the following. This term only depends on time and is obtained by integrating over the illuminated area of the surface as follows [Brown, 1977]

$$\mathrm{FSIR}(t') = \frac{\lambda^2}{(4\pi)^3 L_p} \int_{\mathbb{R}^+ \times [0,2\pi[} \frac{\delta(t' - \frac{2r}{c}) G^2(\rho,\phi)\sigma^0}{r^4} \rho d\rho d\phi \tag{1.6}$$

[2] The measured height h_a is related to h by the formula $h_a = h + \delta h$ where δh is measured from the altimetric echo by the mean of the epoch τ.

where ρ, ϕ are the radius and the angle of the polar coordinates, L_p is the two-way propagation loss, λ is the wavelength, G is the power gain of the radar antenna, $\delta(t)$ is the Dirac delta function, σ^0 is the backscatter coefficient of the surface that is considered as a constant in the rest of this thesis[3] and $r = \sqrt{\rho^2 + h^2}$ is the range between the satellite and the observed surface (see Fig. 1.6). The

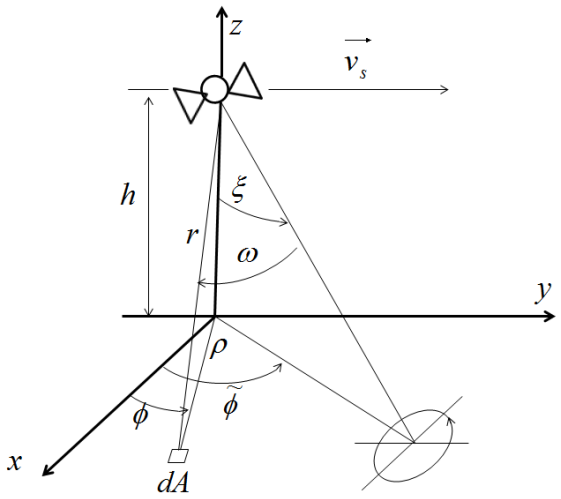

Figure 1.6: Geometry used for computing the flat surface impulse response.

analytical expression of the FSIR has been derived in [Brown, 1977] as an infinite sum of modified Bessel functions as follows

$$\mathrm{FSIR}(t) = P_u \exp\left[-\chi t - \frac{4}{\gamma}\sin^2\xi\right] U(t) \sum_{k=0}^{\infty} \left\{ \frac{(-1)^k \Gamma(k+1/2)}{\sqrt{\pi}\Gamma(k+1)} \left[\frac{\gamma\beta\sqrt{t}}{8\cos^2\xi}\right]^k I_k\left(\beta\sqrt{t}\right) \right\} \tag{1.7}$$

where $U(t)$ is the Heaviside function, $I_k(t)$ is the modified bessel function of the kth order, $\Gamma(k)$ is the gamma function, γ is a parameter related to the antenna aperture, $P_u = \frac{\lambda^2 G_0^2 c\sigma^0}{4(4\pi)^2 L_p h^3}$ is an amplitude term containing parameters from the radar and the observed surface, G_0 is the antenna power gain at boresight, ξ is the antenna mispointing parameter and

$$\begin{aligned} \chi &= \frac{4c}{\gamma h}\cos(2\xi) \\ \beta &= \frac{4}{\gamma}\left[\frac{c}{h}\right]^{1/2}\sin(2\xi). \end{aligned} \tag{1.8}$$

[3] This term may change in the observed scene as shown in [Tournadre et al., 2011].

Equation (1.7) can be considerably simplified by approximating the infinite sum by its first term, which is often a reasonable approximation. The resulting first order approximated FSIR can be written [Amarouche et al., 2004, Brown, 1977, Hayne, 1980]

$$\mathrm{FSIR}(t) \simeq P_u \exp\left[-\chi t - \frac{4}{\gamma}\sin^2\xi\right] I_0\left(\beta\sqrt{t}\right) U(t). \tag{1.9}$$

The necessity to derive an analytical expression for the mean power $s(t)$ has led to consider some other approximations for this formula. The Bessel function of order zero has been approximated by different expressions such as the ones proposed in [Rodriguez, 1988] and [Amarouche et al., 2004] based on a Taylor expansion of $I_0(t)$ [Abramowitz and Stegun, 1965]. In [Rodriguez, 1988], a first order approximation has been considered and has shown good accuracy for small mispointing angle (ξ less than 0.3°). This approximation leads to the following FSIR

$$\mathrm{FSIR}(t) \simeq P_u \exp\left[-\left(\chi - \frac{\beta^2}{4}\right) t - \frac{4}{\gamma}\sin^2\xi\right] U(t). \tag{1.10}$$

In order to process data with a higher mispointing angle, one has to consider the second order approximation proposed in [Amarouche et al., 2004] which provides good performance until $\xi = 0.8°$. This approximation is more general and has shown interesting results in practical applications [Desjonqueres et al., 2010, Thibaut et al., 2004, 2010]

$$I_0\left(\beta\sqrt{t}\right) \simeq 2\exp\left[\frac{\beta^2(t)}{8}\right] - 1. \tag{1.11}$$

This leads to the following FSIR proposed in [Amarouche et al., 2004]

$$\mathrm{FSIR}(t) \simeq 2P_u \exp\left[-\left(\chi - \frac{\beta^2}{8}\right) t - \frac{4}{\gamma}\sin^2\xi\right] U(t) - P_u \exp\left[-\chi t - \frac{4}{\gamma}\sin^2\xi\right] U(t). \tag{1.12}$$

Note also that another FSIR formula has been proposed in [Brown, 1989] to deal with high mispointing angles. Note finally that the FSIR includes 3 altimetric parameters that are the amplitude P_u, the mispointing ξ and the epoch τ. The latter is generally introduced by applying a time delay τ_s in the FSIR formula which (by using the properties of the convolution) results in a delay of the mean power $s(t)$ by τ_s as shown in Fig. 1.4 (the middle of the leading edge is located at time gate τ instead of 0).

Probability density function of the heights of the specular scatterers

The rest of the altimetric parameters is introduced by the PDF of the heights of the specular scatterers. This function is generally approximated by a Gaussian density whose standard deviation is related to the average SWH [Amarouche et al., 2004, Brown, 1977]

$$\mathrm{PDF}(t) = \frac{1}{\sqrt{2\pi}\sigma_s} \exp\left(-\frac{t^2}{2\sigma_s^2}\right) \tag{1.13}$$

with $\sigma_s = \frac{\mathrm{SWH}}{2c}$. A generalization of the PDF has been proposed in [Hayne, 1980, Huang and Long, 1980] by introducing the third order statistic of this distribution (i.e., the skewness λ_s). This generalized formula takes into account the asymmetric shape of the waves which affects the curvature of the leading edge as shown in Fig. 1.4. This leading edge distortion introduces some biases in the estimated sea surface height and its effects have been deeply studied in [Zapevalov, 2012]. Note finally that the PDF may introduce one (SWH) or two altimetric parameters (SWH and λ_s) depending on the considered approximation.

Radar system point target response

The radar point target response is generally expressed as a squared cardinal sine that results from the deconvolution of a frequency modulated chirp. It is given by [Amarouche et al., 2004]

$$\mathrm{PTR}_T(t) = \left| \frac{\sin\left(\pi \frac{t}{T_s}\right)}{\pi \frac{t}{T_s}} \right|^2 \tag{1.14}$$

where $T_s = 1/B$ is the sampling period and B is the reception bandwidth of the altimeter. This expression was approximated in [Amarouche et al., 2001, 2004] by a Gaussian in order to get an analytical expression of the double convolution (1.5)

$$\mathrm{PTR}_T(t) \simeq \frac{1}{\sqrt{2\pi}\sigma_p} \exp\left(\frac{-t^2}{2\sigma_p^2}\right) \tag{1.15}$$

with $\sigma_p = 0.513 T_s$ [MacArthur and Laboratory, 1978] (note also that $\sigma_p = 0.425 T_s$ was used in [Barrick, 1972, Brown, 1977]). This approximation mainly affects the estimation of the significant wave height parameter while it has almost no effect on the epoch τ because of the symmetric shape

of the real PTR_T. This issue can be solved by considering a sum of Gaussians approximation for the PTR_T as shown in many studies [Callahan and Rodriguez, 2004, Rodriguez and Martin, 1994, Zanifé et al., 2006].

Analytical models

Many analytical models have been proposed in the literature for the mean power $s(t)$ depending on the desired accuracy. Indeed, the accuracy of the altimetric model depends on the considered formulas for the three convolved terms and the desired number of altimetric parameters. However, this accuracy comes at the price of a high computational complexity, hence, one has to choose the appropriate model according to the considered application. In this thesis, we have been mainly interested in studying altimetric models that depend on 4 altimetric parameters SWH, τ_s, P_u and ξ. This vector of parameters is often sufficient to describe the main behavior of altimetric echoes and has been considered in many previous studies [Ollivier, 2006, Sandwell and Smith, 2005, Severini, 2010].

Considering this parameter vector, the more famous model is obtained by introducing in (1.5) the analytical expression (1.10) for the FSIR and the Gaussian approximations (1.13) and (1.15) for the PDF and PTR_T, respectively. The resulting analytical model is known as the Brown model and is given by

$$s(t) = \frac{P_u}{2} \exp\left(-v\right) \left[1 + \mathrm{erf}(u)\right] + N_t \tag{1.16}$$

with

$$u = \frac{t - \tau_s - \alpha\sigma_c^2}{\sqrt{2}\sigma_c}, v = \alpha\left(t - \tau_s - \frac{\alpha}{2}\sigma_c^2\right), \alpha = \chi + \frac{4}{\gamma}\sin^2\xi - \beta^2/4$$
$$\sigma_c^2 = \sigma_s^2 + \sigma_p^2. \tag{1.17}$$

where $\mathrm{erf}\left(t\right) = \frac{2}{\sqrt{\pi}} \int_0^t e^{-z^2}\, dz$ stands for the Gaussian error function. Another more accurate model (that was introduced to deal with high antenna mispointing angles as it was the case with Jason-1) was proposed in [Amarouche et al., 2004] and considers the expressions (1.12), (1.13) and (1.15) for the FSIR, PDF and PTR_T, respectively. The resulting model is given by

$$s(t) = P_u \exp\left(-v_1\right) \left[1 + \mathrm{erf}(u_1)\right] - \frac{P_u}{2} \exp\left(-v_2\right) \left[1 + \mathrm{erf}(u_2)\right] + N_t \tag{1.18}$$

with

$$u_1 = \frac{t-\tau_s-\alpha_1\sigma_c^2}{\sqrt{2}\sigma_c}, v_1 = \alpha_1\left(t-\tau_s-\frac{\alpha_1}{2}\sigma_c^2\right), \alpha_1 = \chi+\frac{4}{\gamma}\sin^2\xi-\beta^2/8$$
$$u_2 = \frac{t-\tau_s-\alpha_2\sigma_c^2}{\sqrt{2}\sigma_c}, v_2 = \alpha_2\left(t-\tau_s-\frac{\alpha_2}{2}\sigma_c^2\right), \alpha_2 = \chi+\frac{4}{\gamma}\sin^2\xi. \quad (1.19)$$

The previous models could be simplified by considering an antenna without mispointing ($\xi = 0°$). The resulting model depends on 3 parameters ($\mathrm{SWH}, \tau_s, P_u$) and is given by

$$s(t) = \frac{P_u}{2}\exp\left[-\alpha\left(t-\tau_s-\frac{\alpha}{2}\sigma_c^2\right)\right]\left[1+\mathrm{erf}\left(\frac{t-\tau_s-\alpha\sigma_c^2}{\sqrt{2}\sigma_c}\right)\right]+N_t \quad (1.20)$$

with $\alpha = \frac{4c}{\gamma h}$ and $\sigma_c^2 = \frac{\mathrm{SWH}^2}{4c^2}+\sigma_p^2$.

Speckle noise

Altimeter data are corrupted by multiplicative speckle noise which results in an observed altimetric echo given by

$$y_k = s_k n_k, \quad k = 1,\ldots,K \quad (1.21)$$

where $y_k = y(kT_s)$ is the kth data sample of the observed echo, $s_k = s(kT_s)$ is the kth data sample of the theoretical echo and n_k denotes the kth sample of the multiplicative speckle noise. The influence of this noise is generally reduced by averaging a sequence of L_c consecutive echoes. This operation reduces the noise variance (by $\sqrt{L_c}$ when assuming pulse-to-pulse statistical independence) and the resulting noise is generally assumed to be gamma distributed [Mailhes et al., 2008, Ollivier, 2006]. The noise effects on the statistic of the observed echo is more investigated in the next chapters.

1.3.3 Parameter estimation

This section introduces the parameter estimation strategies (also called retracking methods) used to estimate the geophysical parameters from the observed echoes. These strategies can be characterized according to the considered waveform model, the criterion to minimize and the used optimization algorithms.

There are two classes of waveform models that have been investigated in the literature: the empirical and the physics-based algorithms. The first class uses empirical shapes to estimate the

desired parameters such as the geometrical offset center of gravity (OCOG) algorithm [Wingham et al., 1986], the threshold method [Davis, 1995, 1997] and the improved threshold methods [Bao et al., 2009, Hwang et al., Lee et al., 2008]. These methods are not described in this thesis and we invite the interested reader to consult [Gommenginger et al., 2011b] for more details about them. We will be interested in this thesis on the second class of physics-based algorithms which use the previously described waveform models to estimate the parameters of interest.

One actual popular estimation strategy is based on a maximum likelihood estimation procedure [Challenor et al., 1990, Rodriguez, 1988]. This method maximizes the observation statistics and assumes the knowledge of the noise distribution corrupting the observed echoes. It can be shown that the negative log-likelihood (which is the cost-function to minimize) when considering a gamma distributed noise is given by [Challenor et al., 1990]

$$\mathcal{C} = \text{Cste} + L_c \sum_{k=1}^{K} \frac{y_k}{s_k} - (L_c - 1) \sum_{k=1}^{K} \ln(y_k) + L_c \sum_{k=1}^{K} \ln(s_k) \tag{1.22}$$

where Cste is a constant, $s_k = s(kT_s)$ is the kth data sample of the theoretical echo, K is the number of samples, L_c is the number of looks and $y_k = y(kT_s)$ is the kth data sample of the observed noisy echo. This criteria can be simplified using a Fisher scoring [Green, 1984] technic to obtain a least squares criteria that is widely used in altimetry [Deng and Featherstone, 2006, Dumont, 1985, Rodriguez, 1988]

$$\mathcal{C} = \frac{1}{P_u^2} \sum_{k=1}^{K} (y_k - s_k)^2. \tag{1.23}$$

An intermediate criteria is the weighted least squares (WLS) given by

$$\mathcal{C} = \sum_{k=1}^{K} \left(\frac{y_k - s_k}{w_k} \right)^2 \tag{1.24}$$

where w_k is the weight that is generally equal to s_k (note that the criteria (1.24) reduces to (1.23) for $w_k = P_u$). The choice of this weight is important and has a direct effect on the estimated range as shown in [Maus et al., 1998].

The minimization of these criteria can not be computed in closed-form because of the complexity of the altimetric models. Consequently, numerical optimization techniques have to be used to implement them. Many techniques can be applied such as those based on gradient descent algorithms.

These algorithms included the Levenberg-Marquardt method [Bertsekas, 1995], the Newton-Raphson method (used in the well known MLE3 or MLE4 algorithms [Dumont, 1985, Thibaut et al., 2004]) and the geometrical Nelder-Mead method [Nelder and Mead, 1965]. These methods will be more detailed in the rest of the thesis. Note that the estimation can be achieved using other algorithms such as neural networks [Boer, 2006] or a deconvolution method that extract the PDF in order to estimate sea state parameters [Rodriguez, 1988, Rodriguez and Chapman, 1989]. Finally, one has to note that most algorithms are interested in estimating each echo independently from the others. However, some algorithms use the information of the adjacent waveforms to improve the estimation quality. One can cite the weighted least squares algorithm proposed in [Maus et al., 1998] for a group of waveforms and the Kalman filter based algorithms [Jordi and Wang, 2010].

1.3.4 Limitations

The conventional pulse limited altimetry has an annulus footprint as shown in Fig. 1.3. This footprint presents an increasing radius as a function of time where a large radius mainly affects the trailing edge of the waveform. The main advantage of the resulting large area is that it comprises sufficient random independent scattering elements which is a necessary assumption for the derivation of altimetric models [Brown, 1977]. However, this comes at the price of a reduced resolution since the estimated geophysical parameters result from an averaging over the entire area. Moreover, because of this large footprint, the altimetric waveform can be corrupted by land returns or by the summation of backscattered signals coming from separate reflective ocean surfaces. Thus, the resulting waveform may differ from the usual oceanic echo shape shown in Fig. 1.4. In the case of coastal altimetry, the altimetric footprint spreads partly over ocean and land as shown in Fig. 1.7. In this case, the resulting echo presents peaks whose locations depend on the distance between the satellite nadir point and the coast and on the scattering coefficient of each surface, i.e., the oceanic and land surfaces. Those corrupted echoes were first discarded since they provide false estimated parameters when considering the algorithm designed to oceanic echo. Thus, a non negligible amount of altimetric data were lost close to the coast which was wasteful. However, a great effort is now devoted to process coastal waveforms in order to move the altimetric measurements closer to the coast [Desportes et al., 2007,

2010, Gommenginger et al., 2011b]. Indeed, this altimetric limitation appears to be a new area of study that motivates a lot of satellite missions (AltiKa, Cryosat-2) and research projects such as PISTACH [Mercier *et al*, 1998][4] and COASTALT [Vignudelli et al., 2011][5].

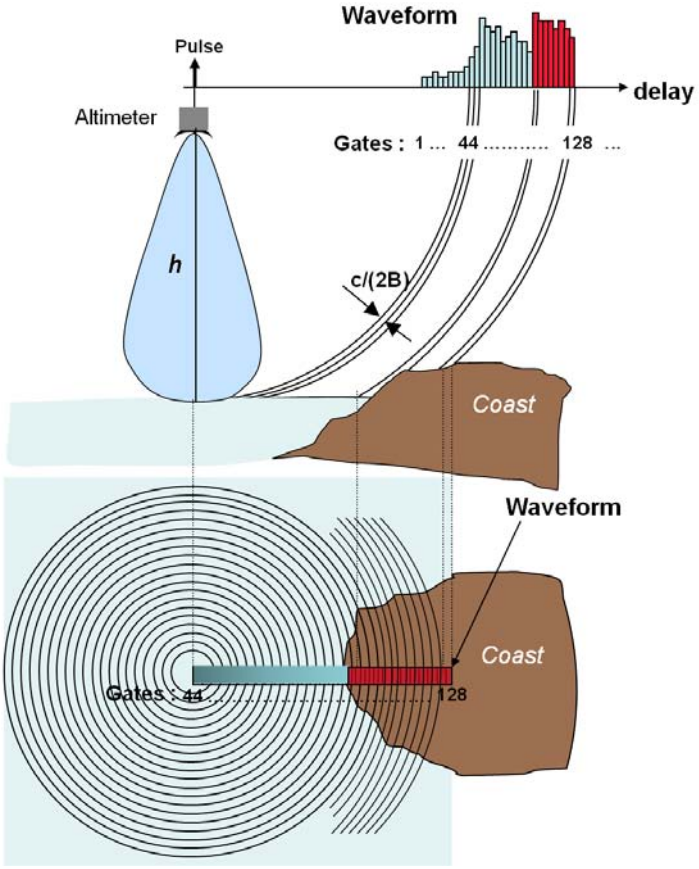

Figure 1.7: Schematic representation of the construction of a coastal altimetric echo [Gommenginger et al., 2011b].

Another limitation is related to the accuracy of the estimated parameters. Indeed, the study of many physical phenomena requires a very good range accuracy as for the climate change phenomena that shows a vertical amplitude of 1 cm (see Table 1.1). Note, however, that the actual conventional altimetric instruments have a range accuracy of about 2 cm for 1 second of data (see Table 1.3). This

[4]The PISTACH project has been funded by CNES.
[5]The COASTALT project has been funded by the European space agency (ESA).

is in part due to the corruption of altimetric echoes by a speckle noise whose effect is generally reduced by averaging many observed waveforms. However, averaging a lot of echoes increases the spatial scale which means that an increase of range accuracy is achieved at a price of an increasing spatial scale. Similarly, the study of low spatial scale phenomena is not well achieved since the averaging is not sufficient. This accuracy problem was considered by proposing new technologies that are described in the next section.

1.4 New altimeters

This section introduces two new technologies that are devoted to enhance the capabilities of the conventional altimeters in order to improve their accuracy and reduce the footprint area. These two technologies are related to Ka-band and delay/Doppler altimeters and are described in the following sections.

1.4.1 AltiKa

As described previously, AltiKa is an altimeter working in the Ka-band instead of the usual Ku-band. Working at high frequency brings many advantages such as a smaller antenna beamwidth (since it is inversely proportional to the frequency) and eliminates the need to use a second frequency to correct the ionospheric effect. However, it has some drawbacks since it is more sensitive to the atmospheric moisture. This altimeter can then be seen as a conventional altimeter in a modern sense since it includes many innovations that can be described as follows [Raney and Phalippou, 2011]:

- The range resolution is improved by increasing the receiver bandwidth B to 480 MHz while it was 320 MHz for Ku-band altimeters. The range resolution becomes 31 cm while it was 46 cm which provides a more accurate SSH. Moreover, increasing the bandwidth induces a smaller footprint which is of great importance for coastal altimetry applications.

- The 3 dB beamwidth is narrower which reduces the footprint area and increases the antenna gain improving the power budget of the altimeter. Note however that the altimeter becomes more sensitive to antenna mispointing.

- A higher pulse repetition frequency (PRF $\simeq$ 4 kHz) is possible because of the increased Walsh bound[6]. This improves noise reduction since it provides more echoes to be averaged for one second.

These innovations show that AltiKa has a smaller footprint which is suitable for coastal applications. Moreover, the accuracy of the estimated parameters is increased because of the higher PRF (more averaged echoes) and the improved range resolution. Note, however, that the altimeter is more sensitive to the atmospheric hydrometeors (water droplets) that may cause less than 4% of data loss. It is also more sensitive to antenna mispointing that should be more carefully monitored. Finally, one has to note that AltiKa is based on the same principle as conventional altimetry which means that the previous models and algorithms could be directly applied on its echoes while of course taking care of changing the values of the instrumental parameters.

1.4.2 Delay/Doppler altimetry

The delay/Doppler altimeter (DDA) is pulse limited across-track and beam limited along-track as first introduced by Raney in [Raney, 1998][7] (see Fig. 1.8). DDA fits into the logic of measurement improvement and has two main objectives as follows

- The first objective is to reduce the measurement noise by increasing the number of observations (looks) which provides better geophysical parameter estimates. Indeed, DDA requires coherent correlation between pulses [Raney, 1998] which is obtained by transmitting pulses with a high PRF (PRF = 18182 Hz for SIRAL altimeter [Wingham et al., 2006]).

- The second objective is to increase the along-track resolution which allows the measurements to remain valid until a distance of about 300 meters from the coast (while it was about 10 km for conventional altimetry). This is achieved by an appropriate processing that uses the

[6] The Walsh bound provides the maximum PRF that can be achieved when avoiding pulse correlations [Walsh., 1982]. Increasing the frequency enhances this bound as shown in [Raney and Phalippou, 2011].

[7] The reader is invited to consult [Chelton, 1989, Sandwell, 2011] for the definition of pulse limited and beam limited footprint. Before DDA, all the altimeters were based on pulse limited footprint since the covered area is smaller than that of beam limited footprint.

Doppler information contained in the data. The resulting footprint is described in Fig. 1.8 which presents the waveform formation of the central beam.

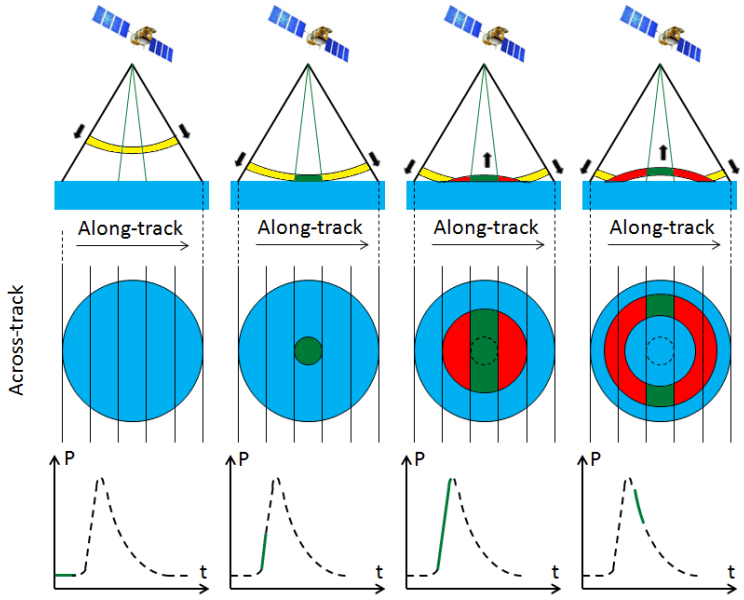

Figure 1.8: Formation of the central beam DDA waveform.

All of these advantages have led to consider DDA in many current and future satellite missions. The first satellite exploiting DDA is the Cryosat-2 satellite which has on board a SIRAL instrument that includes a DDA mode. Other future missions including DDA are Sentinel-3, Jason-CS (Jason Continuité de Service), and SWOT (Surface Water Ocean Topography), which shows the importance of this new technology. Note that the shape of DDA echo differs from that of conventional altimetry and hence requires a new appropriate model in order to process this kind of data.

1.5 Conclusions

This chapter presented the principles of satellite altimetry and provided a state of the art of the different waveform models and estimation strategies available in the literature. Some limitations of conventional altimetry were also described. These limitations are mainly due to the contamination of the echoes by land return in coastal areas because of the large footprint of the observed surface and the accuracy of the estimated parameters that is reduced because of the waveform corruption by speckle noise. The technical solutions that are the Ka-band and the delay/Doppler altimeters were presented and showed to be good solutions to increase the measurement accuracy.

This accuracy improvement can also be achieved by enhancing the quality of the data processing which is the goal of this thesis. Indeed, defining a new model specific to coastal altimetry may improve the processing of these data. This solution is considered in Chapter 2. Moreover, and as stated previously, a new model should be defined in order to use the delay/Doppler data and to thoroughly take advantage of this new technology. Two models are proposed in Chapters 3 and 4.

1.6 Conclusions (in French)

Ce chapitre a présenté les principes de l'altimétrie par satellite et a fourni un état de l'art des différents modèles de formes d'onde ainsi que les stratégies d'estimation disponibles dans la littérature. Certaines limitations de l'altimétrie conventionnelle ont également été décrites. Ces limitations sont principalement dues à la contamination des échos par des retours de la terre dans les zones côtières en raison de la grande tache au sol et la réduction de la précision de mesure en raison de la corruption des formes d'onde par le bruit de chatoiement. Deux solutions techniques, qui se basent sur l'altimètre à bande Ka et l'altimètre SAR/Doppler, ont été présentées. Ces dernières montrent un vrai potentiel pour l'amélioration de la qualité des mesures altimétriques.

L'amélioration de la qualité des paramètres estimés peut également s'obtenir en améliorant la qualité du traitement des données altimétriques qui est l'objectif de cette thèse. En effet, la définition d'un nouveau modèle spécifique à l'altimétrie côtière peut améliorer le traitement de ces données. Cette solution est considérée dans le chapitre 2. Par ailleurs, un nouveau modèle doit être défini pour utiliser les données de l'altimétrie SAR/Doppler et bien profiter des avantages de cette nouvelle technologie. Deux modèles sont proposés dans les chapitres 3 et 4.

Chapter 2

Coastal altimetric waveforms

Contents

2.1 Introduction (in French)

L'écho altimétrique océanique a une forme bien définie qui commence par un front de montée suivi d'une baisse progressive de la puissance sur le reste de la forme d'onde. Cette forme est bien décrite par le modèle Brown [Alberti et al., 2009, Brown, 1977, Naenna and Johnson, 2010] . Cependant, la forme d'onde altimétrique peut être corrompue par l'énergie réfléchie par la terre, par la pluie [Tournadre et al., 2009a,b] ou par des surfaces présentant des coefficients de rétrodiffusion différents de la surface océanique, ce qui rend les algorithmes classiques (décrits dans le précédent chapitre) inefficaces. Cette inefficacité est illustrée dans la figure 2.1 qui montre deux échos côtiers de Jason-2

(courbes noires) et leurs estimations résultant de l'estimateur du maximum de vraisemblance appliqué en utilisant le modèle Brown (courbes bleues). En raison de la présence d'un pic à l'extrémité du front de montée (figure 2.1 (a)) ou au milieu du plateau final (figure 2.1 (b)), le modèle Brown est manifestement incapable de saisir les variations de l'écho altimétrique. Un grand effort est récemment consacré au traitement des formes d'onde côtières afin de déplacer les mesures altimétriques près de la côte [Desportes et al., 2007, 2010]. L'analyse des échos côtiers a récemment été effectuée de manière approfondie dans les deux projets PISTACH [Mercier *et al*, 1998] et COASTALT [Vignudelli et al., 2011]. Dans le cadre du projet PISTACH, visant à améliorer les produits de l'altimétrie cotière, les signaux sont classés selon leurs formes géométriques comme le montre la figure 2.2 [Thibaut and Poisson, 2008]. Le but de cette classification est d'isoler les échos ayant des caractéristiques géométriques similaires afin d'estimer leurs paramètres altimétriques grâce à des algorithmes dédiés à chacune des classes. Comme le montre la figure 2.2, plusieurs classes de signaux étudiées dans le projet PISTACH sont corrompues par des pics. Ces signaux sont fréquemment observés dans les zones côtières. Plus précisément, en océan, environ 95 % des formes d'ondes sont en bon accord avec le modèle Brown. Cependant, ce pourcentage décroit rapidement à l'approche des côtes (ou sur des surfaces polaires). En effet, la figure 2.3 montre qu'environ 30 % des formes d'onde ne sont plus en accord avec le modèle de Brown à une distance de 8 km de la côte.

Ce chapitre introduit un nouveau modèle paramétrique, appelé modèle de Brown avec pic gaussien asymétrique (BAGP), pour les signaux altimétriques présentant un pic. Ces échos sont similaires à ceux des classes 7 et 13 de la figure 2.2 (les figures 2.1 (a) et (b) montrent des exemples d'échos appartenant à ces deux classes). L'idée d'utiliser un pic gaussien pour modéliser les pics des échos altimétriques est apparue dans [Gómez-Enri et al., 2010, Tourneret et al., 2010]. Cependant, le modèle étudié dans ce chapitre est plus général car il tient compte de l'asymétrie éventuelle du pic. Cette asymétrie est très importante pour les signaux de la classe 7 caractérisés par un pic asymétrique situé à l'extrémité du front de montée (voir figure 2.1 (a)). Une propriété intéressante du modèle proposé BAGP est qu'il se réduit au modèle classique de Brown lorsque l'amplitude du pic est nulle. Ainsi, on peut s'attendre à des performances similaires à celles du modèle de Brown lors du traitement des échos océaniques ainsi qu'à une amélioration de la reconstruction des signaux corrompus par des pics.

Par ailleurs, il est intéressant de noter que le modèle BAGP peut gérer les pics symétriques affectant la forme d'onde altimétrique lorsque le coefficient d'asymétrie est mis à zéro. Ainsi, le modèle BAGP devrait également être capable de modéliser avec précision les échos altimétriques de la classe 13 (voir figure 2.1 (b) pour un exemple). Pour résumer, le modèle proposé BAGP convient pour le traitement des échos océaniques ainsi que les échos corrompus soit par un pic symétrique ou asymétrique.

Afin d'estimer les paramètres inconnus du modèle BAGP, nous proposons d'utiliser la méthode du maximum de vraisemblance qui a montré d'intéressants résultats pour le modèle classique de Brown [Dumont, 1985, Rodriguez, 1988]. L'obtention d'une formule analytique de la solution de l'estimateur du maximum de vraisemblance du modèle BAGP est difficile. En conséquence, deux algorithmes numériques sont étudiés pour le calcul de cet estimateur. Le premier est basé sur une stratégie de Newton-Raphson similaire à celle étudiée dans [Dumont, 1985] et [Amarouche et al., 2004]. Le second est basé sur une approche géométrique connue sous le nom de l'algorithme de Nelder-Mead [Nelder and Mead, 1965]. Les bornes de Cramér-Rao des paramètres du modèle BAGP sont aussi déterminées. Ces bornes sont intéressantes car elles fournissent la variance minimale de tout estimateur non biaisé. Une autre propriété intéressante de ces bornes est que la variance de tout estimateur MLE peut être approchée, sous de faibles conditions et pour des échantillons de grande taille, par sa borne. Ces conditions sont par exemple indiquées dans [Kendall and Stuart, 1961, chap.18] (nous devons principalement vérifier que le domaine de définition de la vraisemblance ne dépend pas des paramètres inconnus et que cette dernière est deux fois dérivable en fonction des paramètres inconnus).

Le chapitre est structuré comme suit. La section 2.3 présente le modèle proposé (noté BAGP). Les relations entre le modèle BAGP, le modèle de Brown et celui de Brown avec pic gaussien introduit dans [Tourneret et al., 2010] sont également étudiées. La vraisemblance associée au modèle BAGP est calculée dans la section 2.4. La section 2.5 présente les différents algorithmes servant à maximiser la vraisemblance du modèle BAGP. La section 2.6 calcule les bornes de Cramér-Rao associées aux paramètres du modèle BAGP. Les résultats de simulation obtenus sur des données synthétiques sont présentés dans la section 2.7, alors que l'analyse de signaux réels issus du satellite Jason-2 est présentée dans la section 2.8. Finalement, les sections 2.9 et 2.10 présentent les conclusions et les perspectives.

2.2 Introduction

Over an ocean surface, the altimetric echo has a well-defined shape, with a steeply rising leading edge followed by a gradual decline in power over the rest of the waveform which is accurately modeled by the Brown model [Alberti et al., 2009, Brown, 1977, Naenna and Johnson, 2010]. However, the altimetric waveform can be corrupted by land returns, by rain [Tournadre et al., 2009a,b] or by the summation of backscattered signals coming from separate reflective ocean surfaces which make the conventional algorithms (described in the previous chapter) ineffective. This inefficiency is illustrated in Fig. 2.1 which shows two representative coastal Jason-2 waveforms (black curves) and their estimates resulting from the maximum likelihood (ML) estimator applied to the Brown model (blue curves). Due to the presence of a peak at the end of the leading edge (Fig. 2.1 (a)) or in the middle of the trailing edge (Fig. 2.1 (b)), the Brown model is clearly unable to capture the variations of the altimetric echo. A great effort is now devoted to process coastal waveforms in order to move the altimetric measurements closer to the coast [Desportes et al., 2007, 2010]. The analysis of coastal waveforms has been recently considered intensively in the two projects PISTACH [Mercier *et al*, 1998] and COASTALT [Vignudelli et al., 2011]. In the frame of the PISTACH project aiming at improving coastal altimeter products, waveforms are classified according to geometrical shapes displayed in Fig. 2.2 [Thibaut and Poisson, 2008]. The goal of this classification is to isolate echoes having similar geometrical characteristics in order to estimate the corresponding altimeter parameters thanks to dedicated so-called retracking algorithms. As shown in Fig. 2.2, several signal classes investigated in the PISTACH project are characterized by signals corrupted by peaks. These signals are frequently observed in the coastal areas. More precisely, in open ocean, about 95 % of the waveforms are in good agreement with the Brown model. However, when approaching the coasts (or over polar surfaces), this percentage rapidly decreases. As shown in Fig. 2.3, roughly 25% to 30% of the waveforms are not in agreement with the Brown model at a distance of 8 km off the shorelines.

This chapter introduces a parametric model for peaky altimetric signals (similar to those classified in classes 7 and 13 of Fig. 2.2 - note that Fig. 2.1 (a) and (b) show examples of waveforms from both classes) referred to as Brown with asymmetric Gaussian peak (BAGP) model. The BAGP model is

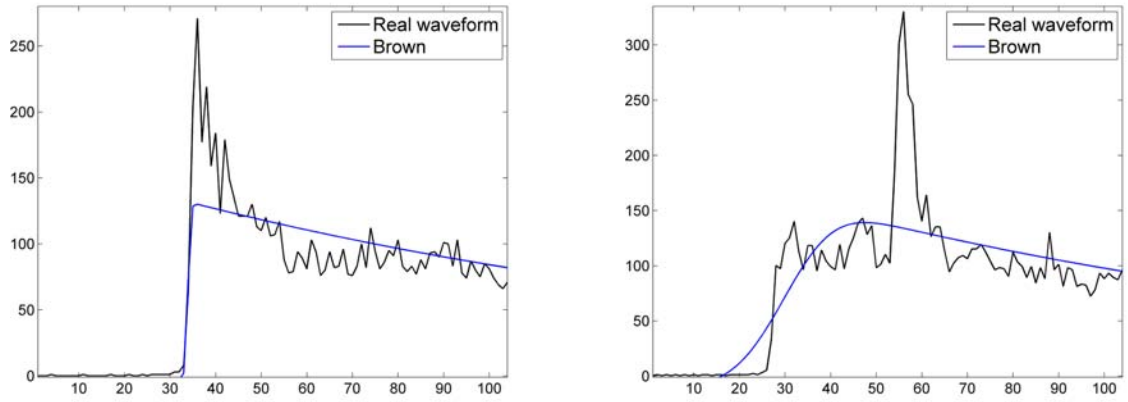

(a) (b)

Figure 2.1: Examples of real JASON-2 waveforms and their Brown model estimations.

appropriate for signals defined as the sum of a Brown echo and a Gaussian peak. The idea of using Gaussian shapes to model peaks in altimetric waveforms has appeared in [Gómez-Enri et al., 2010, Tourneret et al., 2010]. However, the model studied in this chapter is more general since it allows peak asymmetry to be considered. Peak asymmetry is clearly important for signals of class 7 characterized by an asymmetric peak located at the end of the leading edge (see Fig. 2.1 (a) for an example). An interesting property of the proposed BAGP model is that it reduces to the classical Brown model when the amplitude of the peak is zero. Thus, one can expect similar performance with this model and the classical Brown model for oceanic waveforms as well as improved signal reconstructions for waveforms corrupted by peaks. Moreover, it is interesting to note that the BAGP model can handle symmetric peaks affecting the altimetric waveform when the asymmetry coefficient is set to zero. Thus the BAGP model should also be able to model accurately altimetric waveforms from class 13 (see Fig. 2.1 (b) for an example). To summarize, the proposed BAGP model is appropriate to usual oceanic waveforms as well as coastal waveforms corrupted by either a symmetric or an asymmetric peak.

In order to estimate the unknown BAGP model parameters, we propose to use the ML method that has shown interesting results for the classical Brown model [Dumont, 1985, Rodriguez, 1988].

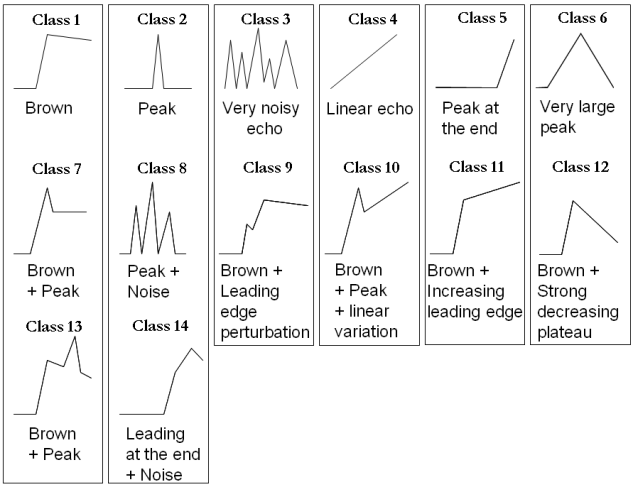

Figure 2.2: Different shapes of altimetric signals resulting from CNES/PISTACH project.

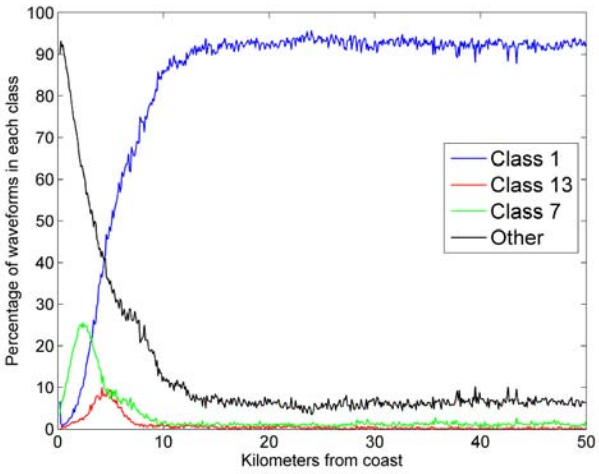

Figure 2.3: Percentages of observed altimetric waveforms in classes 1, 7, 13 and others versus distance to the coast.

Closed-form expressions for the maximum likelihood estimator (MLE) of the BAGP model parameters are difficult to obtain. As a consequence, numerical algorithms are considered for computing this estimator. The first algorithm is based on a Newton-Raphson strategy, similar to the one investigated in [Dumont, 1985] and [Amarouche et al., 2004]. A second algorithm based on a geometrical technique

known as the Nelder-Mead method [Nelder and Mead, 1965] is also studied. The Cramér-Rao bounds (CRBs) associated with the BAGP model parameters are finally determined. These bounds are interesting since they provide the minimum variances for unbiased estimators. Another interesting property of these bounds is that the variance of any MLE estimator can be approximated for large sample size by its corresponding CRB under weak conditions. These conditions are for instance specified in [Kendall and Stuart, 1961, chap. 18] (we mainly have to check that the range of the likelihood does not depend on the unknown parameters and that the likelihood is a twice-differentiable function of its unknown parameters throughout its range).

The chapter is structured as follows. Section 2.3 presents the BAGP model considered in this study. Relationships between the BAGP, the Brown model and the Brown with Gaussian peak model introduced in [Tourneret et al., 2010] are also studied. The likelihood associated with the BAGP model is derived in section 2.4. Section 2.5 introduces the different algorithms used to maximize the likelihood of the BAGP model. Section 2.6 derives the CRBs of the BAGP model parameters. Simulation results obtained with synthetic data are analyzed in Section 2.7, whereas an analysis of real Jason-2 waveforms is presented in Section 2.8. Conclusions and future works are finally reported in Section 2.9.

2.3 Waveform model

A simplification of the Brown's model assumes that the altimetric waveform, associated with oceanic surfaces, is characterized by three parameters. This simplified model was given in (1.20) which showed the continuous expression of the altimetric signal. The discrete altimetric signal is obtained by sampling the continuous-time signal $s(t)$ defined in (1.20) leading to

$$s_k = \frac{P_u}{2}\left[1 + \text{erf}\left(\frac{kT_s - \tau_s - \alpha\sigma_c^2}{\sqrt{2}\sigma_c}\right)\right] \exp\left[-\alpha\left(kT_s - \tau_s - \frac{\alpha\sigma_c^2}{2}\right)\right] + N_t, \tag{2.1}$$

where T_s is the sampling period, $s_k = s(kT_s)$ is the kth data sample of the received altimetric signal and τ_s is the epoch expressed in seconds. The additive noise parameter N_t is generally estimated as the mean value of the first data samples and subtracted from the observed samples s_k, resulting in $N_t = 0$ in model (2.1). The model (2.1) has received considerable attention in the literature and has

been shown to be very accurate for oceanic waveforms. However, it is inappropriate for modeling altimetric waveforms backscattered from non-oceanic surfaces such as ice and land or from coastal areas [Gómez-Enri et al., 2010, Thibaut and Poisson, 2008, Tourneret et al., 2010]. Indeed, over such surfaces, altimetric echoes can show some peaks in their trailing edge due to backscattering returns from non water areas as shown in Fig. 2.4 corresponding to real altimetric waveforms obtained with the Jason-1 altimeter over the Amazonia area. Therefore, this chapter studies a new model (referred

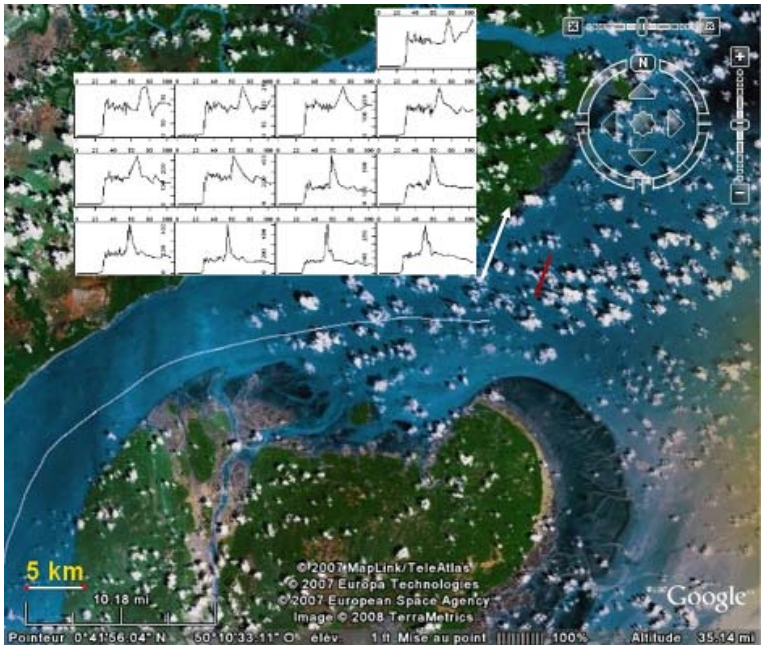

Figure 2.4: Example of observed waveforms obtained with Jason-1 altimeter over Amazonia area (extracted from [Smith et al., 2008]).

to as BAGP for Brown Asymmetric Gaussian Peak) defined as the superposition of a Brown echo s_k and an asymmetric Gaussian peak p_k such that the observed signal is

$$\tilde{s}_k = s_k + p_k \tag{2.2}$$

with

$$p_k = A \exp\left[\frac{-1}{2\sigma^2}\left(kT_s - T\right)^2\right]\left\{1 + \operatorname{erf}\left[\eta\frac{(kT_s - T)}{\sqrt{2}}\right]\right\} \tag{2.3}$$

where A, T, σ, η are the amplitude, location, width and asymmetry coefficient of the peak. It is interesting to note that the Gaussian peak defined in (2.3) reduces to a symmetric Gaussian peak when $\eta = 0$ (thus, the parameter η will be referred to as asymmetry coefficient in this thesis). The resulting model parameterized by A, T, σ is referred to as BGP model (for Brown Gaussian Peak model). Note also that the BAGP and BGP models reduce to the Brown model for $A = 0$. Fig. 2.5 shows the effect of the asymmetry coefficient η on the normalized peak p_k defined in (2.3). A positive value of η squeezes the left side of the peak while a negative value squeezes its right side. Note that for real JASON-2 waveforms, the estimated values of η are mainly positive and located near 0.

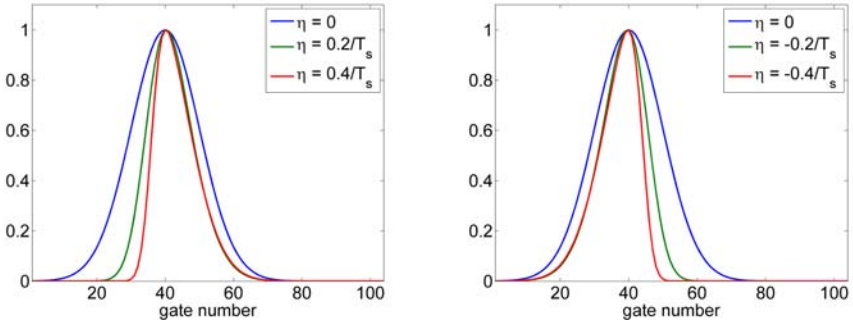

(a) (b)

Figure 2.5: Effect of the asymmetry coefficient on the peak.

The next section introduces an ML estimation method to estimate the unknown parameter vector associated with the BAGP model defined by (2.2) and (2.3). These unknown parameters are displayed in Table 2.1.

2.4 Maximum likelihood estimator

Altimetric data are corrupted by multiplicative speckle noise. In order to reduce the influence of this noise affecting each individual echo, a sequence of L_c consecutive echoes are averaged on-board the satellite. Assuming pulse-to-pulse statistical independence (which is a valid assumption for Jason [Quartly et al., 2001]), the resulting speckle noise sequence is independent and identically distributed according to a gamma distribution whose shape and inverse scale parameters equal the number of

Table 2.1: Description of the model parameters.

Name	Description
P_u	Amplitude of Brown's waveform
τ	The epoch
SWH	Significant wave height
A	Amplitude of the peak
T	Location of the peak
σ	Standard deviation of the Gaussian peak
η	Asymmetry coefficient of the peak

looks L_c, i.e., the number of incoherent summations of consecutive echoes. When using the BAGP model defined in (2.2), an observed altimetric waveform can be expressed as

$$y_k = \tilde{s}_k n_k, \quad k = 1, \ldots, K \tag{2.4}$$

where K is the number of samples. Using (2.4) and the properties of the noise sequence $\boldsymbol{n} = (n_1, ..., n_K)^T$, the likelihood function of the observed samples $f(\boldsymbol{y}|\boldsymbol{\theta})$ can be expressed as follows

$$f(\boldsymbol{y}|\boldsymbol{\theta}) = \left[\frac{L_c^{L_c}}{\Gamma(L_c)}\right]^K \exp\left(-L_c \sum_{k=1}^{K} \frac{y_k}{\tilde{s}_k}\right) \left(\prod_{k=1}^{K} y_k\right)^{L_c-1} \left(\prod_{k=1}^{K} \tilde{s}_k\right)^{-L_c} \left(\prod_{k=1}^{K} \mathcal{I}_{\mathbb{R}^+}(y_k)\right) \tag{2.5}$$

where $\boldsymbol{y} = (y_1, \ldots, y_K)^T$, $\boldsymbol{\theta}_{\mathrm{B}} = (P_u, \tau_s, \mathrm{SWH})^T$ and $\boldsymbol{\theta}_p = (A, T, \sigma, \eta)^T$ contain the unknown Brown and peak parameters, $\boldsymbol{\theta} = \left(\boldsymbol{\theta}_{\mathrm{B}}^T, \boldsymbol{\theta}_p^T\right)^T$ and $\mathcal{I}_{\mathbb{R}^+}(y_k)$ is the indicator function ($\mathcal{I}_{\mathbb{R}^+}(y_k) = 1$ if $y_k \in \mathbb{R}^+$ and $\mathcal{I}_{\mathbb{R}^+}(y_k) = 0$ else). The MLE of $\boldsymbol{\theta}$ (denoted as $\widehat{\boldsymbol{\theta}}_{\mathrm{MLE}}$) is obtained by maximizing the likelihood function $f(\boldsymbol{y}|\boldsymbol{\theta})$ with respect to $\boldsymbol{\theta}$ or equivalently by minimizing the negative log-likelihood (referred to as cost-function in what follows) given by

$$\mathcal{C}(\boldsymbol{\theta}) = -\ln\left[f(\boldsymbol{y}|\boldsymbol{\theta})\right] = \mathrm{Cste} + L_c \sum_{k=1}^{K} \frac{y_k}{\tilde{s}_k} - (L_c - 1) \sum_{k=1}^{K} \ln(y_k) + L_c \sum_{k=1}^{K} \ln(\tilde{s}_k) \tag{2.6}$$

where Cste is an additive constant. The MLE of $\boldsymbol{\theta}$ cannot be computed in closed-form as in the case of a classical Brown model (where there is no peak in the altimetric signal model). Consequently, numerical optimization techniques have to be used to implement the MLE. Two approaches are

investigated in this chapter based on the Newton-Raphson (NR) [Bertsekas, 1995] and Nelder-Mead (NM) methods [Nelder and Mead, 1965]. These methods are presented in the next section.

2.5 Estimation algorithms

This section introduces two estimation algorithms. The first one is the Newton-Raphson algorithm that is widely used in altimetry [Dumont, 1985, Rodriguez, 1988]. This algorithm approximates the maximum likelihood estimator by a gradient descent approach. The second algorithm is a geometrical method called the Nelder-Mead algorithm. This algorithm provides the exact maximum likelihood estimator and is considered as a reference in terms of estimation performance.

2.5.1 Newton-Raphson method

The estimation of the BAGP parameters can be achieved by generalizing the NR algorithm commonly used to estimate the Brown model parameters. This section first summaries the main steps of the NR algorithm when applied to the Brown model. A generalization to the BAGP model is then presented.

Newton-Raphson method for Brown model

The NR method is an iterative algorithm that updates the parameters to be estimated according to the following recursion

$$\boldsymbol{\theta}_{\mathrm{B}}(n+1) = \boldsymbol{\theta}_{\mathrm{B}}(n) - \psi(n)\boldsymbol{H}_{\mathrm{B}}^{-1}(n)\nabla\mathcal{C}_{\mathrm{B}}(n) \tag{2.7}$$

where $\boldsymbol{\theta}_{\mathrm{B}} = (P_u, \tau_s, \mathrm{SWH})^T = (\theta_{\mathrm{B},1}, \theta_{\mathrm{B},2}, \theta_{\mathrm{B},3})^T$, $\psi(n)$ is a stepsize belonging to the interval $[0,1]$ (ensuring the convergence of the algorithm), ∇ is the gradient operator and $\boldsymbol{H}_{\mathrm{B}}$ is a symmetric and invertible matrix defined as the Hessian of the cost function $\mathcal{C}_{\mathrm{B}}$ which is obtained by setting $\tilde{s}_k = s_k$ in (2.6). The gradient of the cost function $\mathcal{C}_{\mathrm{B}}$ (of size (3×1)) with respect to the Brown vector parameters $\boldsymbol{\theta}_{\mathrm{B}}$ is given by

$$\nabla\mathcal{C}_{\mathrm{B}} = \left(-\frac{\partial \ln\left[f_{\mathrm{B}}(\boldsymbol{y}|\boldsymbol{\theta}_{\mathrm{B}})\right]}{\partial\theta_{\mathrm{B,i}}}\right)^T_{i=1,\cdots,3} = L_c\left(\sum_{k=1}^{K}\frac{s_k - y_k}{s_k^2}\frac{\partial s_k}{\partial\theta_{\mathrm{B,i}}}\right)^T_{i=1,\cdots,3} \tag{2.8}$$

where f_{B} is the likelihood obtained by setting $\tilde{s}_k = s_k$ and $\boldsymbol{\theta} = \boldsymbol{\theta}_{\mathrm{B}}$ in (2.5). More precisely, (2.8) can be expressed as

$$\nabla \mathcal{C}_{\mathrm{B}} = L_c \boldsymbol{B}_{\mathrm{B}} \boldsymbol{d}_{\mathrm{B}} \tag{2.9}$$

where $\boldsymbol{d}_{\mathrm{B}} = (d_k)_{k=1,\cdots,K}$ is a $(K \times 1)$ vector with $d_k = \frac{s_k - y_k}{s_k}$ and $\boldsymbol{B}_{\mathrm{B}}$ is a matrix whose components are $B_{i,k} = \frac{1}{s_k} \frac{\partial s_k}{\partial \theta_{\mathrm{B},\mathrm{i}}}$, for $i = 1, \cdots, 3$ and $k = 1, \cdots, K$.

In order to reduce the computational complexity due to the calculation of the Hessian at each iteration, an approximation of this matrix is generally used. This approximation replaces the matrix $\boldsymbol{H}_{\mathrm{B}}$ by its expectation

$$\boldsymbol{F}_{\mathrm{B}} = E\left[\boldsymbol{H}_{\mathrm{B}}\right] = -E \begin{bmatrix} \frac{\partial^2 \ln f_{\mathrm{B}}}{\partial \theta_{\mathrm{B},1}^2} & \frac{\partial^2 \ln f_{\mathrm{B}}}{\partial \theta_{\mathrm{B},1} \theta_{\mathrm{B},2}} & \frac{\partial^2 \ln f_{\mathrm{B}}}{\partial \theta_{\mathrm{B},1} \theta_{\mathrm{B},3}} \\ \frac{\partial^2 \ln f_{\mathrm{B}}}{\partial \theta_{\mathrm{B},2} \theta_{\mathrm{B},1}} & \frac{\partial^2 \ln f_{\mathrm{B}}}{\partial \theta_{\mathrm{B},2}^2} & \frac{\partial^2 \ln f_{\mathrm{B}}}{\partial \theta_{\mathrm{B},2} \theta_{\mathrm{B},3}} \\ \frac{\partial^2 \ln f_{\mathrm{B}}}{\partial \theta_{\mathrm{B},3} \theta_{\mathrm{B},1}} & \frac{\partial^2 \ln f_{\mathrm{B}}}{\partial \theta_{\mathrm{B},3} \theta_{\mathrm{B},2}} & \frac{\partial^2 \ln f_{\mathrm{B}}}{\partial \theta_{\mathrm{B},3}^2} \end{bmatrix} \tag{2.10}$$

where E stands for the mathematical expectation. Note that the matrix $\boldsymbol{F}_{\mathrm{B}}$ is the Fisher information matrix (FIM) that is commonly used to compute the Cramér-Rao bounds [Mailhes et al., 2008]. The iterative formula obtained after replacing $\boldsymbol{H}_{\mathrm{B}}$ by $\boldsymbol{F}_{\mathrm{B}}$ in (2.7) is

$$\boldsymbol{\theta}_{\mathrm{B}}(n+1) = \boldsymbol{\theta}_{\mathrm{B}}(n) - \psi(n) \boldsymbol{F}_{\mathrm{B}}^{-1}(n) \nabla \mathcal{C}_{\mathrm{B}}(n). \tag{2.11}$$

This parameter recursion has shown interesting properties for adaptive filtering and is sometimes referred to as Fisher scoring [Green, 1984]. Determining the matrix $\boldsymbol{F}_{\mathrm{B}}$ requires to compute the expectations of the second order derivatives of f_{B}. It is straightforward to show that

$$E\left[-\frac{\partial^2 \ln f_{\mathrm{B}}}{\partial \theta_{\mathrm{B},\mathrm{i}} \partial \theta_{\mathrm{B},\mathrm{j}}}\right] = L_c \sum_{k=1}^{K} \frac{1}{s_k^2} \frac{\partial s_k}{\partial \theta_{\mathrm{B},\mathrm{i}}} \frac{\partial s_k}{\partial \theta_{\mathrm{B},\mathrm{j}}} \tag{2.12}$$

where the derivatives of s_k are provided in the Appendix A. As a consequence, the matrix $\boldsymbol{F}_{\mathrm{B}}$ can be written as $\boldsymbol{F}_{\mathrm{B}} = L_c \boldsymbol{B}_{\mathrm{B}} \boldsymbol{B}_{\mathrm{B}}^T$ and the recursive formula (2.11) reduces to

$$\boldsymbol{\theta}_{\mathrm{B}}(n+1) = \boldsymbol{\theta}_{\mathrm{B}}(n) - \psi(n) \left(\boldsymbol{B}_{\mathrm{B}} \boldsymbol{B}_{\mathrm{B}}^T\right)^{-1} \boldsymbol{B}_{\mathrm{B}} \boldsymbol{d}_{\mathrm{B}}. \tag{2.13}$$

Note finally that the vectors $\boldsymbol{B}_{\mathrm{B}}$, $\boldsymbol{d}_{\mathrm{B}}$, involved in (2.13), are generally approximated by $d_k = \frac{s_k - y_k}{P_u}$ for $k = 1, \cdots, K$ and $B_{i,k} = \frac{1}{P_u} \frac{\partial s_k}{\partial \theta_{\mathrm{B},\mathrm{i}}}$, for $i = 1, \cdots, 3$ and $k = 1, \cdots, K$. The resulting algorithm reduces to a least squares procedure that is known as MLE3 algorithm [Dumont, 1985, Thibaut et al., 2004].

Newton-Raphson method for the BAGP

In order to generalize the previous NR recursion to the BAGP model, we introduce a $(3 \times K)$ matrix $\widetilde{\boldsymbol{B}}$ whose elements are $\widetilde{B}_{i,k} = \frac{\partial \tilde{s}_k}{\tilde{s}_k \partial \theta_{\mathrm{B,i}}}$ with $i = 1, \cdots, 3$ and $k = 1, \cdots, K$, a $(4 \times K)$ matrix $\widetilde{\boldsymbol{P}}$ whose elements are $\widetilde{P}_{i,k} = \frac{\partial p_k}{\tilde{s}_k \partial \theta_{\mathrm{p,i}}}$ with $i = 1, \cdots, 4$ and $k = 1, \cdots, K$ and a $(K \times 1)$ vector $\widetilde{\boldsymbol{d}}$ with components $\tilde{d}_k = \frac{\tilde{s}_k - y_k}{\tilde{s}_k}$. The unknown parameter vector for the BAGP is $\boldsymbol{\theta} = \left(\boldsymbol{\theta}_{\mathrm{B}}^T, \boldsymbol{\theta}_{\mathrm{p}}^T\right)^T = (\theta_1, \theta_2, \cdots, \theta_7)^T$. We propose to estimate $\boldsymbol{\theta}$ using the following recursive formula

$$\boldsymbol{\theta}(n+1) = \boldsymbol{\theta}(n) - \psi(n) \boldsymbol{F}^{-1}(n) \nabla \mathcal{C}(n) \tag{2.14}$$

where $\boldsymbol{F}(n)$ and $\nabla \mathcal{C}(n)$ are the FIM and gradient of $\mathcal{C}$ evaluated at $\boldsymbol{\theta} = \boldsymbol{\theta}(n)$. Straightforward computations lead to

$$\boldsymbol{F} = -E \begin{bmatrix} \frac{\partial^2 \ln f}{\partial \theta_1^2} & \frac{\partial^2 \ln f}{\partial \theta_1 \theta_2} & \cdots & \frac{\partial^2 \ln f}{\partial \theta_1 \theta_7} \\ \frac{\partial^2 \ln f}{\partial \theta_2 \theta_1} & \frac{\partial^2 \ln f}{\partial \theta_2^2} & \cdots & \frac{\partial^2 \ln f}{\partial \theta_2 \theta_7} \\ \cdots & \cdots & \cdots & \cdots \\ \frac{\partial^2 \ln f}{\partial \theta_7 \theta_1} & \frac{\partial^2 \ln f}{\partial \theta_7 \theta_2} & \cdots & \frac{\partial^2 \ln f}{\partial \theta_7^2} \end{bmatrix} = L_c \begin{pmatrix} \widetilde{\boldsymbol{B}} \widetilde{\boldsymbol{B}}^T & \widetilde{\boldsymbol{B}} \widetilde{\boldsymbol{P}}^T \\ \widetilde{\boldsymbol{P}} \widetilde{\boldsymbol{B}}^T & \widetilde{\boldsymbol{P}} \widetilde{\boldsymbol{P}}^T \end{pmatrix} \tag{2.15}$$

and

$$\nabla \mathcal{C} = L_c \begin{pmatrix} \widetilde{\boldsymbol{B}} \\ \widetilde{\boldsymbol{P}} \end{pmatrix} \widetilde{\boldsymbol{d}}. \tag{2.16}$$

As a consequence, the NR recursion (2.14) can be written

$$\boldsymbol{\theta}(n+1) = \boldsymbol{\theta}(n) - \psi(n) \begin{pmatrix} \widetilde{\boldsymbol{B}} \widetilde{\boldsymbol{B}}^T & \widetilde{\boldsymbol{B}} \widetilde{\boldsymbol{P}}^T \\ \widetilde{\boldsymbol{P}} \widetilde{\boldsymbol{B}}^T & \widetilde{\boldsymbol{P}} \widetilde{\boldsymbol{P}}^T \end{pmatrix}^{-1} \begin{pmatrix} \widetilde{\boldsymbol{B}} \\ \widetilde{\boldsymbol{P}} \end{pmatrix} \widetilde{\boldsymbol{d}}. \tag{2.17}$$

Similarly to the Brown case, the matrices $\widetilde{\boldsymbol{B}}$, $\widetilde{\boldsymbol{P}}$ and $\widetilde{\boldsymbol{d}}$, involved in (2.17), can be simplified by replacing s_k in their denominator by P_u resulting in a least squares procedure. Note finally that the Levenberg-Marquardt (LM) algorithm [Bertsekas, 1995] (which is a gradient descent algorithm) can also be considered since it provides similar estimation performance as the NR algorithm as shown in Appendix B. This LM algorithm will be described in the next chapter.

2.5.2 Nelder-Mead method

The Nelder-Mead method is a simplex method for nonlinear unconstrained optimization used for minimizing an objective function in a many-dimensional subspace [Lagarias et al., 1998, Nelder and Mead, 1965]. This direct search method does not use any information (explicit or implicit) about the derivatives of the cost function. By considering m_p as the length of the parameter vector to estimate ($m_p = 3$ for the Brown model, $m_p = 6$ for the BGP and $m_p = 7$ for the BAGP), the NM algorithm[1] works in an m_p-dimensional subspace that is characterized by $m_p + 1$ distinct vectors that are its vertices and their associated function values. At each step of the search, a new point in or near the current simplex[2] is generated. The cost function is evaluated at the new generated point and compared with its values at the vertices of the simplex. When the cost function is smaller at the generated point, one of the vertices is replaced by this generated point, giving a new simplex. This step is repeated until the diameter of the simplex is less than a specified tolerance (see [Bertsekas, 1995, Lagarias et al., 1998, Nelder and Mead, 1965] for more details).

2.6 Cramér-Rao bounds

The Cramér-Rao bounds (CRBs) provide the minimum variances for unbiased parameters. As a consequence, they can be considered as references in terms of estimation errors. Comparing the mean square errors (MSEs) of estimators to the corresponding CRBs helps us to understand the potential gain in performance we might obtain with other estimation algorithms. The CRBs for the parameters of the Brown model were derived in [Mailhes et al., 2008]. This section generalizes the results of [Mailhes et al., 2008] to the BAGP model. The CRBs are obtained by inverting the FIM of $\boldsymbol{\theta}$. Since the thermal noise parameter N_t has been estimated using the first samples of the altimetric

[1] Note that this algorithm is available in Matlab by the function "fminsearch".

[2] A simplex of dimension m_p is an m_p-dimensional polytope defined as the convex hull of its $m_p + 1$ vertices. For example, a simplex of dimension 2 is a triangle [Rudin, 1976]. Similarly, a polygon is a polytope in two dimensions, a polyhedron in three dimensions, and so on $\cdots$ [Coxeter, 1973]

signal, it has also to be included in the FIM resulting in the (8×8) matrix

$$\boldsymbol{F}_{\mathrm{CRB}} = -E\begin{bmatrix} \frac{\partial^2 \ln f}{\partial \theta_1^2} & \frac{\partial^2 \ln f}{\partial \theta_1 \theta_2} & \cdots & \frac{\partial^2 \ln f}{\partial \theta_1 N_t} \\ \cdots & \cdots & \cdots & \cdots \\ \frac{\partial^2 \ln f}{\partial \theta_7 \theta_1} & \frac{\partial^2 \ln f}{\partial \theta_7 \theta_2} & \cdots & \frac{\partial^2 \ln f}{\partial \theta_7 N_t} \\ \frac{\partial^2 \ln f}{\partial N_t \theta_1} & \frac{\partial^2 \ln f}{\partial N_t \theta_2} & \cdots & \frac{\partial^2 \ln f}{\partial N_t^2} \end{bmatrix} \tag{2.18}$$

whose elements are given by

$$\begin{aligned} E\left[-\frac{\partial^2 \ln f}{\partial \theta_i \partial \theta_j}\right] &= L_c \sum_{k=1}^{K} \frac{1}{\tilde{s}_k^2} \frac{\partial \tilde{s}_k}{\partial \theta_i} \frac{\partial \tilde{s}_k}{\partial \theta_j} \\ E\left[-\frac{\partial^2 \ln f}{\partial N_t \partial \theta_i}\right] &= L_c \sum_{k=1}^{K} \frac{1}{\tilde{s}_k^2} \frac{\partial \tilde{s}_k}{\partial \theta_i}. \end{aligned} \tag{2.19}$$

and the derivatives of s_k and p_k with respect to N_t, the Brown and peak parameters are detailed in the Appendix A. After replacing these derivatives in (2.18), the inverse of the $\boldsymbol{F}_{\mathrm{CRB}}$ can be computed. The BAGP model parameter CRBs are defined as the diagonal elements of the resulting inverse FIM. Note that the Brown CRBs are obtained by considering the parameter vector $\boldsymbol{\theta} = (\theta_1, \theta_2, \theta_3)^T$ and a (4×4) FIM. Similarly, the BGP CRBs are obtained by considering $\boldsymbol{\theta} = (\theta_1, \ldots, \theta_6)^T$ and a (7×7) FIM.

2.7 Simulation results for synthetic waveforms

2.7.1 Estimation performance

This section introduces the criteria used to evaluate the quality of the estimators resulting from the different models (Brown model, BGP, BAGP). The quality of the estimation for synthetic waveforms can be measured by comparing the estimated and true parameters by using the root mean square error (RMSE)

$$\mathrm{RMSE}\left(\theta_i\right) = \sqrt{\frac{1}{N_{\mathrm{MC}}} \sum_{\ell=1}^{N_{\mathrm{MC}}} \left[\theta_i - \hat{\theta}_i(\ell)\right]^2}, \quad i = 1, \cdots, 7 \tag{2.20}$$

where θ_i is the true parameter, $\hat{\theta}_i(\ell)$ is the estimated parameter for the ℓth waveform and N_{MC} is the number of synthetic waveforms. In the case of a real waveform, since the true value of $\boldsymbol{\theta}$ is not

available, the reconstruction error (RE) can be used to evaluate the quality of an estimation method

$$\mathrm{RE} = \sqrt{\frac{1}{K}\sum_{k=1}^{K}(y_k - \hat{y}_k)^2} = \frac{||\boldsymbol{y} - \hat{\boldsymbol{y}}||}{\sqrt{K}} \tag{2.21}$$

where $\hat{y}_k$ denotes the estimated waveform obtained by replacing the unknown parameters by their estimates in $\tilde{s}_k$ defined in (2.2). The average reconstruction error (ARE) given by

$$\mathrm{ARE} = \sqrt{\frac{1}{N_{\mathrm{MC}}\,K}\sum_{i=1}^{N_{\mathrm{MC}}}||\boldsymbol{y}_i - \hat{\boldsymbol{y}}_i||^2} \tag{2.22}$$

can also be used when considering N_{MC} synthetic waveforms, $\boldsymbol{y}_i = (y_{i1}, \cdots, y_{iK})^T$ for $i = 1, \cdots, N_{\mathrm{MC}}$.

2.7.2 Parameter estimation

The first set of simulations shows that the proposed BAGP model can handle Brown waveforms. For this, we have generated synthetic signals according to (2.1) with a sampling time $T_s = 3.125$ ns and parameters $P_u = 130$, $\tau_s = 31\,T_s \approx 96.9$ ns and varying SWH. All results have been averaged using 300 Monte Carlo runs (with different noise realizations) for each value of SWH varying in the interval of interest $[1, 8]$ meters. Figs. 2.6.a, 2.6.c and 2.6.e show that similar RMSEs are obtained for the different models (Brown, BGP or BAGP) when using the NM algorithm for parameter estimation[3]. However, when using the NR algorithm, Figs. 2.6.b, 2.6.d and 2.6.f show that there are slightly different RMSEs from one model to another (note that the scales are different in Figs. 2.6.a, 2.6.c, 2.6.e and Figs. 2.6.b, 2.6.d, 2.6.f). This result can be explained since the NM algorithm provides the exact MLE, while the NR algorithm only approximates the MLE via a descent method. Note that the smallest RMSEs depicted in Fig. 2.6.b, 2.6.d and 2.6.f correspond to the Brown model where less parameters are estimated. However, the estimates obtained using the other two models (BGP and BAGP) are satisfactory even if these models are not needed for Brown waveforms. Note finally that the NM method always provides better results than the NR method at the price of a higher computational time.

[3]The epoch RMSEs are expressed in meters in order to directly evaluate the effect on the estimated satellite height.

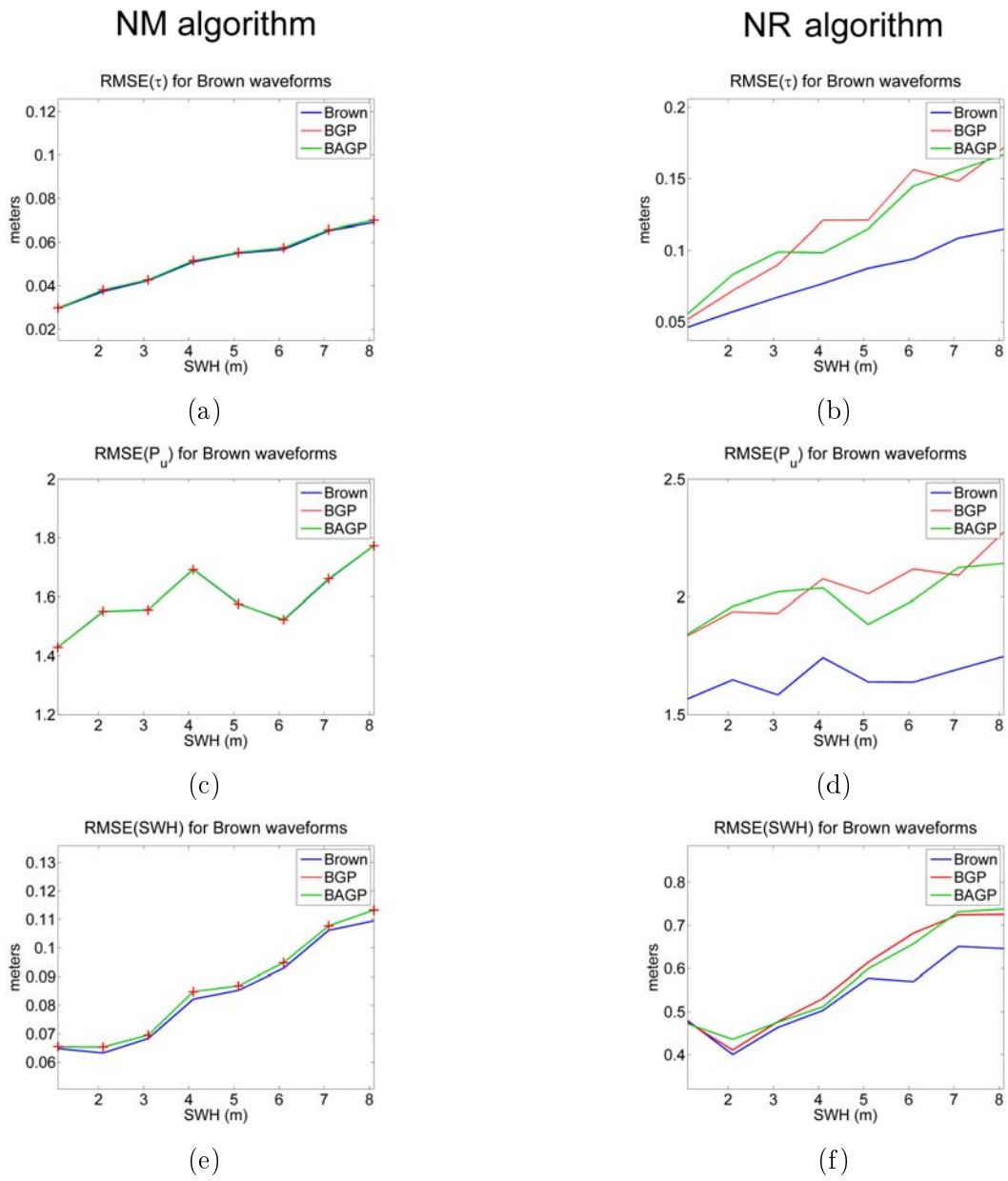

Figure 2.6: Parameter RMSEs for Brown waveforms with NM (left) and NR (right) algorithms when using Brown (blue), BGP (red) and BAGP (green) models.

The second set of simulations has been obtained with synthetic waveforms similar to signals belonging to class 13 of Fig. 2.2. More precisely, we have simulated Brown waveforms corrupted

by a symmetric peak located in the trailing edge with the parameters $P_u = 130, \tau_s = 31\,T_s$ and $A = 200, T = 75\,T_s, \sigma = 3\,T_s, \eta = 0$ (as displayed in Fig. 2.7 (a) which shows a typical waveform of class 13 with SWH = 2 m). Fig. 2.7 shows the RMSEs obtained by using the NM algorithm with the Brown and BGP models (for clarity, the RMSEs of the BAGP have not been presented here since they are very similar to those obtained with the BGP). The Brown model provides larger RMSEs since it does not take into account the peak corrupting the altimetric signal. Conversely, the BGP model shows good performance (note again that the BAGP provides very similar performance for this example). It is interesting to note that the RMSEs for the BGP model are close to the corresponding CRBs when applying the NM algorithm (see section 2.7.3). Fig. 2.8 shows results obtained with the NR method (note that the scales are different in Figs. 2.7 and 2.8) confirming the superiority of the BGP model with respect to the Brown model for peaky altimetric signals. Simulations conducted for different values of T show that the estimation performance is not very sensitive to the peak location as illustrated in Table 2.2 for the NR algorithm. Finally, we have observed that the gain resulting from the application of the BGP and BAGP models is significant when the peak amplitude exceeds 30% of the amplitude of the Brown model. Indeed, the traditional Brown model provides very poor performance for these peak amplitudes (more simulation results are available in Appendix C). However, it is important to note that the Brown model still provides satisfactory results for peaks with small amplitudes.

Table 2.2: RMSEs versus peak location T (NR algorithm).

$\frac{T}{T_s}$	65	75	85	95	105
RMSE(τ) (in meters)	0.121	0.114	0.109	0.109	0.106
RMSE(P_u)	2.06	2.02	1.94	1.94	1.71
RMSE(SWH) (in meters)	0.71	0.68	0.67	0.68	0.66

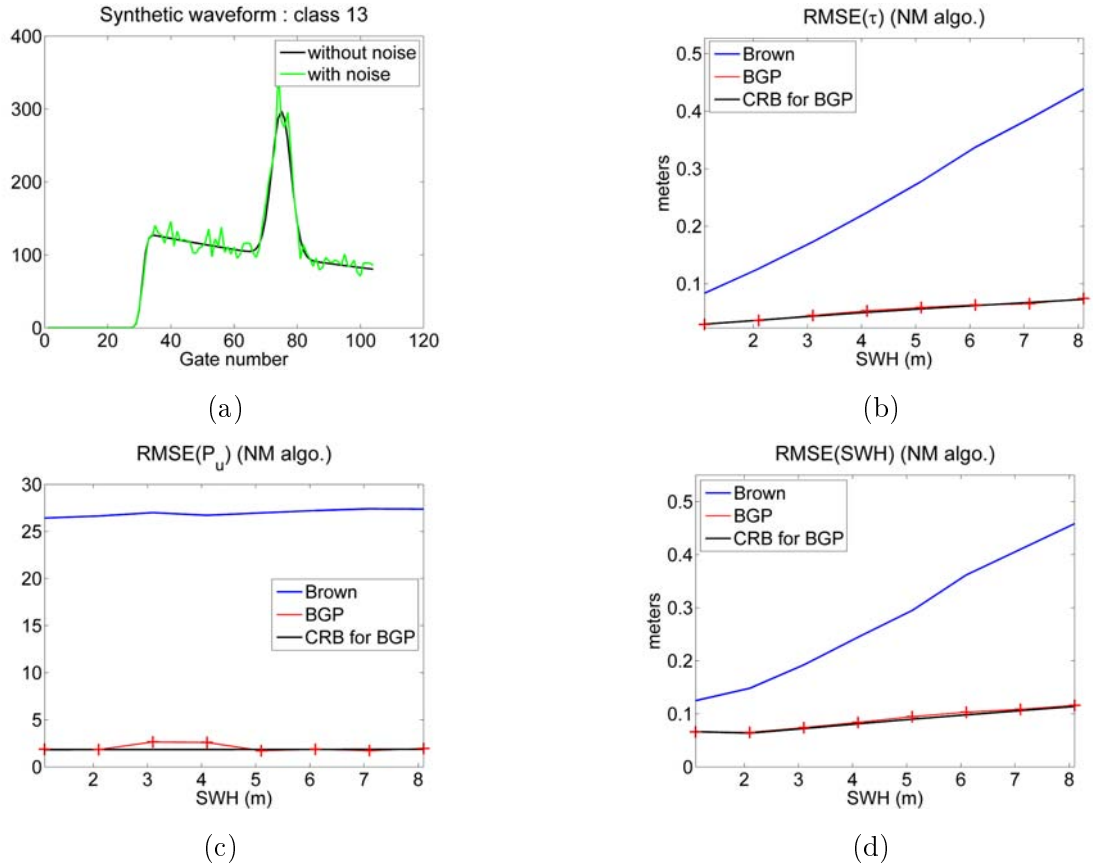

Figure 2.7: Parameter RMSEs for waveforms of the class 13 with the NM algorithm when using Brown (blue) and BGP (red) models. The CRBs of the BGP model parameters are also shown (black) for comparison.

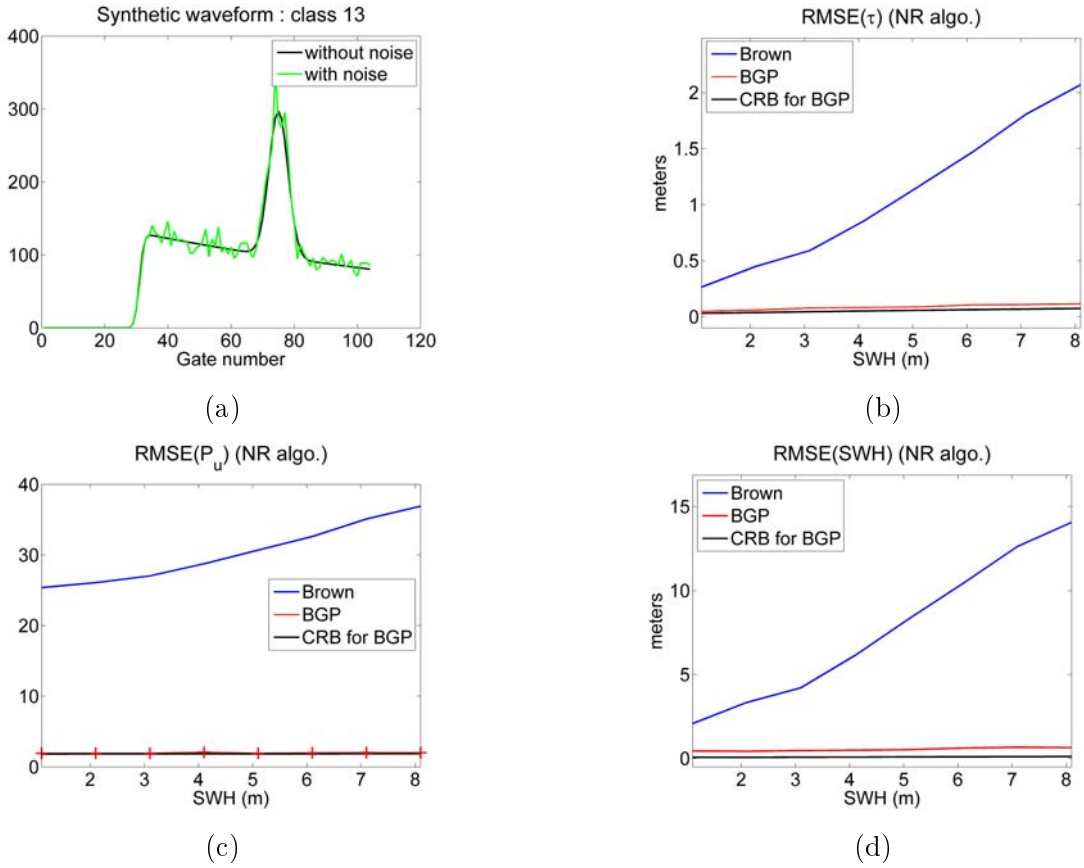

Figure 2.8: Parameter RMSEs for waveforms of class 13 with NR algorithm when using Brown (blue) and BGP (red) models. The CRBs of the BGP model parameters are also shown (black) for comparison.

The third set of simulations has been conducted using synthetic waveforms with a peak located at the end of the leading edge (T is located at the maximum of the Brown model) as displayed in Fig. 2.9 (a) where SWH = 2m. The Brown and peak parameters are $P_u = 130, \tau_s = 31\,T_s$ and $A = 200, \sigma = 3\,T_s, \eta = 1/T_s$. Fig. 2.9 shows the RMSEs obtained with the NM algorithm for the Brown, BGP and BAGP models. The BGP model cannot always handle the asymmetric nature of the peak resulting in poor estimation performance for SWH < 3 m when applying the NM algorithm and for all SWH when applying the NR algorithm (see Fig. 2.10). For small values of SWH, the Brown model is able to capture the leading edge (see Fig. 2.1 (a)) leading to relatively small RMSEs for parameters τ and SWH. However, the amplitude of the echo cannot be estimated accurately as displayed in Fig. 2.9 (c). For larger values of SWH, the performance of the Brown model decreases significantly. The BAGP model is able to model accurately the altimetric waveforms in all scenarios except for very small values of SWH. The application of the NR method confirms the superiority of the BAGP model for this class of waveforms as depicted in Fig. 2.10 (note that the scales are different in Figs. 2.9 and 2.10). Table 2.3 reports the averaged reconstruction errors (AREs) obtained for synthetic signals from classes 1, 7 and 13 with the different algorithms investigated in Section 2.5. Note that the waveforms from classes 7 and 13 have been generated by varying SWH and keeping the other parameters unchanged with respect to the previous experiment. It can be noticed that the proposed BAGP is very robust to different shapes of altimetric waveforms and provides very satisfactory AREs for all models. Table 2.4 shows the corresponding execution times of MATLAB implementations with a 2.93 GHz i7 CPU for one altimetric waveform. These results indicate that the computational time of the BAGP estimation algorithm is reasonable even if it exceeds the one obtained with the other algorithms. From these results, we conclude that the BGP has good properties for signals corrupted by a symmetric peak located in the trailing edge of the Brown's echo (class 13 of Fig. 2.2). However, it is not appropriate for waveforms of class 7. The introduction of an asymmetric peak characterized by the asymmetry coefficient η allows the BAGP to better approximate signals from class 7. Note finally that the effects of the peak is more pronounced for waveforms of class 7 since it directly affects the leading edge of the altimetric echo.

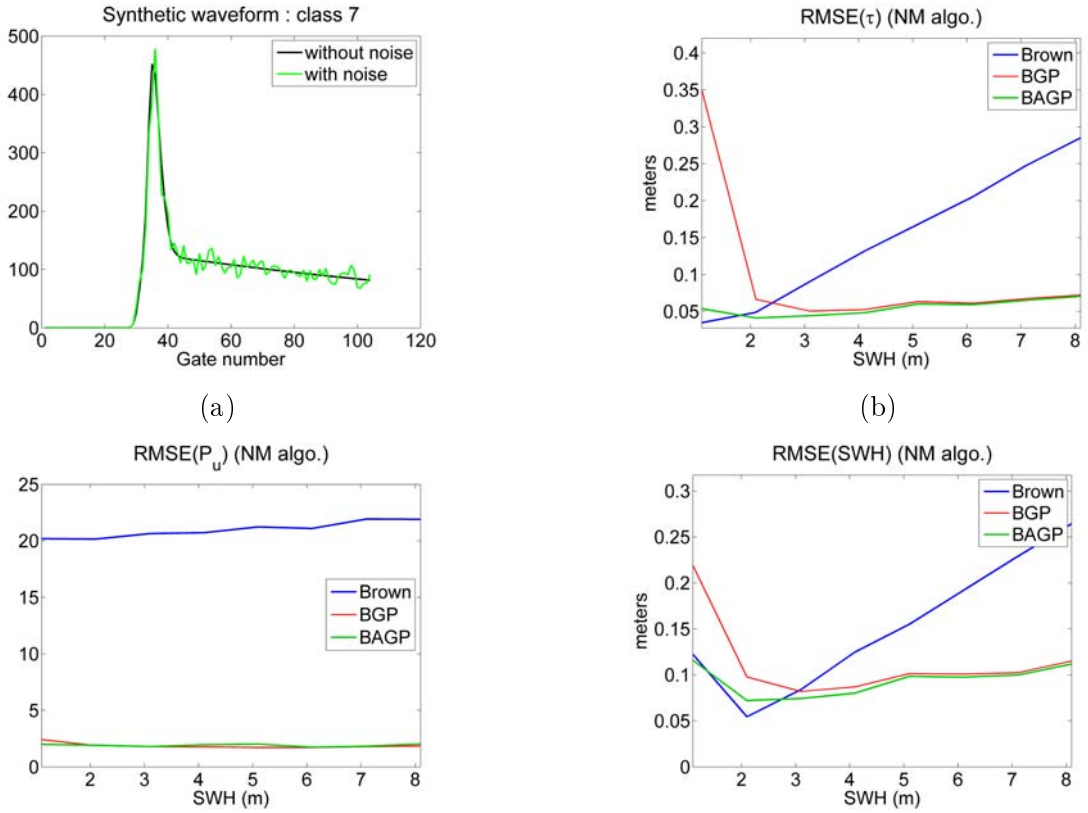

Figure 2.9: Parameter RMSEs for waveforms of class 7 with NM algorithm when using Brown (blue), BGP (red) and BAGP (green) models.

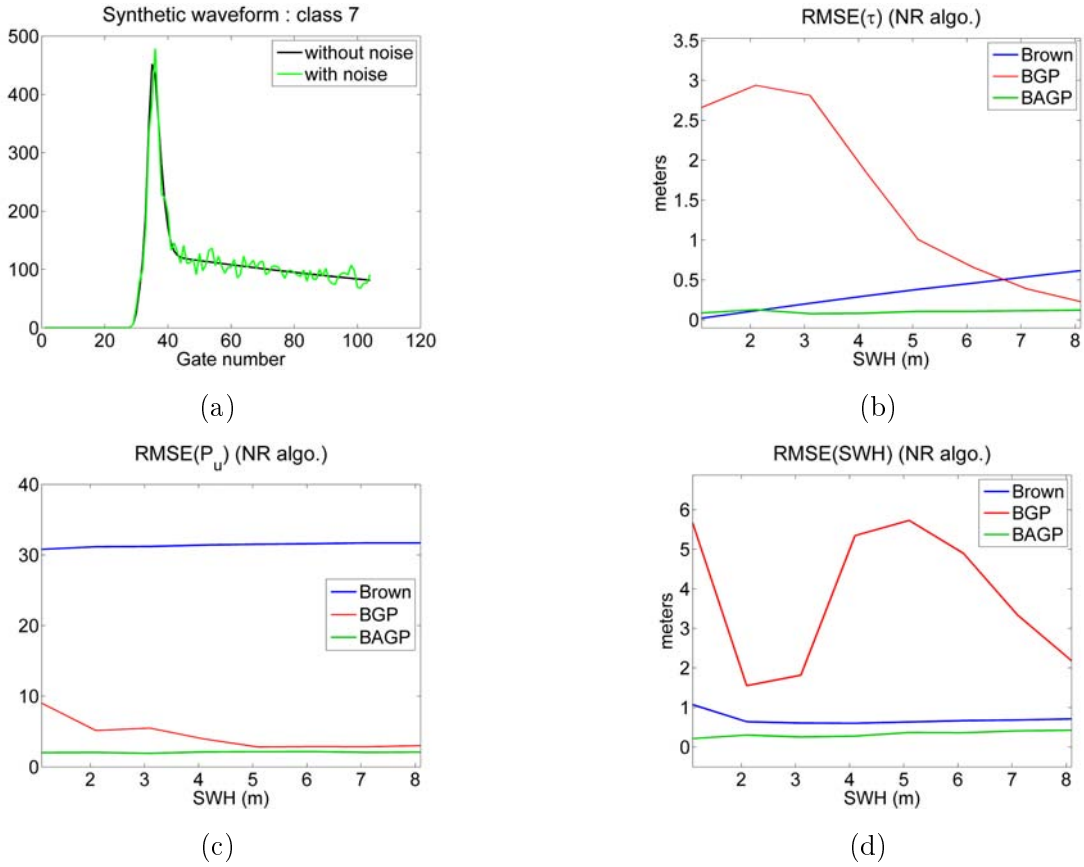

Figure 2.10: Parameter RMSEs for waveforms of class 7 with NR algorithm when using Brown (blue), BGP (red) and BAGP (green) models.

Table 2.3: Averaged reconstruction errors for the estimation algorithms (synthetic waveforms).

		Classes of synthetic waveforms		
		C1	 C13	 C7
NM	Brown	**8.99**	43.46	55.29
	BGP	**8.99**	11.10	15.12
	BAGP	**8.99**	**10.97**	**11.80**
NR	Brown	8.91	42.89	54.73
	BGP	8.75	**10.82**	20.37
	BAGP	**8.53**	**10.82**	**15.56**

Table 2.4: Averaged execution times for the estimation algorithms in seconds (synthetic waveforms).

		Classes of synthetic waveforms		
		C1	 C13	 C7
NM	Brown	0.27	**0.40**	**0.28**
	BGP	**0.21**	0.88	0.90
	BAGP	0.24	0.98	2.73
NR	Brown	**0.014**	**0.018**	**0.006**
	BGP	0.020	0.024	0.022
	BAGP	0.244	0.375	0.257

2.7.3 Cramér-Rao bounds

This section studies the CRBs for the Brown, BGP and BAGP models. We consider waveforms characterized by the peak parameters $A = 200, T = 75\,T_s, \sigma = 3\,T_s$, a number of looks $L_c = 90$ and different values for the parameters P_u, τ_s and SWH as reported in Table 2.5. Figs. 2.11.a and 2.11.b

Table 2.5: Simulation scenarios.

	P_u	τ_s	SWH (m)
Experiment 1 (Figs. 2.11.a and 2.11.b)	130	$31\,T_s$	$\in [1, 8]$
Experiment 2 (Figs. 2.11.c and 2.11.d)	$\in [20, 170]$	$31\,T_s$	5
Experiment 3 (Figs. 2.11.e and 2.11.f)	130	$\in [28\,T_s, 34\,T_s]$	5

show the BAGP, BGP and Brown CRBs as a function of SWH varying from 1 to 8 meters. Note that varying SWH leads to a variation of the slope of the leading edge. For too small values of SWH, the slope of the leading edge is very abrupt and thus, contains few samples, resulting in poor estimation. This corresponds to SWH = 1 m in Fig. 2.11.b where we note an increase in CRB(SWH). For larger values of SWH, the CRB of SWH is an increasing function of this parameter (as shown on Fig. 2.11.b for SWH $>$ 2 m) since the absolute error is directly related to the value of the parameter. Figs. 2.11.c and 2.11.d show the BAGP, BGP and Brown CRBs as a function of P_u. Increasing P_u implies a larger impact of the Brown echo with respect to the Gaussian peak. Thus, CRB(τ) and CRB(SWH) are decreasing functions of P_u. On the other hand, CRB(P_u) increases with P_u reflecting the fact that the estimation errors of P_u is relative to the absolute value of P_u as shown in Fig. 2.12.b (a similar result was observed in [Mailhes et al., 2008]). Figs. 2.11.e, 2.11.f and 2.12.c show the slight influence of τ on the CRBs of τ, SWH and P_u respectively. Note that the square roots of the CRBs (RCRB) have been displayed in order to compare them with the corresponding RMSEs. Note finally that the CRBs of BGP and BAGP model parameters are larger than those of the Brown model because BGP and BAGP involve additional unknown parameters.

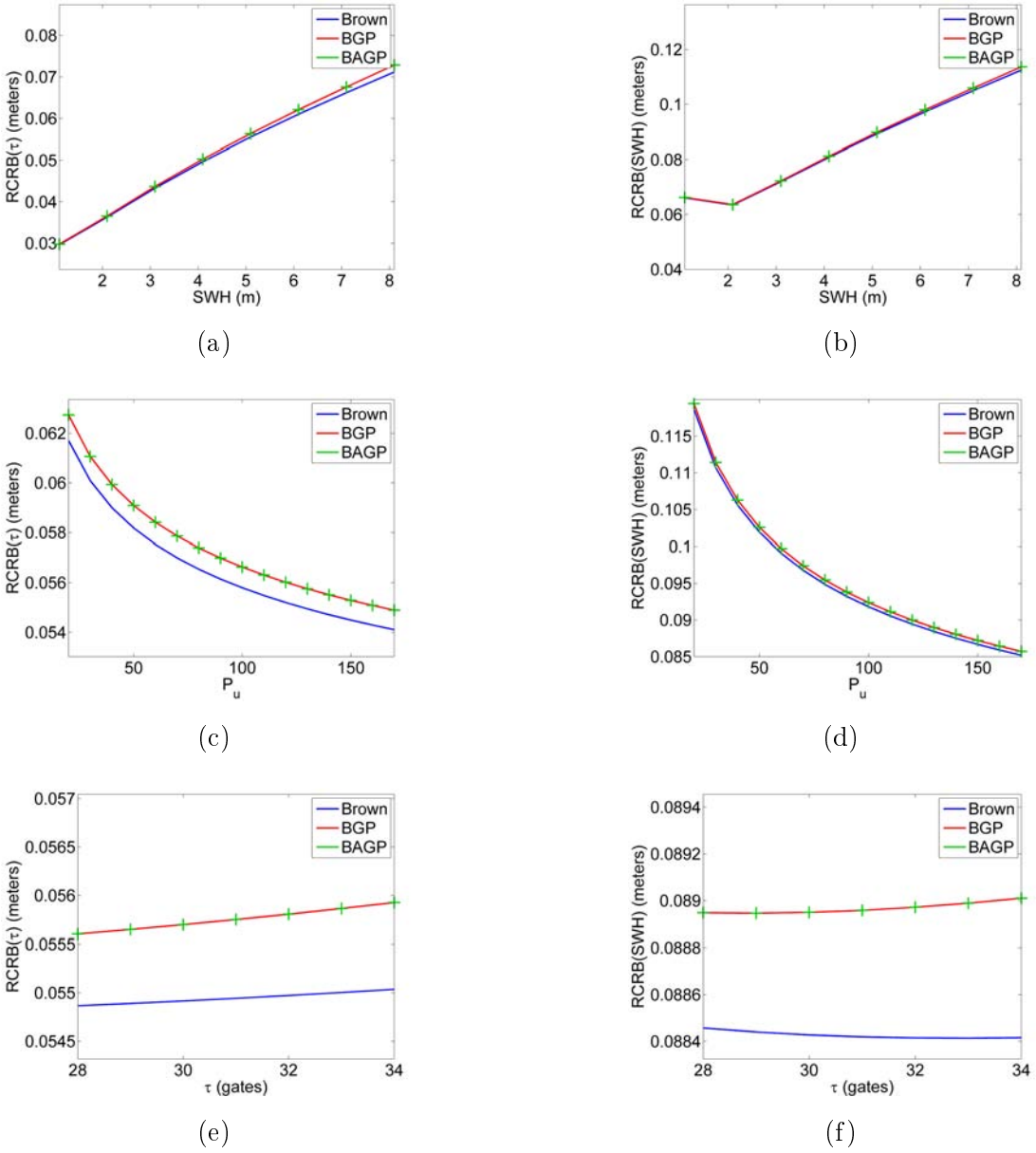

Figure 2.11: RCRBs for the Brown, BGP and BAGP models with parameter vectors $\boldsymbol{\theta}_{\text{Brown}} = (P_u, \tau, \text{SWH})^T = (130, 31, 5)^T$, $\boldsymbol{\theta}_{\text{BGP}} = (P_u, \tau, \text{SWH}, A, T, \sigma)^T = (130, 31, 5, 200, 75\,T_s, \ 3\,T_s)^T$ and $\boldsymbol{\theta}_{\text{BAGP}} = (P_u, \tau, \text{SWH}, A, T, \sigma, \eta)^T = (130, 31, 5, 200, 75\,T_s, 3\,T_s, 0)^T$. The left and right columns are associated with parameters τ and SWH respectively. The top, middle and bottom figures have been obtained by varying SWH, P_u and τ respectively.

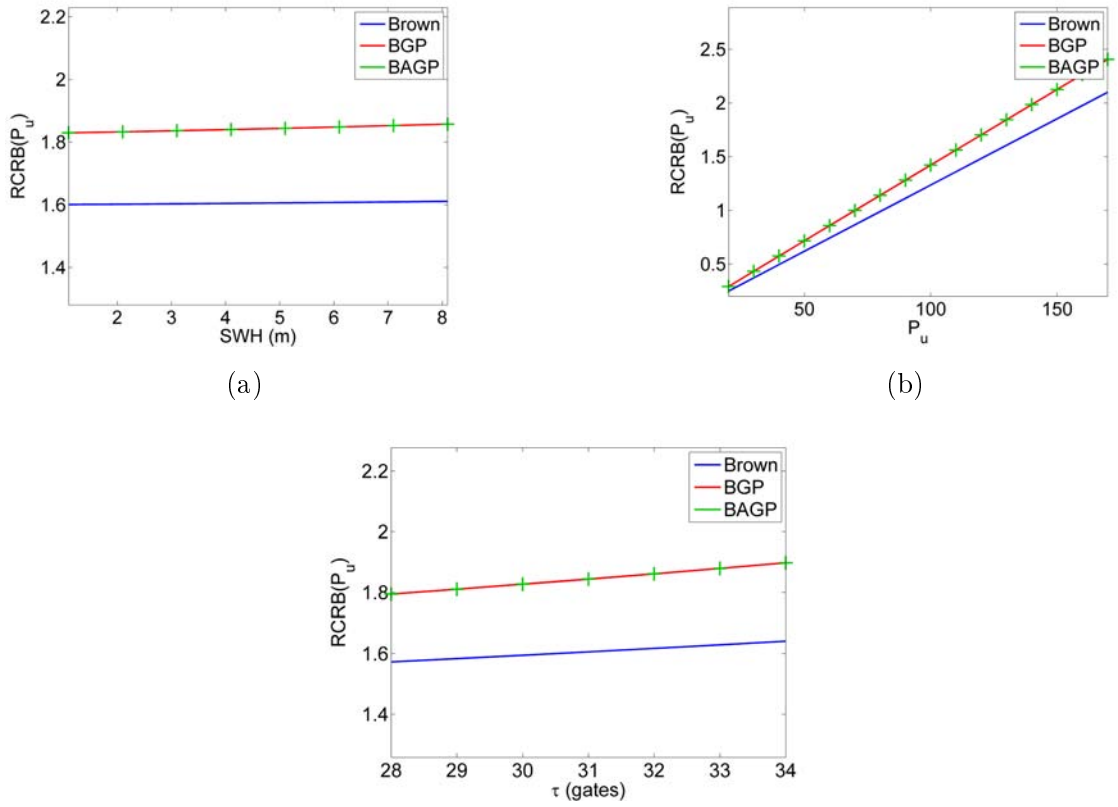

Figure 2.12: RCRBs of P_u for the Brown, BGP and BAGP models with parameter vector $\boldsymbol{\theta}_{\text{Brown}} = (P_u, \tau, \text{SWH})^T = (130, 31, 5)^T$, $\boldsymbol{\theta}_{\text{BGP}} = (P_u, \tau, \text{SWH}, A, T, \sigma)^T = (130, 31, 5, 200, 75\,T_s,\ \ 3\,T_s)^T$ and $\boldsymbol{\theta}_{\text{BAGP}} = (P_u, \tau, \text{SWH}, A, T, \sigma, \eta)^T = (130, 31, 5, 200, 75\,T_s, 3\,T_s, 0)^T$. The left, right and bottom figures correspond to the variation of SWH, P_u and τ respectively.

2.8 Real Jason-2 waveforms

This section evaluates the performance of the proposed model for real Jason-1 and Jason-2 waveforms. The classifier developed within the PISTACH project [Thibaut and Poisson, 2008] was used to isolate waveforms from classes 1 (Brown), 13 (peak on the trailing edge) and 7 (peak at the end of the leading edge). We have first considered Jason-2 waveforms. The reconstruction errors (REs) obtained with these waveforms are displayed in Figs. 2.13, 2.14 and 2.15 for the different models. These results confirm that the BAGP model provides better REs than the other models. Table 2.6 shows the averaged execution times of the different estimation algorithms for real Jason-2 waveforms. This table shows that the NM method requires more computational time than the NR method. Table 2.6 also shows that the computational time is directly related to the number of parameters to be estimated (as expected). Fig. 2.16 shows typical estimated waveforms for signals of classes 7 and 13 which allow the estimation quality to be appreciated. The BGP and BAGP provide very similar results for the signal of class 13 since the associated peak is symmetric. However, the signal from class 7 is better approximated by the BAGP (see in particular the zoom on the leading edge) which allows the asymmetric peak to be estimated more accurately.

Table 2.6: Averaged execution times for the estimation algorithms in seconds (real Jason-2 waveforms).

		Classes of real waveforms		
		C1	C13	C7
NM	Brown	0.313	**0.206**	**0.289**
	BGP	**0.289**	0.541	0.668
	BAGP	0.335	1.733	1.375
NR	Brown	**0.013**	**0.015**	**0.009**
	BGP	0.018	0.022	0.024
	BAGP	0.252	0.277	0.149

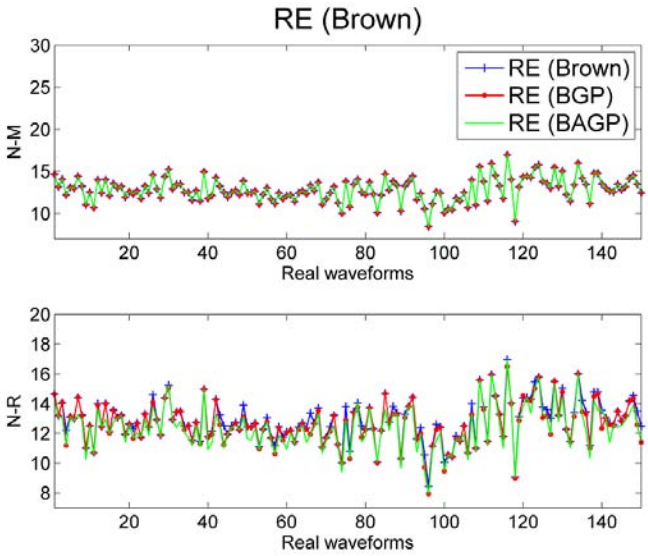

Figure 2.13: REs for 150 waveforms from class 1 with NM (top) and NR (bottom) methods.

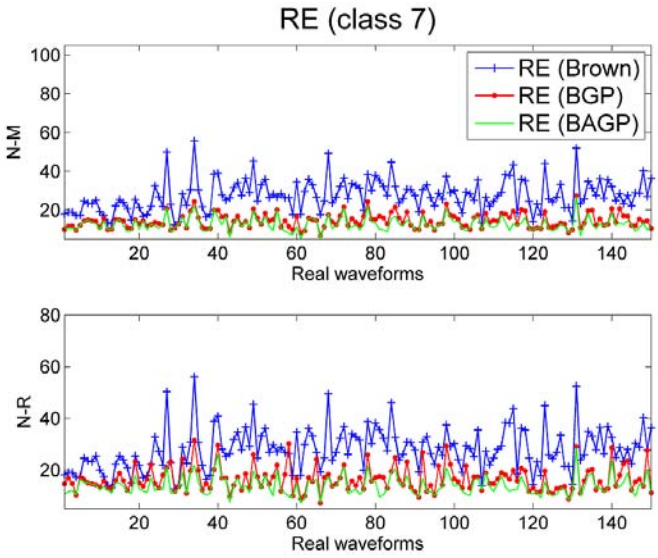

Figure 2.14: REs for 150 waveforms from class 7 with NM (top) and NR (bottom) methods.

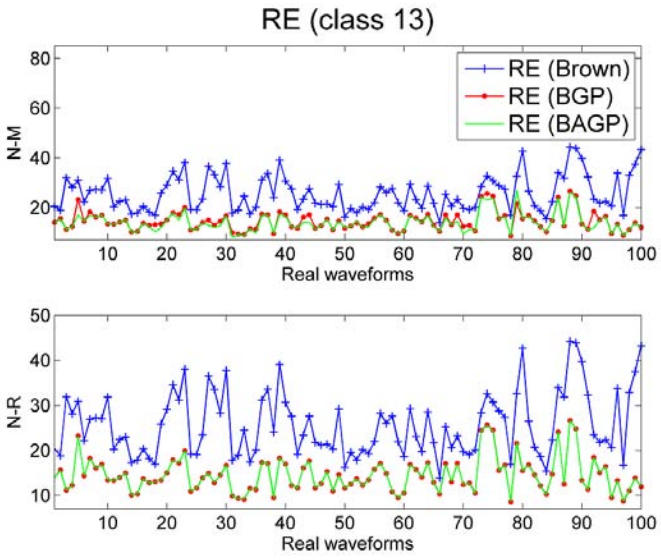

Figure 2.15: REs for 100 waveforms from class 13 with NM (top) and NR (bottom) methods.

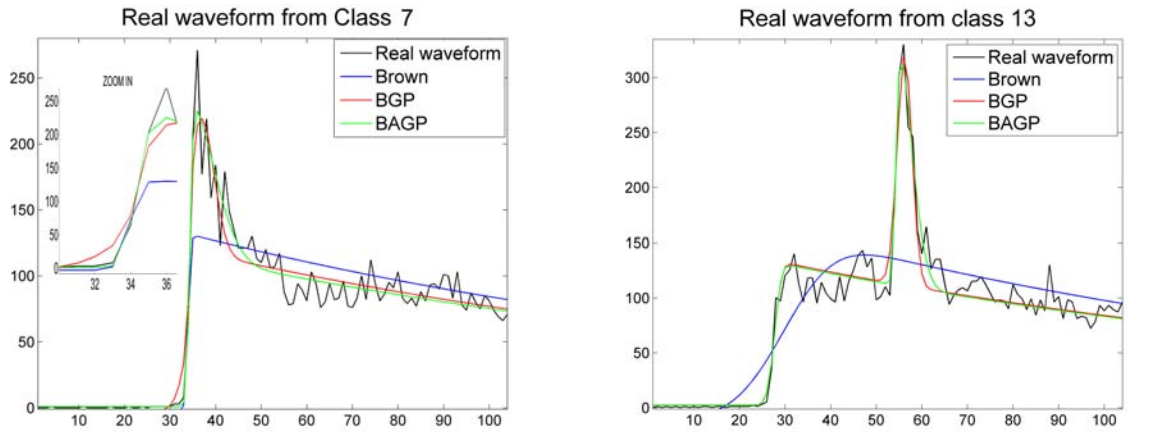

(a) Real waveform from Class 7 and its estimates.

(b) Real waveform from Class 13 and its estimates.

Figure 2.16: Examples of real JASON-2 waveforms and their estimations.

In a second step, we have considered additional Jason-1 data obtained around Ibiza island. This dataset was extracted from the pass 187 of cycle 188 and is represented in Fig. 2.17 (top-left). This figure shows a sequence of echoes as an image where each column represents an altimetric echo. We can clearly see an elliptical behavior (from latitude gate 75 to 110) which is due to the moving of the peak in the trailing edge (class 13). Note also the presence of waveforms from class 7 waveforms (from latitude gate 40 to 65 and latitude gate 110 to 125) which present a high power at the end of the leading edge. The altimetric parameters of these waveforms have been estimated by using the Brown, BGP and BAGP models. Fig. 2.17 shows the reconstructed images for each model by using the corresponding estimated parameters. This figure shows that we get a better fit by using the BGP and BAGP models than the Brown model. In particular the elliptical part of the figure is better recovered with the proposed BGP and BAGP models than with the Brown model. Fig. 2.18 illustrates this result by showing waveforms from classes 1, 7 and 13 and their estimations by using the three models (Note that we recommend to use BGP for waveforms of class 13 and BAGP for waveforms of class 7). Note in particular that the leading edge is not estimated correctly with the Brown model in Fig. 2.18 (e) whereas it is better estimated with the BGP and BAGP models. More estimation results, when considering Jason-2 data, available in Appendix D confirm these results.

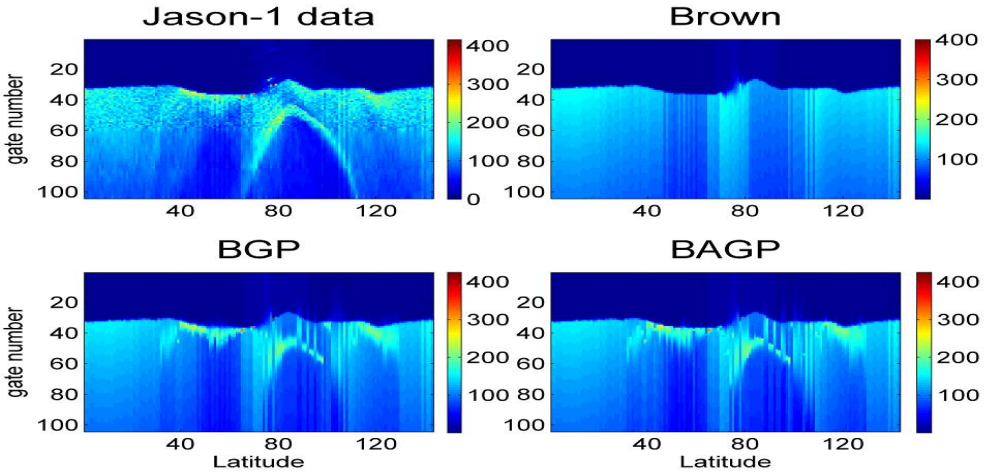

Figure 2.17: Jason-1 waveforms estimated by using Brown (top-right), BGP (bottom-left) and BAGP (bottom-right) models.

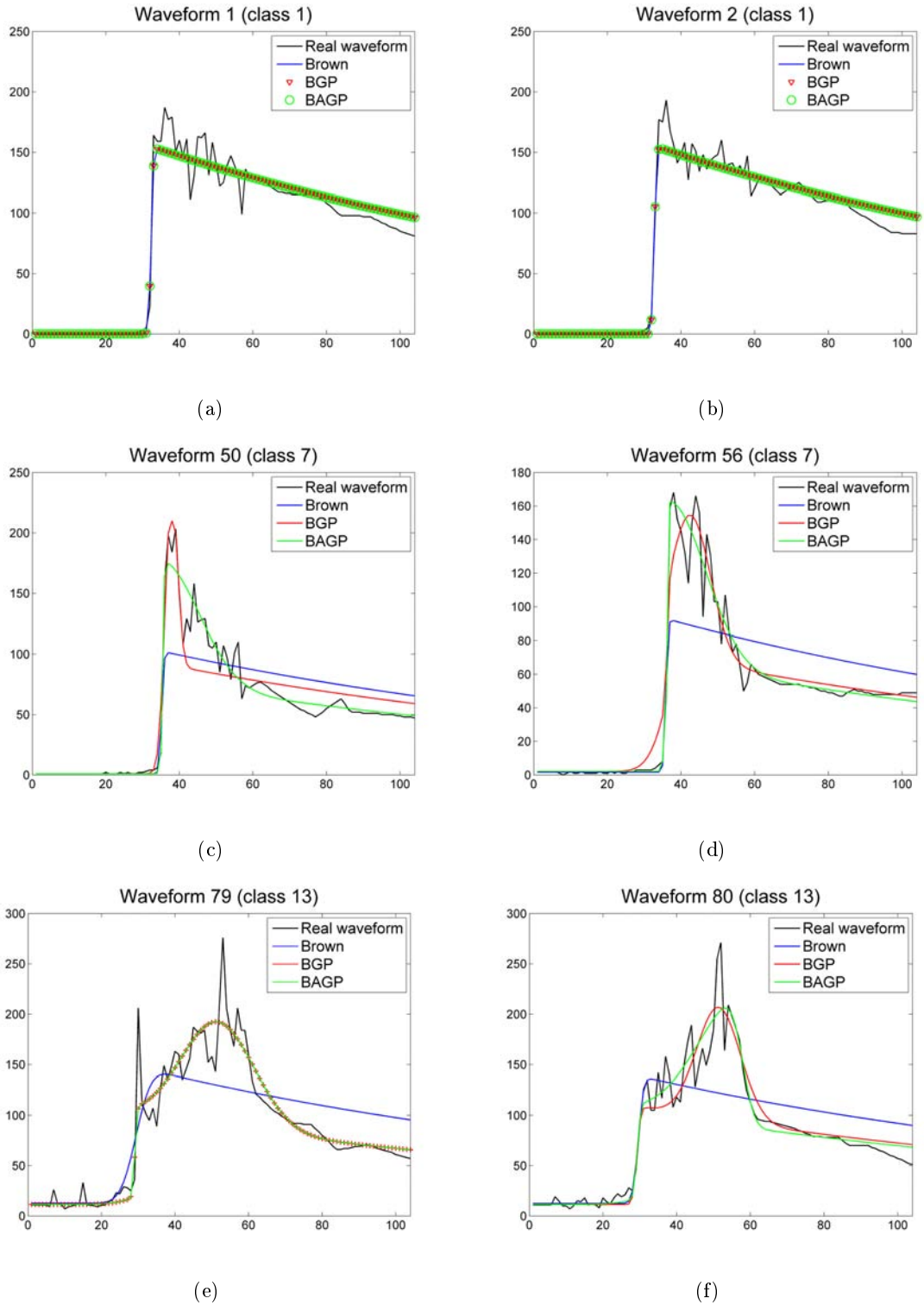

Figure 2.18: Examples of real JASON-1 waveforms and their estimations.

2.9 Conclusions

This chapter studied a new model for altimetric waveforms referred to as "Brown with asymmetric Gaussian peak" model. The parameters of this model were estimated by using the maximum likelihood method. The determination of the maximum likelihood estimator was investigated by two methods based on Newton-Raphson recursion and a Nelder-Mead algorithm. Estimations obtained with the Nelder-Mead method were better in terms of mean square error than those obtained with the Newton-Raphson algorithm. However, the price to pay with the Nelder-Mead algorithm is a higher computational cost. Results obtained in this study showed that the proposed model can be used to retrack efficiently standard oceanic Brown echoes as well as coastal echoes corrupted by symmetric or asymmetric Gaussian peaks. The chapter also derived Cramér-Rao bounds for the parameters of the Brown with asymmetric Gaussian peak model. These bounds were used as references to which mean square errors were compared. The mean square errors of the model parameter estimates obtained using the maximum likelihood principle were shown to be very close to the corresponding Cramér-Rao bounds illustrating the efficiency of the maximum likelihood estimator. The bounds were also used to evaluate the loss of performance for estimating the Brown parameters in presence of a Gaussian peak. This loss of performance is mainly due to more parameters to be estimated when the model contains a symmetric or asymmetric Gaussian peak. Extending the results obtained in this chapter to the four parameter Brown model (including the mispointing as a fourth parameter) is an interesting issue. The proposed Brown with asymmetric Gaussian peak model could also be of interest for retracking echoes affected by σ-blooms or rain cells. We think that these points are very interesting and should be considered in future work.

Contributions

A new altimetric model is proposed for coastal waveforms [Halimi et al., 2011a,b, 2013d]. The parameter estimation is achieved using a maximum likelihood estimator. The Cramér-Rao lower bounds of the model parameters are also derived. These innovations are evaluated via many simulations conducted on synthetic and real data.

2.10 Conclusions (in French)

Ce chapitre a étudié un nouveau modèle d'écho altimétrique affecté par la présence d'un pic asymétrique et adapté aux signaux mesurés par les altimètres le long des zones côtières. Les paramètres de ce modèle ont été estimés en utilisant la méthode du maximum de vraisemblance. La détermination de l'estimateur du maximum de vraisemblance a été effectuée par deux algorithmes qui sont l'algorithme de Newton-Raphson et celui de Nelder-Mead. Ce dernier fournit de meilleurs estimés en termes d'erreur quadratique moyenne. Il présente néanmoins un temps de calcul plus élevé que celui obtenu avec l'algorithme de Newton-Raphson. Les résultats obtenus dans cette étude ont montré que le modèle proposé peut être utilisé efficacement pour le traitement des échos océaniques de Brown ainsi que des échos côtiers corrompus par des pics gaussiens symétriques ou asymétriques. Ce chapitre a également étudié les bornes de Cramér-Rao associées au modèle de Brown avec pic gaussien asymétrique. Ces bornes fournissent une référence pour l'évaluation des erreurs quadratiques moyennes des estimés. Elles ont par ailleurs montré l'efficacité de l'estimateur du maximum de vraisemblance puisqu'il présente des erreurs quadratiques proches des bornes associées. Ces bornes ont aussi permis de quantifier la détérioration des paramètres estimés associés au modèle de Brown lors de l'estimation des paramètres du pic. En effet, l'estimation d'un plus grand nombre de paramètres conduit nécessairement à une augmentation des bornes des paramètres associés au modèle Brown, qui s'est avérée faible dans notre cas. Les travaux futurs s'intéresseront à la généralisation du modèle proposé pour inclure le dépointage de l'antenne. Par ailleurs, le modèle de Brown avec pic gaussien asymétrique pourrait également être utilisé pour le traitement des échos affectés par les cellules de pluie.

Contributions

Un nouveau modèle altimétrique est proposé pour les signaux côtiers [Halimi et al., 2011a,b, 2013d]. L'estimation des paramètres est réalisée en utilisant un estimateur du maximum de vraisemblance. L'expression des bornes de Cramér-Rao des paramètres du modèle est donnée. Ces innovations sont évaluées par de nombreuses simulations effectuées sur des données synthétiques et réelles.

Chapter 3

Semi-analytical model for delay/Doppler altimetry

Contents

3.1 Introduction (in French)

Depuis plus de vingt ans, les altimètres classiques comme Topex, Poseidon-2 ou Poséidon-3, ont fourni des formes d'onde qui sont utilisées pour estimer de nombreux paramètres physiques tels que la distance entre le satellite et la scène observée, la hauteur des vagues et la vitesse du vent. Ces altimètres classiques montrent certaines limitations qui ont été abordées dans le chapitre 1. L'altimétrie SAR/Doppler se présente comme une solution à ces limitations puisqu'elle vise la réduction du bruit de mesure et l'augmentation de la résolution dans la direction de marche du satellite en comparaison avec l'altimétrie conventionnelle.

L'altimétrie SAR/Doppler nécessite une forte corrélation entre les impulsions émises [Raney, 1998] qui est obtenue en utilisant une fréquence de répétition élevée des impulsions (FRI). Par exemple, l'altimètre SIRAL[1] transmet des paquets avec une fréquence d'environ 85 Hz [Wingham et al., 2006]. Chaque paquet contient $N = 64$ impulsions cohérentes (transmises avec une FRI de 18182 Hz) qui sont traitées afin d'obtenir la carte distance/Doppler comme le montre la figure 3.1.

A la différence de l'altimétrie conventionnelle, l'altimétrie SAR/Doppler fait intervenir une transformée de Fourier (TF) rapide dans la direction azimutale c'est à dire dans la direction de marche du satellite (voir la figure 3.1.). Cette opération permet d'extraire l'information Doppler résultante du mouvement du satellite et exprime de ce fait le signal obtenu en fonction de la fréquence Doppler. Par ailleurs, il a été montré dans [Raney, 1998] que chaque fréquence Doppler est liée à un emplacement azimutal sur la surface observée appelé bande ou faisceau Doppler. Par conséquent, la transmission de $N = 64$ impulsions cohérentes résultera en $N = 64$ fréquences Doppler (après application d'une TF azimutale) et fournira ce même nombre de faisceaux Doppler dans la carte distance/Doppler (voir la figure 3.1).

L'exploitation de l'altimétrie océanique SAR/Doppler est basée sur l'analyse de la forme d'onde océanique réfléchie appelée écho multi-vues et obtenue par application d'un traitement Doppler (migration des distances et moyennage) à la carte distance/Doppler. Cet écho multi-vues présente une forme différente de celle d'un écho conventionnel, ce qui nécessite le développement d'un nouveau

[1] L'instrument SIRAL (synthetic aperture interferometric radar altimeter) est le premier altimètre utilisant la technologie SAR/Doppler. Il est mis en orbite à bord du satellite Cryosat-2.

modèle pour ce signal altimétrique. De nombreuses études ont été menées par différentes équipes pour atteindre cet objectif. Par exemple, des modèles numériques ont été proposés dans [Phalippou and Enjolras, 2007, Shuang-Bao et al., 2011] tandis que d'autres modèles étaient développés dans le projet SAMOSA [Gommenginger et al., 2012b, Martin-Puig et al., 2008].

La première contribution de ce chapitre est l'élaboration d'un nouveau modèle pour l'altimétrie SAR/Doppler. Le modèle analytique, relatif à la réponse impulsionnelle d'une mer plate, est basé sur une approche géométrique. Ce dernier tient compte de la courbure de la terre, considère un diagramme d'antenne circulaire sans dépointage et une approximation gaussienne pour le gain de l'antenne [Brown, 1977]. L'expression analytique obtenue pour la FSIR est convoluée numériquement avec la PDF de la hauteur des points de dispersion et la PTR. On obtient ainsi la puissance moyenne d'un écho SAR/Doppler qui dépend de trois paramètres: l'époque τ, la hauteur des vagues SWH et l'amplitude P_u. Le modèle proposé est notée DDA3 pour souligner le fait qu'il considère 3 paramètres[2].

La deuxième contribution de ce chapitre est l'élaboration d'un algorithme d'estimation paramétrique à partir du modèle semi-analytique proposé. Nous proposons d'estimer les paramètres altimétriques par une procédure de moindres carrés basée sur l'algorithme de Levenberg-Marquardt. Les performances de l'estimation paramétrique sont analysées suivant différents scénarios. Le modèle ainsi que l'algorithme proposé seront validés sur des données synthétiques et réelles de Cryosat-2 ce qui fournit une mesure quantitative des avantages de l'altimétrie SAR/Doppler par rapport à l'altimétrie conventionnelle.

Le chapitre est structuré comme suit. La section 3.3 présente le passage du modèle conventionnel à celui proposé pour l'altimétrie SAR/Doppler. La procédure d'estimation par moindres carrés est ensuite décrite dans la section 3.4. La section 3.5 introduit les bornes de Cramér-Rao associées au modèle conventionel ainsi que le modèle proposé pour l'altimétrie SAR/Doppler. La validation du modèle ainsi que l'algorithme d'estimation sur des données synthétiques est décrite dans la section 3.6. La section 3.7 analyse les résultats obtenus lors du traitement d'échos réels obtenus avec Cryosat-2. Les conclusions et perspectives de ce chapitre sont enfin présentés dans les sections 3.8 et 3.9.

[2]L'acronyme DDA3 (resp. $CA3$) est utilisé lorsque l'on considère 3 paramètres altimétriques tandis que nous gardons la notation DDA (resp. CA) pour les notions générales qui restent valides lors de l'utilisation d'un autre vecteur de paramètre comme il sera le cas dans le chapitre suivant.

3.2 Introduction

For more than twenty years, conventional altimeters like Topex, Poseidon-2 or Poseidon-3, have been delivering waveforms which are used to estimate many parameters such as the range between the satellite and the observed scene. These conventional altimeters show some limitations that were addressed in Chapter 1. One of the proposed solution is to consider delay/Doppler altimetry (DDA) which aims at reducing the measurement noise and increasing the along-track resolution in comparison with conventional altimetry (CA).

DDA requires coherent correlation between pulses [Raney, 1998] which is obtained by transmitting pulses with a high pulse repetition frequency (PRF). For instance, the SIRAL altimeter[3] transmits bursts with a frequency of about 85 Hz [Wingham et al., 2006]. Each burst contains $N = 64$ coherent pulses (transmitted at a PRF of 18182 Hz) which are processed in order to obtain the delay/Doppler map (DDM) as shown in Fig. 3.1.

The main difference between CA and DDA is the application of an along-track fast Fourier transform (FFT) in the latter (see Fig. 3.1). This operation expresses the reflected energy as a function of Doppler frequency. In the other hand, it has been shown in [Raney, 1998] that each Doppler frequency is related to an along-track location on the observed surface known as Doppler beam. Therefore, transmitting $N = 64$ coherent pulses results in $N = 64$ Doppler frequencies (after applying along-track FFT) and the same number of spectral Doppler beams in the DDM, as illustrated in Fig. 3.1. The exploitation of the DDA oceanic information is based on the analysis of the reflected oceanic waveform called multi-look echo and obtained by applying Doppler processing (slant range correction and multi-looking) to the DDM. This multi-look waveform has a shape that is different from a CA echo, which requires to develop a new altimetric signal model. Many studies have been conducted by different teams for achieving this goal. For instance, numerical models for delay/Doppler (DD) waveforms have been proposed in [Phalippou and Enjolras, 2007, Shuang-Bao et al., 2011] whereas other models were developed in the SAMOSA project [Gommenginger et al., 2012b, Martin-Puig et al., 2008].

The first contribution of this chapter is the derivation of a new model for DDA. An analytical

[3]The synthetic aperture interferometric radar altimeter (SIRAL) is on board Cryosat-2 satellite and is the first altimeter using the DDA principle.

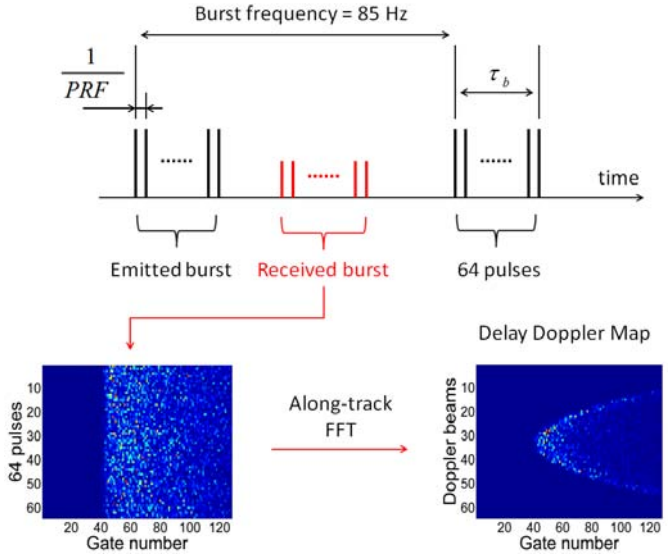

Figure 3.1: Configuration of a delay/Doppler altimeter and construction of a delay/Doppler map.

model for the FSIR is studied based on a geometrical approach. The proposed FSIR model includes Earth curvature, considers a circular antenna pattern without any mispointing and a Gaussian approximation for the antenna gain as in [Brown, 1977]. The resulting analytical expression of the FSIR is numerically convolved with the PDF of the sea wave height and the PTR of the radar. This yields the mean power of a DDA waveform which depends on three parameters: the epoch τ, the significant wave height SWH and the amplitude P_u. The proposed model is denoted as DDA3 to emphasize the fact that it considers 3 parameters[4].

The second contribution of this chapter is to propose and validate an algorithm for estimating the parameters of the proposed DD semi-analytical model. We then propose to estimate the geophysical altimetric parameters by a least squares (LS) approach based on the Levenberg-Marquardt algorithm. The performance of the parameter estimation is analyzed in different scenarios including different noise configurations. Moreover, the evaluation of the estimated parameters, on simulated and real Cryosat-2 data, provides a quantitative measure of the benefits of DDA3 when compared to CA3.

[4]The acronym DDA3 (resp. CA3) is used when considering 3 altimetric parameters while we keep the notation DDA (resp. CA) for the general notions that are also true when considering a different number of parameters as it will be the case in the next chapter.

The chapter is organized as follows. Section 3.3 presents the transition from the conventional altimetric model to the proposed delay/Doppler semi-analytical model. The proposed LS estimation procedure is then introduced in Section 3.4. The CRBs associated with the conventional and delay/Doppler model are then derived in Section 3.5. Section 3.6 validates the proposed model and algorithm with simulated data. The analysis of results associated with real Cryosat-2 waveforms is presented in section 3.7. Conclusions and future work are finally reported in Section 3.8.

3.3 Semi-Analytical model for delay/Doppler altimetry

This section first recalls briefly the CA3 model and then introduces the proposed semi-analytical model for DD waveforms. The multi-look processing and the corruption of the waveforms by speckle noise are also described.

3.3.1 Conventional altimetry

It has been shown in Chapter 1 that the mean power $s(t)$ of a CA waveform is expressed as the convolution of three terms: the FSIR, the PDF of the heights of the specular scatterers and the PTR (see (1.5)). The following subsections describe these three terms.

Flat surface impulse response

The FSIR is of great importance since it includes information about the antenna gain and the backscattering properties of the observed surface. It is obtained by integrating over the illuminated area of the surface as shown in (1.6). In this chapter, we will be considering antenna without mispointing with respect to the z and x axes ($\xi = 0°$ and $\tilde{\phi} = 0°$ in Fig. 1.6). In this case, the integral with respect to ρ in (1.6) can be expressed in closed form when considering a constant value of σ^0 and the same gain antenna as in [Brown, 1977], i.e., a Gaussian approximation and a circular antenna pattern. The FSIR is then given by

$$\mathrm{FSIR}(t) = \frac{P_u}{2\pi}\left(1+\frac{ct}{2h}\right)^{-3} U(t) \int_0^{2\pi} \exp\left(-\frac{4ct}{\gamma h}\right) d\phi \tag{3.1}$$

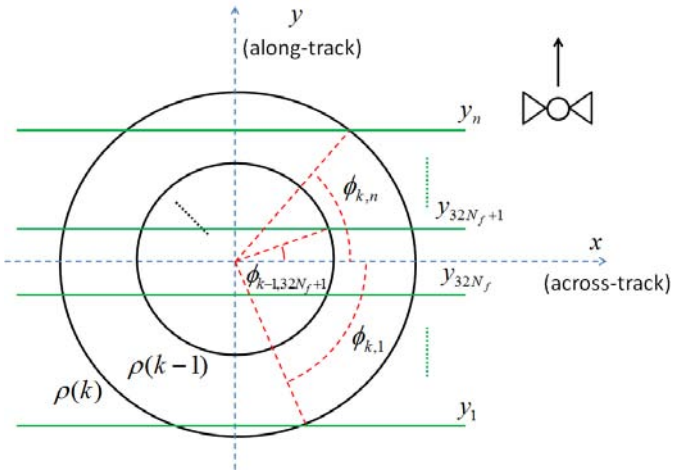

Figure 3.2: Circles of propagation and Doppler beams. In CA, the FSIR is obtained by integrating over the propagation circles. In DDA, the FSIR is obtained by integrating the energy in the intersection between the propagation circles and the Doppler beams.

where $\gamma = \frac{1}{2\ln 2}\sin^2\theta_{3\text{dB}}$ is an antenna beam width parameter, $\theta_{3\text{dB}}$ is the half-power antenna beam width. Equation (3.1) shows that FSIR(t) is obtained by integrating an appropriate function on a circle whose radius $\rho(t)$ depends on time, i.e., for each time instant t we have a given radius (see Fig. 3.2). This radius increases with time since $\rho(t') = \sqrt{\left(\frac{t'c}{2}\right)^2 - h^2}$ which reduces to $\rho(t) \simeq \sqrt{hct}$ when considering the approximation $\frac{ct}{h} << 1$ (valid for spaceborne altimetry [Brown, 1977]). Note also, that in CA, we integrate all along the circle of radius ρ (since $\phi \in [0, 2\pi]$) without having a distinction between across-track and along-track directions (axes x and y in Fig. 3.2 respectively). The conventional FSIR is finally given by [Amarouche et al., 2004, Brown, 1977]

$$\text{FSIR}(t) = P_u \exp\left(-\frac{4ct}{\gamma h}\right) U(t) \tag{3.2}$$

where $\left(1+\frac{ct}{2h}\right)^{-3}$ has been approximated by 1 as in [Brown, 1977] (since $\frac{ct}{h} << 1$).

Probability density function of the heights of the specular scatterers

The PDF of the specular points is generally approximated by a Gaussian density whose standard deviation is related to the average SWH [Amarouche et al., 2004, Brown, 1977]. Its expression has

been presented in chapter 1 and is recalled hereafter

$$\mathrm{PDF}(t) = \frac{1}{\sqrt{2\pi}\sigma_s} \exp\left(-\frac{t^2}{2\sigma_s^2}\right) \tag{3.3}$$

with $\sigma_s = \frac{\mathrm{SWH}}{2c}$.

Radar system point target response

The radar point target response is generally expressed as a squared cardinal sine as follows [Amarouche et al., 2004]

$$\mathrm{PTR}_T(t) = \left| \frac{\sin\left(\pi \frac{t}{T_s}\right)}{\pi \frac{t}{T_s}} \right|^2. \tag{3.4}$$

3.3.2 Delay/Doppler altimetry

As in CA, the mean power $P(t, f)$ of a DD echo can be expressed as the convolution of three terms: the FSIR, the PDF and the time/frequency PTR [Martin-Puig and Ruffini, 2009, Phalippou and Demeestere, 2011]. However, contrary to the signal $s(t)$ of (1.5), the obtained signal $P(t, f)$ depends on time and Doppler frequency as follows

$$P(t, f) = \mathrm{FSIR}(t, f) * \mathrm{PDF}(t) * \mathrm{PTR}(t, f) \tag{3.5}$$

where f denotes the Doppler frequency. The PDF is the same as in (3.3) and the two other terms are introduced below.

Flat surface impulse response

The DDA is pulse-limited across-track and beam-limited along-track as first observed by Raney in [Raney, 1998]. It was proposed in order to increase the along-track resolution by considering the Doppler effect resulting from the satellite velocity. Indeed, the nth Doppler frequency f_n is expressed by

$$f_n = \frac{2}{\lambda} \frac{\vec{r}.\vec{v}_s}{|\vec{r}|} = \frac{2v_s}{\lambda} \cos(\theta_n) \tag{3.6}$$

where $\vec{v}_s$ is the satellite velocity and θ_n is shown in Fig. 3.3. This figure also shows that

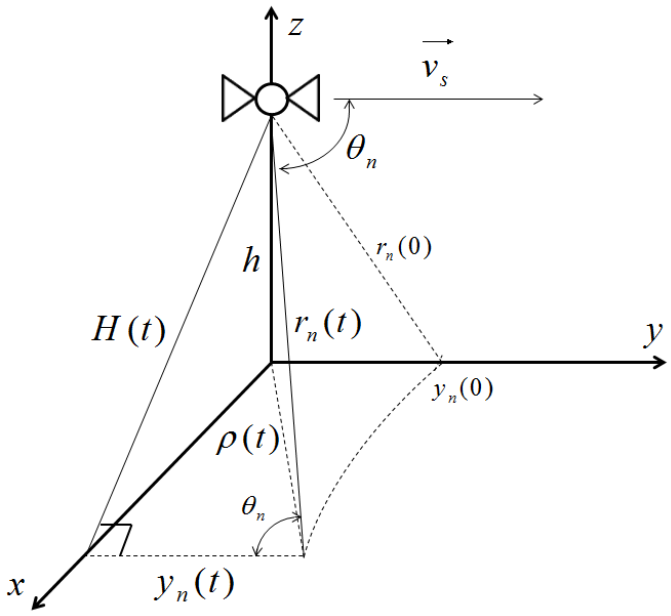

Figure 3.3: Doppler beams geometry.

$$\cos(\theta_n) = \frac{y_n(t)}{r_n(t)} = \frac{y_n(t)}{\sqrt{\rho^2(t) + h^2}}, \quad \text{for } t \geq 0 \tag{3.7}$$

where $y_n(t)$ represents the coordinate of the nth along-track beam. Combining (3.6) and (3.7) leads to the following expression of $y_n(t)$ as a function of t and f_n

$$y_n(t) = \left(\frac{\lambda f_n}{2v_s}\right)\sqrt{\rho^2(t) + h^2}. \tag{3.8}$$

This equation clearly shows how the coordinate of the along-track beam depends on time. An approximation of (3.8) is obtained by considering $\rho(t) << h$ which is a valid assumption for near-vertical small angle geometry as explained in [Raney, 1998] (see Appendix E for more details about this approximation). The simplified width of the Doppler beam is then given by [Raney, 1998]

$$y_n = \frac{h\lambda}{2v_s} f_n \tag{3.9}$$

with $f_n = (n - 32N_f - 0.5)\frac{F}{N_f}$, for $n \in 1, \cdots, 64N_f$ where F is the frequency resolution obtained from the burst length $\tau_b = 1/F$ (see Fig. 3.1) and N_f is the frequency oversampling factor. This equation

shows that the along-track direction (axis y) can be divided into rectangular beams corresponding to different Doppler frequencies displayed in Fig. 3.2.

Fig. 3.2 also shows that the computation of the FSIR for DDA is obtained by integrating ϕ into rectangular beams defined by fixed coordinates y_n and y_{n+1} (we will consider the time independent Doppler coordinate given in (3.9) in the rest of the study). Straightforward computations show that the angles associated with y_n and y_{n+1} are defined by

$$\phi_{t,n} = \mathrm{Re}\left[\mathrm{atan}\left(\frac{y_n}{\sqrt{\rho^2(t) - y_n^2}}\right)\right] \text{ and } \phi_{t,n+1} = \mathrm{Re}\left[\mathrm{atan}\left(\frac{y_{n+1}}{\sqrt{\rho^2(t) - y_{n+1}^2}}\right)\right] \tag{3.10}$$

where atan(.) is the inverse tangent function and $\mathrm{Re}(x)$ denotes the real part of the complex number x. As a consequence, the DDA3 FSIR can be written [5]

$$\mathrm{FSIR}(t,n) = \frac{P_u}{2\pi} U(t) \int_{\mathcal{D}_{t,n}} \exp\left(-\frac{4ct}{\gamma h}\right) d\phi \tag{3.11}$$

where $\mathcal{D}_{t,n} = [\phi_{t,n}, \phi_{t,n+1}] \cup [\pi - \phi_{t,n+1}, \pi - \phi_{t,n}]$. Note that the conventional FSIR can be obtained by considering the angles $\phi_{t,n+1} = \frac{\pi}{2}$ and $\phi_{t,n} = -\frac{\pi}{2}$ in $\mathcal{D}_{t,n}$. This means that the conventional FSIR given in (3.2) can also be obtained by summing the signals of all the Doppler beams before range migration, i.e., by summing the DDM rows of Fig. 3.6.b. Eq. (3.11) leads to following analytical expression of the FSIR

$$\mathrm{FSIR}(t,n) = \frac{P_u}{\pi} \exp\left(-\frac{4ct}{\gamma h}\right) \left(\phi_{t,n+1} - \phi_{t,n}\right) U(t) \tag{3.12}$$

for $n = 1, \cdots, 64N_f$. Note that one has to divide the time t in (3.2) and (3.12) by the curvature factor $\alpha_r = 1 + \frac{h}{R} = 1.11$, where $R = 6378137$ m is the Earth radius, to account for the Earth curvature (see [Chelton, 1989, MacArthur, 1976] and Appendix F for more details about Earth curvature).

Remark: Wingham et al show in [Wingham et al., 2004] that the Doppler model presents a dependence on height that goes as $h^{-5/2}$ for long delays ($t \to \infty$) and as h^{-3} for small delays (similar to pulse limited altimetry). Considering the first limit ($t \to \infty$) in (3.12) gives

$$\mathrm{FSIR}(t,n) \sim \frac{\lambda^3 G_0^2 \sigma^0}{128\pi^3 v_s L_p h^{5/2}} \sqrt{\frac{c}{t}} \exp\left[\frac{-4ct}{\gamma h}\right] (f_{n+1} - f_n) \tag{3.13}$$

[5] A related approach assuming a rectangular shape for the compressed pulse and a rectangular antenna pattern was investigated in [Picardi et al., 1998].

when $t \to \infty$, which shows the $h^{-5/2}$ dependence of the leading coefficient. Furthermore, after considering the second limit ($t \to 0^+$), we obtain $\phi_{n+1} = \frac{\pi}{2}$ and $\phi_n = -\frac{\pi}{2}$ because the propagation circle falls entirely within the Doppler beam (as stated in [Wingham et al., 2004]). Then we have

$$\mathrm{FSIR}(t,n) \sim \frac{\lambda^2 G_0^2 c \sigma^0}{64\pi^2 L_p h^3} \tag{3.14}$$

when $t \to 0^+$, which shows the h^{-3} dependence of the leading coefficient and its independence on time. These results are in agreement with [Raney, 1998, Wingham et al., 2004].

Radar system point target response

The radar system PTR is composed of temporal and Doppler frequency dimensions. In this study, we assume that $\mathrm{PTR}(t,f)$ is the multiplication between a temporal function $\mathrm{PTR}_T(t)$ (corresponding to the radar point target response) and a frequency function $\mathrm{PTR}_F(f)$ (resulting from the Doppler processing). This assumption can be justified by recent results available in the literature [Martin-Puig and Ruffini, 2009, Martin-Puig et al., 2010, Phalippou and Demeestere, 2011] or by a comparison with the measured Cryosat-2 PTR. Indeed, the actual PTR of the Cryosat-2 altimeter can be estimated by using the instrument calibration data which are obtained by emitting burst of impulses and receiving them inside the system (by skipping the antenna). The temporal component $\mathrm{PTR}_T(t)$ can then be obtained as follows. A range FFT is computed for the received $N = 64$ (complex I and Q) signals. The modulus of the resulting signals is then computed. This procedure provides the $\mathrm{PTR}_T(t)$ for each emitted pulse. The 2D PTR associated with delay/Doppler altimetry can also be obtained just by introducing the FFT along-track bloc before the range FFT. The temporal PTR was provided in (3.4) whereas $\mathrm{PTR}_F(f)$ can be approximated accurately by the following squared sine cardinal function

$$\mathrm{PTR}_F(f) = \left| \frac{\sin\left(\pi \frac{f}{F}\right)}{\pi \frac{f}{F}} \right|^2. \tag{3.15}$$

The resulting PTR is then given by

$$\mathrm{PTR}(t,f) = \mathrm{PTR}_T(t)\mathrm{PTR}_F(f). \tag{3.16}$$

Fig. 3.4 (a) shows the measured Cryosat-2 PTR which is in good agreement with the proposed theoretical PTR shown in Fig. 3.4 (b). Figs. 3.5 (a) and (b) compare the measured PTR_T (PTR(t,f) evaluated at the central beam) and PTR_F (PTR(t,f) evaluated at the central time) with the proposed square cardinal sines PTR_T and PTR_F. These figures confirm the good agreement between the measured and theoretical PTRs. It is interesting to note that another PTR could be used without modifying significantly the proposed approach (e.g., PTR(t, f) might be obtained from real measurements). Indeed, the PTR will be convolved numerically with the analytical FSIR derived in this chapter and the PDF defined in (3.3).

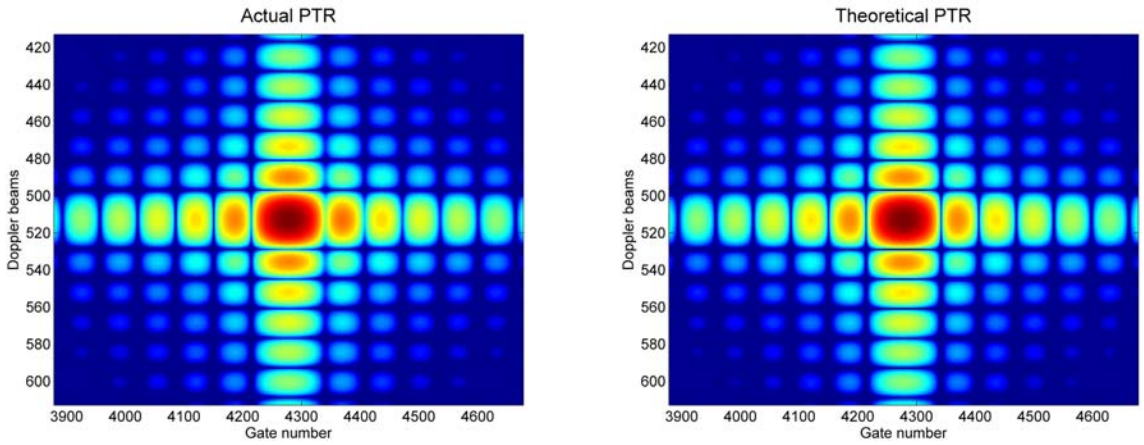

(a) (b)

Figure 3.4: 2D Radar system point target response. (a) Actual Cryosat-2 PTR(t, f), (b) theoretical PTR(t, f).

3.3.3 Reflected power

The reflected DDA3 power $P(t, f)$ (resp. $s(t)$ for CA3) is obtained by a numerical computation of the double convolution (3.5) (resp. (1.5)) between the analytical expressions (3.12), (3.3) and (3.16) (resp. (3.2), (3.3) and (3.4)). This convolution is conducted after oversampling the analytical functions in order to better represent the cardinal sines. Appropriate temporal and frequency oversampling factors have been determined by cross-validation yielding $N_t = 16$ and $N_f = 15$. The resulting oversampled

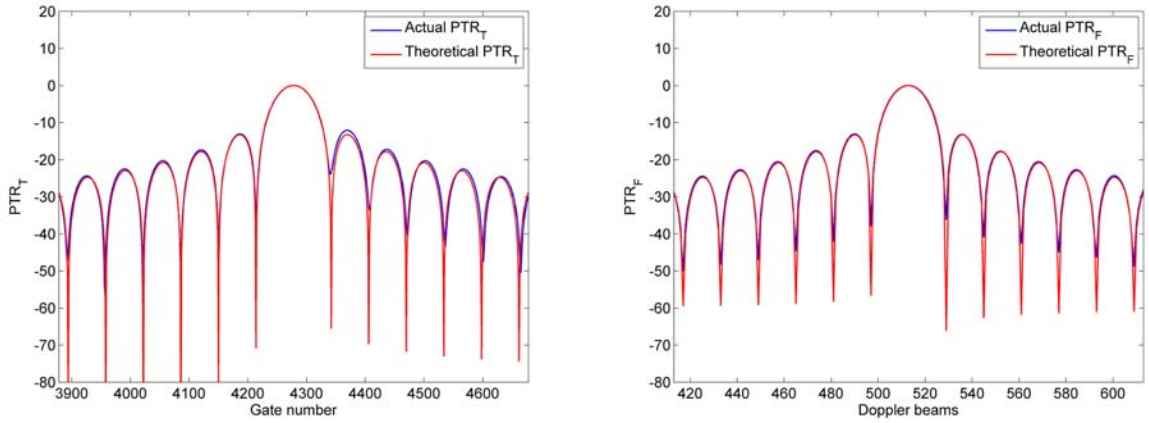

(a) (b)

Figure 3.5: Temporal and frequency radar system point target response. (a) Actual Cryosat-2 PTR_T and the theoretical one, (b) actual Cryosat-2 PTR_F and the theoretical one.

signal is finally undersampled to obtain the required 64×128 DDM. The proposed model (3.5) is semi-analytical in the sense that an analytical formulation is proposed for the FSIR but that the double convolution in (3.5) is computed numerically. Note that the proposed semi-analytical model might be modified by introducing a measured $\mathrm{PTR}(t, f)$ and/or a PDF different from (3.3).

3.3.4 Multi-looking

Section 3.3.2 derived an analytical model for the $\mathrm{FSIR}(t, f)$ which is convolved by $\mathrm{PDF}(t)$ and $\mathrm{PTR}(t, f)$ to compute the reflected power $P(t, f)$. We also showed previously that each time instant t is related to a circle of radius $\rho(t)$ while each Doppler frequency is related to a rectangular along-track beam. Fig. 3.6 summarizes the construction of a DDM. The signal of a given beam is obtained by summing the energies of all scatterers belonging to this beam. For instance, the energy of the signal corresponding to time instant "k" and Doppler beam "n" is obtained by summing the energies of all scatterers belonging to the intersection of the circle of radius $\rho(k)$ with the rectangular nadir beam "n". Note that the rises of the reflected powers in the different Doppler beams occur at different time instants (according to Fig. 3.6, the rise occurs at time instant k for the nadir beam, at

time instant $3k$ for beams "$n+i$" and "$n-i$", etc.). This time shift is related to the range between the satellite and each Doppler beam. Fig. 3.6.b shows an example of DDM obtained by the proposed model. The parabolic shape of this waveform results from the time shifts between the different beams. The multi-looking process aims at gathering all the reflected energies from a single beam. For that,

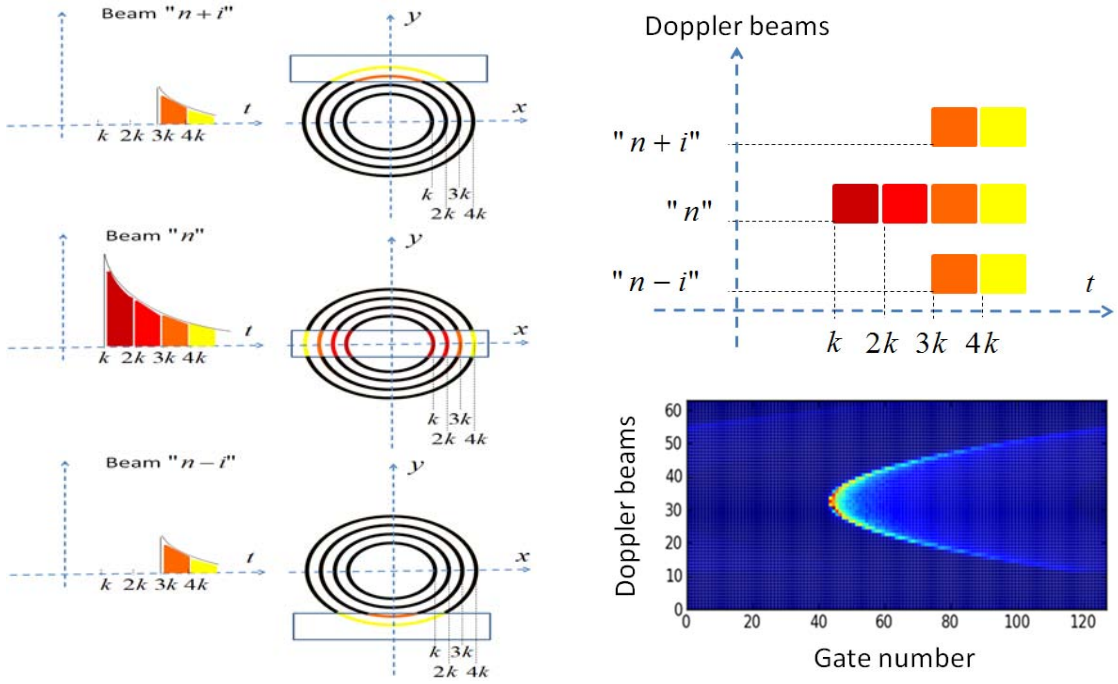

(a) (b)

Figure 3.6: Construction of the delay/Doppler map.

we first have to compensate the time differences between the different beams in order to have signals rising at the same time instant k. This procedure is called delay compensation [Raney, 1998] or range migration. The delay of each beam δr_n is obtained by the difference between the modulus of the position vector $r_n = \sqrt{h^2 + y_n^2}$ (range between the satellite and the Doppler beam n) and the minimum satellite-surface distance h [Raney, 1998]

$$\delta r_n = r_n - h = \sqrt{h^2 + y_n^2} - h. \tag{3.17}$$

Note that (3.17) can be simplified (as proposed in [Raney, 1998]) by considering $y_n << h$ as follows

$$\delta r_n = h\sqrt{1+\left(\frac{y_n}{h}\right)^2} - h \simeq \frac{y_n^2}{2h} = \frac{h\lambda^2}{8v_s^2} f_n^2. \tag{3.18}$$

Note also that the Earth curvature can be considered by introducing a factor α_r yielding [Raney, 1998]

$$\delta r_n = \sqrt{h^2 + \alpha_r y_n^2} - h \simeq \alpha_r \frac{h\lambda^2}{8v_s^2} f_n^2. \tag{3.19}$$

After delay compensation, the signals associated with the Doppler beams are summed to obtain the multi-look waveform as shown in Fig. 3.7 (see also [Phalippou and Demeestere, 2011]).

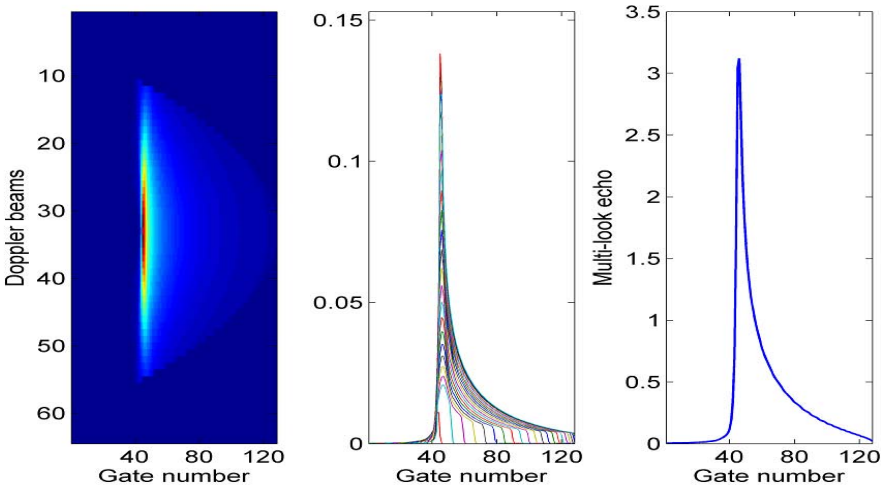

Figure 3.7: Delay/Doppler map after delay compensation (left), migrated signals for all Doppler beams (middle) and the corresponding multi-look waveform (right).

$$s(t) = \sum_{n=1}^{N} P\left(t - \delta t_n, f_n\right) = \sum_{n=1}^{N} m\left(t, f_n\right) \tag{3.20}$$

where $\delta t_n = \frac{2\,\delta r_n}{c}$ is the delay compensation expressed in seconds and $m(t, f_n) = P\left(t - \delta t_n, f_n\right)$ denotes the signal of the n^{th} Doppler beam after delay compensation. Note that the procedure is quite different for real waveforms where we have to collect the reflected energies of different bursts. For example, the selected scene's beam may reflect energy coming from nadir beam (beam #33) for

the burst i_1, from the beam #34 for the burst i_2, etc. Note that this stacking procedure aims at reducing the noise effect and that it assumes that the geophysical parameters of the selected beam do not change from one burst to another.

The signal $s(t)$ is finally sampled at instants $t_k = (k - N_t\tau)\,\frac{T_s}{N_t}$, for $k = 1, \cdots, K\,N_t$, where τ is the epoch and $K = 104$ is the number of samples (without oversampling). An example of resulting DDA3 vector $\boldsymbol{s} = (s_1, \cdots, s_K)^T = [s(t_1), \cdots, s(t_K)]^T$ is shown in Fig. 3.8 and compared with the CA3 echo. The DD echo has a peaky shape around the epoch τ because of delay compensation. This peaky shape was first quantified in [Moore and Williams, 1957] as characteristic of a beam-limited altimeter.

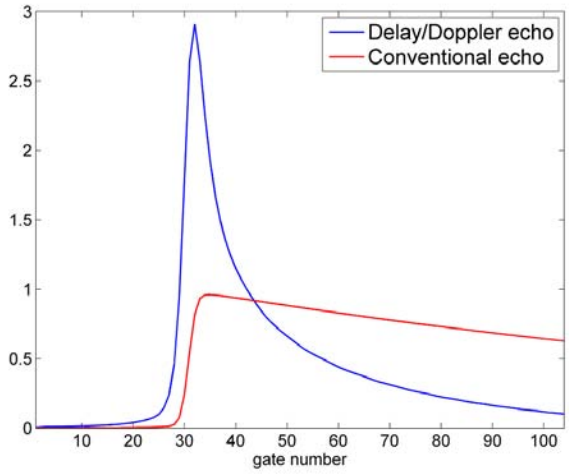

Figure 3.8: Delay/Doppler and conventional echoes for the same altimetric parameters ($P_u = 1$, $\tau = 31$ gates, SWH = 2 m).

3.3.5 Speckle noise

In order to generate realistic data similar to Cryosat-2 echoes, the DDM has to be corrupted by speckle noise. Following the works of [Wingham et al., 2004], a multiplicative speckle noise is applied

to the DDM leading to [6]

$$y(t) = \sum_{n=1}^{N} P\left(t - \delta t_n, f_n\right)\, q(t - \delta t_n, n) = \sum_{n=1}^{N} m\left(t, f_n\right)\, q(t - \delta t_n, n) \tag{3.21}$$

where $q(t-\delta t_n, n)$ is a random variable distributed according to a gamma distribution $\mathcal{G}(L, 1/L)$ (see [Papoulis and Pillai, 2002, p. 87] for the definition of the gamma distribution) and L is the number of bursts observing each Doppler beam ($L = 4$ in our simulations).

3.4 Parameter estimation

3.4.1 Estimation algorithm

This chapter proposes to estimate the parameters of the multi-look waveform by using an LS procedure (as for CA [Maus et al., 1998, Sandwell and Smith, 2005]). The altimetric waveform $\boldsymbol{y} = (y_1, \ldots, y_K)^T$ is a noisy version of $\boldsymbol{s} = (s_1, \ldots, s_K)^T$ which depends on the parameter vector $\boldsymbol{\theta} = (\theta_1, \theta_2, \theta_3)^T = (\text{SWH}, P_u, \tau)^T$ (the estimation is done under the assumption that $\xi = 0°$ in both conventional and delay/Doppler models). The LS method consists of estimating the unknown parameter vector $\boldsymbol{\theta}$ as follows

$$\underset{\boldsymbol{\theta}}{\operatorname{argmin}}\, \boldsymbol{G}(\boldsymbol{\theta}) = \underset{\boldsymbol{\theta}}{\operatorname{argmin}}\, \frac{1}{2} \sum_{k=1}^{K} g_k^2(\boldsymbol{\theta}) \tag{3.22}$$

where $g_k(\boldsymbol{\theta}) = y_k - s_k(\boldsymbol{\theta})$ is a vector of residues. Since $g_k(\boldsymbol{\theta})$ is a complicated nonlinear function of SWH and τ, the optimization problem (3.22) does not admit a closed-form expression. In this study, we propose to solve (3.22) using a numerical optimization method based on the Levenberg-Marquardt algorithm [Bertsekas, 1995]. This choice allows us to use the numerical derivatives of the proposed model while keeping the same estimation performance as the NR algorithm which is widely used in CA (see Appendix B). Moreover, the LM algorithm was also used in the SAMOSA project to estimate the parameter of their DDA model [Gommenginger et al., 2011a, 2012a]. This point motivates our choice of the LM algorithm in order to compare our model to that of SAMOSA. The parameter

[6] In [Wingham et al., 2004], a single-look is assumed to follow an exponential distribution. Moreover, and as mentioned in [Raney, 2012a,b], each Doppler beam is observed by L bursts (denoted as N_{bin} in [Raney, 2012a,b]). Thus, the signal of each beam results from the averaging of L observations. It results that the noise corrupting each beam follows a gamma distribution $\mathcal{G}(L, 1/L)$.

update of the iterative Levenberg-Marquardt algorithm is defined by $\boldsymbol{\theta}^{(i+1)} = \boldsymbol{\theta}^{(i)} + \boldsymbol{e}^{(i)}$, where $\boldsymbol{\theta}^{(i)}$ is the estimate of $\boldsymbol{\theta}$ at the ith iteration. The choice of $\boldsymbol{e}^{(i)}$ is based on a Taylor expansion (at the first order) of $\boldsymbol{g}$ in the neighborhood of $\boldsymbol{\theta}^{(i)}$

$$\boldsymbol{g}(\boldsymbol{\theta}^{(i)} + \boldsymbol{e}^{(i)}) \simeq \boldsymbol{l}(\boldsymbol{e}^{(i)}) = \boldsymbol{g}(\boldsymbol{\theta}^{(i)}) + \boldsymbol{J}(\boldsymbol{\theta}^{(i)})\boldsymbol{e}^{(i)} \tag{3.23}$$

where $\boldsymbol{J}(\boldsymbol{\theta}) = [\boldsymbol{J}_1(\boldsymbol{\theta}), \boldsymbol{J}_2(\boldsymbol{\theta}), \boldsymbol{J}_3(\boldsymbol{\theta})] = \left[\frac{\partial \boldsymbol{g}(\boldsymbol{\theta})}{\partial \theta_1}, \frac{\partial \boldsymbol{g}(\boldsymbol{\theta})}{\partial \theta_2}, \frac{\partial \boldsymbol{g}(\boldsymbol{\theta})}{\partial \theta_3}\right]$ is a $K \times 3$ matrix representing the gradient of $\boldsymbol{g}$. After replacing (3.23) in (3.22) (and removing notation (i) for brevity), the following result is obtained

$$\boldsymbol{G}(\boldsymbol{\theta} + \boldsymbol{e}) \simeq \boldsymbol{L}(\boldsymbol{e}) = \frac{1}{2}\boldsymbol{l}(\boldsymbol{e})^T\boldsymbol{l}(\boldsymbol{e}) = \boldsymbol{G}(\boldsymbol{\theta}) + \boldsymbol{e}^T\boldsymbol{J}(\boldsymbol{\theta})^T\boldsymbol{g} + \frac{1}{2}\boldsymbol{e}^T\boldsymbol{J}(\boldsymbol{\theta})^T\boldsymbol{J}(\boldsymbol{\theta})\boldsymbol{e}. \tag{3.24}$$

The descent direction $\boldsymbol{e}$ is then obtained by minimizing $\boldsymbol{L}(\boldsymbol{e})$. By setting to 0 the derivative $\boldsymbol{L}'(\boldsymbol{e}) = \boldsymbol{J}(\boldsymbol{\theta})^T\boldsymbol{g} + \boldsymbol{J}(\boldsymbol{\theta})^T\boldsymbol{J}(\boldsymbol{\theta})\boldsymbol{e}$, we obtain

$$\boldsymbol{J}(\boldsymbol{\theta})^T\boldsymbol{J}(\boldsymbol{\theta})\boldsymbol{e} = -\boldsymbol{J}(\boldsymbol{\theta})^T\boldsymbol{g}. \tag{3.25}$$

This relation is the basis of the Gauss-Newton recursion [Bertsekas, 1995, Nocedal and Wright, 1999]. Levenberg and Marquardt proposed to add a regularization parameter μ in (3.25) leading to

$$\left[\boldsymbol{J}(\boldsymbol{\theta})^T\boldsymbol{J}(\boldsymbol{\theta}) + \mu\boldsymbol{I}_3\right]\boldsymbol{e} = -\boldsymbol{J}(\boldsymbol{\theta})^T\boldsymbol{g} \tag{3.26}$$

where $\boldsymbol{I}_3$ is the 3×3 identity matrix. Note that the parameter μ controls the convergence speed of the algorithm. Note also that the derivatives appearing in $\boldsymbol{J}(\boldsymbol{\theta})$ can be computed numerically by finite difference as follows

$$\boldsymbol{J}_i(\boldsymbol{\theta}) = -\frac{\partial \boldsymbol{s}(\boldsymbol{\theta})}{\partial \theta_i} \simeq -\frac{\boldsymbol{s}(\theta_i + \Delta\theta_i) - \boldsymbol{s}(\theta_i)}{\Delta\theta_i} \tag{3.27}$$

with $\Delta\boldsymbol{\theta} = (\Delta\text{SWH}, \Delta\tau, \Delta P_u)^T$. In our simulations, we have chosen $\Delta\boldsymbol{\theta} = (0.05 \text{ m}, 0.02 \text{ gates}, 0.05)^T$.

3.4.2 Estimation performance

This section introduces the criteria used to evaluate the quality of the estimators resulting from the proposed model. The quality of the estimation for simulated waveforms can be measured by

comparing the estimated and true parameters by using the RMSE introduced in (2.20). The bias and standard-deviation (STD) of the estimator given by

$$\text{Bias}\left(\theta_i\right) = \frac{1}{N_{\text{MC}}} \sum_{\ell=1}^{N_{\text{MC}}} \hat{\theta}_i(\ell) - \theta_i = \overline{\theta_i} - \theta_i \tag{3.28}$$

and

$$\text{STD}\left(\theta_i\right) = \sqrt{\frac{1}{N_{\text{MC}}} \sum_{\ell=1}^{N_{\text{MC}}} \left[\hat{\theta}_i(\ell) - \overline{\theta_i}\right]^2} \tag{3.29}$$

can also be used to better analyze the obtained results. The normalized reconstruction error (NRE) given by

$$\text{NRE} = \sqrt{\frac{\sum_{k=1}^{K} \left(y_k - \hat{y}_k\right)^2}{\sum_{k=1}^{K} y_k^2}} = \frac{||\boldsymbol{y} - \hat{\boldsymbol{y}}||}{||\boldsymbol{y}||} \tag{3.30}$$

where $\hat{y}_k$ denotes the estimated waveform obtained by replacing the unknown parameters by their estimates in s_k defined in (3.20), has been computed in order to evaluate the performance in the case of a real waveform. This criterion has been introduced instead of the usual RE criterion because the shape of the DDA echo is different from that of the CA echo. This shape difference has motivated the normalization of the RE criterion in order to have comparable values when considering CA and DDA echoes. The average normalized reconstruction error (ANRE) given by

$$\text{ANRE} = \sqrt{\frac{1}{N_{\text{MC}}} \sum_{l=1}^{N_{\text{MC}}} \frac{||\boldsymbol{y}_l - \hat{\boldsymbol{y}}_l||^2}{||\boldsymbol{y}_l||^2}} \tag{3.31}$$

can also be used when considering N_{MC} waveforms, $\boldsymbol{y}_l = (y_{l1}, \cdots, y_{lK})^T$ for $l = 1, \cdots, N_{\text{MC}}$. Note finally that in the case of real data, the estimated DD parameters will be compared to the estimated CA parameters that are considered as a reference.

3.5 Cramér-Rao bounds

This section introduces the CRBs associated with the conventional double convolution model (1.5) (denoted as CA3) and the proposed semi-analytical model for DDA (denoted by DDA3).

3.5.1 CRBs for CA3

The observed altimetric signal $\boldsymbol{s}$ is corrupted by a multiplicative speckle noise distributed according to an exponential distribution. In order to reduce the influence of this noise affecting each individual echo, a sequence of L_c consecutive waveforms is averaged on-board the satellite. Assuming pulse-to-pulse statistical independence and invoking the central limit theorem, the averaged signal can be written $y_k = s_k\left[1 + n_k\right]$, for $k = 1, \cdots, K$, where n_k is approximately distributed according to a zero mean Gaussian distribution with variance $1/L_c$ i.e., $n_k \sim \mathcal{N}(0, 1/L_c)$. An equivalent formulation is

$$y_k = s_k + n'_k, k = 1, \cdots, K \tag{3.32}$$

where $n'_k \sim \mathcal{N}(0, s_k^2/L_c)$. Using (3.32) and assuming independence between the signal samples, the likelihood function of the vector of observations $\boldsymbol{y}$ can be computed. It is the probability density function of a multivariate Gaussian distribution (denoted as $f(\boldsymbol{y}|\boldsymbol{\theta})$) with mean $\boldsymbol{s}$ and covariance matrix $\boldsymbol{\Sigma}\left(\boldsymbol{\theta}, L_c\right)$. The covariance matrix $\boldsymbol{\Sigma}\left(\boldsymbol{\theta}, L_c\right)$ is diagonal with diagonal elements $\Sigma_k(\boldsymbol{\theta}, L_c) = s_k^2/L_c$, for $k = 1, \cdots, K$. The FIM of the parameter vector $\boldsymbol{\theta}$ can then be computed by differentiating twice the log-likelihood function leading to [Bangs, 1971, Delmas and Abeida, 2004, Slepian, 1954]

$$F_c(i,j) = \frac{\partial \boldsymbol{s}^T}{\partial \theta_i}\boldsymbol{\Sigma}^{-1}(\boldsymbol{\theta}, L_c)\frac{\partial \boldsymbol{s}}{\partial \theta_j} + \frac{1}{2}\mathrm{tr}\left(\boldsymbol{\Sigma}^{-1}(\boldsymbol{\theta}, L_c)\frac{\partial \boldsymbol{\Sigma}(\boldsymbol{\theta}, L_c)}{\partial \theta_i}\boldsymbol{\Sigma}^{-1}(\boldsymbol{\theta}, L_c)\frac{\partial \boldsymbol{\Sigma}(\boldsymbol{\theta}, L_c)}{\partial \theta_j}\right) \tag{3.33}$$

where

$$\frac{\partial \boldsymbol{\Sigma}(\boldsymbol{\theta}, L_c)}{\partial \theta_i} = \begin{bmatrix} \frac{\partial \Sigma_1}{\partial \theta_i} & 0 & \cdots & 0 \\ 0 & \frac{\partial \Sigma_2}{\partial \theta_i} & \cdots & 0 \\ \vdots & \vdots & \vdots & \vdots \\ 0 & 0 & \cdots & \frac{\partial \Sigma_K}{\partial \theta_i} \end{bmatrix}. \tag{3.34}$$

Straightforward computations yield

$$\boldsymbol{F}_c = \boldsymbol{D}_c^T\boldsymbol{\Sigma}^{-1}(\boldsymbol{\theta}, L_c + 2)\boldsymbol{D}_c \tag{3.35}$$

where $\boldsymbol{D}_c$ is a $(K \times 3)$ matrix whose components are $D_c(k,i) = \frac{\partial s_k}{\partial \theta_i}$, for $k = 1, \cdots, K$ and $i = 1, \cdots, 3$. The analytical expressions of these matrix components are available in Appendix G.1. The CRBs

are then obtained by considering the diagonal elements of the inverse FIM denoted by $\boldsymbol{F}_c^{-1}$. Note that the proposed CRBs differ from those derived in [Mailhes et al., 2008] since the present paper considers the double convolution model (1.5) whereas the Brown model [Brown, 1977] was used in [Mailhes et al., 2008].

3.5.2 CRBs for DDA3

Each Doppler beam has a size of about 300 meters which means that it is observed by the satellite during 43 ms (after taking into account the satellite velocity). Moreover, the satellite transmits 85 bursts of $N = 64$ pulses per second. As a consequence, each Doppler beam is observed by approximately 4 independent bursts, i.e., it is observed by $N_p = 256$ pulses. The observed discrete multi-looked echo can be expressed as

$$y_k = \sum_{n=1}^{N} m\left(k,n\right) q(k,n) \tag{3.36}$$

where $q(k,n)$ is an independent and gamma distributed speckle noise (whose shape and inverse scale parameters equal $L = 4$) resulting from the average of 4 bursts. Invoking the generalized central limit theorem for sums of independent non-identically distributed random variables (e.g., the Lyapunov condition [Billingsley, 1995]), it makes sense to approximate the distribution of y_k by a Gaussian distribution whose mean is $\sum_{n=1}^{N} m\left(k,n\right)$ and whose covariance matrix $\boldsymbol{\Lambda}\left(\boldsymbol{\theta}\right)$ is diagonal with diagonal elements $\Lambda_k\left(\boldsymbol{\theta}\right) = \frac{1}{4}\sum_{n=1}^{N} m^2\left(k,n\right)$, for $k = 1, \cdots, K$. The FIM of the parameter vector $\boldsymbol{\theta}$ can then be computed leading to

$$\boldsymbol{F}_d = \boldsymbol{D}_d^T \boldsymbol{\Lambda}^{-1}\left(\boldsymbol{\theta}\right) \boldsymbol{D}_d + \boldsymbol{H}_d \tag{3.37}$$

where $\boldsymbol{D}_d$ is a $(K \times 3)$ matrix whose components are $D_d(k,i) = \frac{\partial s_k}{\partial \theta_i}$, for $k = 1, \cdots, K$ and $i = 1, \cdots, 3$ and $\boldsymbol{H}_d$ is given by

$$H_d(i,j) = 2\sum_{k=1}^{K} \frac{h_i(m,k) h_j(m,k)}{\left[\sum_{n=1}^{N} m^2(k,n)\right]^2} \tag{3.38}$$

with

$$h_i(m,k) = \sum_{n=1}^{N} m(k,n) \frac{\partial m(k,n)}{\partial \theta_i} \tag{3.39}$$

for $(i,j) \in \{1,2,3\}^2$. The analytical expressions of the partial derivatives of $m(k,n)$ with respect to P_u, τ and SWH are available in Appendix G.2. Note that the covariance matrix $\boldsymbol{\Lambda}(\boldsymbol{\theta})$ of the observed signal $\boldsymbol{y}$ (which depends on the different signals $m(k,n)$) can be rewritten as a function of the multi-look echo $\boldsymbol{s}$. For that purpose, an "effective number of looks" can be defined for the kth observation [Wingham et al., 2004]

$$N_{\text{eff}}(k) = \frac{E^2[y_k]}{E\left\{[y_k - E(y_k)]^2\right\}} = \mu_k N_p \tag{3.40}$$

where the components of the vector $\boldsymbol{\mu} = (\mu_1, \cdots, \mu_K)^T$ are

$$\mu_k = \frac{\left[\sum_{n=1}^{N} m(k,n)\right]^2}{N\sum_{n=1}^{N} m^2(k,n)} = \frac{s_k^2}{N\sum_{n=1}^{N} m^2(k,n)}. \tag{3.41}$$

Note that μ_k is smaller than 1 accounting for the fact that $N_{\text{eff}}(k)$ is smaller than N_p (see [Wingham et al., 2004]). Using the previous notations, the kth diagonal element of the covariance matrix $\boldsymbol{\Lambda}(\boldsymbol{\theta})$ can be written $\Lambda_k(\boldsymbol{\theta}) = \frac{s_k^2}{N_p \mu_k}$, for $k = 1, \cdots, K$. This expression is similar to the one obtained for CA3 (the number of looks L_c has been replaced by $N_p\mu_k$ in the kth element of $\boldsymbol{\Lambda}$). Assuming a small variation of $\boldsymbol{\mu}$ with respect to the altimetric parameters, (i.e., $\frac{\partial \boldsymbol{\mu}}{\partial \theta_i} \approx \mathbf{0}$, for $i \in \{1,2,3\}$) leads to

$$\boldsymbol{F}_d \approx \boldsymbol{D}_d^T \boldsymbol{\Delta}^{-1}(\boldsymbol{\theta}) \boldsymbol{D}_d \tag{3.42}$$

where $\boldsymbol{\Delta}$ is a diagonal matrix with elements $\Delta_k(\boldsymbol{\theta}) = \frac{s_k^2}{N_p\mu_k + 2}$, for $k = 1, \cdots, K$. Note that the FIM (3.42) has the same form as the one obtained for CA3 (3.35). The DDA CRBs are finally obtained by considering the diagonal elements of $\boldsymbol{F}_d^{-1}$.

3.6 Results for simulated data

This section first describes how simulated echoes have been generated. The behavior of the proposed DD model as a function of the Doppler frequency is then analyzed. The effect of range migration on the performance of the LS estimator is also investigated. The next study is interested in evaluating the number of Doppler beams (that are used to form the multi-look echo) and its effects on the estimation quality. The last part compares the CRBs of CA3 and DDA3 in order to illustrate the

expected improvement of the DD mode. This improvement is also validated by the comparison of the estimation performance using CA3 and DDA3 (as shown in [Jensen and Raney, 1998, Phalippou and Enjolras, 2007] for a simulated scene and in [Martin-Puig and Ruffini, 2009] for another Doppler model).

3.6.1 Simulation scenario

This section describes how Cryosat-2 echoes have been generated and introduces the denominations of the related simulated echoes. The Cryosat-2 altimeter called SIRAL presents three modes that are: the low resolution mode (LRM), the synthetic aperture radar mode (SARM) and the synthetic aperture radar interferometric mode (SARInM) [Wingham et al., 2006]. The data of the LRM are used to generate CA echoes (also denoted by CA-LRM echoes) while those of SARM provide DD echoes. However, as the two modes operate separately, the collected data do not result from the same scene and cannot be used to compare the same scenario. Hence, the data of SARM are also used to generate conventional echoes called in the present study CA-SARM for conventional altimetric echoes from SAR mode[7]. However, the resulting echoes are affected by a level of noise that is higher than for CA-LRM echoes. Indeed, the observed CA echoes are corrupted by a speckle noise resulting from the incoherent summations of $L_c = 90$ consecutive echoes for Poseidon-3 altimeter [Desjonqueres et al., 2010]. The CA-SARM results from averaging approximately 32 uncorrelated echoes (the other correlated echoes will not reduce significantly the noise level) inducing a noise increasing factor of $\sqrt{3}$ between the CA and CA-SARM echoes [Giles et al., 2012]. Fig. 3.9 summarizes the different steps performed to obtain the considered simulated echoes and their denominations in the rest of the thesis, i.e., multi-look (or DD), delay/Doppler without migration, CA (or CA-LRM) and CA-SARM echoes. Note again that the considered number of parameters will also be specified at the end of each acronym[8].

[7] These echoes are known under different names: LRM-like [Phalippou and Demeestere, 2011], pseudo-LRM [Boy et al., 2012, Gommenginger et al., 2012a, Smith and Scharroo, 2012] or reduced-SAR (RDSAR) [Boy et al., 2012, Gommenginger et al., 2012a]. The denomination CA-SARM has been chosen for clarity.

[8] This choice of notation is used to distinguish between the proposed 3 parameters model of this chapter and that of the next chapter which considers 3, 4 or 5 parameters.

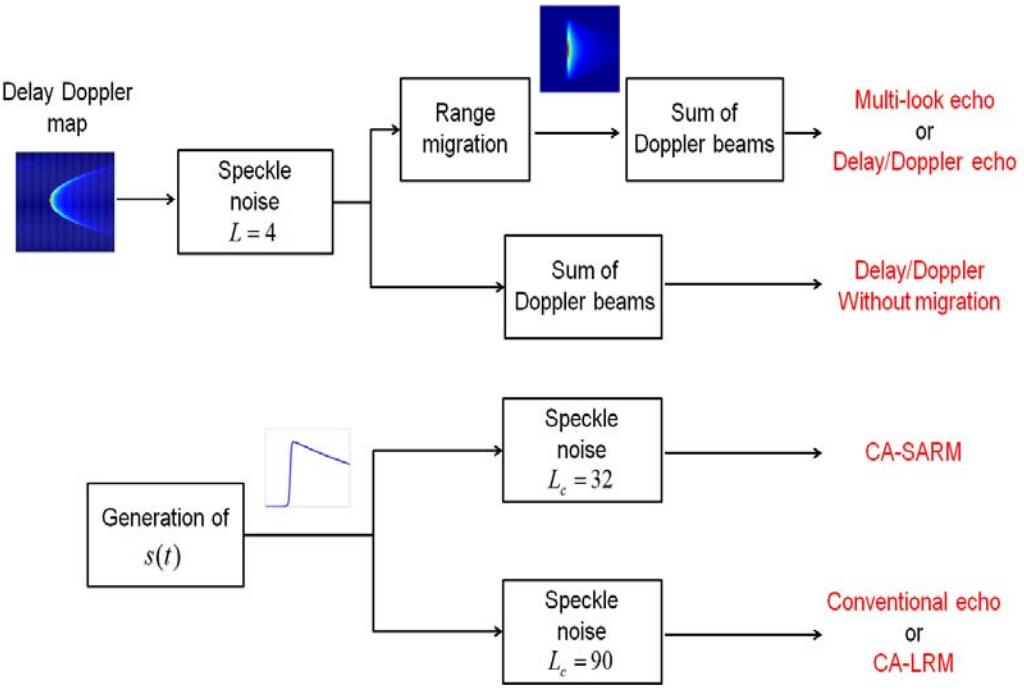

Figure 3.9: Construction of the observed echoes and related terminology.

3.6.2 Model analysis

This section analyses the behavior of the reflected power as a function of the Doppler frequency. An example of simulation scenario corresponding to the altimetric parameters $P_u = 1$, SWH $= 0$ m and $\tau = 31$ gates is summarized in Table 3.1. Fig. 3.10 shows the corresponding altimetric echoes (normalized by the maximum of the nadir echo) for different Doppler frequencies $(0, 2, 4$ and 6 kHz). As expected, the higher power occurs at nadir, i.e., $f = 0$ Hz. This figure also shows that the echo broadens as the frequency increases which can be explained as follows. The Doppler frequency is proportional to the along-track distance (see (3.9)). As a consequence, the high frequencies correspond to far Doppler beams (from nadir) that intersect the large propagation circles. However, propagation circles have an increasing radius and a narrowing width for increasing time [Walsh., 1982]. This means that the Doppler beams far from nadir intersect a lot of propagation circles (each circle correspond to a time instant) and thus the reflected echoes spread over a lot of range gates. Fig. 3.10 (bottom) shows examples of DD echoes obtained after range migration (this figure is similar to Fig. 7 of [Wingham

Parameter	Value
Frequency	13.575 GHz
Wavelength (λ)	2.21 cm
Bandwidth (B)	320 MHz
Altitude (h)	730 km
Burst repetition frequency (BRF)	85 Hz
Pulse repetition frequency (PRF)	18182 Hz
3 dB antenna beam width ($\theta_{3\text{dB}}$)	1.1388 degrees
Velocity (v_s)	7000 m/s
Pulses per burst	64 pulses
Burst length (τ_b)	3.5 ms
Doppler beam width	327 m

Table 3.1: Simulation parameters.

et al., 2004]). Note that the leading edge of the multi-look echo, obtained by summing the migrated echoes, is directly affected by the high Doppler frequency echoes because of their large shape and slower leading edge. Considering echoes associated with different time gates (gates $31, 51, 71, 91$ and 111), Fig. 3.11 (top) shows a decrease of the power according to Doppler frequency which is due to the weighting of the power by the Gaussian antenna gain [Phalippou and Enjolras, 2007]. This figure also shows a symmetrical shape of the echoes with respect to the zero Doppler frequency which is due to the absence of mispointing angle $\xi = 0°$ (note that the situation can be very different in presence of mispointing as shown in [Walsh., 1982]). These results are confirmed in Fig. 3.11 (bottom) which shows the Doppler spectra resulting from the summation of the powers associated with the different Doppler frequencies.

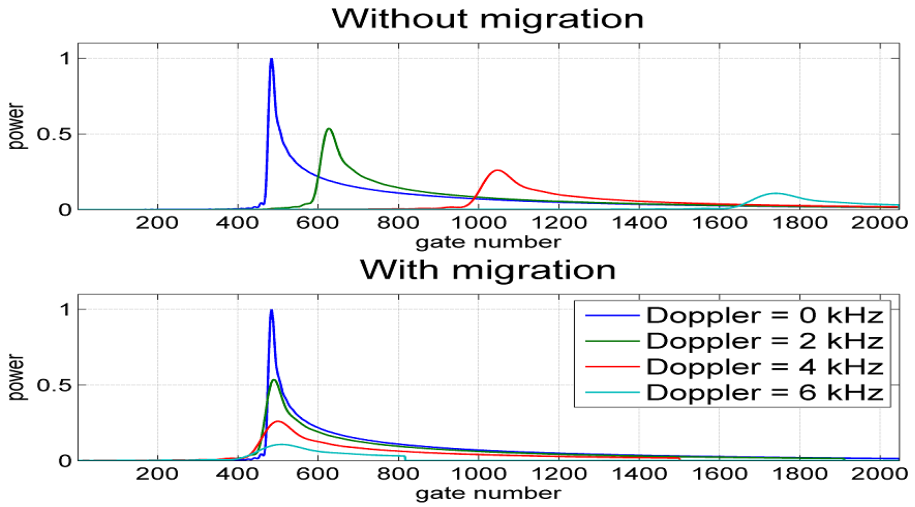

Figure 3.10: Echoes for different Doppler frequencies $(0, 2, 4$ and 6 kHz). (top) without range migration, (bottom) with range migration. The temporal scale has been oversampled by a factor of $N_t = 16$.

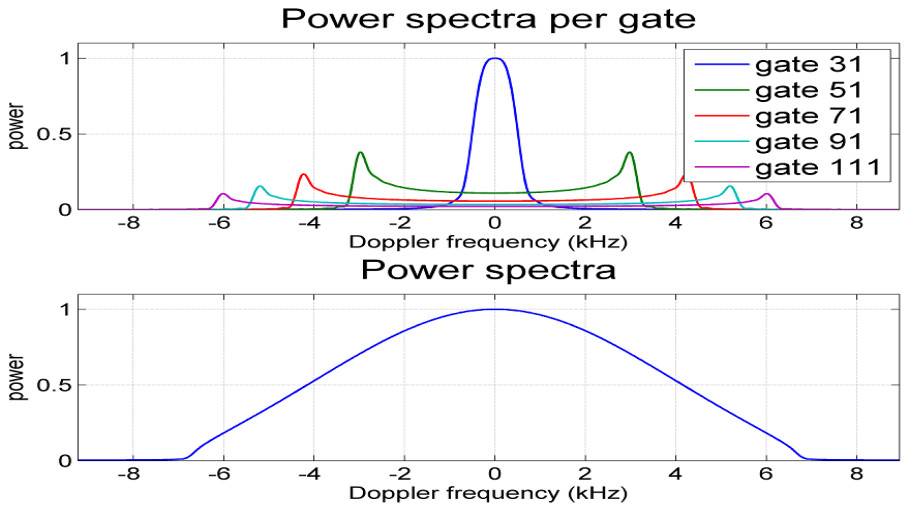

Figure 3.11: (top) reflected power versus Doppler frequency for different gate numbers, (bottom) Doppler spectra after summing the powers associated with each Doppler frequency (sum of the rows of Fig. 3.7 (left)). The frequency scale has been oversampled by a factor of $N_f = 15$.

3.6.3 Importance of range migration

This section is interested in analyzing the effect of range migration on the quality of the estimated parameters. The RMSEs of the estimated parameters obtained with and without range migration (with the same noise level, i.e., $L = 4$) are shown in Fig. 3.12 versus the sea wave height (SWH) (additional results versus τ and P_u are available in Appendix H). These RMSEs have been obtained using $N_{\text{MC}} = 1000$ simulated waveforms (see (2.20)). The parameters SWH and τ are better estimated by considering migrated DD echoes since the errors on SWH and τ are reduced by $\simeq 30$ cm and $\simeq 6$ cm respectively. However, the estimation of P_u is slightly better without migration because the echo is broader and its amplitude is less sensitive to noise.

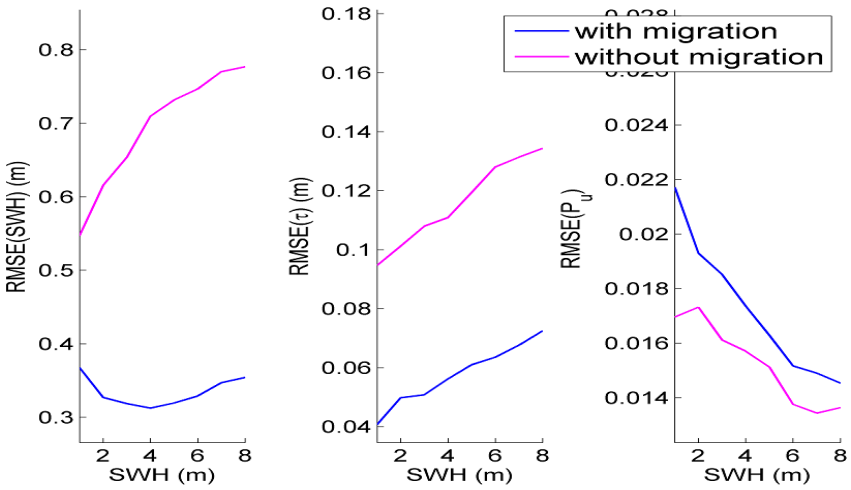

Figure 3.12: Parameter RMSEs for migrated and non-migrated delay/Doppler echoes (1000 Monte-Carlo realizations) versus SWH with $P_u = 1$ and $\tau = 31$ gates.

3.6.4 Choice of beams

The multi-look echo is obtained by summing the Doppler beams after delay compensation. This section is interested in studying the influence of the considered number of the Doppler beams on the estimation performance. [Raney, 2012a,b] studied the importance of the number of looks by considering the number of looks within each Doppler beam (denoted by N_{bin}), the number of beams

crossed by the over-passing radar in a period of dt (denoted by N_{dt}) and the number of useful beams N_{useful} that contribute to the averaged waveform. The first number is considered as constant ($L = 4$ in our case) since the burst are uncorrelated as stated in [Raney, 2012a]. The number N_{dt} is also a constant that depends on the satellite velocity and the width of the Doppler beam. We will be interested in this section on the evaluation of the necessary number of beams when estimating echoes that were generated using the 64 Doppler beams. This will provide an estimation of N_{useful}. To do that, we introduce a new variable $N_b \in \{0, \cdots, 31\}$ and estimate the parameters of the model (generated using the 64 beams) using the $N_{\text{useful}} = 2N_b + 1$ Doppler beams belonging to $\{33 - N_b, \cdots, 33 + N_b\}$. Fig. 3.13 shows the parameter RMSEs versus N_b. The RMSEs are decreasing functions of N_b for $N_b \leq 20$ and stabilize for $N_b > 20$. This means that the beams $\in [1, 12] \cup [54, 64]$ do not contain useful information for parameter estimation, which is in agreement with Fig. 3.7 (left) showing very weak signal contributions resulting from these beams. Note, however, that considering few beams can cause the presence of bias for the estimated parameters as shown in Fig. 3.14. This figure shows that the bias is more important for $N_b < 12$ especially for the SWH and τ parameters and that it stabilizes for $N_b \geq 12$. From here we can deduce that using $N_{\text{useful}} = 41$ beams for the parameter estimation will provide similar performance than using all the 64 beams. Considering the equation of N_{useful} in [Raney, 2012b]

$$N_{\text{useful}} = \frac{2hn_r h_r}{y_{\text{dop}}^2} \tag{3.43}$$

where h_r is the single-pulse range resolution of the altimeter, y_{dop} is the width of the Doppler beam and n_r is a value that establishes the tolerable amount of rise time degradation relative to resolution, one can evaluate the value of n_r for $N_{\text{useful}} = 41$. We find for this case that $n_r \simeq 6$ which is more flexible than the value $n_r = 3$ proposed in [Raney, 2012b]. Note finally that using fewer beams significantly reduces the computational time which is an important factor for real time processing.

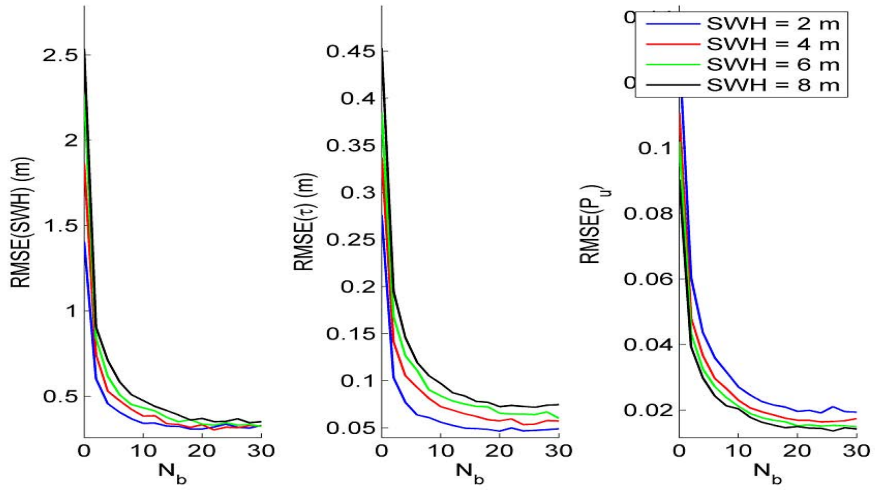

Figure 3.13: Parameter RMSE versus number of considered Doppler beams (1000 Monte-Carlo runs).

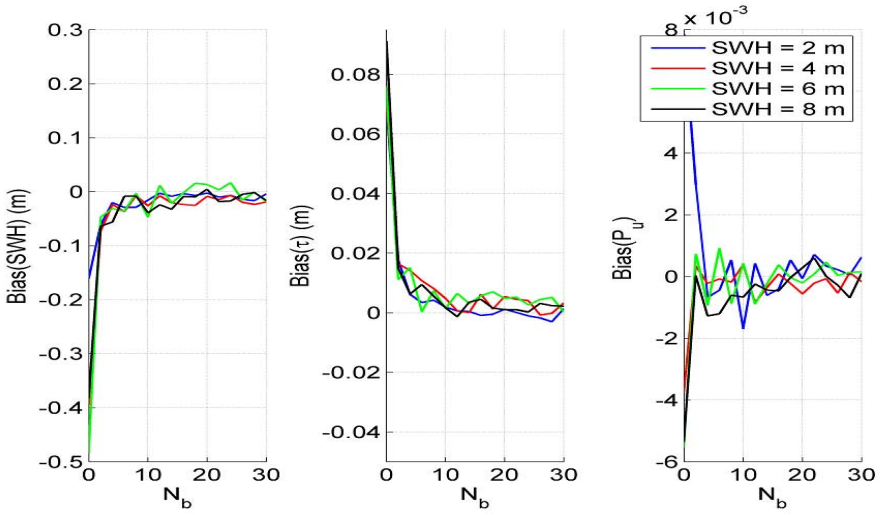

Figure 3.14: Parameter Biases versus number of considered Doppler beams (1000 Monte-Carlo runs).

3.6.5 Comparison between CA3 and DDA3

This section is interested in the comparison between CA3 and DDA3 by first comparing the associated CRBs and then the RMSEs. Fig. 3.15 shows the RCRBs of the three altimetric parameters for both

CA3 (green curves) and DDA3 (black curves) when varying SWH in the interval $[1, 8]$ meters. This figure shows a clear improvement for RCRB(τ) and RCRB(P_u) when considering DDA3. For instance, for SWH $= 2$ m, we note an improvement by a factor of 1.7 for RCRB(τ) and by a factor of 1.28 for RCRB(P_u). It can also be observed that for small sea wave heights (i.e., SWH < 5 m), RCRB(SWH) is slightly higher for DDA3 than for CA3. However, the possible improvement in the estimation of the epoch and amplitude is clearly of major importance. Fig. 3.15 also shows the RMSEs associated with CA3 and DDA3 when considering the LS algorithm. These RMSEs have been computed using $N_{\text{MC}} = 1000$ simulated waveforms (see (2.20)). The DDA3 RMSEs for τ and SWH (blue curves) are lower than those obtained with CA3 (red curves) which shows the interest of using the Doppler procedure. However, one can notice that CA3 provides better results for RMSE(SWH) for very small values of SWH which is in agreement with the CRBs behavior (this result was also observed in [Phalippou and Demeestere, 2011]). Note finally that the obtained RMSEs are very close to the STDs since the proposed estimator provides very small biases (the interested reader is invited to consult Appendix H for more simulation results).

The quality of the proposed DDA3 estimation procedure can also be evaluated by comparing the derived DDA3 CRBs (black curves) to the DDA3 RMSEs. This CRBs show that there is some space to improve the LS algorithm performance when considering the three estimated parameters SWH, τ and P_u. Note that a study of other estimation strategies (such as MLE and weighted LS) has been conducted and is provided in Appendix I. This study shows that it is possible to reach the CRBs performance at a price of higher computational time.

The last comparison concerns the theoretical parameter correlations that can be evaluated using the following formula

$$\text{Cor}(\theta_i, \theta_j) = \left| \frac{F^{-1}(i,j)}{\sqrt{F^{-1}(i,i)}\sqrt{F^{-1}(j,j)}} \right|, \text{ for } (i,j) \in \{1,2,3\}^2 \tag{3.44}$$

where $\boldsymbol{F}^{-1}$ denotes the inverse of the FIM (the inverse of $\boldsymbol{F}_c$ for CA3 and $\boldsymbol{F}_d$ for DDA3). Fig. 3.16 shows that the correlation between (SWH, τ) is less important for DDA3 which is a great advantage for DDA3. Indeed, the parameter correlation is not desired as stated in [Sandwell and Smith, 2005] which has proposed an algorithm to reduce it in the case of CA. A similar correlation reduction

is observed between (τ, P_u) while the reduction is only observed for small SWH when considering (SWH, P_u). These results confirm the superiority of DDA in terms of the quality of the estimated parameters.

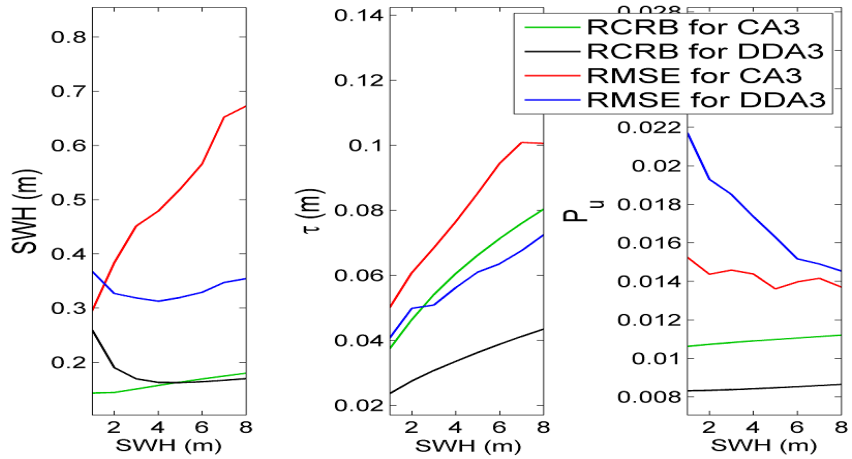

Figure 3.15: RCRBs and RMSEs for delay/Doppler altimetry (DDA3) and conventional altimetry (CA3) versus SWH with $P_u = 1$ and $\tau = 31$ gates (1000 Monte-Carlo realizations).

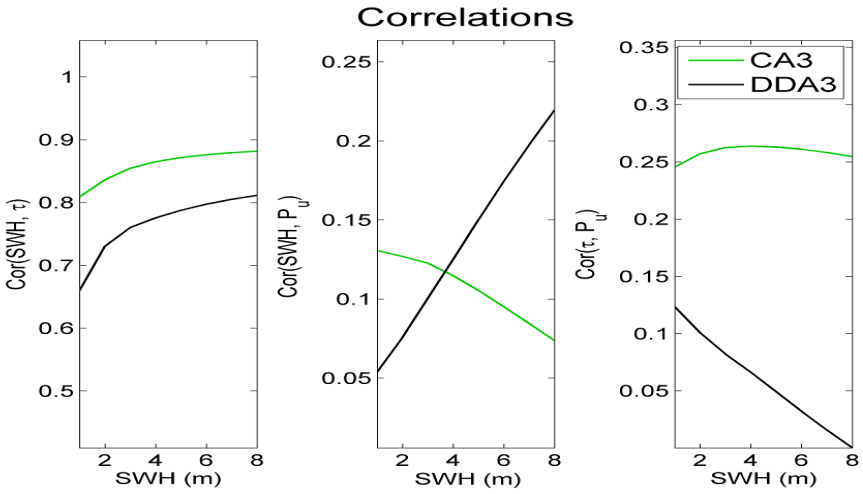

Figure 3.16: Theoretical parameter correlations for delay/Doppler altimetry (DDA3) and conventional altimetry (CA3) versus SWH with $P_u = 1$ and $\tau = 31$ gates.

3.7 Results for CRYOSAT-2 waveforms

This section is devoted to the validation of the proposed semi-analytical model for oceanic Cryosat-2 waveforms. The considered waveforms were obtained in August 2011 (the estimation was applied to the whole month of data) and were provided by the Cryosat processing prototype developed by CNES which is doing the level 1 processing and in particular the Doppler, range migration and multi-looking processings [Boy et al., 2012]. The estimated parameters of DD echoes are first compared to the results obtained with a 3 parameter estimator designed for CA-SARM3 echoes[9]. This will provide a good evaluation of the proposed delay/Doppler model. Figs. 3.17 shows examples of estimated Cryosat-2 echoes using the proposed model for different values of SWH. The top figures show a good fit between these two echoes especially in the leading and trailing edges of the waveform. This result is confirmed when considering the bottom figures which show the error (difference) between both echoes. Note that the maximum difference between the real echo and its estimation is of the order of 10 % which is a small value due to the presence of noise. Table 3.2 shows the ANREs obtained for different classes of SWH values when estimating Cryosat-2 echoes. This table shows small values of ANRE which confirms the good fitting of the proposed model.

Table 3.2: Averaged normalized reconstruction errors for Cryosat-2 echoes.

SWH (m)	$[0,1]$	$[1,2]$	$[2,3]$	$[3,4]$	$[4,5]$	$[5,6]$	$[6,7]$
ANRE ($\times 10^{-2}$)	8.55	8.86	9.56	10.01	10.33	10.42	10.51

[9] The parameters of CA-SARM3 echoes were estimated by the least squares procedure described in Section 3.4.1, where $s_k(\boldsymbol{\theta})$ is defined by (1.5).

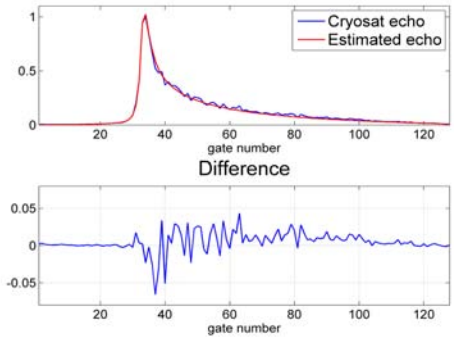

(a) SWH = 0.57 m and NRE = 0.07.

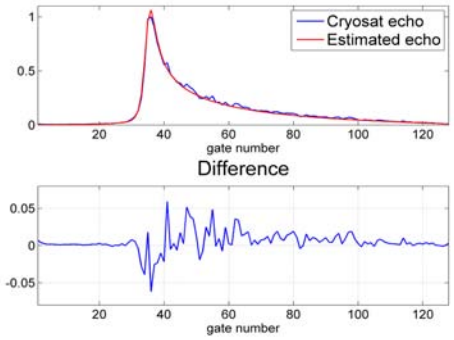

(b) SWH = 1.56 m and NRE = 0.065.

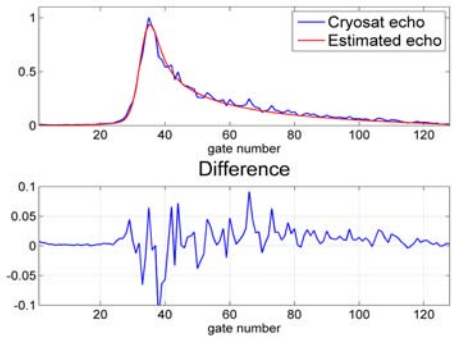

(c) SWH = 3.6 m and NRE = 0.12.

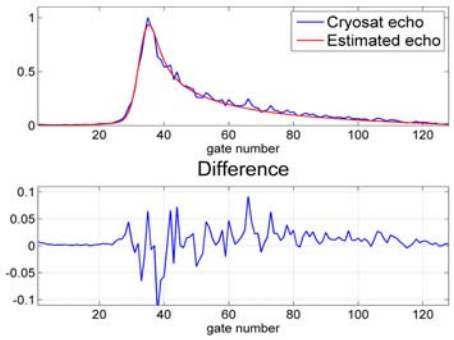

(d) SWH = 3.92 m and NRE = 0.101.

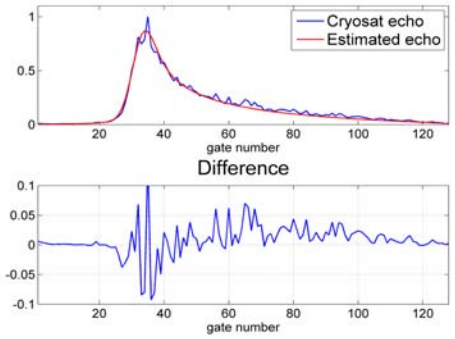

(e) SWH = 5.26 m and NRE = 0.112.

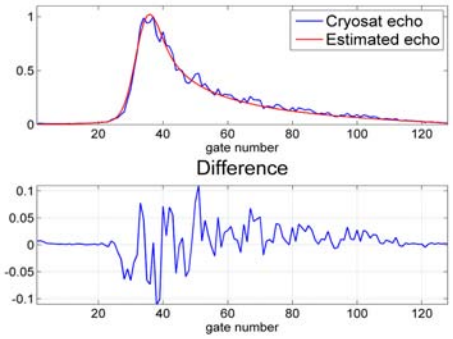

(f) SWH = 5.84 m and NRE = 0.102.

Figure 3.17: Examples of estimated Cryosat-2 echoes and corresponding normalized reconstruction errors (NRE) for different values of SWH.

Considering the estimated parameters, the good agreement between the estimated DDA3 and CA-SARM3 parameters is illustrated in Fig. 3.18 which shows the estimated SWH and sea surface height anomaly (SSHA) parameters for 2 minutes of data (the SSHA is obtained by applying all environmental corrections on the estimated epoch). This agreement is confirmed in Fig. 3.19 showing similar correlations between the estimated SWH and SSHA using the two estimation procedures.

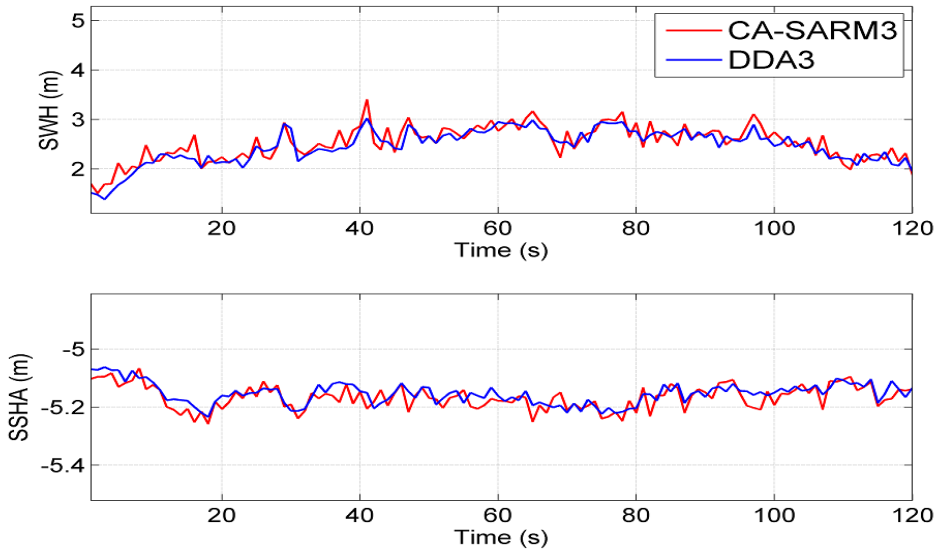

Figure 3.18: Parameter estimates for 2 minutes of Cryosat-2 data using DDA3 and CA-SARM3. (top) SWH (bottom) SSHA.

Table 3.3 shows the averaged differences between the estimated parameters of CA-SARM3 and DDA3. These results are represented for SWH < 4 m since more than 90% of the processed data satisfy this constraint. The differences between the CA-SARM3 and DDA3 estimation are very low. Table 3.3 also shows the averaged STDs[10] for parameters SWH and SSHA. These STDs have been obtained by considering groups of $N_{\mathrm{MC}} = 20$ successive parameters (see (3.29)), i.e., one value of STD is obtained every second (the resulting STDs are known as 20 Hz STDs[11]). As expected, DDA3 provides lower STDs than CA-SARM3 which is in agreement with the results of Section 3.6.5. Note

[10] The averaged STDs have been obtained by averaging the obtained STDs for each 1 meter interval of SWH.
[11] The 1 Hz STDs can be deduced from the 20 Hz STDs by dividing all results by the factor $\sqrt{20}$.

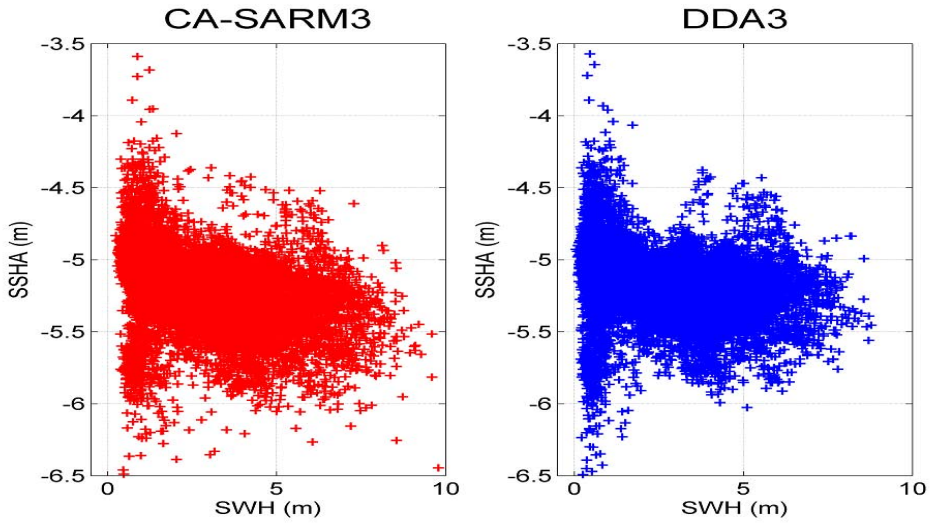

Figure 3.19: Correlations between estimated SWH and SSHA parameters for CA-SARM3 (left) and DDA3 (right).

that the equivalent CA3 STDs can be obtained by dividing the CA-SARM3 STDs by a factor of $\sqrt{3}$ as explained previously. This provides a good evaluation of DDA3 when compared to CA3 (used in the previous altimeters such as in Poseidon-3). The STD improvement can be evaluated by computing the ratio between the CA3 STDs and the DDA3 STDs (referred to as improvement factor in Table 3.4). At SWH = 2 m, we obtain an SWH STD of 55 cm for CA3 and of 43 cm for DDA3 which shows an improvement factor of 1.28. Considering SSHA, we notice a CA3 STD of 8.16 cm and a DDA3 STD of 6.47 cm resulting in an improvement factor of about 1.26. Table 3.4 compares these improvement factors with results available in the literature. The obtained results are clearly in good agreement with those of [Giles et al., 2012, Gommenginger et al., 2011a] (the small differences are due to the fact that it is not possible to reproduce exactly the same simulation scenario).

Note finally that the STD results presented in Table 3.3 are similar to those obtained in the simulation (see Fig. 3.15) where we have obtained better results for DDA3 altimetry except for small values of SWH where CA3 performs slightly better. The improvement factors are also in agreement with those of simulated waveforms since we have obtained 1.24 for τ and 1.19 for SWH at SWH = 2 m. These similarities between simulated and real data results validate the proposed model.

Table 3.3: Comparison between the estimated parameters of CA-SARM3 and DDA3.

		SWH intervals (m)			
		$[0,1]$ m	$[1,2]$ m	$[2,3]$ m	$[3,4]$ m
Averaged difference between CA-SARM3 and DDA3	SWH (m)	0.21	0.24	0.19	0.17
	SSHA (cm)	1.34	−0.68	−2.15	−3.70
STD(SWH) at 20Hz (m)	DDA3	0.46	0.43	0.43	0.46
	CA-SARM3	0.73	0.92	0.97	0.97
	equivalent CA3	0.42	0.53	0.56	0.56
STD(SSHA) at 20Hz (cm)	DDA3	6.32	5.97	6.87	7.96
	CA-SARM3	11.15	13.11	14.88	16.05
	equivalent CA3	6.44	7.57	8.59	9.27

Table 3.4: Improvement factors of DDA3 with respect to CA3.

	Studies		
	This study	[Giles et al., 2012]	[Gommenginger et al., 2011a]
SSHA	1.26	1.18	1.43
SWH	1.28	1.31	1.26

3.8 Conclusions

This chapter defined a new semi-analytical model for delay/Doppler altimetry. A geometrical approach was used for computing an analytical expression of the flat surface impulse response. The analytical expression was obtained assuming a circular antenna pattern, no mispointing, no vertical speed effect and a uniform scattering. This analytical expression was convolved with the probability density function of the heights of the specular scatterers and the point target response of the radar leading to the mean power of a delay/Doppler altimetric waveform. A least squares approach based on the Levenberg-Marquardt algorithm was then proposed to estimate the parameters of delay/Doppler altimetric echoes. The Cramér-Rao bounds were also derived to provide a reference in terms of estimation performance. These bounds were used to evaluate the performance of the proposed estimation strategy and to compare it with other estimation procedures such as the maximum likelihood estimator and the weighted least squares procedure (derived in Appendix I). Simulation results performed on simulated data showed the importance of range migration and that of the central Doppler beams that contain most of the information. It also showed the good potential of delay/Doppler altimetry when compared to conventional altimetry in terms of error reduction. The analysis of real Cryosat-2 waveforms confirmed the good performance of the proposed delay/Doppler model. Extending the results obtained in this chapter to a model including the mispointing angles is an interesting issue since the Cryosat-2 echoes are known to present a mispointing of about 0.1 degree in across-track and along-track directions [Smith and Scharroo, 2011]. This generalization is considered in the next chapter.

Contributions

A three parameter semi-analytical model was proposed for delay/Doppler altimetry [Halimi et al., 2012, 2013b,e]. The related estimation strategy is based on a least squares criterion. The Cramér-Rao lower bounds of the model parameters were then derived in order to evaluate the performance of the proposed least squares estimation procedure [Halimi et al., 2013a]. The proposed model was validated using synthetic and real Cryosat-2 data.

3.9 Conclusions (in French)

Ce chapitre a introduit un nouveau modèle semi-analytique pour l'altimétrie SAR/Doppler. Le modèle proposé est basé sur une approche géométrique pour le calcul de la réponse impulsionnelle d'une mer plate. L'expression analytique a été obtenue en supposant un diagramme d'antenne circulaire sans dépointage, aucun effet de la vitesse verticale du satellite et un coefficient de rétrodiffusion constant dans la surface observée. La puissance moyenne de l'écho SAR/Doppler est alors obtenue en convoluant numériquement la formule analytique proposée avec la densité de probabilité de la hauteur des points de dispersion et la réponse impulsionnelle du radar. L'estimation des paramètres altimétriques est effectuée à l'aide de la méthode des moindres carrés en utilisant l'algorithme de Levenberg-Marquardt. Les bornes de Cramér-Rao ont aussi été développées afin de fournir une référence pour l'évaluation de la qualité d'estimation. Ces bornes ont été utilisées pour évaluer la méthode d'estimation proposée et la comparer avec d'autres méthodes d'estimation comme celle du maximum de vraisemblance et celle basée sur un critère des moindres carrés pondérés (voir l'annexe I). L'étude des signaux synthétiques a montré l'intérêt du traitement de migration en distance ainsi que l'importance des bandes Doppler centrales qui contiennent la majorité de l'information. Cette étude a aussi montré la supériorité de l'altimétrie SAR/Doppler par rapport à l'altimétrie conventionnelle en termes de réduction de l'erreur d'estimation. Cette supériorité a été confirmée par l'analyse d'échos réels issus du satellite Cryosat-2. La généralisation du modèle proposé afin de tenir compte du dépointage de l'antenne est une piste intéressante. En effet, l'étude effectuée dans [Smith and Scharroo, 2011] montre l'existence d'un dépointage de l'antenne de l'ordre de 0.1 degré dans les directions azimutale et transverse. Cette généralisation est considérée dans le chapitre suivant.

Contributions

Un modèle semi-analytique à trois paramètres est proposé pour l'altimétrie SAR/Doppler [Halimi et al., 2012, 2013b,e]. La stratégie d'estimation s'appuie sur un critère des moindres carrés. Les bornes inférieures de Cramér-Rao sont ensuite établies afin d'évaluer les performances de la procédure d'estimation par moindres carrés [Halimi et al., 2013a]. Le modèle proposé est validé sur des données synthétiques ainsi que sur des données réelles fournies par le satellite Cryosat-2.

Chapter 4

Generalized semi-analytical model for delay/Doppler altimetry

Contents

4.1 Introduction (in French)

Comme expliqué dans le chapitre précédent, la puissance moyenne d'un écho SAR/Doppler est exprimée par une convolution entre trois termes qui sont la PDF de la hauteur des diffuseurs spéculaires, la PTR et la FSIR [Martin-Puig and Ruffini, 2009, Phalippou and Demeestere, 2011]. La FSIR constitue le terme le plus important car elle comprend les informations de forme sur l'écho altimétrique

résultant. Ce terme a été approximé numériquement dans [Phalippou and Enjolras, 2007, Shuang-Bao et al., 2011] (plus exactement, c'est la double convolution qui a été approximée numériquement) alors qu'un modèle analytique a été proposé dans le chapitre 3. Cependant, le modèle développé dans le chapitre 3 ne tient pas compte du dépointage de l'antenne ce qui peut conduire à une réduction des performances d'estimation.

La première contribution de ce chapitre est le développement d'un modèle analytique généralisé pour la FSIR qui tient compte du dépointage de l'antenne. L'expression analytique proposée considère également la courbure de la Terre, un diagramme d'antenne circulaire et une approximation gaussienne pour le gain de l'antenne comme dans [Brown, 1977, Halimi et al., 2013e]. Cette expression analytique est obtenue moyennant deux approximations qui sont analysées et justifiées. En effet, l'erreur entre la FSIR exacte et la formule analytique proposée a été bornée par une formule analytique. La carte distance/Doppler est ensuite obtenue en calculant la numériquement la double convolution entre la FSIR proposée, la PDF de la hauteur des diffuseurs spéculaires et la PTR. Cette carte dépend de cinq paramètres altimétriques qui sont l'époque τ, la hauteur des vagues SWH, l'amplitude P_u, l'angle de dépointage azimutal ξ_{al} et l'angle de dépointage transverse ξ_{ac}. Un traitement approprié, qui comprend la migration des distances et le moyennage, est ensuite appliqué à la carte distance/Doppler afin d'obtenir l'écho SAR/Doppler. Le comportement de cet écho est par la suite étudié en fonction de la direction du dépointage de l'antenne. En effet, l'effet du dépointage diffère suivant le principe altimétrique utilisé qui peut être à impulsion limitée ou à faisceau limité [Chelton, 1989, Raney and Phalippou, 2011]. L'étude du dépointage est alors effectuée en séparant les deux directions azimutale et transverse puisque l'altimétrie SAR/Doppler est à faisceau limité dans la direction azimutale et à impulsion limitée dans la direction transverse [Raney, 1998].

La deuxième contribution de ce chapitre porte sur l'estimation des paramétriques altimétriques de l'écho SAR/Doppler. Cette estimation peut être obtenue en utilisant le principe du maximum de vraisemblance [Rodriguez, 1988] ou des moindres carrés [Maus et al., 1998, Sandwell and Smith, 2005]. On utilisera dans cette étude, comme dans le chapitre 3, un algorithme de Levenberg-Marquardt pour optimiser le critère des moindres carrés. Ceci dit, l'analyse de l'effet du dépointage de l'antenne fait apparaître une forte corrélation entre le dépointage azimutal et l'amplitude. Ainsi, il s'est avéré

intéressant de proposer une stratégie d'estimation à quatre paramètres plutôt que l'estimation des cinq paramètres d'intérêt. Ces stratégies d'estimation sont par la suite évaluées en comparant leurs résultats d'estimation avec ceux du modèle à trois paramètres (proposé dans le chapitre précédent) et ceux obtenus en utilisant l'altimétrie conventionnelle. L'analyse des résultats d'estimation sur échos synthétiques et réels montre une nette amélioration de la qualité des paramètres estimés et confirme de ce fait la pertinence du modèle proposé.

Le chapitre est organisé comme suit. La section 4.3 présente le modèle semi-analytique généralisé pour l'altimétrie SAR/Doppler. L'algorithme d'estimation par moindres carrés ainsi que les critères d'évaluation des performances sont ensuite introduits dans la section 4.4. La première partie de la section 4.5 justifie les approximations utilisées pour obtenir la FSIR analytique. La deuxième partie analyse le comportement du modèle proposé suivant le dépointage de l'antenne. La troisième et dernière partie valide le modèle proposé et les algorithmes d'estimation associés sur des données synthétiques. L'analyse des résultats obtenus sur données réelles de Cryosat-2 est présentée dans la section 4.6. Les conclusions et les perspectives sont finalement présentées dans les sections 4.7 et 4.8.

4.2 Introduction

As explained in the previous chapter, the mean power of a delay/Doppler echo is expressed by a convolution of three terms that are the PDF of the heights of the specular scatterers, the time/frequency PTR of the radar and the FSIR [Martin-Puig and Ruffini, 2009, Phalippou and Demeestere, 2011]. The FSIR is the most important term since it includes the shape information about the resulting altimetric echo. This term has been approximated numerically in [Phalippou and Enjolras, 2007, Shuang-Bao et al., 2011] (more exactly, the double convolution echo was expressed numerically) whereas an analytical model was proposed in Chapter 3. However, the model developed in Chapter 3 did not take into account any antenna mispointing which may lead to reduced estimation performance.

The first contribution of this chapter is the derivation of a generalized analytical model for the FSIR that accounts for antenna mispointing. The proposed analytical expression for the FSIR also considers Earth curvature, a circular antenna pattern and a Gaussian approximation for the antenna gain as in [Brown, 1977, Halimi et al., 2013e]. This analytical expression is established using two approximations that are analyzed and justified by deriving an upper bound for the error between the actual FSIR and its approximation. The two dimensional delay/Doppler map (DDM) is then obtained by a numerical computation of the convolution between the proposed analytical FSIR expression, the PDF of the sea wave height and the time/frequency PTR. The resulting DDM depends on five altimetric parameters that are the epoch τ, the significant wave height SWH, the amplitude P_u, the along-track mispointing angle ξ_{al} and the across-track mispointing angle ξ_{ac}. Appropriate processing, including range migration and multi-looking, is applied to the resulting DDM yielding the multi-look echo. The behavior of this echo is analyzed as a function of the direction of antenna mispointing. The mispointing has a different behavior on beam-limited and pulse-limited altimetry [Chelton, 1989, Raney and Phalippou, 2011] and the DDA is pulse-limited across-track and beam-limited along-track [Raney, 1998]. Thus, our study has been conducted by separating along-track and across-track mispointing angles.

The second contribution of this chapter is the derivation of estimators for the parameters associated with the multi-look echo. This estimation can be achieved using the maximum likelihood

principle [Rodriguez, 1988] or least squares techniques [Maus et al., 1998, Sandwell and Smith, 2005]. As in Chapter 3, this chapter considers a least squares technique based on a Levenberg-Marquardt algorithm for parameter estimation. However, the study of the effect of antenna mispointing will show high correlation between the along-track mispointing and the echo's amplitude. Thus, it will be interesting to propose a four parameter estimation strategy rather than the mere estimation of the five parameters of interest. In order to evaluate these strategies, we compare their estimation performance to that obtained using the three parameter model derived in the previous chapter and to CA. Validation of the proposed model and the corresponding algorithms is achieved on simulated and real Cryosat-2 data. The obtained results are very promising and confirm the accuracy of the proposed model.

The chapter is organized as follows. Section 4.3 presents the generalized semi-analytical model for delay/Doppler altimetry. The least squares estimation algorithms and the criteria for performance evaluation are then introduced in Section 4.4. Section 4.5 first justifies the approximations used to obtain the analytical FSIR. Second, it analyzes the behavior of the proposed model according to antenna mispointing. Third, it validates the proposed model and estimation algorithms with simulated data. The analysis of results obtained with Cryosat-2 data is presented in Section 4.6. Conclusions and future work are finally reported in Section 4.7.

4.3 Generalized semi-analytical model for delay/Doppler altimetry

This section recalls briefly the CA4 model and introduces the proposed semi-analytical model for delay/Doppler waveforms. The interest of this model compared to that of the previous chapter is that it includes parameters related to antenna mispointing.

4.3.1 Conventional altimetry (CA4)

This section recalls the conventional altimetric model when considering antenna mispointing. This model is expressed as the convolution between the FSIR, the PDF and the PTR as follows

$$s(t) = \mathrm{FSIR}(t) * \mathrm{PDF}(t) * \mathrm{PTR}_T(t) \tag{4.1}$$

with

$$\mathrm{FSIR}(t) = P_u \exp\left[-\chi t - \frac{4}{\gamma}\sin^2\xi\right] I_0\left(\beta\sqrt{t}\right) U(t) \tag{4.2a}$$

$$\mathrm{PDF}(t) = \frac{1}{\sqrt{2\pi}\sigma_s}\exp\left(-\frac{t^2}{2\sigma_s^2}\right) \tag{4.2b}$$

$$\mathrm{PTR}_T(t) = \left|\frac{\sin\left(\pi\frac{t}{T_s}\right)}{\pi\frac{t}{T_s}}\right|^2 \tag{4.2c}$$

where χ and β have been defined in (1.8), γ is a parameter related to the antenna aperture and T_s is the sampling period. The resulting model is denoted by CA4 since it depends on four altimetric parameters that are SWH (through $\sigma_s = \frac{\mathrm{SWH}}{2c}$), τ, P_u and ξ.

4.3.2 The delay/Doppler convolution model

The mean power of a delay/Doppler echo can be expressed as the convolution of three terms: the FSIR, the PDF of the heights of the specular scatterers and the time/frequency PTR of the radar as follows [Martin-Puig and Ruffini, 2009, Phalippou and Demeestere, 2011]

$$P(t,f) = \mathrm{FSIR}(t,f) * \mathrm{PDF}(t) * \mathrm{PTR}(t,f) \tag{4.3}$$

with

$$\mathrm{PDF}(t) = \frac{1}{\sqrt{2\pi}\sigma_s}\exp\left(-\frac{t^2}{2\sigma_s^2}\right) \tag{4.4a}$$

$$\mathrm{PTR}(t,f) = \mathrm{PTR}_T(t)\mathrm{PTR}_F(f) \tag{4.4b}$$

$$\mathrm{PTR}_T(t) = \left|\frac{\sin\left(\pi\frac{t}{T_s}\right)}{\pi\frac{t}{T_s}}\right|^2, \qquad \mathrm{PTR}_F(f) = \left|\frac{\sin\left(\pi\frac{f}{F}\right)}{\pi\frac{f}{F}}\right|^2. \tag{4.4c}$$

An analytical expression for the first term (FSIR) is derived in the following subsection.

4.3.3 The proposed analytical model for FSIR

In conventional altimetry, the FSIR depends only on time and is obtained by integrating the power of the backscattered altimetric echo over the illuminated area of the surface as follows [Brown, 1977]

$$\mathrm{FSIR}(t') = \frac{\lambda^2}{(4\pi)^3 L_p} \int_{\mathbb{R}^+ \times [0,2\pi[} \frac{\delta(t' - \frac{2r}{c}) G^2(\rho,\phi)\sigma^0}{r^4} \rho d\rho d\phi \tag{4.5}$$

As already detailed in Section 1.3.2. The delay/Doppler altimeter was proposed in order to increase the along-track resolution by considering the Doppler effect resulting from the satellite velocity. The corresponding FSIR is then obtained by integrating over each Doppler beam. The nth Doppler beam at time instant t depicted in Fig. 4.1 is characterized by an angle ϕ varying in the interval $D_{t,n} = [\phi_{t,n}, \phi_{t,n+1}] \cup [\phi'_{t,n}, \phi'_{t,n+1}]$ leading to

$$\mathrm{FSIR}(t', n) = \frac{\lambda^2}{(4\pi)^3 L_p} \int_{\mathbb{R}^+ \times D_{t,n}} \frac{\delta(t' - \frac{2r}{c}) G^2(\rho,\phi)\sigma^0}{r^4} \rho d\rho d\phi. \tag{4.6}$$

The integral with respect to ρ in (4.6) can be computed analytically by considering a Gaussian

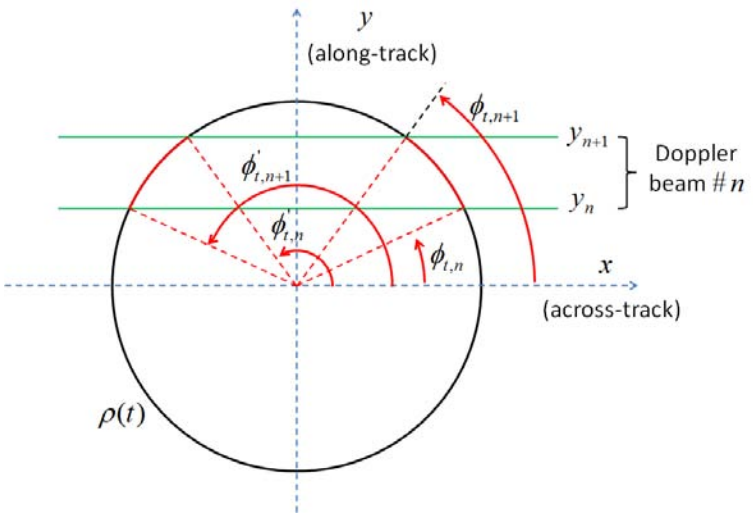

Figure 4.1: Integrating angles for a given circle of propagation and a specific Doppler beam.

approximation for the antenna gain and $\frac{ct}{h} << 1$ (as in [Brown, 1977]). The following result is

obtained

$$\mathrm{FSIR}(t,n) = \frac{P_u}{2\pi}\left(1+\frac{ct}{2h}\right)^{-3} U\left(t\right) \times \left\{ \int_{\phi_{t,n}}^{\phi_{t,n+1}} \exp\left\{ f\left[\tilde{\phi}-\phi,\epsilon(t),\xi\right]\right\} d\phi + \int_{\phi'_{t,n}}^{\phi'_{t,n+1}} \exp\left\{ f\left[\tilde{\phi}-\phi,\epsilon(t),\xi\right]\right\} d\phi \right\} \tag{4.7}$$

where ξ and $\tilde{\phi}$ denote mispointing angles with respect to the z axis and the x axis respectively (see Fig. 1.6) and

$$f\left[\tilde{\phi}-\phi,\epsilon(t),\xi\right] = -\frac{4}{\gamma}\left[1-\frac{\cos^2\left(\xi\right)}{1+\epsilon^2(t)}\right] + b(t,\xi) + a(t,\xi)\cos\left(\tilde{\phi}-\phi\right) - b(t,\xi)\sin^2\left(\tilde{\phi}-\phi\right) \tag{4.8}$$

with

$$\begin{aligned}
\epsilon^2(t) &= \left(\frac{\rho}{h}\right)^2 \simeq \frac{ct}{h} \\
P_u &= \frac{\lambda^2 G_0^2 c\sigma^0}{4(4\pi)^2 L_p h^3} \\
a(t,\xi) &= \frac{4\epsilon(t)}{\gamma}\frac{\sin(2\xi)}{1+\epsilon^2(t)} \\
b(t,\xi) &= \frac{4\epsilon^2(t)}{\gamma}\frac{\sin^2(\xi)}{1+\epsilon^2(t)} \\
\phi_{t,n} &= \mathrm{Re}\left[\mathrm{atan}\left(\frac{y_n}{\sqrt{\rho^2(t)-y_n^2}}\right)\right] = \pi - \phi'_{t,n+1} \\
\phi_{t,n+1} &= \mathrm{Re}\left[\mathrm{atan}\left(\frac{y_{n+1}}{\sqrt{\rho^2(t)-y_{n+1}^2}}\right)\right] = \pi - \phi'_{t,n} \\
y_n &= \frac{h\lambda}{2v_s} f_n.
\end{aligned} \tag{4.9}$$

In the above notations, $f_n = (n - 32N_f - 0.5)\frac{F}{N_f}$, with $n \in \{1, \cdots, 64N_f\}$, is the nth Doppler frequency[1], N_f is the frequency oversampling factor, G_0 is the antenna power gain at boresight, $\gamma = \frac{1}{2\ln 2}\sin^2\theta_{3\mathrm{dB}}$ is an antenna beam width parameter, $\theta_{3\mathrm{dB}}$ is the half-power antenna beam width, y_n is the coordinate of the nth along-track beam, v_s is the satellite velocity and $\mathrm{Re}(x)$ denotes the real part of the complex number x. In the previous chapter, an analytical expression of $\mathrm{FSIR}(t,n)$

[1]We considered the case of $N = 64$ Doppler beams that results from the emission of $N = 64$ pulses per burst.

was derived by considering the case of an antenna without mispointing angle, i.e., $\xi = 0°$. In the present chapter, the case of a non-zero mispointing angle ξ is taken into consideration.

A change of variables $u = \tilde{\phi} - \phi$ in (4.7) leads to

$$\begin{aligned}\mathrm{FSIR}(t,n) = \frac{P_u}{2\pi}\left(1+\frac{ct}{2h}\right)^{-3} U\left(t\right)\exp\left\{-\frac{4}{\gamma}\left[1-\frac{\cos^2\left(\xi\right)}{1+\epsilon^2(t)}\right]+b(t,\xi)\right\} \\ \left[Q\left(\tilde{\phi}-\phi_{t,n+1},\tilde{\phi}-\phi_{t,n}\right)+Q\left(\tilde{\phi}-\phi'_{t,n+1},\tilde{\phi}-\phi'_{t,n}\right)\right]\end{aligned} \tag{4.10}$$

with

$$Q\left(u_1,u_2\right) = \exp\left(-\frac{b}{2}\right)\int_{u_1}^{u_2}\exp\left[a\cos\left(u\right)+\frac{b}{2}\cos\left(2\,u\right)\right]du \tag{4.11}$$

where the parameters (t,ξ) in a and b are omitted for brevity. Using the results of [Abramowitz and Stegun, 1965, p. 376] (see equation (9.6.34)), the following expressions are obtained

$$\begin{aligned}\exp\left[a\cos(u)\right] &= I_0(a)+2\sum_{k=1}^{+\infty}I_k(a)\cos(ku) \\ \exp\left[\frac{b}{2}\cos(2u)\right] &= I_0\left(\frac{b}{2}\right)+2\sum_{k=1}^{+\infty}I_k\left(\frac{b}{2}\right)\cos(2ku)\end{aligned} \tag{4.12}$$

where I_k is the kth order modified Bessel function of the first kind.

First approximation

The infinite sum of Bessel functions appearing in (4.12) can be reduced to

$$\exp\left[\frac{b}{2}\cos(2u)\right] \simeq I_0\left(\frac{b}{2}\right) \tag{4.13}$$

with a small loss of accuracy because of the very small values of the positive variable b. Indeed, the zero order Bessel function is sufficient to approximate this sum since the maximum value of $b(t,\xi)$ (considering a pessimistic case $\xi = 1$ degree) is less than 8×10^{-4}. The error associated with this value of b is upper bounded as follows

$$\left|\exp\left[\frac{b}{2}\cos(2u)\right]-I_0\left(\frac{b}{2}\right)\right| \leq \left|\exp\left(\frac{b}{2}\right)-I_0\left(\frac{b}{2}\right)\right| = 4\times10^{-4}, \forall u \tag{4.14}$$

which is a negligible error since it represents 0.04% of $\exp\left(\frac{b}{2}\right)$ (this approximation will be further justified in the rest of the chapter). By using (4.13), we obtain the approximation $\mathrm{FSIR}(t,n) \simeq \mathrm{FSIR}_1(t,n)$ where

$$\mathrm{FSIR}_1(t,n) = \frac{P_u}{\pi}\left(1+\frac{ct}{2h}\right)^{-3} U(t) \exp\left[-\frac{4}{\gamma}\left(1-\frac{\cos^2(\xi)}{1+\epsilon^2(t)}\right)+\frac{b}{2}\right] I_0\left(\frac{b}{2}\right) \times \left[I_0(a)\left(\phi_{t,n+1}-\phi_{t,n}\right)+\sum_{k=1}^{+\infty}\frac{1}{k} I_k(a)\, h_{k,n}(\tilde{\phi})\right] \tag{4.15}$$

and

$$h_{k,n}(\tilde{\phi}) = \sin\left[k\left(\tilde{\phi}-\phi_{t,n}\right)\right] - \sin\left[k\left(\tilde{\phi}-\phi_{t,n+1}\right)\right] + \sin\left[k\left(\tilde{\phi}-\phi'_{t,n}\right)\right] - \sin\left[k\left(\tilde{\phi}-\phi'_{t,n+1}\right)\right]. \tag{4.16}$$

Using the relations $\phi_{t,n} = \pi - \phi'_{t,n+1}$ and $\phi_{t,n+1} = \pi - \phi'_{t,n}$, straightforward computations allow $h_{k,n}(\tilde{\phi})$ to be expressed as

$$h_{k,n}(\tilde{\phi}) = \begin{cases} 2\cos\left(k\tilde{\phi}\right)\left[\sin\left(k\phi_{t,n+1}\right)-\sin\left(k\phi_{t,n}\right)\right], & \text{for even } k \\ -2\sin\left(k\tilde{\phi}\right)\left[\cos\left(k\phi_{t,n+1}\right)-\cos\left(k\phi_{t,n}\right)\right], & \text{for odd } k \end{cases}. \tag{4.17}$$

Second approximation

The infinite sum in (4.15) can be truncated by keeping a finite number m of elements according to the desired precision. The FSIR including the mispointing angles ξ and $\tilde{\phi}$ can be finally approximated as $\mathrm{FSIR}(t,n) \simeq \mathrm{FSIR}_2(t,n)$ where

$$\mathrm{FSIR}_2(t,n) = \frac{P_u}{\pi}\left(1+\frac{ct}{2h}\right)^{-3} U(t) \exp\left[-\frac{4}{\gamma}\left(1-\frac{\cos^2(\xi)}{1+\epsilon^2(t)}\right)+\frac{b}{2}\right] I_0\left(\frac{b}{2}\right) \times \left[I_0(a)\left(\phi_{t,n+1}-\phi_{t,n}\right)+\sum_{k=1}^{m}\frac{1}{k} I_k(a)\, h_{k,n}(\tilde{\phi})\right] \tag{4.18}$$

where $\left(1+\frac{ct}{2h}\right)^{-3}$ can be approximated by 1 as in [Brown, 1977]. Note that the proposed model (4.18) reduces to the model of Chapter 3 for $\xi = 0°$ (absence of mispointing angle) since $a(t,\xi=0) = b(t,\xi=0) = 0$. Finally, the Earth curvature can be introduced by dividing the time t in (4.18) by the curvature factor $\alpha_r = 1+\frac{h}{R} = 1.11$ [Chelton, 1989, Halimi et al., 2013e, MacArthur, 1976].

4.3.4 The multi-look echo

The reflected power $P(t,f)$ associated with a DDM is finally obtained by a numerical computation of the double convolution (4.3) where $\mathrm{FSIR}(t,f)$ is approximated by the analytical expression (4.18) and $\mathrm{PDF}(t)$, $\mathrm{PTR}(t,f)$ are given in (4.4)[2]. This convolution has to be computed after applying appropriate time and frequency oversampling, a time shift by the epoch τ_s and an undersampling as in Chapter 3. The multi-look echo is then formed by summing the migrated Doppler beams as follows

$$s(t) = \sum_{n=1}^{N} P_2\left(t - \delta t_n, f_n\right) \tag{4.19}$$

where $P_2(t,f) = \mathrm{FSIR}_2(t,f) * \mathrm{PDF}(t) * \mathrm{PTR}(t,f)$ and $\delta t_n \simeq \alpha_r \frac{h\lambda^2}{4cv_s^2} f_n^2$ is the delay compensation expressed in seconds. Note that the proposed model is parameterized by the parameter vector $\boldsymbol{\theta} = (\mathrm{SWH}, P_u, \tau, \xi_{\mathrm{ac}}, \xi_{\mathrm{al}})^T$ where ξ_{ac} and ξ_{al} denote the across-track and along-track mispointing angles defined as (see also Fig. 4.2)

$$\xi_{\mathrm{al}} = \xi \sin\left(\tilde{\phi}\right) \text{ and } \xi_{\mathrm{ac}} = \xi \cos\left(\tilde{\phi}\right). \tag{4.20}$$

An example of reflected power $P(t,f)$ is displayed in Fig. 4.3 (left) for 64 Doppler beams, 128 gates, the altimetric parameters $P_u = 1$, $\mathrm{SWH} = 1$ m, $\tau = 44$ gates and $\xi_{\mathrm{al}} = \xi_{\mathrm{ac}} = 0.1°$. This figure shows a parabolic shape of the waveform resulting from the increasing slant range when going away from the central nadir beam. Fig. 4.3 (middle) shows an example of a DDM obtained after range migration whereas Fig. 4.3 (right) shows the resulting multi-look echo obtained after summing the contributions of the migrated Doppler beams. Note finally that the discrete multi-look echo is gathered in the vector $\boldsymbol{s} = (s_1, \cdots, s_K)^T$, where $K = 128$ is the number of samples (or so-called "gates").

[2]Note that the proposed model allows the use of other models for PDF and PTR. For instance, a PDF including the skewness could be used to better represent the distribution of the heights of the specular scatterers. Moreover, a measured PTR could also be used instead of (4.4).

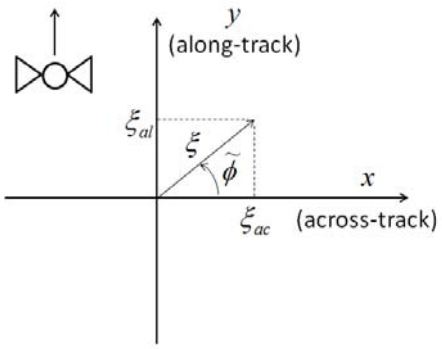

Figure 4.2: Relation between the parameters ξ and $\tilde{\phi}$ and the along-track and across-track mispointing angles ξ_{al} and ξ_{ac}.

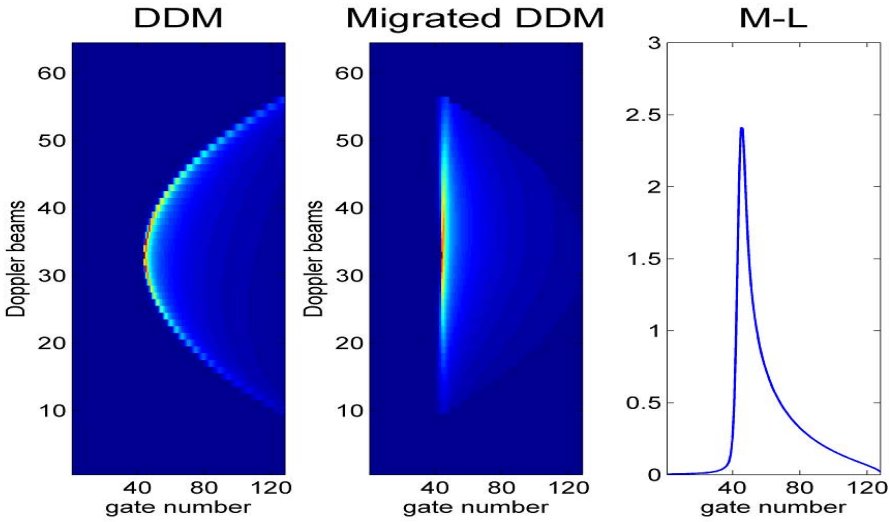

Figure 4.3: Construction of a multi-look waveform. (left) a delay/Doppler map (DDM), (middle) DDM after range migration, and (right) multi-look (M-L) echo.

4.4 Parameter estimation

4.4.1 Estimation algorithm

As in Chapter 3, the estimation of the multi-look waveform is achieved by a least squares procedure, i.e., by minimizing the following criterion

$$\mathcal{C} = \underset{\boldsymbol{\theta}}{\operatorname{argmin}} \frac{1}{2} \sum_{k=1}^{K} g_k^2(\boldsymbol{\theta}) \tag{4.21}$$

where $g_k(\boldsymbol{\theta}) = y_k - s_k(\boldsymbol{\theta})$ is the vector of residues, $\boldsymbol{y} = (y_1, \ldots, y_K)^T$ is a noisy version of $\boldsymbol{s} = (s_1, \ldots, s_K)^T$ which depends on the parameter vector of interest $\boldsymbol{\theta}$. The cost function $\mathcal{C}$ in (4.21) is minimized using the same numerical optimization method as in the previous chapter, i.e., by using the Levenberg-Marquardt algorithm [Bertsekas, 1995]. This algorithm uses a gradient descent approach to update the vector of parameters $\boldsymbol{\theta}$ as follows

$$\boldsymbol{\theta}^{(i+1)} = \boldsymbol{\theta}^{(i)} - \left[\boldsymbol{J}^T\left(\boldsymbol{\theta}^{(i)}\right)\boldsymbol{J}\left(\boldsymbol{\theta}^{(i)}\right) + \mu \boldsymbol{I}_{m_p}\right]^{-1} \boldsymbol{J}^T\left(\boldsymbol{\theta}^{(i)}\right)\boldsymbol{g}\left(\boldsymbol{\theta}^{(i)}\right) \tag{4.22}$$

where $\boldsymbol{\theta}^{(i)}$ is the estimate of $\boldsymbol{\theta}$ at the ith iteration, $\boldsymbol{J}\left(\boldsymbol{\theta}^{(i)}\right) = \left[\frac{\partial \boldsymbol{g}(\boldsymbol{\theta}^{(i)})}{\partial \theta_1}, \cdots, \frac{\partial \boldsymbol{g}(\boldsymbol{\theta}^{(i)})}{\partial \theta_{m_p}}\right]$ is a $K \times m_p$ matrix representing the gradient of $\boldsymbol{g}$, m_p is the number of parameters to estimate, $\boldsymbol{I}_{m_p}$ is the $m_p \times m_p$ identity matrix and μ is a regularization parameter. Note finally that the derivatives of $\boldsymbol{g}$ are numerically evaluated as follows (as in Chapter 3)

$$\frac{\partial \boldsymbol{g}(\boldsymbol{\theta})}{\partial \theta_j} = -\frac{\partial \boldsymbol{s}(\boldsymbol{\theta})}{\partial \theta_j} \simeq -\frac{\boldsymbol{s}(\theta_j + \Delta\theta_j) - \boldsymbol{s}(\theta_j)}{\Delta\theta_j}, \text{ for } j \in \{1, \cdots, m_p\}. \tag{4.23}$$

4.4.2 Estimation performance

The evaluation of the estimation quality is achieved using the same criteria as in Chapter 3, i.e., using the RMSE, the Bias, the STD and the NRE that have been defined in Section 3.4.2.

4.5 Simulation results

This section presents simulation results obtained with proposed model. First, the approximations used to obtain the analytical FSIR are justified. Second, the behavior of the proposed model according

to antenna mispointing is analyzed. The last part of this section is interested in the estimation of simulated waveforms when considering different scenarios.

4.5.1 Justification of the FSIR approximations

This section validates the semi-analytical model (4.18) by comparison with an "exact model" resulting from a numerical computation of the integral (4.11) appearing in (4.10). This validation is conducted by analyzing the errors introduced by the two successive approximations. The normalized quadratic error (NQE) defined by

$$\mathrm{NQE}(\boldsymbol{s},\boldsymbol{s}_e)=\sqrt{\frac{\sum_{k=1}^{K}\left(s_k-s_{e_k}\right)^2}{\sum_{k=1}^{K}s_{e_k}^2}} \tag{4.24}$$

is used to compare the exact multi-look echo $\boldsymbol{s}_e$ obtained by convolving numerically the FSIR (4.10) with (4.4a) and (4.4b) and the approximated multi-look echo $\boldsymbol{s}$ obtained using the proposed approximated FSIR (4.18). Before evaluating this overall error, let us consider the error of each approximation separately. The measure of $\mathrm{NQE}_1=\mathrm{NQE}(\boldsymbol{s}_1,\boldsymbol{s}_e)$, where $\boldsymbol{s}_1$ is the semi-analytical model obtained after considering the first approximation only, provides a good evaluation of the first approximation error. Fig. 4.4 shows that the measured error is increasing with the along-track and across-track mispointing angles ξ_{al} and ξ_{ac} (red curves). Appendix J derives the following upper bound for $\mathrm{NQE}(\boldsymbol{s}_1,\boldsymbol{s}_e)$

$$\mathrm{NQE}(\boldsymbol{s}_1,\boldsymbol{s}_e)\leq\mathrm{NQE}_1^{\max}=\sqrt{\frac{\sum_{k=1}^{K}\left[E_{\mathrm{P1}}^{\max}(k)\right]^2}{\sum_{k=1}^{K}s_{e_k}^2}} \tag{4.25}$$

with

$$E_{\mathrm{P1}}^{\max}(t)=\sum_{n=1}^{N}\left[E_{\mathrm{FSIR}_1}^{\max}(t-\delta t_n,n)*\mathrm{PDF}(t)*\mathrm{PTR}(t,n)\right] \tag{4.26}$$

and

$$\begin{aligned}E_{\mathrm{FSIR}_1}^{\max}(t,n)=\frac{P_u}{\pi}\left(1+\frac{ct}{2h}\right)^{-3}U\left(t\right)\exp\left[-\frac{4}{\gamma}\left(1-\frac{\cos^2\left(\xi\right)}{1+\epsilon^2(t)}\right)+\frac{b}{2}+a\right]\\ \times\left[\exp\left(\frac{b}{2}\right)-I_0\left(\frac{b}{2}\right)\right]\left|\phi_{t,n+1}-\phi_{t,n}\right|\end{aligned} \tag{4.27}$$

where $E_{\mathrm{FSIR}_i}^{\max}$ (resp. $E_{\mathrm{P}i}(t)$) denotes the maximum error on the FSIR (resp. multi-look echo) by applying the ith approximation. Fig. 4.4 shows that the measured error is below this theoretical

maximum error $\mathrm{NQE}_1^{\max}$ (blue curves). Moreover, it shows that the first approximation is very reasonable (as an example, the estimation of a noisy waveform will provide a minimum normalized error of about 5×10^{-2}) which shows that the first approximation is valid and does not introduce a sensitive error. Finally, Fig. 4.4 shows that NQE_1 has a similar behavior versus the across-track and along-track mispointing angles.

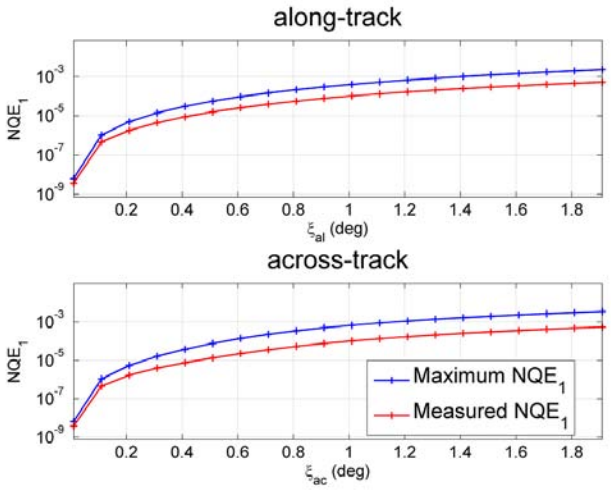

Figure 4.4: Error of approximation 1 versus (top) the along-track mispointing angle ξ_{al}, (bottom) the across-track mispointing angle ξ_{ac}.

A similar study is conducted for the second approximation by evaluating the criteria $\mathrm{NQE}_2 = \mathrm{NQE}(\boldsymbol{s}, \boldsymbol{s}_1)$. Note that the study of this error will allow us to fix the number m of terms in (4.18). Fig. 4.5 shows the measured error (continuous line) and the maximum one (crossed line) that is derived in Appendix J. These errors are represented as a function of m for different mispointing angles (the across-track and along-track mispointing provide similar results). Note that the error decreases with m while it is an increasing function of the mispointing angle ξ. Note also that the error due to the second approximation (limiting the infinite sum of (4.15) to a finite number of terms) is larger than the one obtained after the first approximation.

Appendix J shows that the error due to the second approximation can be upper bounded as follows

$$\mathrm{NQE}(\boldsymbol{s},\boldsymbol{s}_1) \leq \mathrm{NQE}_2^{\max} = \sqrt{\frac{\sum_{k=1}^{K}\left[E_{\mathrm{P2}}^{\max}(k)\right]^2}{\sum_{k=1}^{K} s_1^2}} \tag{4.28}$$

with

$$E_{\mathrm{P2}}^{\max}(t) = \sum_{n=1}^{N}\left[E_{\mathrm{FSIR}_2}^{\max}(t-\delta t_n, n) * \mathrm{PDF}(t) * \mathrm{PTR}(t,n)\right] \tag{4.29}$$

and

$$\begin{aligned} E_{\mathrm{FSIR}_2}^{\max}(t,n) = \frac{P_u}{\pi}\left(1+\frac{ct}{2h}\right)^{-3} U(t) \exp\left[-\frac{4}{\gamma}\left(1-\frac{\cos^2(\xi)}{1+\epsilon^2(t)}\right)+\frac{b}{2}\right] I_0\left(\frac{b}{2}\right) \\ \times\left[\exp(a) - I_0(a) - 2\sum_{k=1}^{m} I_k(a)\right] |\phi_{t,n+1} - \phi_{t,n}|. \end{aligned} \tag{4.30}$$

Fig. 4.5 shows that the measured error due to the second approximation is lower than its upper bound.

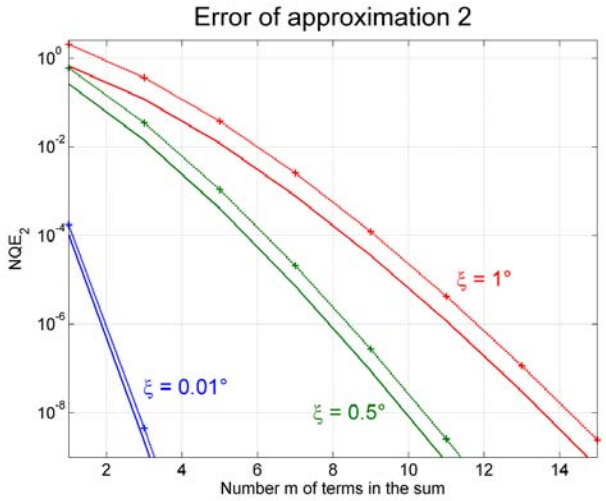

Figure 4.5: Error of approximation 2 versus the mispointing angle ξ and the number of terms in the sum m. Measured NQE_2 (continuous line), maximum NQE_2 (crossed line) for $\xi = 0.01°$ (in blue), $\xi = 0.5°$ (in green) and $\xi = 1°$ (in red)

The final error due to our two approximations can be upper bounded as follows

$$E_{\mathrm{FSIR}}^{\max}(t,n) = E_{\mathrm{FSIR}_1}^{\max}(t,n) + E_{\mathrm{FSIR}_2}^{\max}(t,n). \tag{4.31}$$

Using (4.31), one can establish the overall maximum error echo $E_{\mathrm{P}}(t)$ (i.e., the maximum error for the resulting multi-look echo) and the maximum normalized quadratic error as follows

$$\mathrm{NQE}^{\max}(\boldsymbol{s}, \boldsymbol{s}_e) = \sqrt{\frac{\sum_{k=1}^{K} E_{\mathrm{P}}^2(k)}{\sum_{k=1}^{K} s_{e_k}^2}}. \tag{4.32}$$

Fig. 4.6 shows that NQE (resp. $\mathrm{NQE}^{\max}$) has the same behavior as NQE_2 (resp. $\mathrm{NQE}_2^{\max}$) for small m while it is quite constant for high m. Indeed, for high m, the error introduced by the second approximation becomes negligible and the overall error only depends on the first approximation error. Note that some simulation results have shown that the minimum NQE obtained between a noisy echo

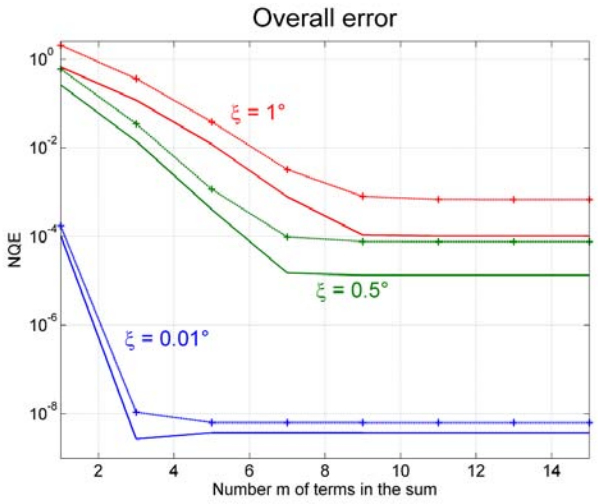

Figure 4.6: Overall error versus the mispointing angle ξ and the number of terms in the sum m. Measured NQE (continuous line), maximum NQE (crossed line) for $\xi = 0.01°$ (in blue), $\xi = 0.5°$ (in green) and $\xi = 1°$ (in red)

and an echo without noise is about 5×10^{-2} (i.e., the NQE due to the noise presence) which means that we have to consider a value of m that provides a lower error. In the pessimistic case $\xi = 1°$, $m = 6$ is sufficient to obtain the desired error level. This value of m will be used in all our simulations.

4.5.2 Analysis of FSIR versus mispointing angles

The antenna mispointing is introduced by means of two variables ξ and $\tilde{\phi}$ which are directly related to the along-track and across-track mispointing angles as shown in (4.20), hence the necessity to analyze their effects on the resulting echo. The proposed model sums the reflected energy to give a two dimension response FSIR(t, f). The temporal dimension is introduced by the propagation circles where each time instant is related to a circle radius $\rho(t) = \sqrt{hct}$, whereas the frequential dimension is introduced by the rectangular Doppler beams (see Fig. 4.1). While this mapping is constant for any mispointing, the reflected energy depends on mispointing since the antenna gain depends on ξ and $\tilde{\phi}$. The Gaussian antenna gain is given by [Brown, 1977]

$$G(\xi,\tilde{\phi}) \simeq G_0 \exp\left\{-\frac{2}{\gamma}\sin^2\left[\omega(\xi,\tilde{\phi})\right]\right\}, \text{with } \cos\left[\omega(\xi,\tilde{\phi})\right] = \frac{\cos(\xi) + \frac{\rho(t)}{h}\sin(\xi)\cos\left(\tilde{\phi}-\phi\right)}{\sqrt{1+\frac{\rho^2(t)}{h^2}}}. \quad (4.33)$$

Fig. 4.7 shows the behavior of the antenna gain for different values of mispointing. In absence of mispointing, the maximum of the antenna gain occurs at $x = y = 0$ and the Gaussian shape response is centered (Fig. 4.7 top-left). However, and as expected, the along-track mispointing (Fig. 4.7 bottom-left) moves the maximum along the y axis while the across-track mispointing (Fig. 4.7 bottom-right) moves it along the x axis (as expected). This will induce different effects on the corresponding multi-look echo. Let us first consider the along-track mispointing. Fig. 4.8 shows the obtained DDM when considering $\xi_{\text{al}} = 0.5°$. This figure shows an energy migration from the lower Doppler beams to the higher ones (because of the move of the antenna gain along the y axis). This along-track mispointing reduces the amplitude of the multi-look echo as shown in Fig. 4.9 (top) while it does not change the shape of the waveform as shown in Fig. 4.9 (bottom) representing normalized waveforms. Fig. 4.10 shows the obtained DDM when considering an across-track mispointing angle $\xi_{\text{ac}} = 0.5°$. This figure shows an energy migration from the low time gates to the high gates (because of the move of the antenna gain in the x axis). This across-track mispointing reduces the amplitude of the multi-look echo as shown in Fig. 4.11 (top) but it also changes the shape of the waveform as shown in Fig. 4.11 (bottom) representing normalized waveforms[3]. This analysis shows that the

[3]These results are in agreement with the results of the SAMOSA project [Gommenginger et al., 2011a].

shape of the delay/Doppler waveform is affected by the value of the across-track mispointing angle ξ_{ac} whereas ξ_{al} has an impact on the waveform amplitude mainly. Note that the change of amplitude due to ξ_{al} can be compensated by changing the value of P_u.

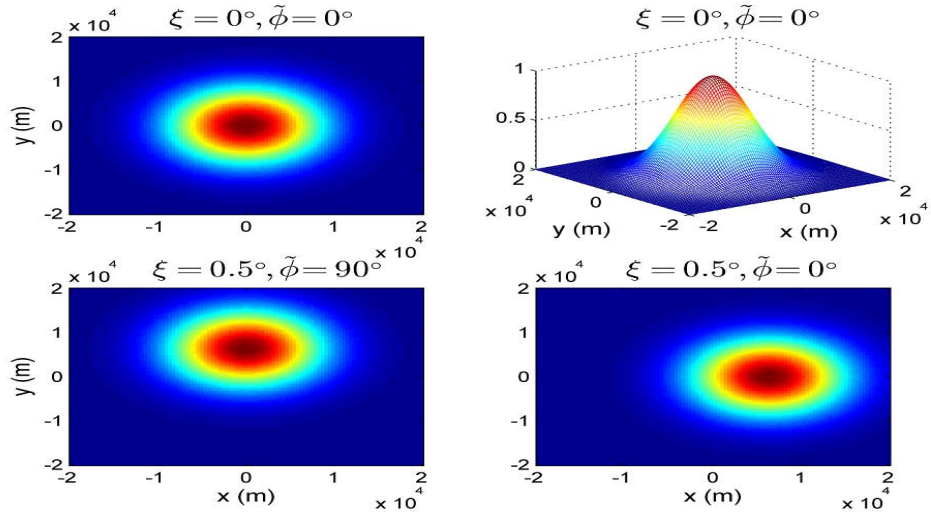

Figure 4.7: Antenna gain with different mispointing angles.

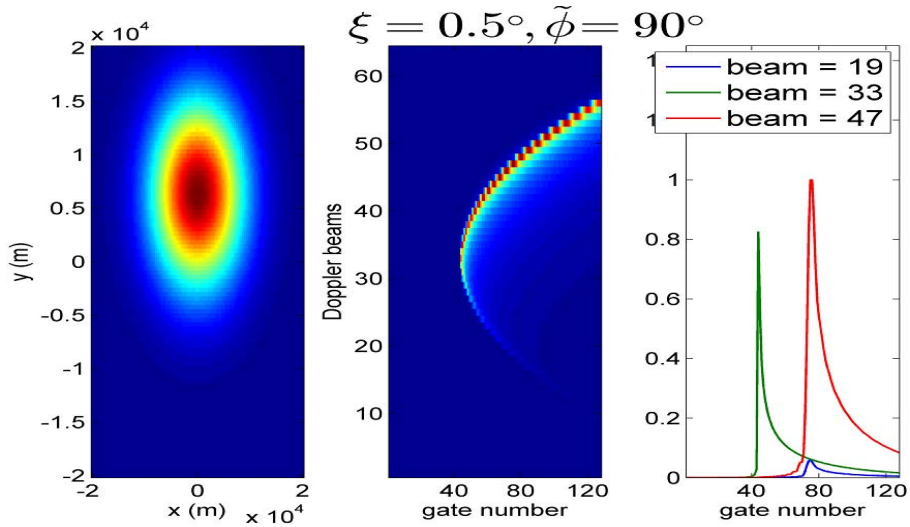

Figure 4.8: Antenna gain, DDM, and Doppler echoes representation for an along-track mispointing ($\xi_{\text{ac}} = 0°$ and $\xi_{\text{al}} = 0.5°$).

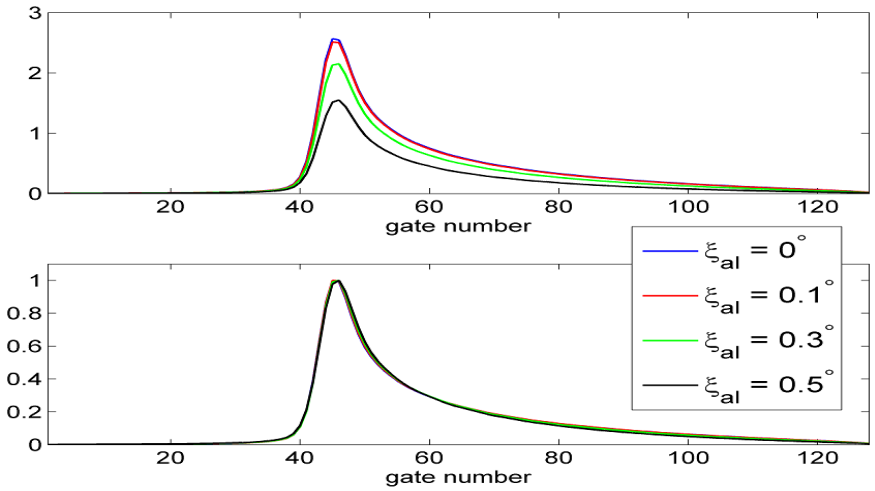

Figure 4.9: Effect of the along-track mispointing on (top) the multi-look echoes and (bottom) the normalized multi-look echoes (obtained with $P_u = 1$, $\tau = 44$ gates, SWH $= 3$ meters and $\xi_{\text{ac}} = 0°$).

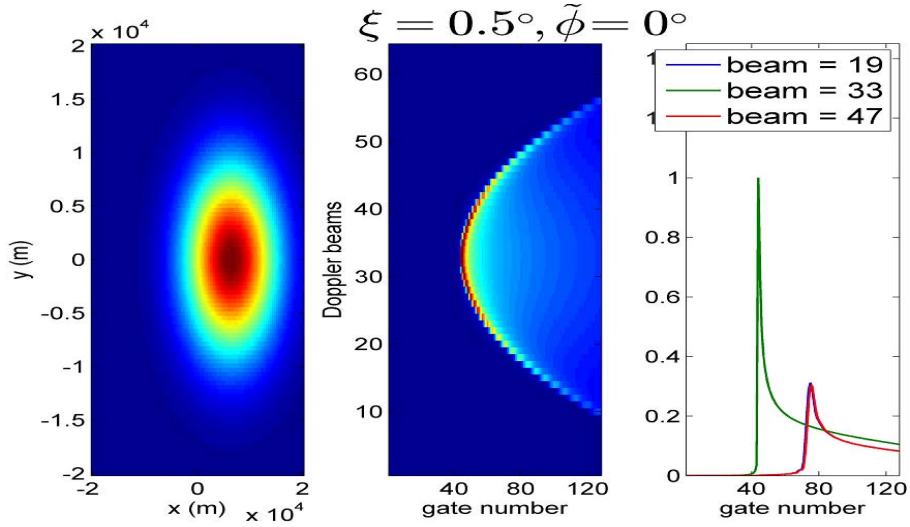

Figure 4.10: Antenna gain, DDM, and Doppler echoes representation for an across-track mispointing ($\xi_{\text{ac}} = 0.5°$ and $\xi_{\text{al}} = 0°$).

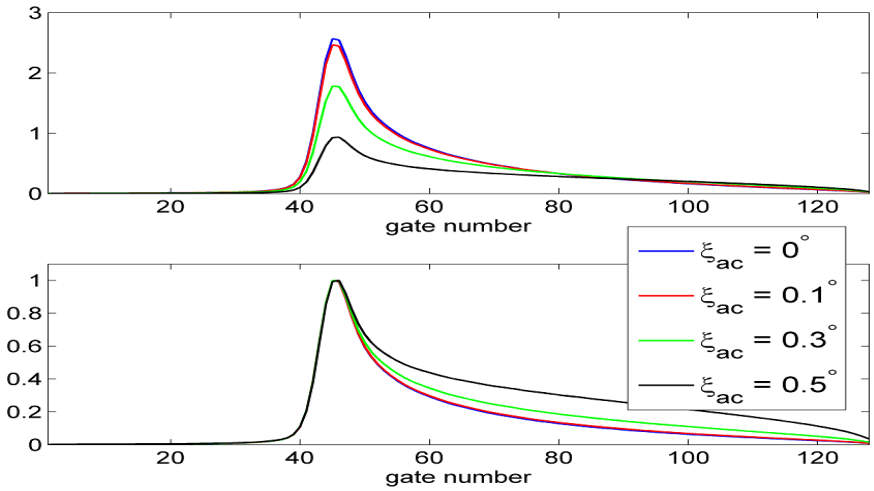

Figure 4.11: Effect of the across-track mispointing on (top) the multi-look echoes and (bottom) the normalized multi-look echoes (obtained with $P_u = 1$, $\tau = 44$ gates, SWH $= 3$ meters and $\xi_{\text{al}} = 0°$).

4.5.3 Performance on simulated waveforms

Generation of simulated waveforms

In order to generate realistic waveforms, the multi-look echo has to be corrupted by speckle noise as in Chapter 3 resulting in the noisy multi-look echo $y(t)$ given by

$$y(t) = \sum_{n=1}^{N} P\left(t - \delta t_n, f_n\right)\, q(t - \delta t_n, n) \tag{4.34}$$

where $q(t, n)$ is a multiplicative i.i.d. speckle noise sequence distributed according to a gamma distribution $\Gamma(L, 1/L)$ ($L = 4$ in our simulations) where L is the number of looks. The reader is invited to consult the previous chapter for more details about the speckle noise generation.

Estimation scenarios

The proposed multi-look echo depends on five altimetric parameters $\boldsymbol{\theta}_5 = (\text{SWH}, P_u, \tau, \xi_{\text{ac}}, \xi_{\text{al}})^T$. The first estimation estimates these five parameters and is denoted by DDA5. However, it has been shown in the previous section that the along-track mispointing ξ_{al} mainly affects the echo amplitude and

has a small effect on its shape. Hence, one can expect high correlation between ξ_{al} and P_u which may reduce the estimation performance[4]. Therefore, we propose a second strategy denoted by DDA4, estimating a four parameter vector $\boldsymbol{\theta}_4 = (\text{SWH}, P_u, \tau, \xi)^T$ with the constraint $\tilde{\phi} = 0°$ (i.e., $\xi = \xi_{\text{ac}}$). Note that this strategy might be limited to scenarios with small values of ξ_{al} (see Appendix. K).

In order to evaluate the performance of DDA5 and DDA4, we compare their estimation performance to those obtained using the model of Chapter 3 which considers the three first parameters $\boldsymbol{\theta}_3 = (\text{SWH}, P_u, \tau)^T$ only (denoted by DDA3). It is a special case of the proposed model (4.18) assuming $\xi = \tilde{\phi} = 0°$. We also consider a 3 parameter based model obtained by replacing known values of ξ_{ac} and ξ_{al} (or equivalently $\tilde{\phi}$ and ξ) in (4.19). These known values of $(\xi_{\text{ac}}, \xi_{\text{al}})$ are for instance available in the case of Cryosat-2 data (see [Smith and Scharroo, 2011] for more details). The resulting estimation strategy is a generalization of DDA3 and is denoted by G-DDA3. In the following, the performance of the four estimation strategies DDA3, G-DDA3, DDA4 and DDA5 is evaluated and compared to CA4 when considering simulated and real data.

Estimation on simulated waveforms

This section evaluates the performance of the proposed algorithms on simulated multi-look waveforms generated using the altimetric parameters $(P_u, \tau, \xi_{\text{ac}}, \xi_{\text{al}})^T = (1, 31 \text{ gates}, 0°, 0°)^T$ when varying SWH and $(\text{SWH}, P_u, \tau, \xi_{\text{al}})^T = (2 \text{ m}, 1, 31 \text{ gates}, 0°)^T$ when varying ξ_{ac}. Note that all results have been averaged using $N_{\text{MC}} = 500$ Monte Carlo realizations.

Fig. 4.12 shows the parameter RMSEs when varying SWH in the interval [1, 8] m. This figure shows similar performance between DDA3, DDA4 and DDA5 for the parameters SWH and τ (G-DDA3 is the same as DDA3 since $\xi_{\text{ac}} = \xi_{\text{al}} = 0°$). Note however that the performance of DDA5 decreases for parameter P_u because of the correlation that is introduced by estimating ξ_{al}. This decrease of performance is not observed for DDA4 which provides similar RMSEs as DDA3. Note also that DDA4 performs better than DDA5 for the parameter ξ_{ac} probably because DDA4 estimates less parameters.

[4]The estimation of the five parameter vector could be achieved when considering the DDM matrix instead of the multi-look echo. Indeed, the effect of ξ_{al} is different in this case from that of P_u as shown in Fig. 4.8. This strategy may provide better estimation performance as shown in [Phalippou et al., 2012] but will not be pursued in this thesis.

Partial conclusion 1: These results show the interest of DDA4 since it provides similar performance than DDA3 when considering the 3 first parameters while it outperforms DDA5 when considering ξ_{ac}.

The performance of the proposed algorithms was also evaluated when varying ξ_{ac} in the interval $[0, 0.7]$ degrees as shown in Fig. 4.13. As previously, G-DDA3 (in which we consider the actual values of mispointing angles), DDA4 and DDA5 behave similarly for SWH and τ. The RMSEs of these two parameters are quite constant for different values of ξ_{ac}. This shows that the presence of across-track mispointing does not affect their estimation. The amplitude P_u is better estimated with G-DDA3 and DDA4 than with DDA5 as previously. Note that RMSE(ξ_{ac}) decreases with respect to ξ_{ac} since the shape of the echo strongly depends on this parameter (see Fig. 4.11) which facilitates its estimation. Note finally that DDA3 is sensitive to mispointing and that it shows acceptable performance for $\xi_{ac} < 0.2°$. Beyond this value, the parameter RMSEs increase drastically mainly because of the presence of a bias as shown in Appendix K which shows the obtained Biases and STDs[5].

Partial conclusion 2: These results confirm the good performance of DDA4 algorithm and its superiority since it shows similar results than G-DDA3 while it provides additional information about across-track mispointing.

[5]The results of Appendix K show that the DDA3 parameter STDs remain acceptable until a value of $\xi_{ac} = 0.4°$ which can be exploited by elaborating bias correction tables (as for MLE4 [Thibaut et al., 2004]) in order to use the DDA3 for more mispointed data.

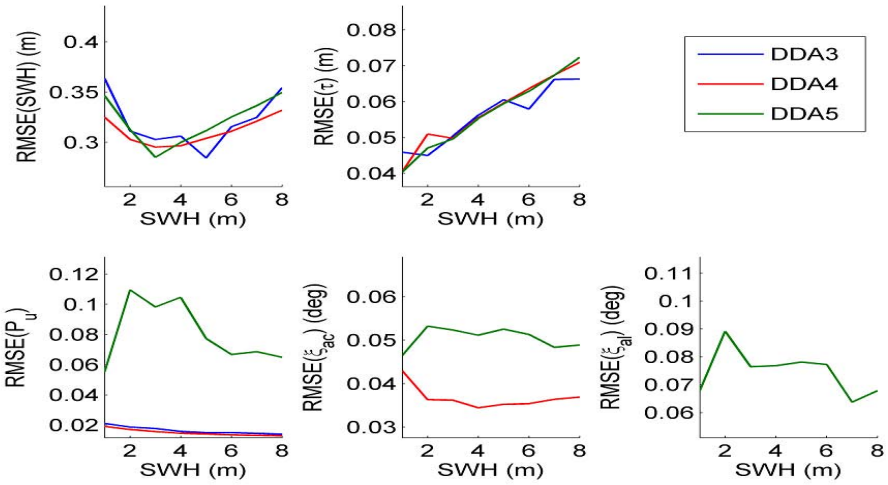

Figure 4.12: Parameter RMSEs versus SWH when considering echoes without mispointing estimated with DDA3, DDA4 and DDA5. The simulation has been obtained using 500 Monte-Carlo realizations with the parameters $P_u = 1$, $\tau = 31$ gates and $\xi_{\text{al}} = \xi_{\text{ac}} = 0°$.

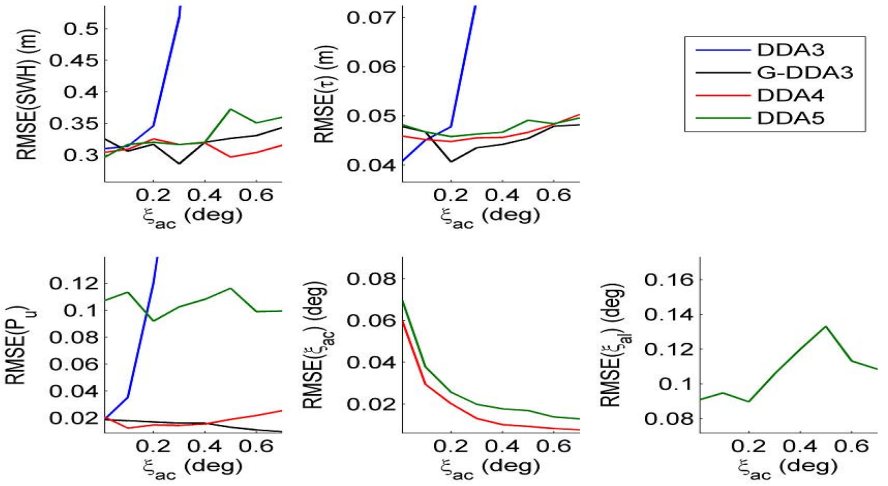

Figure 4.13: Parameter RMSEs versus ξ_{ac} when considering DDA3, G-DDA3, DDA4 and DDA5. The simulation has been obtained using 500 Monte-Carlo realizations with the parameters $P_u = 1$, SWH $= 2$ m, $\tau = 31$ gates and $\xi_{\text{al}} = 0°$.

Comparison between CA4 and DDA4

This section is interested in the comparison between DDA4 that has shown interesting estimation performance and CA4. The comparison is based on the evaluation of the RMSEs when varying SWH and ξ (with $\tilde{\phi} = 0°$ which means that $\xi = \xi_{\text{ac}}$) while keeping the same parameter configuration as in the previous section. Fig. 4.14 shows the RMSEs of CA4 and DDA4 when varying SWH in the interval $[1, 8]$ m. This figure shows an RMSE improvement when considering DDA4 for the parameters SWH, τ, ξ_{ac}. It also shows that the estimation of P_u with DDA4 improves for high values of SWH. Note finally that the obtained results are in agreement with those obtained for CA3 and DDA3 for the three first parameters SWH, τ and P_u (see Fig. 3.15).

Fig. 4.15 shows the RMSEs when varying ξ_{ac} in the interval $[0°, 0.7°]$. It can be seen that SWH is less sensitive to the variation of ξ_{ac} when considering DDA4 since a constant RMSE level can be observed while it slightly increases when considering CA4. On the other hand, the RMSEs of P_u and ξ_{ac} are similar for CA4 and DDA4. Note that the epoch error is lower for DDA4 and that the constant level of RMSE is probably due to the uncorrelation between τ and ξ_{ac} for both CA4 and DDA4. These results confirm the good performance of DDA4 and illustrate its superiority when compared to CA4.

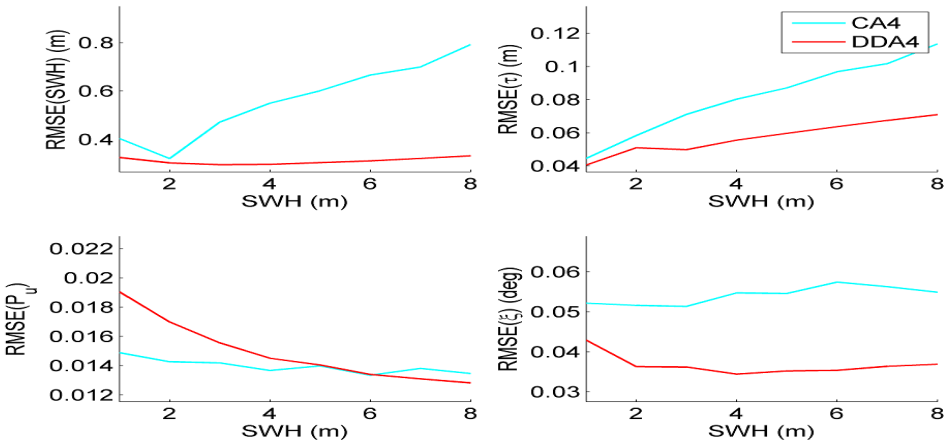

Figure 4.14: Parameter RMSEs versus SWH when considering CA4 and DDA4. The simulation has been obtained using 500 Monte-Carlo realizations with the parameters $P_u = 1$, $\tau = 31$ gates, $\xi_{\text{al}} = \xi_{\text{ac}} = 0°$.

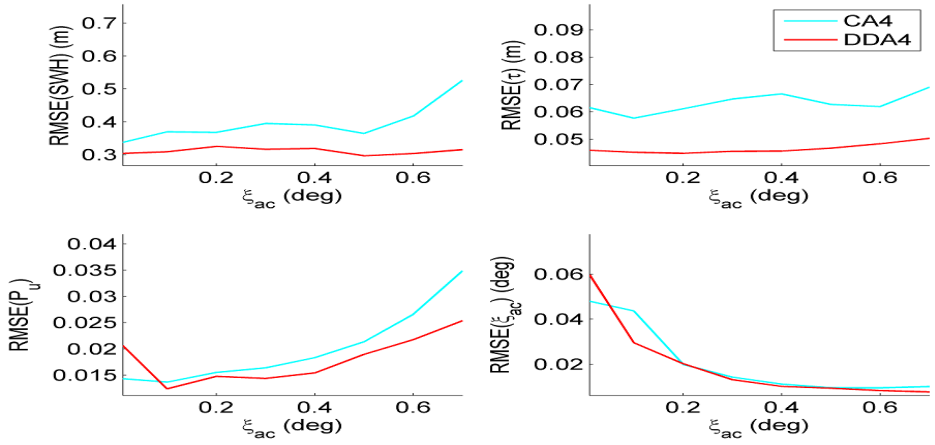

Figure 4.15: Parameter RMSEs versus ξ_{ac} when considering CA4 and DDA4. The simulation has been obtained using 500 Monte-Carlo realizations with the parameters $P_u = 1$, SWH $= 2$ m, $\tau = 31$ gates and $\xi_{\text{al}} = 0°$.

4.6 CRYOSAT-2 waveforms

This section evaluates the performance of the proposed model and algorithms for oceanic Cryosat-2 waveforms. The considered data lasts approximately 400 seconds and were obtained in May 2012. These data were provided by the Cryosat processing prototype developed by CNES which is doing the level 1 processing [Boy et al., 2012].

Waveform fitting

Fig. 4.16 shows an estimated Cryosat-2 echo by the DDA4. As for DDA3 (see chapter 3), this figure shows an excellent fit between the two echoes and a very low difference between them. The good fit can be quantified by the NRE criteria introduced in Section 3.4.2. Fig. 4.17 shows the obtained NREs when considering the 4 estimation strategies for 100 seconds of data. The obtained NREs are globally good since they are lower than 10 %. In particular, one can notice the excellent performance of DDA4 and DDA5 that fit perfectly the Cryosat-2 echoes. The G-DDA3 shows better fit than DDA3 but still

does not reach the performance of DDA4 and DDA5 in terms of fitting. Table 4.1 shows the obtained ANREs when considering the different DDA strategies and CA-SARM4. This table shows that DDA strategies present lower NREs than CA-SARM4. Moreover, we can observe that the DDA5 ANRE is the lowest but that DDA4 still perform very well in terms of fitting the echoes. This performance was expected since the estimation of more parameters leads generally to a better fit. However, the similarity between the DDA4 and DDA5 may suggest that there is no need to estimate 5 parameters. This result is confirmed when evaluating the estimated parameters.

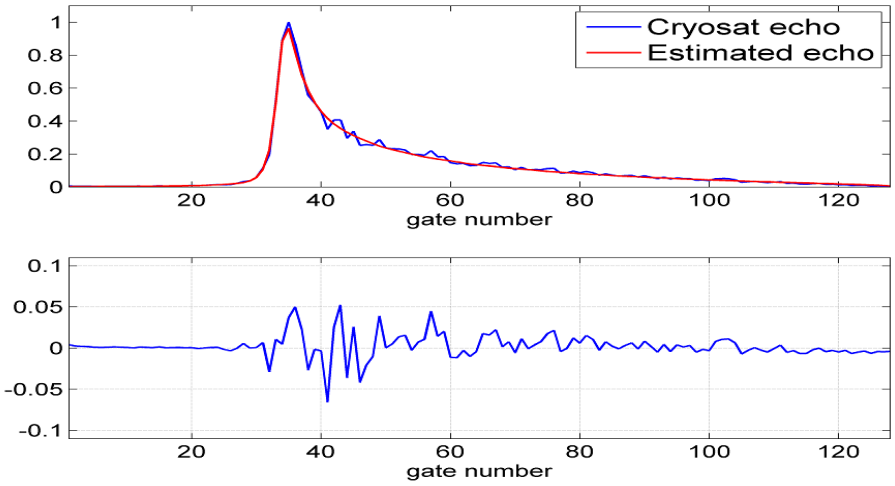

Figure 4.16: Estimated Cryosat-2 echo using the proposed DDA4 model (NRE = 0.065). (top) real Cryosat-2 echo superimposed with its estimation, (bottom) difference between the real Cryosat-2 echo and its estimation.

Table 4.1: Averaged normalized reconstruction error when considering DDA3, G-DDA3, DDA4, DDA5 and CA-SARM4.

	DDA3	G-DDA3	DDA4	DDA5	CA-SARM4
ANRE ($\times 10^{-2}$)	8.08	7.78	7.35	7.32	10.76

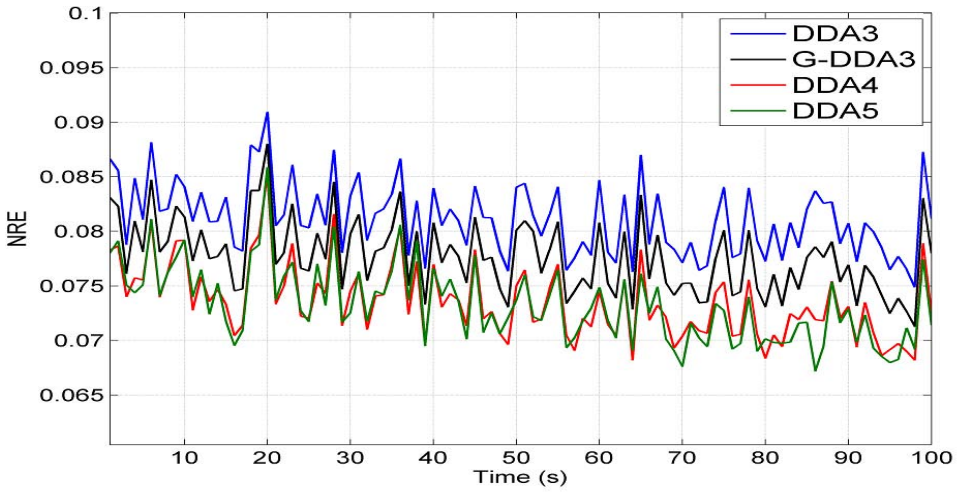

Figure 4.17: NRE estimates for 100 seconds of Cryosat-2 data when considering DDA3, G-DDA3, DDA4 and DDA5.

Estimated parameters

Figs. 4.18 and 4.19 show the estimated parameters SWH and τ for 100 seconds of data when considering DDA and CA-SARM echoes. This figure highlights a difference of about 10 cm between DDA5 and the other DDA strategies for SWH. It also shows a good agreement between CA-SARM4 and DDA estimates. Fig. 4.19 shows an excellent agreement between the 4 DDA strategies and CA-SARM4 when considering the epoch τ. Fig. 4.20 shows the histograms of the estimated across-track mispointing angle ξ_{ac} obtained using DDA4, DDA5 and CA-SARM4 algorithms. This figure shows similar histogram shapes with approximately the same standard-deviations for the three strategies. Note that a negligible difference (less than 0.02°) appears between the estimates of the three strategies. Table 4.2 summarizes the obtained means and standard-deviations when considering the 4 DDA estimation strategies and CA-SARM4. The means of the estimated parameter τ are similar for CA-SARM4 and the proposed DDA algorithms. However, the means of the estimated SWH differ slightly with a maximum value for DDA3 and a minimum one for DDA5. These values are in agreement with the ones obtained with CA-SARM4 since we observe a small difference that is reduced when estimating more mispointing angles. Concerning the STDs, it can be seen that the best results are obtained

with DDA4 while DDA5 shows high STDs for parameters SWH and P_u. This table shows high value for the STDs of the estimated τ since we have only applied a tracker correction on the estimated τ values (the other corrections were not available for the considered data). Table 4.2 confirms that the DDA algorithms yield smaller estimation variances than CA-SARM4.

Summary of Cryosat-2 results

To summarize, the DDA strategies perform better than the CA-SARM4 method which highlights the superiority of this new technology. The similarities between the estimated parameters using CA-SARM4 and DDA strategies validate the proposed model. The best algorithm in terms of echo fitting and quality of the estimated parameters is DDA4. The DDA5 algorithm suffers from the correlation existing between the along-track mispointing angle and the amplitude which reduces its estimation performance. G-DDA3 appears to be a useful tool to reach better estimation results while keeping the simplicity of DDA3 which allows fast estimation with low computational times.

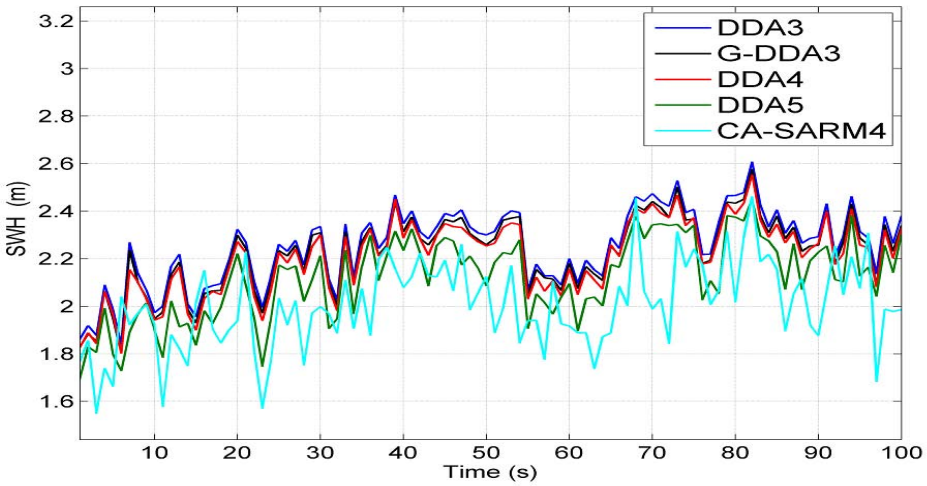

Figure 4.18: SWH estimates for 100 seconds of Cryosat-2 data when considering DDA3, G-DDA3, DDA4, DDA5 and CA-SARM4.

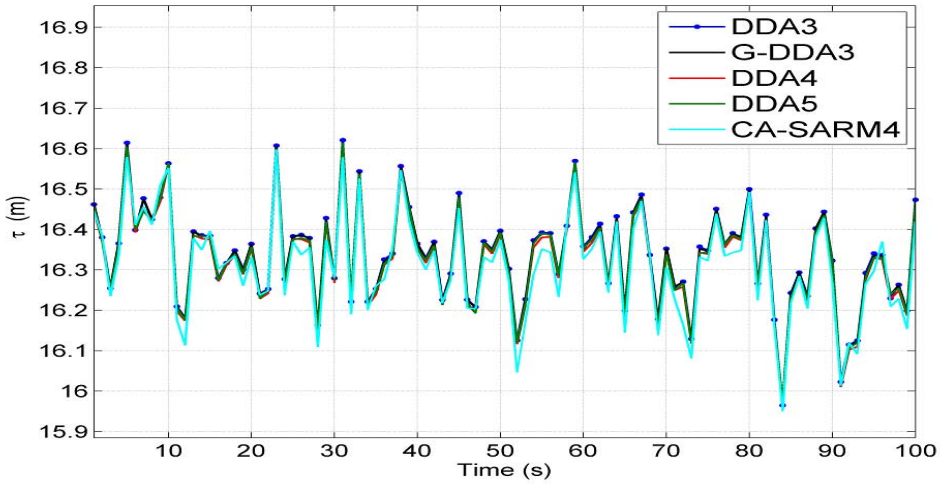

Figure 4.19: τ estimates for 100 seconds of Cryosat-2 data when considering DDA3, G-DDA3, DDA4, DDA5 and CA-SARM4.

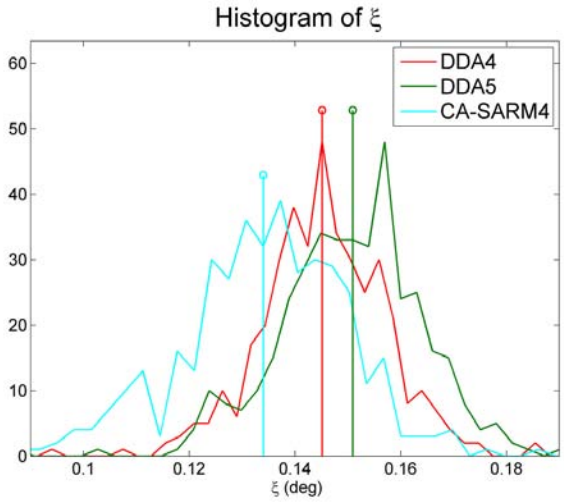

Figure 4.20: Histograms of the estimated across-track mispointing angle ξ_{ac} (in degree) using DDA4, DDA5 and CA-SARM4 algorithms.

Table 4.2: Means and standard deviations for DDA3, G-DDA3, DDA4, DDA5 and CA-SARM4 algorithms.

		τ (m)	SWH (m)	P_u	ξ_{ac} (deg)	ξ_{al} (deg)	ξ (deg)
Means	DDA3	16.274	2.289	90.213	-	-	-
	G-DDA3	16.270	2.247	92.803	0.083	0.0572	0.109
	DDA4	16.262	2.234	96.993	0.146	-	0.146
	DDA5	16.266	2.144	102.192	0.151	0.099	0.181
	CA-SARM4	16.249	2.015	102.89	-	-	0.134
STDs (20 Hz)	DDA3	0.0843	0.355	1.933	-	-	-
	G-DDA3	0.0845	0.354	1.987	1.01×10^{-4}	7×10^{-4}	4×10^{-4}
	DDA4	0.0827	0.351	1.871	0.031	-	0.031
	DDA5	0.0828	0.416	13.446	0.0413	0.0922	0.0866
	CA-SARM4	0.127	0.676	8.346	-	-	0.0461

4.7 Conclusions

This chapter defined a generalized semi-analytical model for delay/Doppler altimetry. The proposed model considers antenna mispointing, a circular antenna pattern, no vertical speed effect and a uniform scattering. The approximations used in order to elaborate the proposed analytical formula for the flat surface impulse response were studied and quantified. The obtained model was analyzed and the effect of the mispointing was studied as function of across-track and along-track directions. It was shown that the across-track mispointing angle affects the echo's shape while the along-track mispointing angle mainly affects the amplitude of the multi-look echo. This behavior can yield problems when estimating five parameters from the multi-look echo. A solution that consists of estimating four parameters was proposed and validated. The performance of this new estimation strategy are better than the three parameter estimation strategy proposed in Chapter 3 in terms of quality of the estimated parameters and echo fitting. A related estimation strategy was also proposed by introducing the estimated mispointing parameters in the proposed model and estimating only three parameters. This solution seems to be a useful tool to reach better estimation results without increasing the computational times. It can be applied easily to altimeters such as Cryosat-2. A comparison between conventional and delay/Doppler altimetry clearly showed some advantages for the delay/Doppler processing.

Finally, we think that generalizing the maximum likelihood estimator established in Appendix I to 4 and 5 parameters is an interesting issue. Moreover, and in order to improve the 5 parameter estimation, one can estimate the parameters from the whole delay/Doppler map instead of using the multi-look echoes. Including the vertical speed effect and the antenna ellipticity are also important issues that should be considered in future studies.

Contributions

The Chapter 3 model is generalized to a five parameter model that accounts for antenna mispointing [Halimi et al., 2013c]. The new model is analyzed and its approximations are justified. Several estimation strategies based on the least squares estimation procedure are proposed to estimate its parameters. Processing simulated and real Cryosat-2 data allow this new model to be validated.

4.8 Conclusions (in French)

Ce chapitre a introduit un nouveau modèle semi-analytique généralisé pour l'altimétrie SAR/Doppler. L'expression analytique de la réponse impulsionnelle d'une mer plate a été obtenue en supposant un diagramme d'antenne circulaire avec dépointage, aucun effet de la vitesse verticale du satellite et un coefficient de rétrodiffusion constant dans la surface observée. Les approximations utilisées pour établir la formule analytique proposée ont été étudiées et leurs erreurs quantifiées. Le modèle ainsi obtenu a été analysé et l'effet du dépointage a été étudié suivant les directions azimutale et transverse. Il a été montré que le dépointage transverse affecte la forme et l'amplitude de l'écho SAR/Doppler alors que le dépointage azimutal n'affecte que son amplitude. Ce comportement peut causer des problèmes lors de l'estimation de cinq paramètres à partir de l'écho multi-vues. Une solution qui consiste à estimer quatre paramètres a été proposée et validée. Cette stratégie offre de meilleures performances que celles du chapitre précédent puisqu'elle fournit une meilleure qualité des paramètres estimés ainsi qu'une parfaite adéquation entre l'écho observé et son estimé. Ce chapitre a aussi défini une autre procédure d'estimation qui introduit les valeurs des angles de dépointage estimés dans le modèle proposé et estime ensuite trois paramètres. Cette solution semble être un outil intéressant pour obtenir une meilleure qualité des paramètres estimés sans pour autant augmenter le temps de calcul. Cette stratégie peut facilement être appliquée à l'altimètre SIRAL de Cryosat-2 puisqu'il fournit une mesure du dépointage par l'utilisation du senseur stellaire. A noter enfin qu'une comparaison entre l'altimétrie conventionnelle et SAR/Doppler a clairement montré la supériorité de cette dernière.

Finalement, nous pensons que la généralisation de l'estimateur du maximum de vraisemblance, établi dans l'annexe I, pour tenir compte de 4 ou de 5 paramètres est une piste intéressante. Par ailleurs, et afin d'améliorer l'estimation à 5 paramètres, on pourrait estimer les paramètres de la carte distance Doppler au lieu d'utiliser les échos multi-vues. Tenir compte de l'effet de la vitesse verticale et de l'ellipticité de l'antenne sont également des questions importantes qui doivent être prises en compte dans les études futures.

Contributions

Le modèle précédent est généralisé pour tenir compte du dépointage de l'antenne [Halimi et al., 2013c]. Le nouveau modèle est analysé et ses approximations justifiées. Plusieurs algorithmes d'estimation basés sur un critère de moindres carrés sont proposés. La validation du modèle proposé est réalisée en traitant des échos synthétiques et réels.

Chapter 5

Conclusions and future work

Conclusions

Satellite altimetry aims at the observation of the ocean and the measure of its surface topography. However, conventional altimetry has some limitations that are mainly due to the contamination of the echoes by land return in coastal areas because of the large footprint of the observed surface and the reduction of the measurement accuracy due to the corruption of the waveforms by speckle noise. The objective of this thesis was to deal with these limitations and to propose solutions in order to improve the measurement accuracy by a better use of the available data.

The first solution considered in Chapter 2 dealt with the issue of coastal altimetry by proposing a "Brown with asymmetric Gaussian peak" model for these echoes. The proposed model is a generalization of the models defined in [Gómez-Enri et al., 2010, Tourneret et al., 2010] since it considers an additional asymmetry parameter. The parameters of this model were estimated by using the maximum likelihood principle and two estimation algorithms based on Newton-Raphson recursion and a Nelder-Mead algorithm. The Nelder-Mead algorithm showed better estimation performance at a price of a higher computational times. Results obtained in this study also showed that the proposed model can be used to retrack efficiently standard oceanic Brown echoes as well as coastal echoes corrupted by symmetric or asymmetric Gaussian peaks. The evaluation of the Cramér-Rao bounds showed the good performance of the Nelder-Mead algorithm. These bounds were also used to evaluate the loss of performance for estimating the Brown parameters in presence of a Gaussian peak. This loss of performance is mainly due to more parameters to be estimated when the model contains a symmetric or asymmetric Gaussian peak.

The second solution was based on the study of delay/Doppler altimetry. This new technology was proposed to deal with the conventional altimetry limitations by reducing the noise level affecting the echoes and increasing the along-track resolution. However, the obtained echoes are different from those of conventional altimetry and then require a new model to estimate their parameters. The main objective of Chapter 3 was to propose a model for these echoes and the corresponding estimation algorithm. A geometrical approach was used for computing an analytical expression of the flat surface impulse response. The analytical expression was obtained assuming a circular antenna pattern, no mispointing, no vertical speed effect and a uniform scattering. This analytical expression was convolved with the probability density function of the heights of the specular scatterers and the point target response of the radar leading to the mean power of a delay/Doppler altimetric waveform. The analysis of the proposed model had shown the importance of range migration and that of the central Doppler beams that contain most of the information. A least squares approach based on the Levenberg-Marquardt algorithm was then proposed to estimate the parameters of delay/Doppler altimetric echoes. The choice of this algorithm allows the use of numerical derivatives and to compare the proposed model to that of SAMOSA that used the same algorithm. The Cramér-Rao bounds were also derived to provide a reference in terms of estimation performance. These bounds were used to evaluate the performance of the proposed estimation strategy and to compare it with other estimation procedures such as the maximum likelihood estimator and the weighted least squares procedure. The obtained results showed the good potential of delay/Doppler altimetry when compared to conventional altimetry in terms of error and correlation reduction.

The proposed model of Chapter 3 did not take into account any antenna mispointing which may lead to reduced estimation performance. This point was considered in Chapter 4 which defined a generalized semi-analytical model for delay/Doppler altimetry. The proposed model considers antenna mispointing, a circular antenna pattern, no vertical speed effect and a uniform scattering. The approximations used in order to elaborate the proposed analytical formula for the flat surface impulse response were studied and quantified. The obtained model was analyzed as well as the effect of the mispointing studied according to across-track and along-track directions. It was shown that the across-track mispointing affects the echo's shape while the along-track mispointing mainly affects

the amplitude of the multi-look echo. This behavior appears as a difficulty when estimating five parameters from the multi-look echo. A solution that consists of estimating four parameters was proposed and validated. The performance of this new estimation strategy is better than the three parameter estimation strategy proposed in Chapter 3 in terms of quality of the estimated parameters and echo fitting. An intermediate estimation strategy was proposed by introducing the estimated mispointing parameters in the proposed model and estimating only three parameters. This solution appears to be useful to reach better estimation results without increasing the computational times and can be applied to altimeters such as Cryosat-2. The comparison of conventional altimetry with the proposed delay/Doppler estimation strategies showed the superiority of this new technology.

Future work

A lot of perspectives could be considered for future work. In the first topic of the PhD, an interesting issue is the extension of the proposed model to the four parameter Brown model (including the mispointing as a fourth parameter). This model could also be generalized to account for multiple peaks instead of considering only one peak. The proposed Brown with asymmetric Gaussian peak model could also be of interest for retracking echoes affected by σ-blooms or rain cells. In the proposed approach, the Brown model was generalized by adding a Gaussian peak. Another approach to tackle the problem of coastal altimetry could be to elaborate an FSIR model that takes into account the nature of the observed surface, i.e., water and land in the coastal case.

Considering the delay/Doppler altimetry, the first point should be the comparison of the proposed model with the analytical model of SAMOSA. This point was not achieved in the present work because of the absence of literature about the SAMOSA model which is not yet published. A second point consists of the generalization of the proposed model to account for antenna ellipticity, the vertical speed effect and a non constant backscattering coefficient. Moreover, one can think about elaborating a complete analytical model for the multi-look echo which may introduce more approximations. The latter should be carefully analyzed in order to control the behavior of the resulting model. Considering the parameter estimation aspect, one can think about estimating the whole DDM matrix instead of

the multi-look echo in order to improve the quality of the estimated 5 parameters. It is also interesting to generalize the maximum likelihood estimator established in Appendix I to the 4 and 5 parameter cases.

The last point considers parameter estimation for both conventional and delay/Doppler altimetry. Indeed, the present thesis dealt with the parameter estimation by considering echoes independently. However, it is well known that adjacent echoes may share similar altimetric parameters because of their physical nature. Therefore, it is of great interest to derive estimation algorithms that consider this correlation in order to reduce the measurement noise and/or the estimation computational times.

Chapter 6

Conclusions et perspectives

Conclusions

L'altimétrie satellitaire a pour but l'observation de l'océan et la mesure de sa topographie de surface. Cependant, l'altimétrie conventionnelle présente certaines limitations qui sont principalement dues à la contamination des échos par des retours de la terre dans les zones côtières en raison de la grande tache au sol et la réduction de la précision de mesure en raison de la corruption des formes d'onde par le bruit de chatoiement. L'objectif de cette thèse était de faire face à ces limitations en proposant des solutions qui permettent l'amélioration de la qualité des paramètres estimés et une meilleure utilisation des données disponibles.

La première solution, considérée dans le chapitre 2, s'est intéressée à l'altimétrie côtière en proposant un nouveau modèle appelé Brown avec pic gaussien asymétrique. Le modèle proposé généralise les modèles définis dans [Gómez-Enri et al., 2010, Tourneret et al., 2010] car il considère un paramètre d'asymétrie supplémentaire. Les paramètres de ce modèle ont été estimés en se basant sur le principe du maximum de vraisemblance et en utilisant deux algorithmes d'estimation qui sont l'algorithme de Newton-Raphson et celui de Nelder-Mead. L'algorithme de Nelder- Mead a montré une meilleure qualité d'estimation au prix d'un plus grand temps de calcul. Les résultats obtenus dans cette étude ont montré que le modèle proposé peut être utilisé efficacement pour le traitement des échos océaniques de Brown ainsi que les échos côtiers corrompus par des pics gaussiens symétriques ou asymétriques. L'évaluation des bornes de Cramér-Rao a confirmé les bonnes performances de l'algorithme de Nelder-Mead. Ces bornes ont aussi permis de quantifier la détérioration des paramètres estimés associés au modèle de Brown lors de l'estimation des paramètres du pic. En effet, l'estimation d'un plus grand

nombre de paramètres conduit nécessairement à une augmentation des bornes des paramètres associés au modèle Brown, qui s'est avérée faible dans notre cas.

La deuxième solution est basée sur l'étude de l'altimétrie SAR/Doppler. Cette nouvelle technologie se présente comme une solution aux limitations de l'altimétrie conventionnelle puisqu'elle vise la réduction du bruit de mesure et l'augmentation de la résolution dans la direction de marche du satellite. Toutefois, les échos obtenus sont différents de ceux de l'altimétrie conventionnelle et nécessitent, de ce fait, l'élaboration d'un nouveau modèle propre à cette technologie. L'objectif principal du chapitre 3 était de proposer un modèle pour ces échos ainsi que l'algorithme d'estimation correspondant. Le modèle proposé est basé sur une approche géométrique pour le calcul de la réponse impulsionnelle d'une mer plate. L'expression analytique a été obtenue en supposant un diagramme d'antenne circulaire sans dépointage, aucun effet de la vitesse verticale du satellite et un coefficient de rétrodiffusion constant dans la surface observée. La puissance moyenne de l'écho SAR/Doppler est alors obtenue en convoluant numériquement la formule analytique proposée avec la densité de probabilité de la hauteur des points de dispersion et la réponse impulsionnelle du radar. L'étude des signaux synthétiques a montré l'intérêt du traitement de migration en distance ainsi que l'importance des bandes Doppler centrales qui contiennent la majorité de l'information. L'estimation des paramètres altimétriques est effectuée à l'aide de la méthode des moindres carrés en utilisant l'algorithme de Levenberg-Marquardt. Le choix de cet algorithme permet l'utilisation de dérivées numériques du modèle et de comparer nos résultats avec ceux du modèle de SAMOSA qui utilise le même algorithme. Les bornes de Cramér-Rao ont aussi été développées afin de fournir une référence pour l'évaluation de la qualité d'estimation. Ces bornes ont été utilisées pour évaluer la méthode d'estimation proposée et la comparer avec d'autres méthodes d'estimation tels que l'estimateur du maximum de vraisemblance et la méthode des moindres carrés pondérés. Les résultats obtenus ont montré la supériorité de l'altimétrie SAR/Doppler par rapport à l'altimétrie conventionnelle en termes de la qualité des paramètres estimés et la réduction de leurs corrélations.

Le modèle développé dans le chapitre 3 ne tient pas compte du dépointage de l'antenne ce qui peut conduire à une réduction des performances d'estimation. Ce point a été étudié dans le chapitre 4 qui propose un nouveau modèle généralisé pour l'altimétrie SAR/Doppler. Le modèle proposé considère

un diagramme d'antenne circulaire avec dépointage, aucun effet de la vitesse verticale du satellite et un coefficient de rétrodiffusion constant dans la surface observée. Les approximations utilisées pour établir la formule analytique proposée ont été étudiées et leurs erreurs quantifiées. Le modèle ainsi obtenu a été analysé et l'effet du dépointage a été étudié suivant les directions azimutale et transverse. Il a été montré que le dépointage transverse affecte la forme et l'amplitude de l'écho SAR/Doppler alors que le dépointage azimutal n'affecte que son amplitude. Ce comportement peut causer des problèmes lors de l'estimation de cinq paramètres à partir de l'écho multi-vues. Une solution qui consiste à estimer quatre paramètres a été proposée et validée. Cette stratégie offre de meilleures performances que celles du chapitre précédent puisqu'elle fournit une meilleure qualité des paramètres estimés ainsi qu'une parfaite adéquation entre l'écho observé et son estimé. Ce chapitre a aussi défini une autre procédure d'estimation qui introduit les valeurs des angles de dépointage estimés dans le modèle proposé et estime ensuite trois paramètres. Cette solution semble être un outil intéressant pour obtenir une meilleure qualité des paramètres estimés sans pour autant augmenter le temps de calcul. Cette stratégie peut facilement être appliquée à l'altimètre SIRAL de Cryosat-2 puisqu'il fournit une mesure du dépointage par l'utilisation du senseur stellaire. A noter enfin qu'une comparaison entre l'altimétrie conventionnelle et SAR/Doppler a clairement montré la supériorité de cette dernière.

Perspectives

Plusieurs études peuvent être envisagées pour les travaux futurs. Concernant la première partie de la thèse, une première piste serait la généralisation du modèle côtier à quatre paramètres afin de tenir compte du dépointage de l'antenne. Ce modèle pourrait également être généralisé pour tenir compte du cas à plusieurs pics au lieu de ne considérer qu'un seul pic. Dans l'approche proposée, le modèle Brown a été généralisé en lui ajoutant un pic gaussien. Une autre approche pour résoudre le problème de l'altimétrie côtière pourrait être d'élaborer un modèle de FSIR qui prend en compte la nature de la surface observée, c'est à dire, de l'eau et de la terre dans le cas du littoral. Ce point offrirait peut être une interprétation physique des paramètres du pic.

Concernant l'altimétrie SAR/Doppler, le premier point devrait être la comparaison du modèle

proposé avec celui de SAMOSA. Ce point n'a pas été fait dans le présent ouvrage en raison de l'absence de documentation sur le modèle SAMOSA qui n'est pas encore publié. Un deuxième point consiste en la généralisation du modèle proposé pour tenir compte de l'ellipticité de l'antenne, l'effet de la vitesse verticale et un coefficient de rétrodiffusion non constant dans la surface observée. Par ailleurs, une piste intéressante consisterait en l'élaboration d'un modèle analytique complet pour l'écho multi-vues. Ce calcul fera forcément intervenir plus d'approximations, qu'il convient de bien analyser afin de contrôler le comportement du modèle résultant. Concernant l'estimation paramétrique, on pourrait envisager l'estimation des paramètres à partir de la carte distance/Doppler à la place des échos multi-vues afin d'améliorer la qualité des 5 paramètres d'intérêt. Il est aussi intéressant de généraliser l'estimateur du maximum de vraisemblance établi dans l'annexe I au cas de 4 et 5 paramètres.

Le dernier point s'intéresse à la procédure d'estimation paramétrique pour à la fois l'altimétrie conventionnelle et SAR/Doppler. En effet, la présente thèse s'est intéressée à l'estimation paramétrique en considérant les échos de façon indépendante. Cependant, il est bien connu que les échos adjacents présentent des paramètres altimétriques similaires en raison de leur nature physique. Par conséquent, il est d'un grand intérêt d'établir des algorithmes d'estimation qui prennent en considération cette corrélation afin de réduire le bruit de mesure et/ou le temps de calcul.

Appendices

Appendix A

Derivatives of Brown echoes and Gaussian peaks

As explained by (2.12), the computation of the FIM requires the elaboration of the first order derivatives of the Brown signal s_k and the asymmetric Gaussian peak p_k.

Brown signal

The derivatives of the Brown signal are given by

$$\begin{aligned}
&\frac{\partial s_k}{\partial N_t} = 1, \quad \frac{\partial s_k}{\partial P_u} = M_{k,\tau,\mathrm{SWH}} \\
&\frac{\partial s_k}{\partial \tau_s} = -\frac{P_u}{\sqrt{2\pi}\sigma_c} \exp\left(C_{k,\tau,\mathrm{SWH}} - B^2_{k,\tau,\mathrm{SWH}}\right) + \alpha P_u M_{k,\tau,\mathrm{SWH}} \\
&\frac{\partial s_k}{\partial \mathrm{SWH}} = \frac{\mathrm{SWH}}{4\sigma_c c^2}\left[P_u \sigma_c \alpha^2 M_{k,\tau,\mathrm{SWH}} + \frac{P_u}{\sqrt{\pi}} \exp\left(C_{k,\tau,\mathrm{SWH}} - B^2_{k,\tau,\mathrm{SWH}}\right) G_{k,\tau,\mathrm{SWH},\alpha}\right]
\end{aligned} \tag{A.1}$$

with

$$\begin{aligned}
B_{k,\tau,\mathrm{SWH}} &= \frac{kT_s - \tau_s - \alpha\sigma_c^2}{\sqrt{2}\sigma_c} \\
C_{k,\tau,\mathrm{SWH}} &= -\alpha\left(kT_s - \tau_s - \frac{\alpha\sigma_c^2}{2}\right) \\
M_{k,\tau,\mathrm{SWH}} &= \frac{1}{2}\exp\left(C_{k,\tau,\mathrm{SWH}}\right)\left[1 + \mathrm{erf}(B_{k,\tau,\mathrm{SWH}})\right] \\
G_{k,\tau,\mathrm{SWH},\alpha} &= -\sqrt{2}\alpha - \frac{B_{k,\tau,\mathrm{SWH}}}{\sigma_c}
\end{aligned} \tag{A.2}$$

Asymmetric Gaussian peak

The derivatives of the Gaussian peak are given by

$$\begin{aligned}
&\tfrac{\partial p_k}{\partial N_t} = 0, \;\; \tfrac{\partial p_k}{\partial A} = \tfrac{p_k}{A} \\
&\tfrac{\partial p_k}{\partial T} = p_k \tfrac{kT_s - T}{\sigma^2} - \sqrt{\tfrac{2}{\pi}} A\eta \, \exp\left(D_{k,\sigma,T} - E^2_{k,\eta,T}\right) \\
&\tfrac{\partial p_k}{\partial \sigma} = -\tfrac{2}{\sigma} p_k D_{k,\sigma,T} \\
&\tfrac{\partial p_k}{\partial \eta} = \tfrac{\sqrt{2}A(kT_s - T)}{\sqrt{\pi}} \, \exp\left(D_{k,\sigma,T} - E^2_{k,\eta,T}\right)
\end{aligned} \tag{A.3}$$

with

$$D_{k,\sigma,T} = \tfrac{-1}{2\sigma^2} \left(kT_s - T\right)^2, \;\; E_{k,\eta,T} = \eta \tfrac{(kT_s - T)}{\sqrt{2}} \tag{A.4}$$

Appendix B

Comparison between NR and LM algorithms

The Levenberg-Marquardt algorithm is similar to the Newton-Raphson algorithm in that it is a gradient descent algorithm. Both algorithms use a matrix inversion when updating the vector of parameters (see Section 3.4.1 for the description of the LM algorithm). The difference between the two algorithms is that instead of inverting the matrix of interest, the LM algorithm adds a regularization parameter to this matrix which provides more robustness in the inversion and allows to better control the algorithm convergence. Note that the NR algorithm performs well when considering the analytical derivatives of the model as shown in Section 2.7.2. However, when considering numerical derivatives, it is better to consider the LM algorithm to avoid numerical issue. Fig. B.1 shows the parameter RMSEs and REs (defined in Section 2.7.1) when estimating Brown echoes and considering the two NR and LM algorithms. Two cases are considered for the LM. The first one considers analytical derivatives of the Brown model and is denoted by LM-AD for LM with analytical derivatives. The second case approximates the derivatives as follows

$$\frac{\partial \boldsymbol{s}(\boldsymbol{\theta})}{\partial \theta_i} \simeq \frac{\boldsymbol{s}\left(\theta_i + \Delta\theta_i\right) - \boldsymbol{s}\left(\theta_i\right)}{\Delta\theta_i} \tag{B.1}$$

and is denoted by LM-ND for LM with numerical derivatives. The obtained results show the robustness of the LM to the derivative computations and illustrate the similar behavior of the LM and NR algorithms.

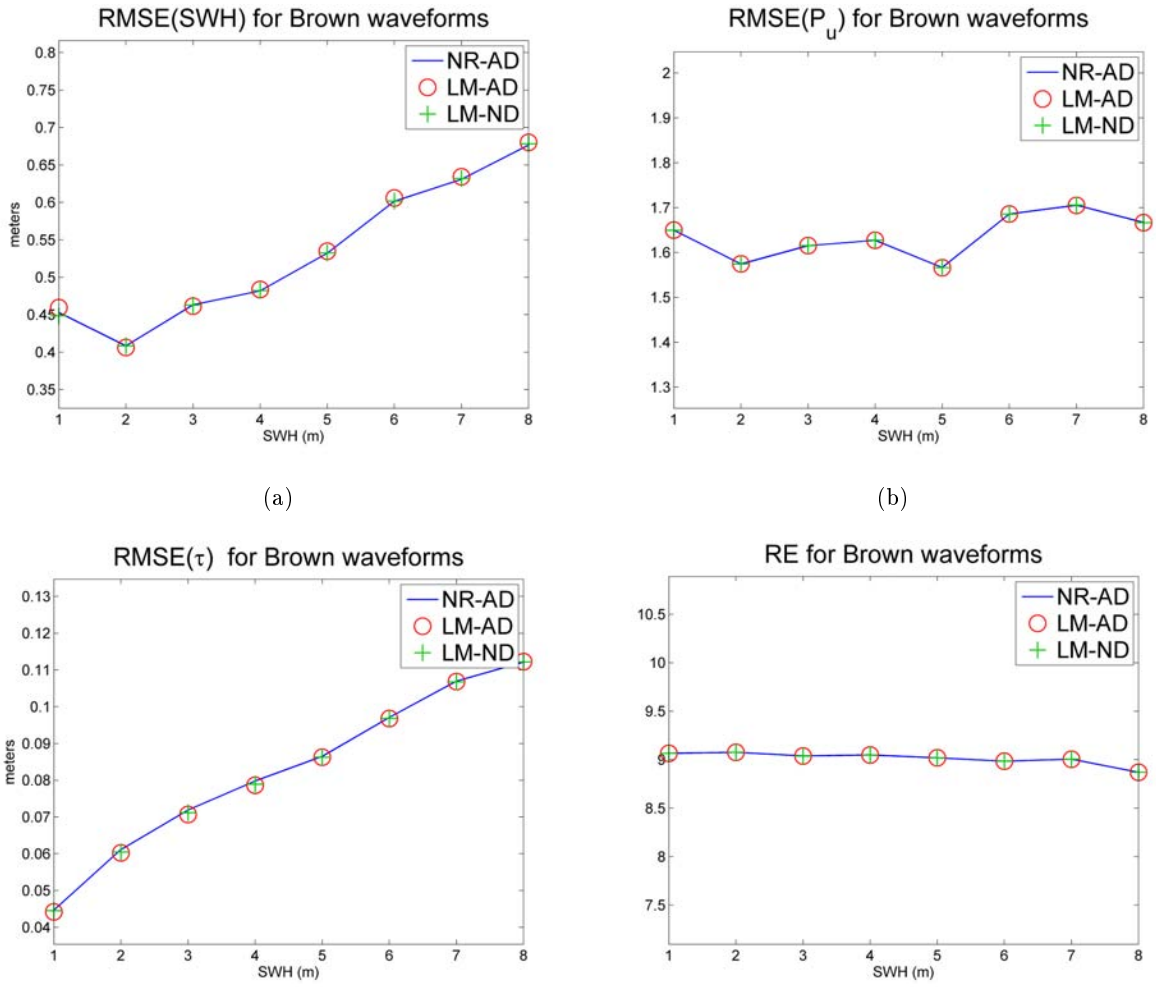

Figure B.1: REs and RMSEs for the Newton-Raphson with analytical derivatives (NR-AD), Levenberg-Marquardt with analytical derivatives (LM-AD) and Levenberg-Marquardt with numerical derivatives (LM-ND) algorithms.

Appendix C

Peak's amplitude importance

The importance of the peak's amplitude on the estimates was evaluated by estimating class 13 waveforms when varying A from 10 to 200 while keeping $P_u = 130$ constant, as well as $\tau = 31\,T_s$, SWH $= 5, T = 75\,T_s, \sigma = 3\,T_s, \gamma = 0$. Fig. C.1 presents the RMSEs obtained for the three parameters τ, P_u and SWH, using NM or NR algorithm, and in the case of the three possible models; Brown (in blue), BGP (in red) and BAGP (in green). It can be seen that RMSEs are equivalent when using any of the three models while the amplitude of the peak A remains lower than 30% of the peak of the Brown part (P_u). Above this threshold, lower RMSEs are obtained when considering BGP or BAGP. Therefore, when the amplitude of the peak represents more than 30% of the Brown peak, it is of increasing interest to consider these models.

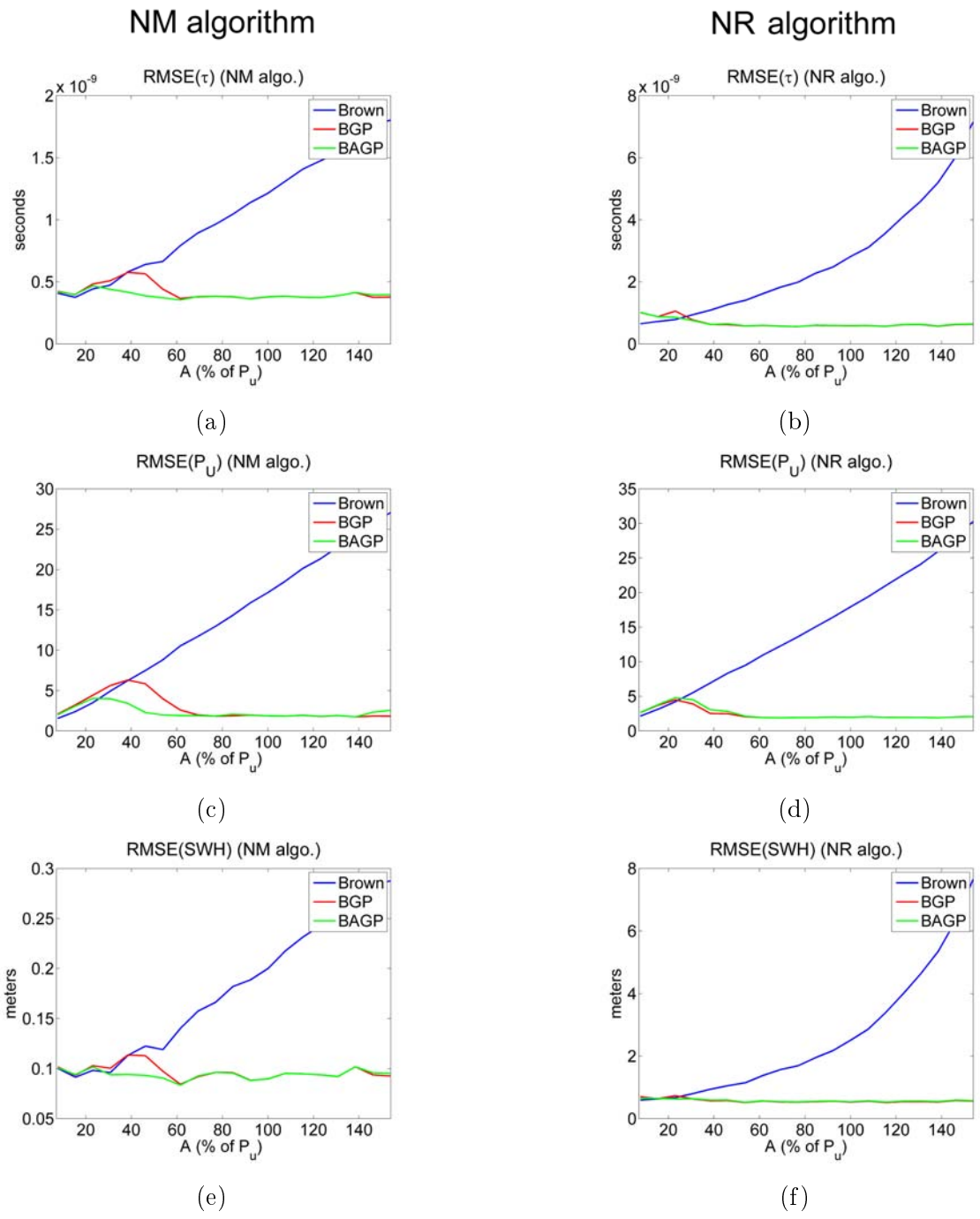

Figure C.1: RMSEs for signals of class 13 with NM (left) and NR (right) algorithms when using Brown (blue), BGP (red) or BAGP (green) models. The top, middle and bottom figures are associated with τ, P_u and SWH respectively.

The CRBs for the three models (Brown model, BGP and BAGP) were also evaluated when varying the peak amplitude A from 10 to 200. The parameter vector is the same as above. The results are shown in Fig. C.2. Note the slight influence of A on the CRBs of τ, P_u and SWH.

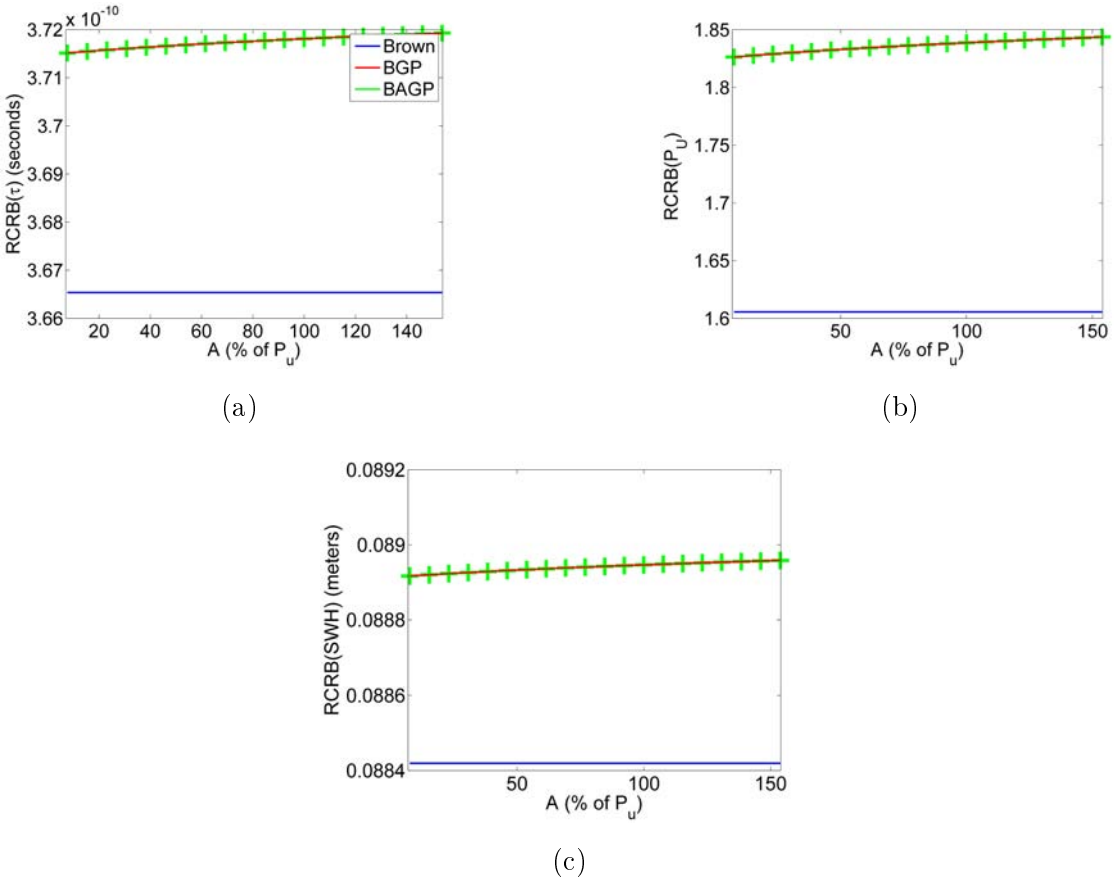

Figure C.2: RCRBs for the Brown, BGP and BAGP models versus A with parameter vectors $\boldsymbol{\theta}_{\text{Brown}} = (P_u, \tau, \text{SWH})^T = (130, 31\,T_s, 5)^T$, $\boldsymbol{\theta}_{\text{BGP}} = (P_u, \tau, \text{SWH}, T, \sigma)^T = (130, 31\,T_s, \ \ 5, 75\,T_s, 3\,T_s)^T$ and $\boldsymbol{\theta}_{\text{BAGP}} = (P_u, \tau, \text{SWH}, T, \sigma, \gamma)^T = (130, 31\,T_s, 5, 75\,T_s, 3\,T_s, 0)^T$.

Appendix D

Results for real Jason-2 waveforms

Other datasets have also been analyzed providing the results shown in Figs. D.1, D.2, D.3 and D.4.

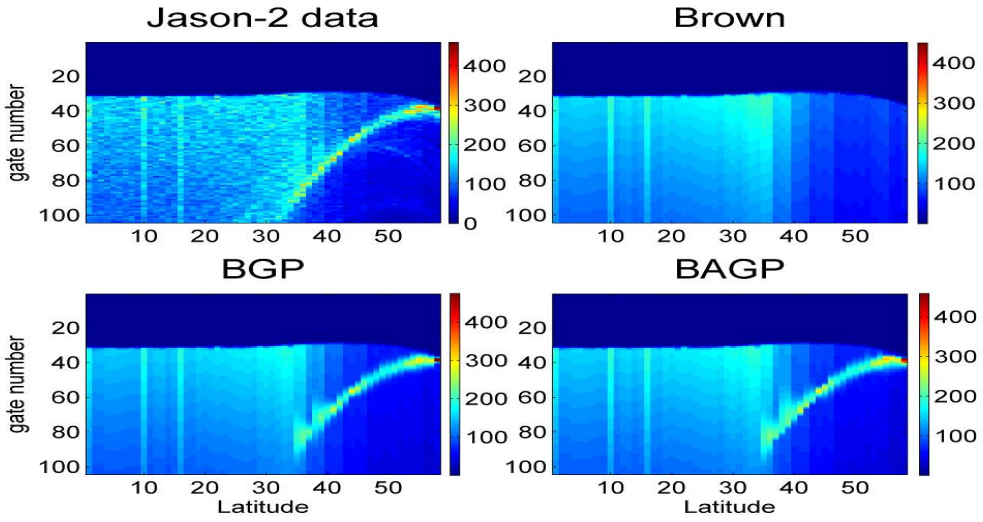

Figure D.1: Jason-2 waveforms estimated by using Brown (top-right), BGP (bottom-left) and BAGP (bottom-right) models. The waveforms were extracted from pass 33 of cycle 8 around Aegean Sea.

The BGP and BAGP models are clearly able to reconstruct the power changes due to the presence of peaks in the altimetric waveforms. Examples of waveforms that cannot be processed accurately with the Brown model are shown in Fig. D.5.

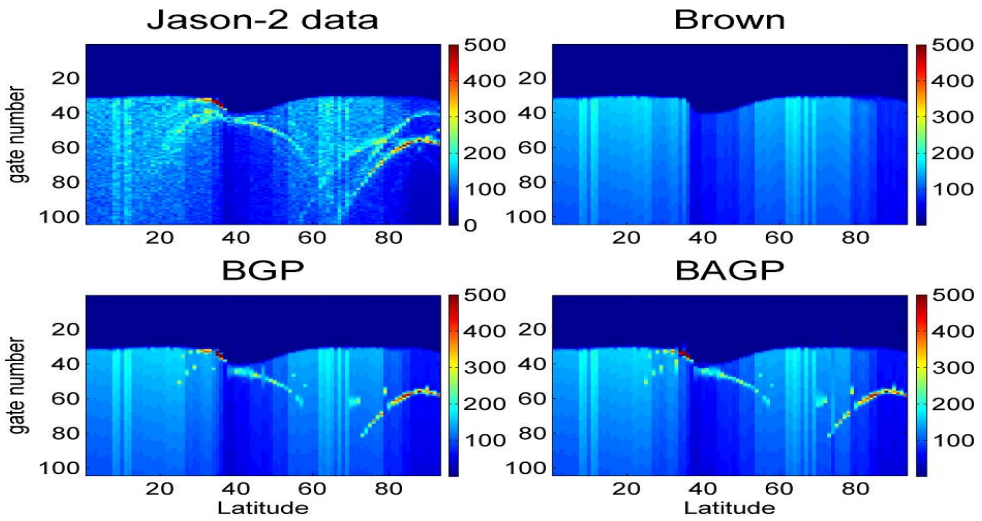

Figure D.2: Jason-2 waveforms estimated by using Brown (top-right), BGP (bottom-left) and BAGP (bottom-right) models. The waveforms were extracted from pass 61 of cycle 8 around Brest (France).

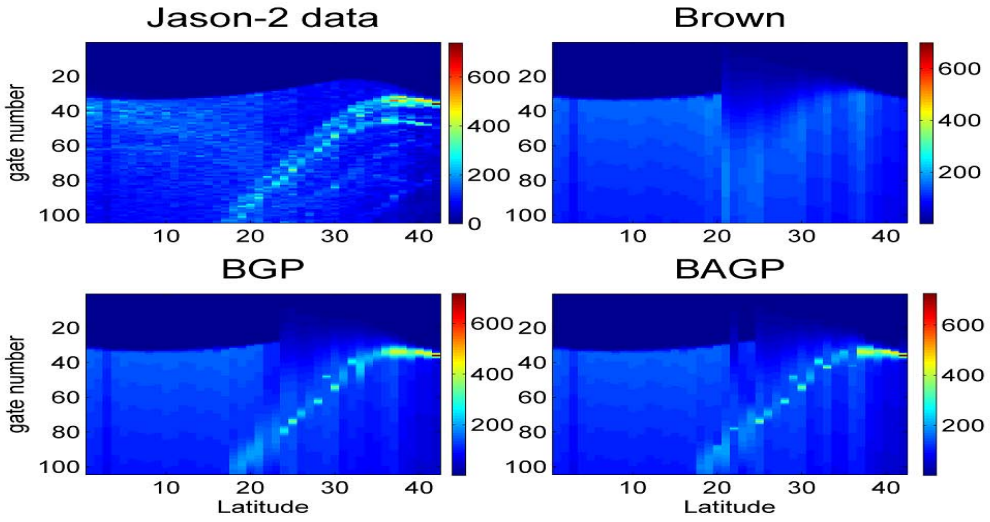

Figure D.3: Jason-2 waveforms estimated by using Brown (top-right), BGP (bottom-left) and BAGP (bottom-right) models. The waveforms were extracted from pass 137 of cycle 8 around Belle-$\widehat{I}$le-en-Mer Island (France).

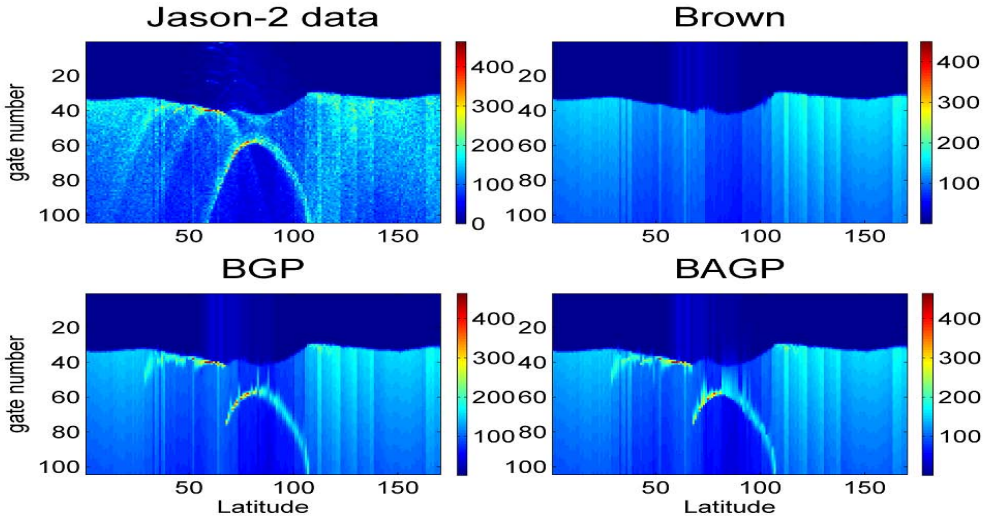

Figure D.4: Jason-2 waveforms estimated by using Brown (top-right), BGP (bottom-left) and BAGP (bottom-right) models. The waveforms were extracted from pass 187 of cycle 8 around Ibiza Island.

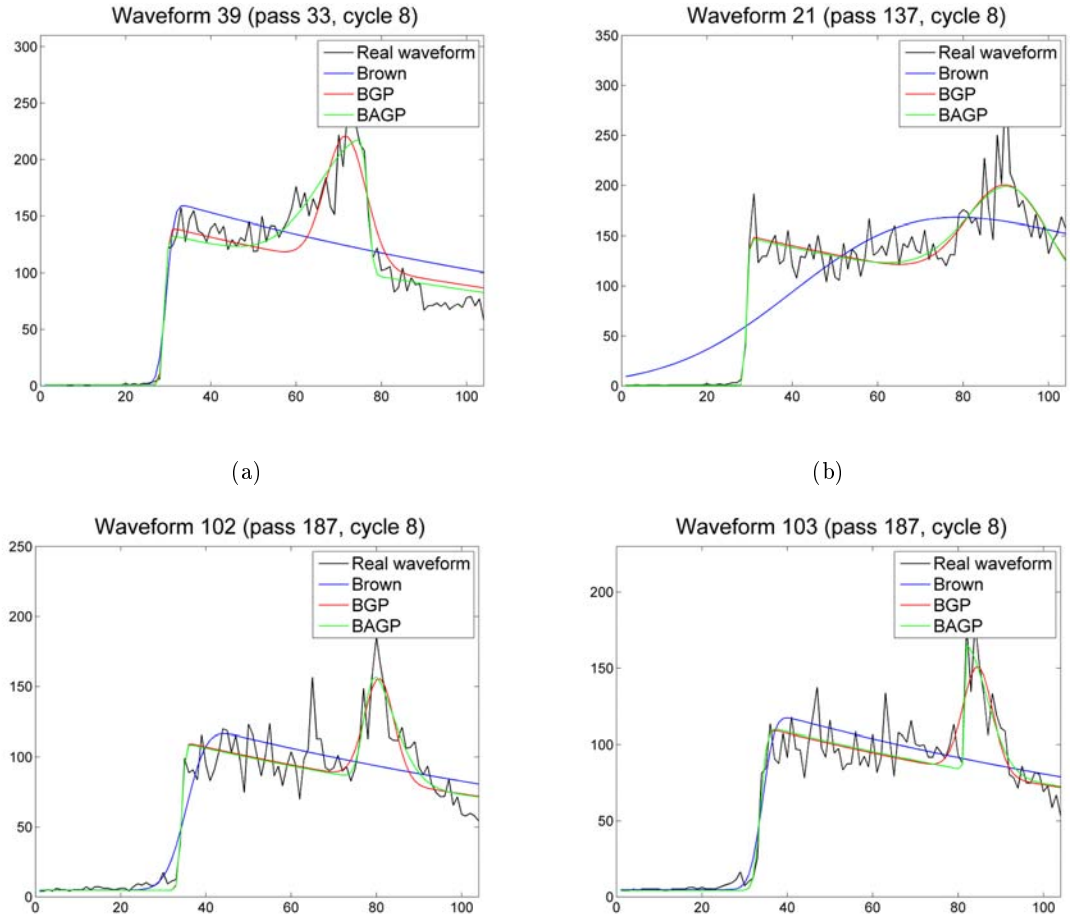

Figure D.5: Examples of real JASON-2 waveforms and their estimations.

Appendix E

An approximation of the Doppler beam formula

This section is concerned with the study of the approximation (3.9). As explained in section 3.3.2, the coordinate of the along-track beam (also called along-track band) is given by (3.8). This formula provides an hyperbolic shape for the coordinate $y_n(t)$. This appendix discusses the approximation made in order to obtain (3.9) and allowing $y_n(t)$ to be time independent (y_n is constant in the across-track direction). Fig. E.1 shows 32 beams obtained by using (3.8) and (3.9) where (3.8) corresponds to hyperbolic beams and (3.9) to rectangular beams. This figure shows an excellent agreement between both expressions validating the approximation $\rho(t) << h$. Fig. E.2 shows zooms of beams #33 (central beam) and #64 (the furthest beam from nadir). Note that the difference between the hyperbolic and rectangular central beams is less than 2 cm. This negligible difference occurs at a distance of ≈ 10 km which only affects the end of the trailing-edge of the Doppler waveform. Fig. E.2 (right) finally shows the hyperbolic and rectangular beams when considering the last extreme beam #64. The difference between the two beams (about 1 m) is negligible compared to the along-track distance which is of the order of 10 km. Note finally that the approximation (3.9) was also proposed in [Raney, 1998].

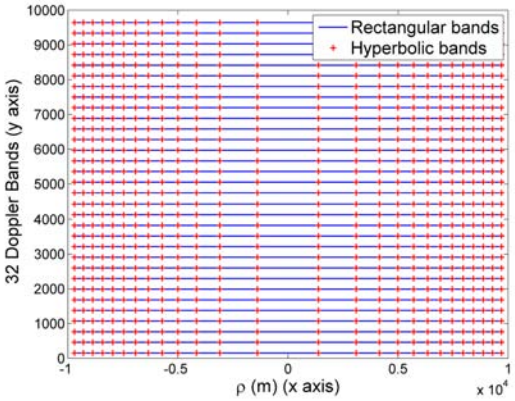

Figure E.1: Rectangular and hyperbolic Doppler beams.

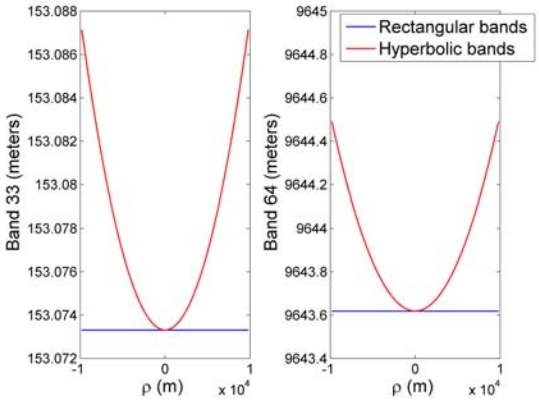

Figure E.2: Rectangular and hyperbolic Doppler beams for the beam #33 (left) and the beam #64 (right).

Appendix F

Earth curvature

Equations (3.2) and (3.12) introduced the analytical model when considering flat Earth surface. Some corrections have to be included in order to take into account the Earth curvature. Figs. F.1.a and F.1.b show the geometry of the scene in the two cases. Introducing Earth curvature is obtained by

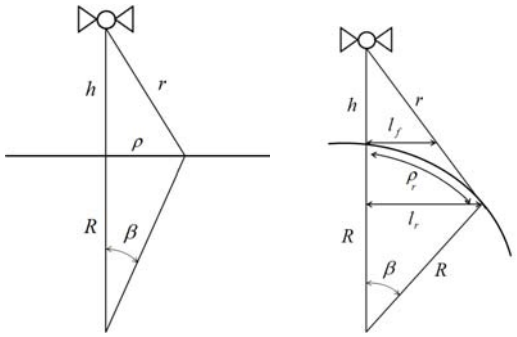

(a) (b)

Figure F.1: Geometry for (a) flat Earth surface and (b) round Earth surface.

changing the expression of r in (1.6). In the case of a round Earth, ρ_r and l_r are related according to the following expression

$$\rho_r = R \operatorname{asin}\left(\frac{l_r}{R}\right) \tag{F.1}$$

where $R = 6378137$ m is the Earth radius, asin(.) is the inverse sine function and l_r is the distance between the illuminated point and the line linking the satellite to the center of Earth (see Fig. F.1.b). This equation shows that $\rho_r \approx l_r$ for small angle geometry. Indeed, by considering a pessimistic case corresponding to the large value of $l_r = 10$ km, we obtain $\rho_r - l_r = 4$ mm which is a negligible difference. Therefore, we will consider $\rho_r = l_r$ in the rest of this section. The distance r between the

satellite and the observed surface is given by the following formula

$$r = \sqrt{(R\sin\beta)^2 + (h + R - R\cos\beta)^2} \tag{F.2}$$

where β is the angle between the illuminated point and the line linking the satellite to the center of Earth (see Fig. F.1.b). Considering that $R\sin\beta = \rho_r$ and $\rho_r^2 << R^2$, (F.2) reduces to

$$r \simeq \sqrt{h^2 + \alpha_r \rho_r^2} \tag{F.3}$$

where $\alpha_r = 1 + \frac{h}{R} = 1.11$ is the curvature factor. By replacing (F.3) in (1.6), straightforward computations show that $\rho_r(t') = \frac{1}{\sqrt{\alpha_r}}\sqrt{\left(\frac{t'c}{2}\right)^2 - h^2}$. When using the two-way incremental ranging time $t = t' - \frac{2h}{c}$ and the approximation $\frac{ct}{h} << 1$ (valid for spaceborne altimetry [Brown, 1977]), we can see that $\rho(t) \simeq \sqrt{hct}$ used for a flat Earth has to be replaced by $\rho_r(t) \simeq \sqrt{\frac{hct}{\alpha_r}}$ for a round Earth. In other words, to move from a flat Earth to a round Earth, it is sufficient to divide t by α_r. Note that the same change of variable was proposed in [Rodriguez, 1988] for conventional altimetry. Note finally the negligible effect of Earth curvature on Doppler band. This result can be justified by considering the Doppler beam formula for round Earth which is obtained by generalizing the expression of $r_n(t)$ given in (3.7) as follows

$$r_n(t) = \sqrt{h^2 + \alpha_r \rho_r^2(t)} \tag{F.4}$$

which leads to the following width of the along-track beam

$$y_n(t) = \left(\frac{\lambda f_n}{2v_s}\right)\sqrt{h^2 + \alpha_r \rho_r^2(t)}. \tag{F.5}$$

Note that we always have $\alpha_r \rho_r^2(t) << h^2$ which means that the effect of Earth curvature (represented in (F.5) by α_r and ρ_r) is negligible since we can simplify (F.5) to (3.9) as explained in Section 3.3.2.

Appendix G

Derivatives of CA3 and DDA3

G.1 Derivatives of conventional model

This section provides the derivatives of the conventional model with respect to the altimetric parameters P_u, SWH and τ. Before that, note that the conventional signal $s(t)$ could be written in a different manner which will facilitate the derivatives computation. Indeed, the epoch τ only introduce a shift in time in FSIR which will result in a time shift in $s(t)$. The shifted FSIR can then be expressed as follows

$$\mathrm{FSIR}(t) = P_u \left[g_c(t) * \delta(t - \tau_s) \right] \tag{G.1}$$

with

$$g_c(t) = \exp\left[-\frac{4ct}{\gamma h} \right] U(t) \,. \tag{G.2}$$

The properties of the convolution product (commutativity and associativity) lead to the following expression for the signal $s(t)$

$$s(t) = P_u \left[\mathrm{PDF}(t - \tau_s) * g_c(t) * \mathrm{PTR}_T(t) \right] \tag{G.3}$$

The derivatives of $s(t)$ are then given by

$$\begin{aligned} \frac{\partial s}{\partial P_u} &= \mathrm{PDF}(t - \tau_s) * g_c(t) * \mathrm{PTR}_T(t) \\ \frac{\partial s}{\partial \mathrm{SWH}} &= P_u \left[\frac{\partial \mathrm{PDF}(t - \tau_s)}{\partial \mathrm{SWH}} * g_c(t) * \mathrm{PTR}_T(t) \right] \\ \frac{\partial s}{\partial \tau} &= P_u \left[\frac{\partial \mathrm{PDF}(t - \tau_s)}{\partial \tau} * g_c(t) * \mathrm{PTR}_T(t) \right] \end{aligned} \tag{G.4}$$

with

$$\begin{aligned}\frac{\partial \mathrm{PDF}(t-\tau_s)}{\partial \mathrm{SWH}} &= \frac{2c}{\sqrt{2\pi}\mathrm{SWH}^2}\left\{\left[\frac{2c(t-\tau_s)}{\mathrm{SWH}}\right]^2-1\right\}\exp\left\{-2\left[\frac{c(t-\tau_s)}{\mathrm{SWH}}\right]^2\right\}\\ \frac{\partial \mathrm{PDF}(t-\tau_s)}{\partial \tau} &= \frac{4T_s c^2(t-\tau_s)}{\mathrm{SWH}^2}\times \mathrm{PDF}(t-\tau_s)\end{aligned} \tag{G.5}$$

since, in (G.3), only the PDF depends on the altimetric parameters SWH and τ. The matrix $\boldsymbol{D}_c$ is finally obtained by gathering the discrete derivatives of the vector $\boldsymbol{s}$ as follows $\boldsymbol{D}_c = \left(\frac{\partial \boldsymbol{s}_c}{\partial \mathrm{SWH}}, \frac{\partial \boldsymbol{s}_c}{\partial \tau}, \frac{\partial \boldsymbol{s}_c}{\partial P_u}\right)$.

G.2 Derivatives of delay/Doppler model

As in conventional altimetry, the FSIR can be expressed as

$$\mathrm{FSIR}(t,n) = P_u\left[g_d(t,n) * \delta(t-\tau_s)\right] \tag{G.6}$$

with

$$g_d(t,n) = \exp\left[-\frac{4ct}{\gamma h}\right]\frac{\left(\phi_{t,n+1}-\phi_{t,n}\right)}{\pi}U(t)$$

for $n = 1, \cdots, N$. It results the following expression for the signal $P(t,n)$

$$P(t,n) = P_u\left[\mathrm{PDF}(t-\tau_s) * g_d(t,n) * \mathrm{PTR}(t,n)\right]. \tag{G.7}$$

The derivatives of $P(t,n)$ are then given by

$$\begin{aligned}\frac{\partial P(t,n)}{\partial P_u} &= \mathrm{PDF}(t-\tau_s) * g_d(t,n) * \mathrm{PTR}(t,n)\\ \frac{\partial P(t,n)}{\partial \mathrm{SWH}} &= P_u\left[\frac{\partial \mathrm{PDF}(t-\tau_s)}{\partial \mathrm{SWH}} * g_d(t,n) * \mathrm{PTR}(t,n)\right]\\ \frac{\partial P(t,n)}{\partial \tau} &= P_u\left[\frac{\partial \mathrm{PDF}(t-\tau_s)}{\partial \tau} * g_d(t,n) * \mathrm{PTR}(t,n)\right]\end{aligned} \tag{G.8}$$

where the PDF derivatives are the same as in (G.5). The matrix $\boldsymbol{D}_d$ is then obtained as follows $\boldsymbol{D}_d = \left(\frac{\partial \boldsymbol{s}}{\partial \mathrm{SWH}}, \frac{\partial \boldsymbol{s}}{\partial \tau}, \frac{\partial \boldsymbol{s}}{\partial P_u}\right)$ where the derivatives of $s(t)$ can be easily deduced from those of $P(t,n)$ using (3.20). Note finally that the derivatives of the signal $m(t,n)$ can be deduced from those of $P(t,n)$ as follows $\frac{\partial m(t,n)}{\partial \theta_i} = \frac{\partial P(t-\delta t_n,n)}{\partial \theta_i}$, for $i \in \{1,2,3\}$.

Appendix H

Results on simulated DDA3 and CA3 echoes

Parameter RMSEs obtained with and without range migration (with the same noise level, i.e., $L = 4$) and by the CA are shown in Fig. H.1 versus the sea wave height (SWH), the epoch (τ) and the amplitude (P_u). These RMSEs are very close to the STDs (see Fig. H.2) since the proposed estimator provides very small biases (see Fig. H.3).

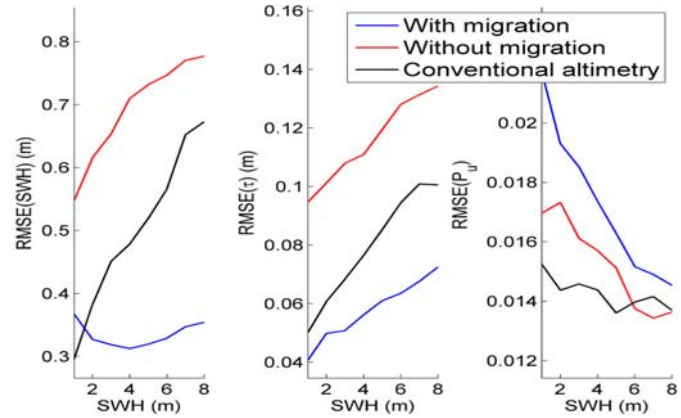

(a)

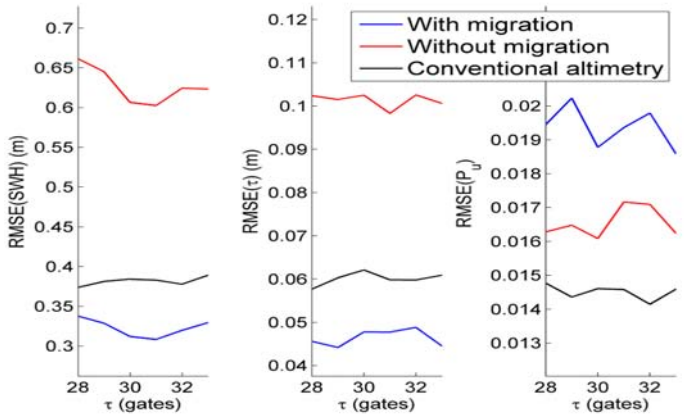

(b)

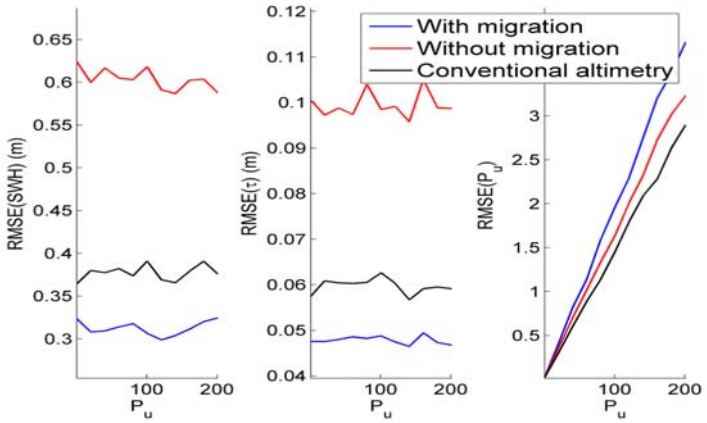

(c)

Figure H.1: Parameter RMSEs for migrated and non-migrated delay/Doppler echoes and conventional echoes (1000 Monte-Carlo realizations). (a) versus SWH with $P_u = 1$ and $\tau = 31$ gates, (b) versus the epoch τ with $P_u = 1$ and SWH $= 2$ m, and (c) versus the amplitude P_u with $\tau = 31$ gates and SWH $= 2$ m.

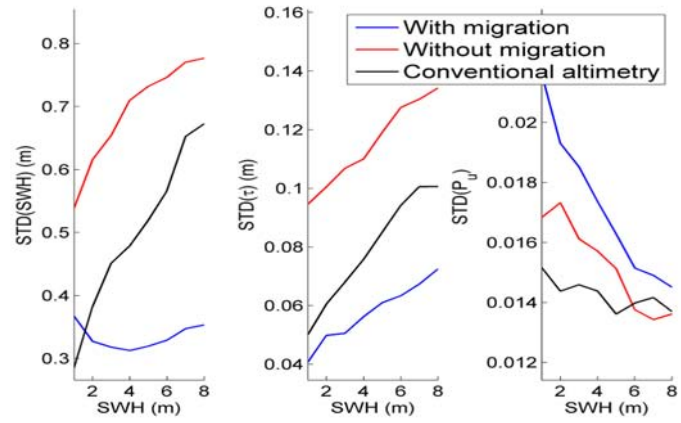

(a)

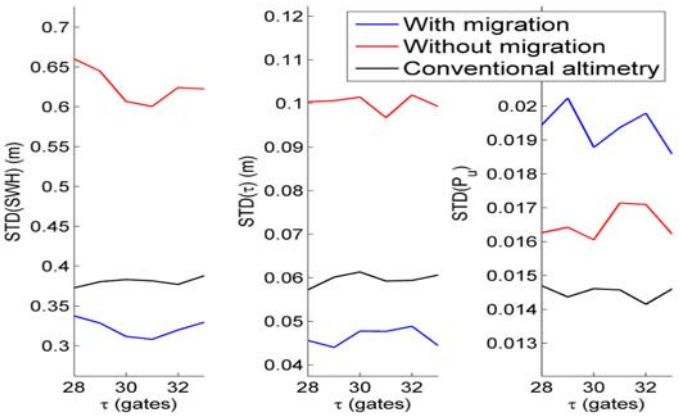

(b)

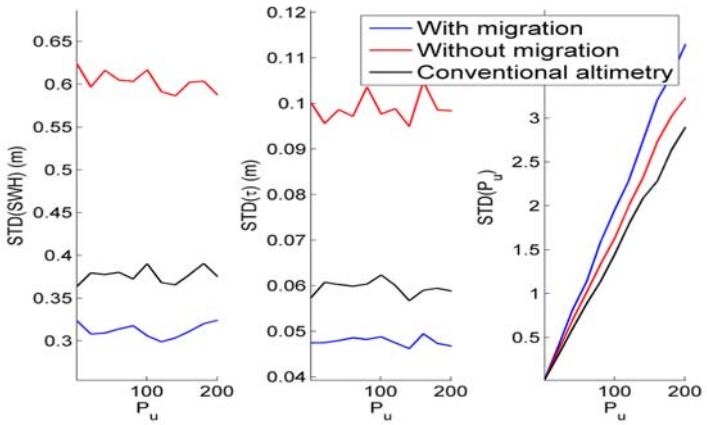

(c)

Figure H.2: Parameter STDs for migrated and non-migrated Doppler echoes and conventional echoes (1000 Monte-Carlo realizations). (a) versus SWH with $P_u = 1$ and $\tau = 31$ gates, (b) versus the epoch τ with $P_u = 1$ and SWH $= 2$ m, and (c) versus the amplitude P_u with $\tau = 31$ gates and SWH $= 2$ m.

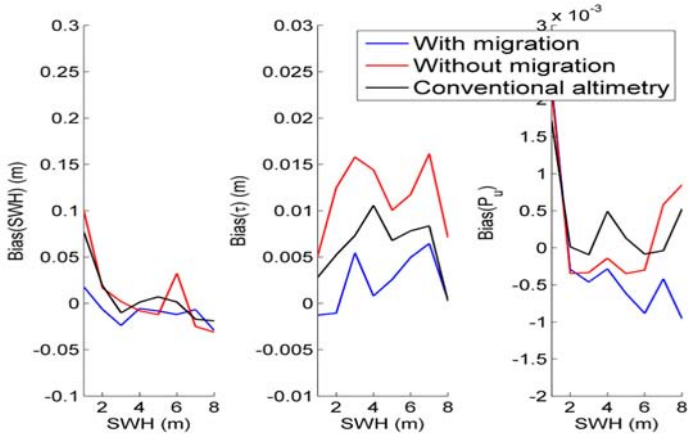

(a)

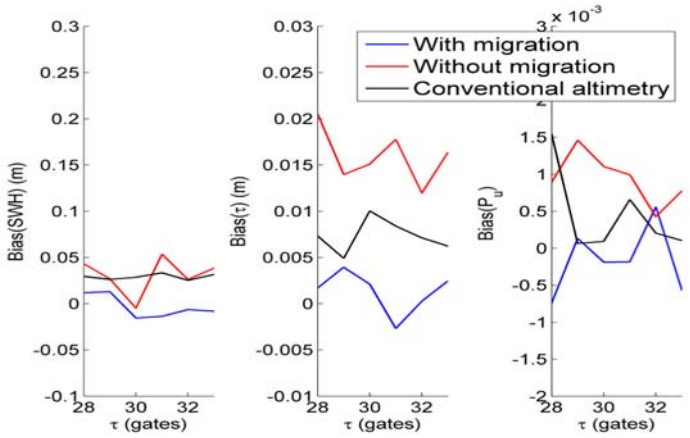

(b)

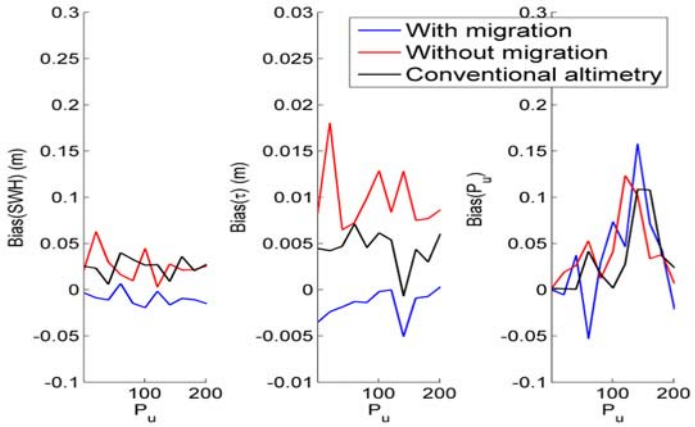

(c)

Figure H.3: Parameter Biases for migrated and non-migrated Doppler echoes and conventional echoes (1000 Monte-Carlo realizations). (a) versus SWH with $P_u = 1$ and $\tau = 31$ gates, (b) versus the epoch τ with $P_u = 1$ and SWH $= 2$ m, and (c) versus the amplitude P_u with $\tau = 31$ gates and SWH $= 2$ m.

Appendix I

Estimation algorithms for DDA3

I.1 Estimation methods

This section compares the proposed least squares procedure to other estimation strategies when considering the proposed DDA3 model. The LS method, that has received much attention in the literature [Amarouche et al., 2004, Dumont, 1985, Rodriguez, 1988], is first reminded. The second method is based on the maximum likelihood principle which provides asymptotically efficient estimators. A third estimator constructed from a WLS criterion is finally investigated.

I.1.1 Least squares estimator

The LS estimator is classically defined as

$$\widehat{\theta}_{\mathrm{LS}} = \underset{\boldsymbol{\theta}}{\operatorname{argmin}} \left[\boldsymbol{y} - \boldsymbol{s}(\boldsymbol{\theta})\right]^T \left[\boldsymbol{y} - \boldsymbol{s}(\boldsymbol{\theta})\right] \tag{I.1}$$

where $\boldsymbol{y}$ is the observed DDA echo, $\boldsymbol{s}(\boldsymbol{\theta})$ is the semi-analytical DDA3 waveform parameterized by $\boldsymbol{\theta} = (\mathrm{SWH}, \tau, P_u)^T$. Since $\boldsymbol{s}(\boldsymbol{\theta})$ is a complicated nonlinear function of SWH and τ, the optimization problem (I.1) does not admit a closed-form expression. We have proposed to solve (I.1) using a numerical optimization method based on the Levenberg-Marquardt (LM) algorithm [Bertsekas, 1995].

I.1.2 Maximum likelihood estimator

The MLE of $\boldsymbol{\theta}$ denoted as $\widehat{\theta}_{\mathrm{ML}}$ is obtained by maximizing the likelihood function $f(\boldsymbol{y}|\boldsymbol{\theta})$ with respect to $\boldsymbol{\theta}$ or by minimizing the negative log-likelihood. Straightforward computations show that the MLE

of $\boldsymbol{\theta}$ reduces to minimize the following cost function

$$\begin{aligned} \mathcal{C}(\boldsymbol{\theta}) &= \ln\left[\det\left(\boldsymbol{\Lambda}(\boldsymbol{\theta})\right)\right] + \left[\boldsymbol{y}-\boldsymbol{s}(\boldsymbol{\theta})\right]^T \boldsymbol{\Lambda}^{-1}(\boldsymbol{\theta})\left[\boldsymbol{y}-\boldsymbol{s}(\boldsymbol{\theta})\right] \\ &= \sum_{k=1}^{K} \ln\left[\Lambda_k(\boldsymbol{\theta})\right] + \sum_{k=1}^{K} \frac{\left[y_k - s_k(\boldsymbol{\theta})\right]^2}{\Lambda_k(\boldsymbol{\theta})}. \end{aligned} \tag{I.2}$$

The MLE is asymptotically efficient and is thus expected to provide the smallest estimation variances. Unfortunately, the LM algorithm, which solves LS problems, cannot be applied to optimize (I.2) because of its form. In this study, we have optimized (I.2) using the Nelder-Mead (NM) algorithm [Bertsekas, 1995].

I.1.3 Weighted least squares estimator

The MLE $\widehat{\theta}_{\mathrm{ML}}$ has nice asymptotical properties (it is asymptotically unbiased, convergent and asymptotically efficient) under mild assumptions. However, its application to delay/Doppler altimetry requires the use of an optimization algorithm (such as the NM algorithm) whose computational cost can be prohibitive [Halimi et al., 2013d]. An alternative is the WLS estimator defined as

$$\widehat{\theta}_{\mathrm{WLS}} = \underset{\boldsymbol{\theta}}{\operatorname{argmin}} \left[\boldsymbol{y}-\boldsymbol{s}(\boldsymbol{\theta})\right]^T \boldsymbol{\Lambda}^{-1}(\boldsymbol{\theta})\left[\boldsymbol{y}-\boldsymbol{s}(\boldsymbol{\theta})\right]. \tag{I.3}$$

An interesting property of this estimator is that the optimization problem (I.3) can be solved by using the LM algorithm (contrary to the optimization problem associated with the MLE). Note that a WLS estimator using a constant weighting matrix was proposed in [Phalippou and Enjolras, 2007]. The estimator (I.3) differs from this estimator since the weighting matrix $\boldsymbol{\Lambda}^{-1}(\boldsymbol{\theta})$ depends on $\boldsymbol{\theta}$. Motivations for using this weighting matrix can be found in [Porat and Friedlander, 1989].

I.2 Results on synthetic data

This section evaluates the performance of the three estimation algorithms introduced in Section I.1 for DDA3. This comparison is conducted by comparing the root mean square errors (RMSEs) of the different estimators. The RCRBs (derived in Section 3.5.2) of the different parameters are also displayed to show whether there is some hope for improving estimation performance or not.

Fig. I.1 compares the RMSEs of the different estimators for the altimetric parameters (SWH (a), P_u (b) and τ (c)). The RCRBs are also displayed providing a reference in terms of estimation performance. The MLE and WLS perform very similarly. The LS estimator shows the worst performance when compared to the ML and WLS estimators. For instance, we can observe a gain of about 20 cm for SWH when using WLS or MLE instead of LS. The RMSEs of the WLS and MLE associated with the parameters SWH and P_u are very close to the corresponding CRBs showing there is no space for improving estimation performance for these two parameters. The situation is different for the epoch parameter since the RMSEs of the WLS and MLEs are 1 cm higher than the RCRBs. Thus, there is some space for developing better estimators for this parameter. This difference between the RMSEs of the MLE and the RCRB may be explained by the fact that asymptotic region has not been reached for $K = 104$ samples.

Finally, it is interesting to mention that the computation cost of the WLS estimator is significantly smaller than that of the MLE. Indeed, estimating the parameters of a DDA3 waveform by the WLS method takes 7.4 seconds (with a MATLAB implementation and a 2.93 GHz i7 CPU) whereas it needs 31 seconds for the MLE. This time reduction is mainly due to the formulation of the WLS that allows the use of the LM algorithm instead of the NM algorithm. Note also that the LS algorithm is the faster algorithm (2.6 seconds for estimating the parameters of a given waveform) but it shows reduced performance because it does not take into account the nature of the noise and in particular the structure of the noise covariance matrix.

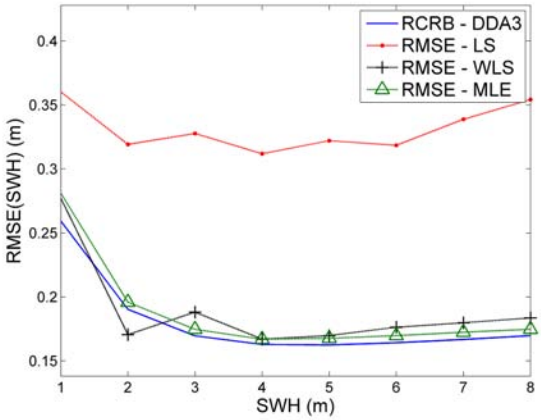

(a)

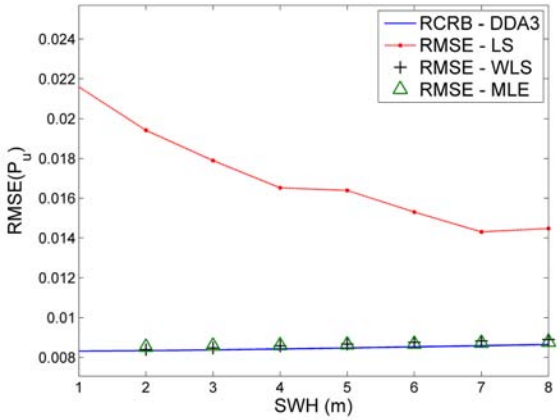

(b)

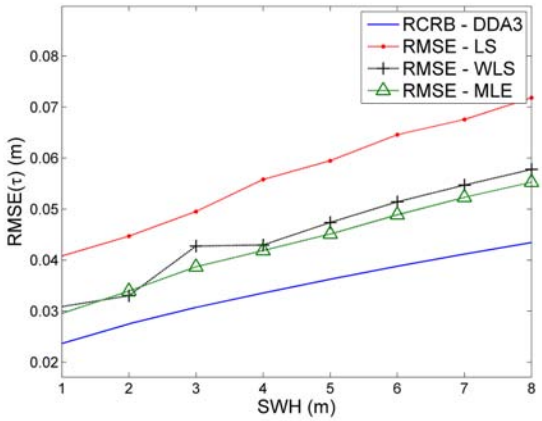

(c)

Figure I.1: RCRBs and RMSEs for the LS, WLS and ML algorithms.

Appendix J

Bounds for the approximation errors

This section studies the error of the first approximation proposed in Section 4.3.3 by determining the maximum achievable error on the FSIR and the multi-look echo. The first approximation introduces an error in the FSIR that is given by

$$\begin{aligned} E_{\mathrm{FSIR}_1}(t,n) &= |\mathrm{FSIR}(t,n) - \mathrm{FSIR}_1(t,n)| \\ &= \frac{P_u}{2\pi}\left(1+\frac{ct}{2h}\right)^{-3} U(t) \exp\left[-\frac{4}{\gamma}\left(1-\frac{\cos^2(\xi)}{1+\epsilon^2(t)}\right)+b\right] E_1(t,n) \end{aligned} \tag{J.1}$$

with

$$E_1(t,n) = \left|\exp\left(-\frac{b}{2}\right)\int_{\tilde{D}_{t,n}} \exp\left[a\cos(\phi)\right]\left[2\sum_{k=1}^{+\infty} I_k\left(\frac{b}{2}\right)\cos(2k\phi)\right]d\phi\right| \tag{J.2}$$

and $\tilde{D}_{t,n} = \left[\tilde{\phi}-\phi_{t,n+1}, \tilde{\phi}-\phi_{t,n}\right] \cup \left[\tilde{\phi}-\phi'_{t,n+1}, \tilde{\phi}-\phi'_{t,n}\right]$. Using the property $|\exp(a\cos\phi)| \leq \exp(a)$, $\forall a>0, \forall\phi$, the following result can be obtained

$$E_1(t,n) \leq 2\exp\left(a-\frac{b}{2}\right)\int_{\tilde{D}_{t,n}}\left|\sum_{k=1}^{+\infty} I_k\left(\frac{b}{2}\right)\cos(2k\phi)\right|d\phi \tag{J.3}$$

Using (4.12), we finally obtain the following expression

$$E_1(t,n) \leq E_1^{\max}(t,n) = 2\exp\left(a-\frac{b}{2}\right)\left[\exp\left(\frac{b}{2}\right)-I_0\left(\frac{b}{2}\right)\right]|\phi_{t,n+1}-\phi_{t,n}| \tag{J.4}$$

which allows to obtain the maximum of the FSIR error $E^{\max}_{\mathrm{FSIR}_1}(t,n)$ by replacing (J.4) in (J.1) as follows

$$\begin{aligned} E^{\max}_{\mathrm{FSIR}_1}(t,n) = \frac{P_u}{\pi}\left(1+\frac{ct}{2h}\right)^{-3} U(t)\exp\left[-\frac{4}{\gamma}\left(1-\frac{\cos^2(\xi)}{1+\epsilon^2(t)}\right)+\frac{b}{2}+a\right] \\ \times\left[\exp\left(\frac{b}{2}\right)-I_0\left(\frac{b}{2}\right)\right]|\phi_{t,n+1}-\phi_{t,n}|. \end{aligned} \tag{J.5}$$

Note that (J.5) provides a theoretical maximum error for the FSIR when considering the first approximation. This maximum error depends on the mispointing parameter ξ (through $\cos\left(\xi^2\right)$ and the variables a and b) while it is not sensitive to $\tilde{\phi}$ which means that the FSIR maximum error is the same whether the mispointing is along-track or across-track. Fig. J.1 (top) shows theoretical maximum error for the FSIR versus delay and Doppler beams when considering a mispointing angle $\xi = 0.5°$. Fig. J.1 (middle) and Fig. J.1 (bottom) show the measured FSIR errors (obtained by comparing the semi-analytical model including the first approximation (4.15) to the exact numerical model) when considering, respectively, along-track mispointing ($\xi_{\text{al}} = 0.5°$) and across-track mispointing ($\xi_{\text{ac}} = 0.5°$). This figure shows that the measured errors are below the theoretical maximum error as expected. Furthermore, it shows that the measured error has a different behavior according to the nature of mispointing (along-track or across-track) which can be explained by the fact that along-track or across-track mispointing angles act differently on the FSIR as detailed in Section 4.5.2.

The upper bounds for the FSIR error given by $E^{\max}_{\text{FSIR}_1}$ is directly used to derive the theoretical maximum error of the resulting multi-look echo (denoted by $E^{\max}_{\text{P1}}(t)$). It can be shown that the maximum multi-look error is obtained by considering $E^{\max}_{\text{FSIR}_1}(t,n)$ instead of $\text{FSIR}(t,n)$ in (4.3) and applying the Doppler processing on the resulting mean power as follows

$$E^{\max}_{\text{P1}}(t) = \sum_{n=1}^{N} \left[E^{\max}_{\text{FSIR}_1}(t-\delta t_n, n) * \text{PDF}(t) * \text{PTR}(t,n)\right]. \tag{J.6}$$

$E^{\max}_{\text{P1}}$ represents the maximum error that we can obtain when comparing the semi-analytical multi-look echo to the exact echo obtained by a numerical computation of (4.10). The maximum normalized quadratic error associated with the first approximation is finally given by

$$\text{NQE}^{\max}_1 = \sqrt{\frac{\sum_{k=1}^{K}\left[E^{\max}_{\text{P1}}(k)\right]^2}{\sum_{k=1}^{K} s^2_{e_k}}}. \tag{J.7}$$

A similar study allows the error introduced by the second approximation to be maximized. Lets

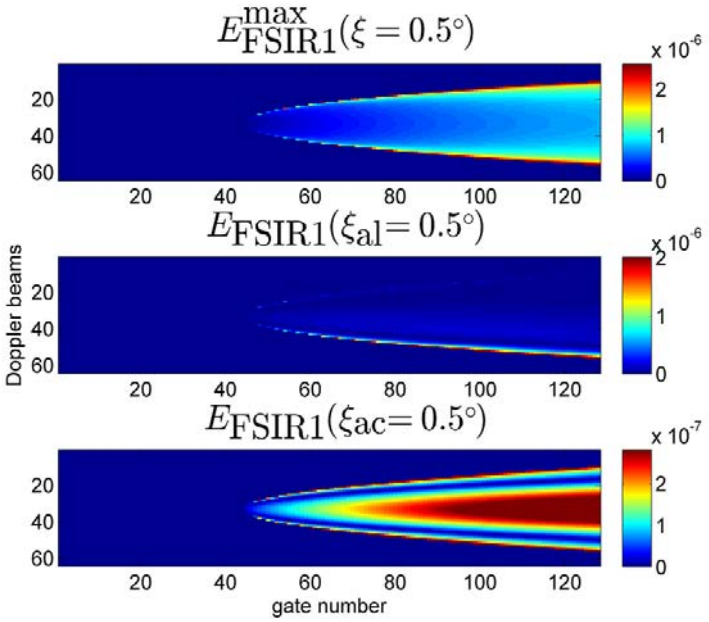

Figure J.1: Error of approximation 1 for the FSIR. (top) maximum theoretical error of the FSIR for $\xi = 0.5°$, (middle) measured error when considering $\xi_{\mathrm{al}} = 0.5°$ and (bottom) measured error when considering $\xi_{\mathrm{ac}} = 0.5°$ (note the scale change).

define the FSIR error by

$$E_{\mathrm{FSIR}_2}(t,n) = |\mathrm{FSIR}_1(t,n) - \mathrm{FSIR}_2(t,n)|$$
$$= \frac{P_u}{2\pi}\left(1+\frac{ct}{2h}\right)^{-3} U(t) \exp\left[-\frac{4}{\gamma}\left(1-\frac{\cos^2(\xi)}{1+\epsilon^2(t)}\right)+b\right] E_2(t,n) \tag{J.8}$$

with

$$E_2(t,n) = \left|2\exp\left(-\frac{b}{2}\right) I_0\left(\frac{b}{2}\right) \int_{\tilde{D}_{t,n}} \left[\sum_{k=m+1}^{+\infty} I_k(a)\cos(k\phi)\right] d\phi\right| \tag{J.9}$$

where $\tilde{D}_{t,n} = \left[\tilde{\phi}-\phi_{t,n+1}, \tilde{\phi}-\phi_{t,n}\right] \cup \left[\tilde{\phi}-\phi'_{t,n+1}, \tilde{\phi}-\phi'_{t,n}\right]$. Straightforward computations lead to the following maximum for $E_2(t,n)$

$$E_2^{\max}(t,n) = 2\exp\left(-\frac{b}{2}\right) I_0\left(\frac{b}{2}\right) \left[\exp(a) - I_0(a) - 2\sum_{k=1}^{m} I_k(a)\right] |\phi_{t,n+1} - \phi_{t,n}| . \tag{J.10}$$

Hence, the theoretical maximum FSIR error associated with the second approximation is given by

$$E^{\max}_{\mathrm{FSIR}_2}(t,n) = \frac{P_u}{\pi}\left(1+\frac{ct}{2h}\right)^{-3} U(t) \exp\left[-\frac{4}{\gamma}\left(1-\frac{\cos^2(\xi)}{1+\epsilon^2(t)}\right)+\frac{b}{2}\right] I_0\left(\frac{b}{2}\right) \times \left[\exp(a) - I_0(a) - 2\sum_{k=1}^{m} I_k(a)\right] |\phi_{t,n+1} - \phi_{t,n}|. \tag{J.11}$$

As explained previously, approximation 2 reduces the number of terms in the infinite sum (4.15) to m terms. The maximum error will then depend on this parameter as shown in (J.11). Note also that this maximum error does not depend on the parameter $\tilde{\phi}$ and thus it is not sensitive to the nature of mispointing. Fig. J.2 (top) shows the theoretical maximum error for $\xi = 0.5°$ when considering $m = 5$ terms. Fig. J.2 (middle) and Fig. J.2 (bottom) show two measured errors when considering along-track and across-track mispointing respectively. Note that the error level is higher than the one introduced by the first approximation which means that the overall error will mainly result from the second approximation (for small values of m) as shown in the Section 4.5.1. As for the first approximation, $E^{\max}_{\mathrm{FSIR}_2}(t,n)$ can be used to derive the maximum multi-look error of the second approximation $E^{\max}_{\mathrm{P2}}(t)$ and its associated normalized quadratic maximum error $\mathrm{NQE}^{\max}_2$ given by

$$\mathrm{NQE}^{\max}_2 = \sqrt{\frac{\sum_{k=1}^{K}\left[E^{\max}_{\mathrm{P2}}(k)\right]^2}{\sum_{k=1}^{K} s_1^2(k)}}. \tag{J.12}$$

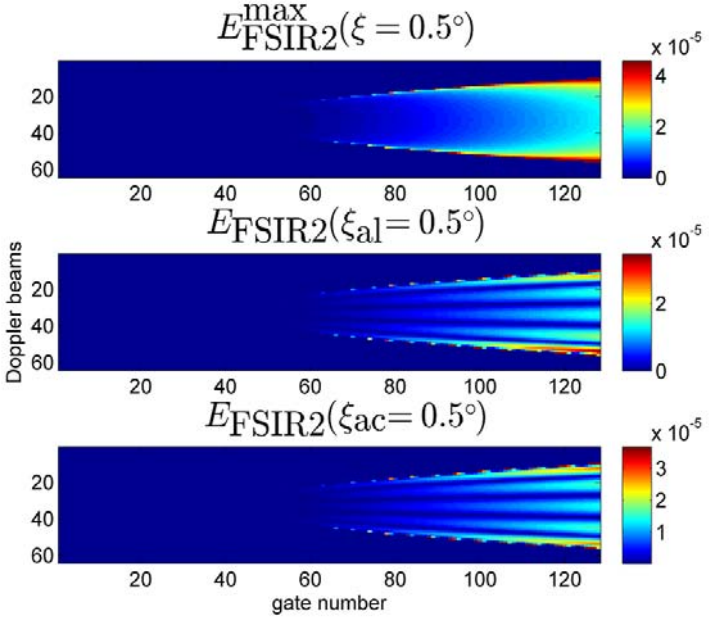

Figure J.2: Error of approximation 2 on the FSIR. (top) maximum theoretical error of the FSIR for $\xi = 0.5°$, (middle) measured error when considering $\xi_{\mathrm{al}} = 0.5°$ and (bottom) measured error when considering $\xi_{\mathrm{ac}} = 0.5°$ (note the scale change).

Appendix K

Results for DDA strategies

This section introduces the parameter STDs and biases when using the four DDA estimation strategies of Chapter 4. Considering the variation of SWH, Fig. K.1 shows that the STDs are very similar to the obtained RMSEs. This is justified by the very low biases especially when estimating SWH and τ as shown in Fig. K.2. Note also that the correlation between P_u and ξ_{al} leads to large biases and STDs for DDA5.

Considering the variation of ξ_{ac}, it can be seen that the large DDA3 RMSEs are mainly due to the presence of parameter biases as shown in Fig. K.4. Indeed, Fig. K.3 shows that the DDA3 parameter STDs remain acceptable until a value of $\xi_{\text{ac}} = 0.4°$ which can be exploited by elaborating bias correction tables in order to use the DDA3 for more mispointed data. The other estimation strategies present a low bias except for DDA5 when considering the correlated parameters P_u and ξ_{al}.

The last results are interested in the variation of ξ_{al}. Fig. K.6 shows the obtained biases using the different DDA strategies. The best results in terms of bias are obtained with G-DDA3 since it considers the exact values of mispointing angles. Moreover, we observe a similar behavior using DDA3, DDA4 and DDA5 for the 3 first parameters with low bias for small values of ξ_{al}. This result shows that there is no need to estimate ξ_{al} from the multi-look echo. This observation is confirmed by considering the STD results (see Fig. K.5) that show a similar behavior using the DDA strategies for SWH and τ. These results confirm the good performance of DDA4 since it provides similar results to DDA5 when varying ξ_{al}. Note finally that the DDA strategies provide good results for $\xi_{\text{al}} < 0.2°$ which is a common case for radar altimeter.

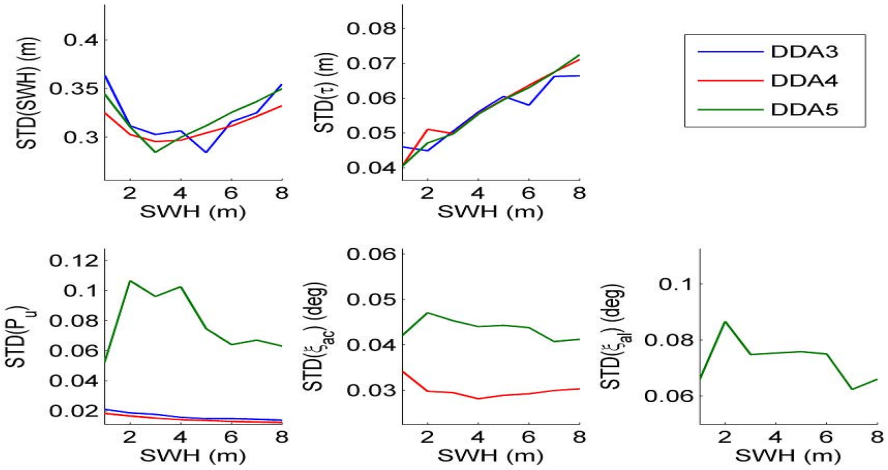

Figure K.1: Parameter STDs versus the sea wave height SWH when considering echoes without mispointing estimated with DDA3, DDA4 and DDA5. The simulation has been obtained using 500 Monte-Carlo realizations with the parameters $P_u = 1$, $\tau = 31$ gates, $\xi_{\text{al}} = 0°$ and $\xi_{\text{ac}} = 0°$.

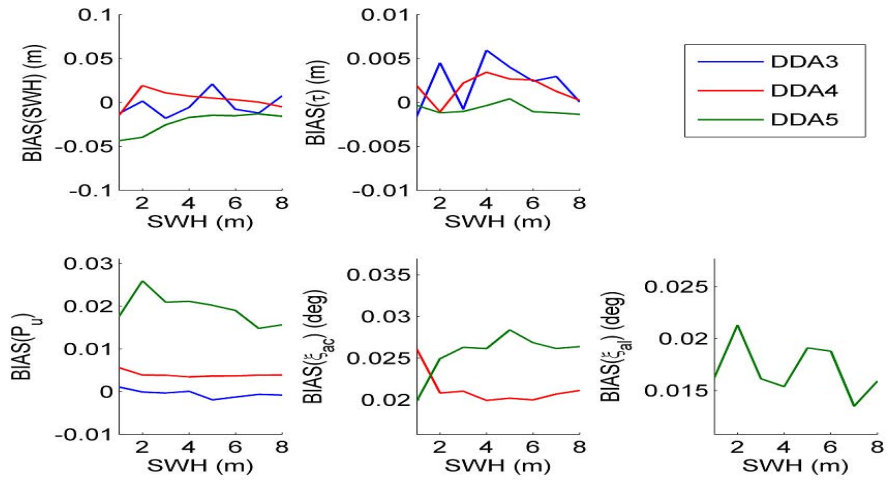

Figure K.2: Parameter biases versus the sea wave height SWH when considering echoes without mispointing estimated with DDA3, DDA4 and DDA5. The simulation has been obtained using 500 Monte-Carlo realizations with the parameters $P_u = 1$, $\tau = 31$ gates, $\xi_{\text{al}} = 0°$ and $\xi_{\text{ac}} = 0°$.

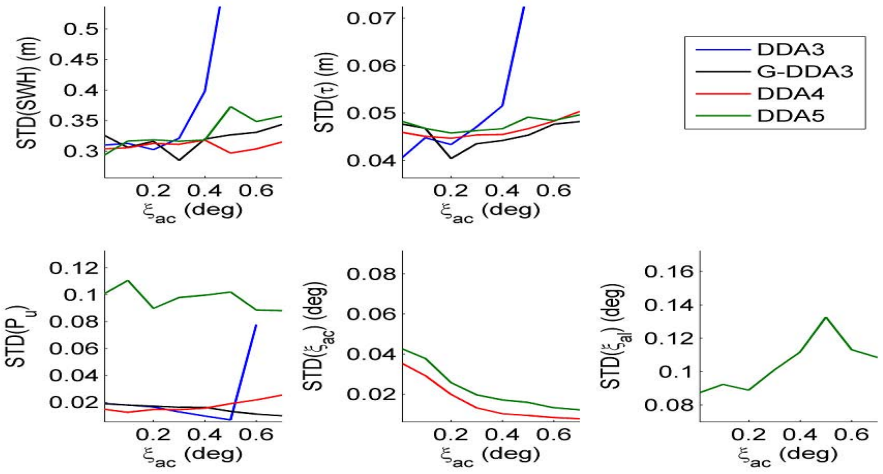

Figure K.3: Parameter STDs versus ξ_{ac} when considering DDA3, G-DDA3, DDA4 and DDA5. The simulation has been obtained using 500 Monte-Carlo realizations with the parameters $P_u = 1$, SWH $= 2$ m, $\tau = 31$ gates and $\xi_{\text{al}} = 0°$.

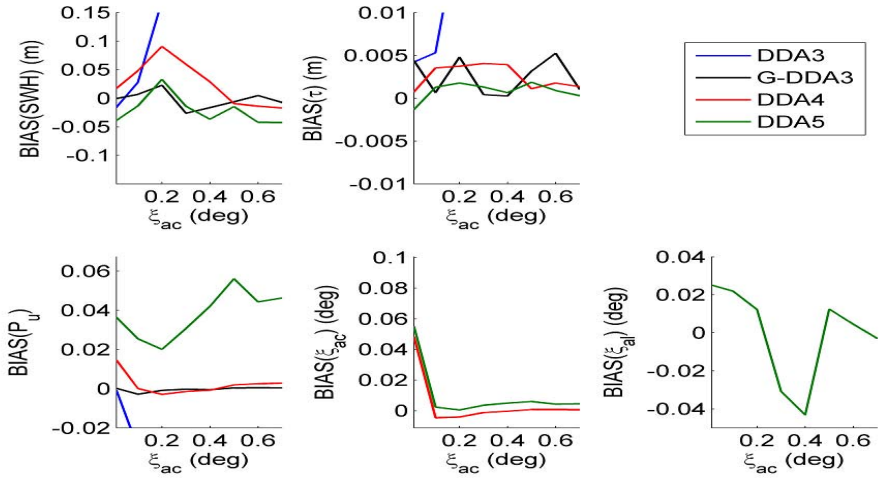

Figure K.4: Parameter biases versus ξ_{ac} when considering DDA3, G-DDA3, DDA4 and DDA5. The simulation has been obtained using 500 Monte-Carlo realizations with the parameters $P_u = 1$, SWH $= 2$ m, $\tau = 31$ gates and $\xi_{\text{al}} = 0°$.

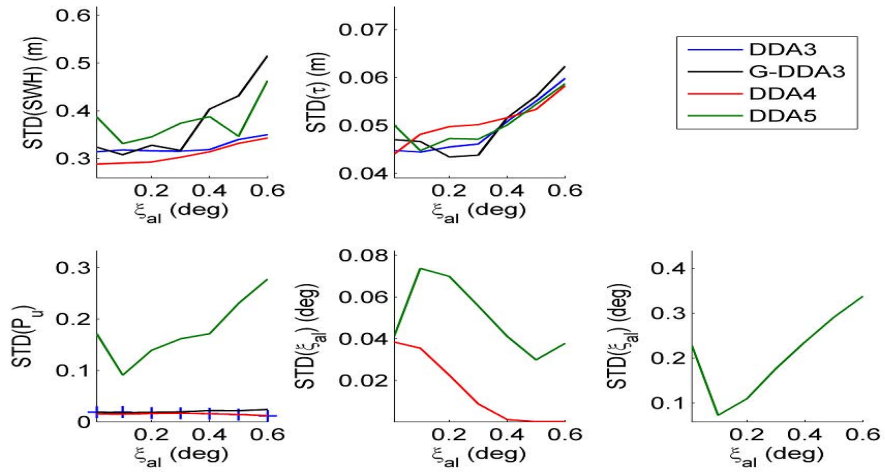

Figure K.5: Parameter STDs versus ξ_{al} when considering DDA3, G-DDA3, DDA4 and DDA5. The simulation has been obtained using 500 Monte-Carlo realizations with the parameters $P_u = 1$, SWH $=$ 2 m, $\tau = 31$ gates and $\xi_{\text{ac}} = 0°$.

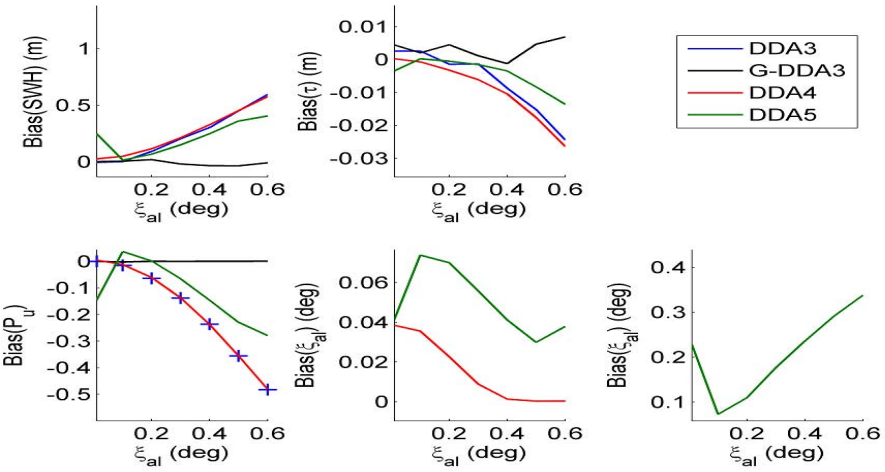

Figure K.6: Parameter biases versus ξ_{al} when considering DDA3, G-DDA3, DDA4 and DDA5. The simulation has been obtained using 500 Monte-Carlo realizations with the parameters $P_u = 1$, SWH $=$ 2 m, $\tau = 31$ gates and $\xi_{\text{ac}} = 0°$.

Bibliography

M. Abramowitz and I. A. Stegun. *Handbook of mathematical functions with formulas, graphs, and mathematical tables.* Courier Dover Publications, New york, 1965.

G. Alberti, L. Festa, C. Papa, and G. Vingione. A waveform model for near-nadir radar altimetry applied to the Cassini mission to Titan. *IEEE Trans. Geosci. and Remote Sensing*, 47(7):2252 –2261, July 2009.

L. Amarouche, E. Thouvenot, B. Chapron, and O.-Z. Zanife. A new estimator of the sea state bias using a three frequency radar altimeter. In *Proc. IEEE Int. Conf. Geosci. and Remote Sensing (IGARSS)*, pages 2510–2512, Sydney, Australia, July 9-13, 2001.

L. Amarouche, P. Thibaut, O. Z. Zanife, J.-P. Dumont, P. Vincent, and N. Steunou. Improving the Jason-1 ground retracking to better account for attitude effects. *Marine Geodesy*, 27(1-2):171–197, Aug. 2004.

G. W. Bangs. *Array processing with generalized beamformers.* PhD thesis, Yale University, New Haven, CT, USA, 1971.

L. Bao, Y. Lu, and Y. Wang. Improved retracking algorithm for oceanic altimeter waveforms. *Progress in Natural Science*, 19(2):195 – 203, 2009.

D. Barrick. Remote sensing of the sea state by radar. In *Remote sensing of the troposphere, V. E. Derr (ed.)*, Washington, DC: US Govt. Printing Office, 1972.

D. E. Barrick and B. J. Lipa. Analysis and interpretation of altimeter sea echo. *Advances in Geophysics*, 27:61–100, 1985.

J. Benveniste. Radar altimetry: Past, Present and Future. In S. Vignudelli, A. G. Kostianoy, P. Cipollini, and J. Benveniste, editors, *Coastal Altimetry*, pages 61–101. Springer Verlag, Berlin, 2011.

D. P. Bertsekas. *Nonlinear programming*. Athena Scientific, Belmont, Massachusetts, 1995.

P. Billingsley. *Probability and Measure*. John Wiley & Sons, Inc., United States of America, 3nd edition, 1995.

J. R. D. Boer. Estimation des paramètres altimétriques par réseau de neurones. Master's thesis, Institut National Polytechnique de Toulouse, Toulouse, France, 2006.

F. Boy, J.-D. Desjonqueres, A. Halimi, P. Thibaut, T. Moreau, and N. Picot. Cryosat Processing Prototype, LRM and SAR processing on CNES side and a comparison to DUACS SLA. In *Ocean Surface Topography Science Team Meeting*, Venice, Italy, Sept. 2012.

G. Brown. The average impulse response of a rough surface and its applications. *IEEE Trans. Antennas and Propagation*, 25(1):67–74, Jan. 1977.

G. Brown. A useful approximation for the Flat Surface Impulse Response. *IEEE Trans. Antennas and Propagation*, 37(6):764 – 767, June 1989.

P. Callahan and E. Rodriguez. Retracking of Jason-1 data. *Marine Geodesy*, 27(3):391–407, Oct. 2004.

P. Challenor, M. Srokosz, and R. T. Tokmakian. Maximum likelihood estimation for radar altimetry. In *Monitoring the Sea, IEE Colloquium on*, pages 10/1–10/3, Dec. 1990.

D. B. Chelton. Pulse compression and sea level tracking in satellite altimetry. *Journal of Atmospheric and Oceanic Technology*, 6(3):407–438, June 1989.

D. B. Chelton, J. C. Ries, B. J. Haines, L.-L. Fu, and P. S. Callahan. Chapter 1 satellite altimetry. In L.-L. Fu and A. Cazenave, editors, *Satellite Altimetry and Earth Sciences A Handbook of Techniques and Applications*, volume 69 of *International Geophysics*, pages 1 – ii. Academic Press, 2001.

H. S. M. Coxeter. *Regular Polytopes*. Dover Publications, Inc., New York, 1973.

C. Davis. Growth of the greenland ice sheet: a performance assessment of altimeter retracking algorithms. *IEEE Trans. Geosci. and Remote Sensing*, 33(5):1108–1116, 1995.

C. Davis. A robust threshold retracking algorithm for measuring ice-sheet surface elevation change from satellite radar altimeters. *IEEE Trans. Geosci. and Remote Sensing*, 35(4):974–979, 1997.

J.-P. Delmas and H. Abeida. Stochastic cramér-rao bound for noncircular signals with application to doa estimation. *Signal Processing, IEEE Transactions on*, 52(11):3192–3199, 2004.

X. Deng and W. E. Featherstone. A coastal retracking system for satellite radar altimeter waveforms: Application to ERS-2 around australia. *Journal of Geophysical Research: Oceans*, 111(C6):n/a–n/a, 2006.

J. D. Desjonqueres, G. Carayon, N. Steunou, and J. Lambin. Poseidon-3 radar altimeter: New modes and in-flight performances. *Marine Geodesy*, 33(sup1):53–79, Aug. 2010.

C. Desportes, E. Obligis, and L. Eymard. On the wet tropospheric correction for altimetry in coastal regions. *IEEE Trans. Geosci. and Remote Sensing*, 45(7):2139–2149, july 2007.

C. Desportes, E. Obligis, and L. Eymard. One-dimensional variational retrieval of the wet tropospheric correction for altimetry in coastal regions. *IEEE Trans. Geosci. and Remote Sensing*, 48(3):1001 –1008, march 2010.

J.-P. Dumont. *Estimation optimale des paramètres altimétriques des signaux radar Poséidon*. PhD thesis, Institut National Polytechnique de Toulouse, Toulouse, France, 1985.

K. Giles, D. Wingham, N. Galin, R. Cullen, and W. Smith. Precise estimates of ocean surface

parameters from cryosat. In *Ocean Surface Topography Science Team Meeting*, Venice, Italy, Sept. 2012.

J. Gómez-Enri, S. Vignudelli, G. D. Quartly, C. P. Gommenginger, P. Cipollini, P. G. Challenor, and J. Benveniste. Modeling ENVISAT RA-2 waveforms in the coastal zone: Case study of calm water contamination. *IEEE Geosci. and Remote Sensing Lett.*, 7(3):474–478, July 2010.

C. Gommenginger, C. Martin-Puig, S. Dinardo, D. Cotton, M. Srokosz, and J. Benveniste. Improved altimetric accuracy of SAR altimeters over the ocean: observational evidence from Cryosat-2 SAR and Jason-2. In *Ocean Surface Topography Science Team Meeting*, San Diego, California, Oct. 2011a.

C. Gommenginger, P. Thibaut, L. Fenoglio-Marc, G. Quartly, X. Deng, J. Gomez-Enri, P. Challenor, and Y. Gao. Retracking altimeter waveforms near the coasts. In S. Vignudelli, A. G. Kostianoy, P. Cipollini, and J. Benveniste, editors, *Coastal Altimetry*, pages 61–101. Springer Verlag, Berlin, 2011b.

C. Gommenginger, P. Cipollini, D. Cotton, S. Dinardo, and J. Benveniste. Finer, better, closer: Advanced capabilities of SAR altimetry in the open ocean and the coastal zone. In *Ocean Surface Topography Science Team Meeting*, Venice, Italy, Sept. 2012a.

C. Gommenginger, C. Martin-Puig, S. Dinardo, D. Cotton, and J. Benveniste. Improved altimetric performance of Cryosat-2 SAR mode over the open ocean and the coastal zone. In *Proc. IEEE Int. Conf. Geosci. and Remote Sensing (IGARSS)*, Munich, Germany, July 22-27, 2012b.

P. J. Green. Iteratively reweighted least squares for maximum likelihood estimation, and some robust and resistant alternatives. *Journal of the Royal Statistical Society. Series B (Methodological)*, 46 (2):149–192, 1984.

A. Halimi, C. Mailhes, J.-Y. Tourneret, and P. Thibaut. Modélisation des signaux altimétriques en présence de pics. In *Actes du XXIIIième Colloque GRETSI*, Bordeaux, France, Sept. 2011a.

A. Halimi, C. Mailhes, J.-Y. Tourneret, and P. Thibaut. A new model for peaky altimetric waveforms. In *Proc. IEEE Int. Conf. Geosci. and Remote Sensing (IGARSS)*, pages 2825–2828, Vancouver, Canada, July 24-29, 2011b.

A. Halimi, C. Mailhes, J.-Y. Tourneret, F. Boy, N. Picot, and P. Thibaut. An analytical model for Doppler altimetry and its estimation algorithm. In *Ocean Surface Topography Science Team Meeting*, Venice, Italy, September 2012.

A. Halimi, C. Mailhes, and J.-Y. Tourneret. Cramér-Rao bounds and estimation algorithms for delay/Doppler and conventional altimetry. In *EUSIPCO-13*, Marrakech, Marocco, Sept. 2013a.

A. Halimi, C. Mailhes, J.-Y. Tourneret, and T. Boy, Moreau. Modèle semi-analytique pour l'altimétrie SAR/Doppler sur océan. In *Actes du XXIVième Colloque GRETSI*, Brest, France, Sept. 2013b.

A. Halimi, C. Mailhes, J.-Y. Tourneret, T. Moreau, and F. Boy. A generalized semi-analytical model for delay/Doppler altimetry and its estimation algorithms. 2013c. submitted.

A. Halimi, C. Mailhes, J.-Y. Tourneret, P. Thibaut, and F. Boy. Parameter estimation for peaky altimetric waveforms. *IEEE Trans. Geosci. and Remote Sensing*, 51(3):1568–1577, March 2013d.

A. Halimi, C. Mailhes, J.-Y. Tourneret, P. Thibaut, and F. Boy. A semi-analytical model for delay/Doppler altimetry and its estimation algorithm. *IEEE Trans. Geosci. and Remote Sensing*, 2013e. to appear.

G. Hayne. Radar altimeter mean return waveforms from near-normal-incidence ocean surface scattering. *IEEE Trans. Antennas and Propagation*, 28(5):687 – 692, Sept. 1980.

N. E. Huang and S. R. Long. An experimental study of the surface elevation probability distribution and statistics of wind-generated waves. *J. of Fluid Mechanics*, 101(1):179–200, Nov. 1980.

C. Hwang, J. Guo, X. Deng, H.-Y. Hsu, and Y. Liu.

J. Jensen and R. Raney. Delay/Doppler radar altimeter: better measurement precision. In *Proc.*

IEEE Int. Conf. Geosci. and Remote Sensing (IGARSS), pages 2011–2013, Seattle, U.S.A., July 6-10, 1998.

A. Jordi and D. P. Wang. Application of ensemble kalman filter for satellite altimetry data assimilation in the mediterranean sea. In *International Workshop on Modeling the Ocean*, Norfolk, VA, U.S.A., May 24-26, 2010.

M. Kendall and A. Stuart. *The advanced theory of statistics. Vols. II.* Charles Griffin & Company limited, London, 1961.

J. C. Lagarias, J. A. Reeds, M. H. Wright, and P. E. Wright. Convergence properties of the nelder-mead simplex method in low dimensions. *SIAM J. Optim.*, 9(1):112–147, 1998.

H. Lee, C. Shum, Y. Yi, A. Braun, and C.-Y. Kuo. Laurentia crustal motion observed using topex/poseidon radar altimetry over land. *Journal of Geodynamics*, 46(3-5):182 – 193, 2008.

J. MacArthur. Design of the Seasat-A radar altimeter. pages 222 –229, Washington, U.S.A., Sept. 13-15, 1976.

J. MacArthur and J. H. U. A. P. Laboratory. *SEASAT - a radar altimeter design description.* Johns Hopkins University Applied Physics Laboratory, 1978.

C. Mailhes, J.-Y. Tourneret, J. Severini, and P. Thibaut. Cramér-rao bounds for radar altimeter waveforms. In *EUSIPCO-08*, Lausanne, Switzerland, 28 August 2008.

C. Martin-Puig and G. Ruffini. SAR altimeter retracker performance bound over water surfaces. In *Proc. IEEE Int. Conf. Geosci. and Remote Sensing (IGARSS)*, pages 449 –452, South Africa, July 12-17, 2009.

C. Martin-Puig, G. Ruffini, J. Marquez, D. Cotton, M. Srokosz, P. Challenor, R. K. Raney, and J. Benveniste. Theoretical model of SAR altimeter over water surfaces. In *Proc. IEEE Int. Conf. Geosci. and Remote Sensing (IGARSS)*, pages 242 – 245, Boston, U.S.A., July 7-11, 2008.

C. Martin-Puig, P. Berry, R. Smith, C. Gommenginger, G. Ruffini, P. Cipollini, L. Stenseng, A. O., P. Cotton, J. Benveniste, and S. Dinardo. SAR altimetry over water surfaces. In *Oceans from Space*, Venice, Italy, April 2010.

S. Maus, C. M. Green, and J. D. Fairhead. Improved ocean-geoid resolution from retracked ERS-1 satellite altimeter waveforms. *Geophys. J. Int.*, 134(1):243–253, Feb. 1998.

F. Mercier *et al.* The PISTACH project for coastal altimetry: status, products and early results. In *Ocean Surface Topography Science Team Meeting*, Seattle, WA, 1998.

R. Moore and C. Williams. Radar terrain return at near-vertical incidence. *Proceedings of the IRE*, 45(2):228–238, Feb. 1957.

P. Naenna and J. Johnson. A Monte Carlo study of altimeter pulse returns and the electromagnetic bias. *IEEE Trans. Geosci. and Remote Sensing*, 48(8):3218–3224, aug. 2010.

J. A. Nelder and R. Mead. A simplex method for function minimization. *Computer Journal*, 7(4): 308–313, 1965.

J. Nocedal and S. Wright. *Numerical Optimization.* Springer, New-York, 1999.

A. Ollivier. *Nouvelle approche pour l'extraction de paramètres géophysiques à partir des mesures en altimétrie radar.* PhD thesis, Institut National Polytechnique de Grenoble, Grenoble, France, 2006.

A. Papoulis and S. U. Pillai. *Probability, Random Variables and Stochastic Processes.* McGraw Hill Higher Education, 2002.

L. Phalippou and F. Demeestere. Optimal re-tracking of SAR altimeter echoes over open ocean: from theory to results for SIRAL2. In *Ocean Surface Topography Science Team Meeting*, San Diego, California, Oct. 2011.

L. Phalippou and V. Enjolras. Re-tracking of SAR altimeter ocean power-waveforms and related accuracies of the retrieved sea surface height, significant wave height and wind speed. In *Proc.*

IEEE Int. Conf. Geosci. and Remote Sensing (IGARSS), pages 3533–3536, Barcelona, Spain, July 23-27, 2007.

L. Phalippou, E. Caubet, F. Demeestere, J. Richard, L. Rys, M. Deschaux-Beaume, R. Francis, and R. Cullen. Reaching sub-centimeter range noise on Jason-CS with the Poseidon-4 continuous SAR interleaved mode. In *Ocean Surface Topography Science Team Meeting*, Venice, Italy, Oct. 2012.

G. Picardi, R. Seu, and S. Sorge. Extensive non-coherent averaging in Doppler beam sharpened space-borne radar altimeters. In *Proc. IEEE Int. Conf. Geosci. and Remote Sensing (IGARSS)*, pages 2643–2645, Seattle, U.S.A., July 6-10, 1998.

B. Porat and B. Friedlander. Performance analysis of parameter estimation algorithms based on high-order moments. *Int. J. Adapt. Control Signal Process*, 3(3):191–229, September 1989.

G. D. Quartly, M. A. Srokosz, and A. C. McMillan. Analyzing altimeter artifacts: statistical properties of ocean waveforms. *Journal of Atmospheric and Oceanic Technology*, 18:2074Ũ2091, December 2001.

R. K. Raney. The delay/Doppler radar altimeter. *IEEE Trans. Geosci. and Remote Sensing*, 36(5): 1578–1588, Sept. 1998.

R. K. Raney. Cryosat SAR-mode looks revisited. *IEEE Geosci. and Remote Sensing Lett.*, 9(3): 393–397, May 2012a.

R. K. Raney. Maximizing the intrinsic precision of radar altimetric measurements. In *20 Years of Progress in Radar Altimetry*, Venice, Italy, Sept. 2012b.

R. K. Raney and L. Phalippou. The future of coastal altimetry. In S. Vignudelli, A. G. Kostianoy, P. Cipollini, and J. Benveniste, editors, *Coastal Altimetry*, pages 535–559. Springer Verlag, Berlin, 2011.

I. S. Robinson. *The methods of satellite oceanography.* Springer Praxis Books. Springer Berlin Heidelberg, 2010.

E. Rodriguez. Altimetry for non-Gaussian oceans: height biases and estimation of parameters. *J. Geophys. Res.*, 93(C11):14107–14120, Nov. 1988.

E. Rodriguez and B. Chapman. Extracting ocean surface information from altimeter returns: the deconvolution method. *J. Geophys. Res.*, 94, 1989.

E. Rodriguez and J.-M. Martin. Assessment of the TOPEX altimeter performance using waveform retracking. *J. Geophys. Res.*, 99(C12):24957–24969, Dec. 1994.

V. Rosmorduc, J. Benveniste, O. Lauret, C. Maheu, M. Milagro, and N. Picot. Radar altimetry tutorial. Technical report, 2009. URL http://www.altimetry.info.

W. Rudin. *Principles of Mathematical Analysis (Third Edition)*. McGraw-Hill, New York, 1976.

D. T. Sandwell. Radar altimetry. Technical report, University of California San Diego, 2011. URL topex.ucsd.edu/rs/altimetry.pdf.

D. T. Sandwell and W. H. F. Smith. Retracking ERS-1 altimeter waveforms for optimal gravity field recovery. *Geophys. J. Int.*, 163(1):79–89, Oct. 2005.

J. Severini. *Estimation et classification des signaux altimétriques*. PhD thesis, Institut National Polytechnique de Toulouse, Toulouse, France, 2010.

Y. Shuang-Bao, L. He-Guang, X. Ke, and X. Xi-Yu. The mean echo model and data process of SAR altimeter. In *Proc. IEEE Int. Conf. Geosci. and Remote Sensing (IGARSS)*, pages 2077 – 2080, Vancouver, Canada, July 24-29, 2011.

D. Slepian. Estimation of signal parameters in the presence of noise. *Information Theory, Transactions of the IRE Professional Group on*, 3(3):68–89, 1954.

W. H. F. Smith and R. Scharroo. Retracking range, SWH, sigmanaught, and attitude in Cryosat conventional ocean data. In *Ocean Surface Topography Science Team Meeting*, San Diego, California, Oct. 2011.

W. H. F. Smith and R. Scharroo. Pulse-to-pulse correlation in Cryosat SAR echoes from ocean surfaces: implications for optimal pseudo-LRM waveform averaging. In *Ocean Surface Topography Science Team Meeting*, Venice, Italy, Sept. 2012.

W. H. F. Smith, P. Thibaut, P. Berry, and L. Fenoglio-Marc. Tracking and retracking. In *Coastal Altimetry Workshop*, Silver Spring, United States of America, 2008.

P. Thibaut and J. C. Poisson. Waveforms processing in PISTACH project. In *2nd Coastal Altimetry Workshop*, Pisa, Italy, 2008.

P. Thibaut, L. Amarouche, O. Z. Zanife, N. Steunou, P. Vincent, and P. Raizonville. Jason-1 altimeter ground processing look-up correction tables. *Marine Geodesy*, 27(3-4):409–431, July 2004.

P. Thibaut, J. C. Poisson, E. Bronner, and N. Picot. Relative performance of the MLE3 and MLE4 retracking algorithms on jason-2 altimeter waveforms. *Marine Geodesy*, 33(sup1):317–335, March 2010.

J. Tournadre, J. Lambin-Artru, and N. Steunou. Cloud and rain effects on AltiKa/SARAL Ka-band radar altimeter – part I: Modeling and mean annual data availability. *IEEE Trans. Geosci. and Remote Sensing*, 47(6):1806–1817, june 2009a.

J. Tournadre, J. Lambin-Artru, and N. Steunou. Cloud and rain effects on ALTIKA/SARAL Ka-band radar altimeter – part II: Definition of a rain/cloud flag. *IEEE Trans. Geosci. and Remote Sensing*, 47(6):1818 –1826, june 2009b.

J. Tournadre, B. Chapron, and N. Reul. High-resolution imaging of the ocean surface backscatter by inversion of altimeter waveforms. *Journal of Atmospheric and Oceanic Technology*, 28(8):1050–1062, aug 2011.

J.-Y. Tourneret, C. Mailhes, J. Severini, and P. Thibaut. Parameter estimation for peaky altimetric waveforms. In *Oceans from Space*, Venise, Italy, 26-30 April 2010.

S. Vignudelli, A. G. Kostianoy, P. Cipollini, and J. Benveniste. *Coastal Altimetry*. Springer Verlag, Berlin, 2011.

E. J. Walsh. Pulse-to-pulse correlation in satellite radar altimeters. *Radio Science,*, 17(4):786–800, Aug. 1982.

D. Wingham, L. Phalippou, C. Mavrocordatos, and D. Wallis. The mean echo and echo cross product from a beamforming interferometric altimeter and their application to elevation measurement. *IEEE Trans. Geosci. and Remote Sensing*, 42(10):2305 – 2323, Oct. 2004.

D. Wingham, C. R. Francis, S. Baker, C. Bouzinac, D. Brockley, R. Cullen, P. de Chateau-Thierry, S. Laxon, U. Mallow, C. Mavrocordatos, L. Phalippou, G. Ratier, L. Rey, F. Rostan, P. Viau, and D. Wallis. Cryosat: A mission to determine the fluctuations in Earth's land and marine ice fields. *Advances in Space Research*, 37(4):841 – 871, July 2006.

D. J. Wingham, C. G. Rapley, and H. Griffiths. New techniques in satellite altimeter tracking systems. In *Proc. IEEE Int. Conf. Geosci. and Remote Sensing (IGARSS)*, pages 1339–1344, Zurich, aug 1986.

O. Zanifé, P. Thibaut, L. Amarouche, B. Picard, P. Vincent, and N. Picot. Assesment of the JASON-1 look-up tables using multiple gaussian functions as an approximation of the PTR. In *Ocean Surface Topography Science Team Meeting*, Venice, Italy, March 2006.

A. Zapevalov. Effect of skewness and kurtosis of sea-surface elevations on the accuracy of altimetry surface level measurements. *Izvestiya, Atmospheric and Oceanic Physics*, 48(2):200–206, April 2012.